ELECTRODEPOSITION OF ULTRATHIN Pd, Co AND Bi FILMS ON WELL-DEFINED NOBLE-METAL ELECTRODES: STUDIES BY ULTRAHIGH VACUUM-ELECTROCHEMISTRY (UHV-EC)

A Dissertation

by

JACK HESS L. BARICUATRO

Submitted to the Office of Graduate Studies of
Texas A&M University
in partial fulfillment of the requirements for the degree of

DOCTOR OF PHILOSOPHY

August 2006

Major Subject: Chemistry

ELECTRODEPOSITION OF ULTRATHIN Pd, Co AND Bi FILMS ON WELL-DEFINED NOBLE-METAL ELECTRODES: STUDIES BY ULTRAHIGH VACUUM-ELECTROCHEMISTRY (UHV-EC)

A Dissertation

by

JACK HESS L. BARICUATRO

Submitted to the Office of Graduate Studies of
Texas A&M University
in partial fulfillment of the requirements for the degree of

DOCTOR OF PHILOSOPHY

Approved by:

Chair of Committee,	Manuel P. Soriaga
Committee Members,	Paul S. Cremer
	Gyula Vigh
	Michael B. Weimer
Head of Department,	Emile A. Schweikert

August 2006

Major Subject: Chemistry

ABSTRACT

Electrodeposition of Ultrathin Pd, Co and Bi Films on Well-defined Noble-metal Electrodes: Studies by Ultrahigh Vacuum-Electrochemistry (UHV-EC). (August 2006)

Jack Hess L. Baricuatro, B.S.; M.S., University of San Carlos

Chair of Advisory Committee: Dr. Manuel P. Soriaga

Three illustrative cases involving the electrodeposition of ultrathin metal films of varying reactivities onto noble-metal substrates were investigated: (*i*) Pd on Pt(111), a noble admetal on a noble-metal surface; (*ii*) Bi on Pd(111), a less noble admetal on a noble-metal surface; and (*iii*) Co on polycrystalline Pd and Pd(111), a reactive metal on a noble-metal surface. The interfacial electrochemistry of these prototypical systems was characterized using a combination of electrochemical methods (voltammetry and coulometry) and ultrahigh vacuum electron spectroscopies (Auger electron spectroscopy, AES; low energy electron diffraction, LEED; and X-ray photoelectron spectroscopy, XPS).

Potential-controlled adsorption-desorption cycles of aqueous bromide exerted surface smoothening effects on ultrathin Pd films with defect sites (steps). This procedure, dubbed as electrochemical (EC) annealing, constituted a nonthermal analogue to conventional annealing. EC-annealed ultrathin Pd films exhibited long-range surface order and remained free of oxygen adspecies. Pd

adatoms occupying step-sites were selectively dissolved and/or rearranged to assume equilibrium positions in a well-ordered (1x1) film.

Electrodeposition of Co was found to be highly surface-structure-sensitive. While virtually no Co electrodeposition transpired on a clean Pd(111) surface, Co was voltammetrically deposited on (*i*) a Pd(111) electrode roughened by oxidation-reduction cycles; and (*ii*) thermally annealed polycrystalline Pd, which is a composite of the (111) and (100) facets. Electrodeposition of Co was also observed to be kinetically hindered and slow potential scan rates (0.1 mV/s) were required.

Well-defined ultrathin Bi films were potentiostatically electrodeposited onto Pd(111); a Stranski-Krastanov growth mode was indicated. The electrochemical reactivity of ultrathin Bi films was characterized using two surface probes: aqueous iodide and D-glucose. (*i*) Exposure of the prepared Bi adlayers ($\Theta_{Bi} \geq 0.33$) to aqueous iodide gave rise to (√3x√7) I-*on*-Bi superlattice. The same superlattice was obtained if Bi was electrodeposited onto Pd(111)(√3x√3)R30°-I. (*ii)* With respect to electrooxidation of D-glucose on Pd(111), the presence of Bi adlayers inhibited the by-product-induced "surface poisoning" of Pd(111) but reduced its electrocatalytic efficiency.

DEDICATION

The completion of this research work is a personal crucible that fuses, tempers and purifies both character and conviction. Anyone who has willfully chosen to finish an academic endeavor like this can attest to the arduous nature of the task. A wellspring of hope and caring attention from family and friends can certainly cultivate a man to do more in order to be more. No words, no gifts, no fiery oblations materially exist to honor fully the following people who have greatly influenced my life:

Dr. Francisco G. Baricuatro, my dad, whom I lost too early before the start of my academic career, would have been proud to see another "doctor" in the family; my mom, Estrellita, for her unqualified love; my brother, Farley, for the personal sacrifices only a loyal big brother can muster; and my sister, Lea, for unselfishly giving me the luxurious New York taste of life;

Leonarda C. Mission, my *yaya*, who gave up her life in the service of my family;

co-volunteers at the Saturday church service of St. Mary's Catholic Church, College Station, specifically Vernon and Elaine Newland, Karen Thompson and Helen Meyer; you have become my spiritual strength and compass in a distant land away from home;

and all my mentors who have engendered my passion for science and love for words.

This work is, hence, an offering so that in all things God may be glorified.

ACKNOWLEDGMENTS

The author is indebted to Dr. Manuel P. Soriaga who, in his capacity as research advisor and mentor, has amply provided expert counsel and intellectual support for this project. Much of the success of this work stems from the creative freedom nurtured in a laboratory that thrives upon his wisdom, compassion and edifying admonition.

Fruitful discussions with Dr. Paul S. Cremer, Dr. Gyula Vigh and Dr. Michael B. Weimer are gratefully acknowledged.

Contributions from past and present members of the Electrochemical Surface Science Laboratory have enriched the depth and scope of this project. The author, during his early years at Texas A&M University, has benefited from the mentorship rendered by a pool of talented research-group alumni: Dr. Yeon-Geun Kim, Dr. Yeon Su Park and Dr. Xiaole Chen. Logistical and manual assistance from Mohammad Akhtar Hossain, Juan Cruz and Ding Li has facilitated the maintenance of the ultrahigh vacuum-electrochemistry chamber used in this work. The author deeply appreciates the company of and cerebral conversations with Jean Sanabria-Chinchilla and his wife Silvia Sanchez, in and out of the laboratory.

Funding for this research was provided by The Welch Foundation and the National Science Foundation.

TABLE OF CONTENTS

Page

LIST OF FIGURES

Page

Page

Page

Page

Page

Page

LIST OF TABLES

INTRODUCTION

The platinum-group metals are the main workhorses in the field of catalysis [1]. This group consists of Pt, Pd, Rh, Ir, Ru, and Os. Although these metals are characteristically bulk-oxidation-resistant, noble-metal surfaces have provided a dynamic arena of industrially and technologically important chemical reactions. The physico-chemical properties of these metals find important applications, *inter alia*, in fuel cells, synthetic organic chemistry, petrochemical refining and processing, and electronics.

Palladium is an atypical member of the platinum group in several respects: (*i*) Although still considered to be a noble metal, Pd dissolves in concentrated strong acids such as HCl and HNO_3, especially in the presence of O_2 [2]. (*ii*) Pd has the ability to adsorb *and* absorb hydrogen; its hydrogen uptake can reach up to 900 times its own volume at room temperature [3,4]. (*iii*) The intermetallic Pd-Pd bonds are anomalously weak, thereby facilitating the formation of adsorbate-substrate bonds [5]. Such combination of idiosyncratic properties poses a fascinating prototypical case study for surface physicists, materials scientists, and electrochemists whose ultimate goal is the fundamental understanding and atomic-level manipulation of these properties for advanced and novel applications.

This dissertation follows the style of the Journal of Electroanalytical Chemistry.

Modifying the Interfacial Properties of Pd

The inherent interfacial properties of Pd can be dramatically altered in many ways. Alloy formation is a classical strategy of fusing together two or more metals. Alloying can be typically accomplished either by thermal treatment [6] or electrodeposition [7]. The resultant properties are concentration-dependent and often manifest as hybrid features of the constituents. Because of the changes in the electronic structure of the base metal, the emergence of unique attributes is not unusual. A caveat to this preparative strategy is the occurrence of surface segregation upon equilibration [8]. The component with the lowest surface free-energy floats to the surface; consequently, the intended bulk composition significantly varies from the surface composition [9].

Ultrathin film formation is an experimental tactic that can tailor physico-chemical properties of metals. The term "ultrathin film" is used in stark contradistinction to classical "thin films" of micrometer thicknesses. In this investigation, discrete well-defined atomic layers are prepared such that an *ideal* full monolayer (ML) coverage constitutes a thickness in the order of 3 to 5 Å for adsorbates occupying three-fold hollow surface-sites. The highest surface coverage explored in this study is 8 ML.

Ultrathin film deposition involves the growth of discrete atomic layers onto a given substrate. Depending on the lattice parameters of the substrate and the adsorbate, the film growth mode may occur in any of the following fashion: (*i*) Frank-van der Merwe (layer-by-layer formation), (*ii*) Volmer-Weber (three-dimensional island formation), or (*iii*) Stranski-Krastanov (island formation

preceded by an epitaxial "wetting" layer) [9, 10]. Except at the substrate-adsorbate interface of a highly miscible metal pair, atomic intermixing and compound formation are very limited, if not absent, under highly controlled deposition; in contrast, such occurrences are sought for in vintage alloy formation when drastic thermal or potential perturbation is employed [11]. Investigations on thin film formation are currently on an upsurge due to the possibility of tailoring these ultrathin films into nanometer-scale surface structures that exhibit size-quantization effects [12, 13].

High quality multimetallic thin films with well-characterized interfaces have been prepared using a host of vacuum-based techniques such as vapor deposition and sputtering [14]. While the successes of these preparative routes are well documented, the stringent experimental protocols and the large capital investment associated with these techniques make them difficultly accessible for most laboratories. An inexpensive yet powerful alternative to vacuum-based techniques is electrochemical deposition [13]. Electrochemical methods allow, at ambient conditions, thermodynamic and kinetic control of the deposition process by fine-tuning the applied potential, scan rate, solution pH, and electrolyte composition.

Electronic and geometric effects on metal surfaces can be recognized and analyzed by the systematic introduction of a family of elements onto a chosen catalyst [15, 16, 17, 18, 19]. This combinatorial approach constitutes a permutative scheme of discovering effective bimetallic catalysts [20] and probing the mechanism behind their distinctive catalytic performance. For this

purpose, a gamut of metals and semi-metals has already been deposited on both polycrystalline and low-index single crystals of Pd and Pt. Previous electrodeposition studies on the platinum-group metal surfaces are driven by three-fold goals: (*i*) the quest for an ideal fuel cell electrode [21, 22] (*ii*) fabrication of advanced materials and devices [23, 24, 25], and (*iii*) acquisition of fundamental knowledge on the electrocatalytic phenomenon [26, 27]. This research attempts to enrich the remarkably interesting, yet sparsely documented, interfacial chemistry of ultrathin Pd films and ultrathin-film-modified Pd(111).

Ultrathin Pd Films on Pt

Considerable interest on the growth of ultrathin Pd films on well-defined Pt surfaces stems from the fact that the Pd-Pt pair represents a prototypical bimetallic system whose constituents share similar lattice parameters and atomic radii but have different cohesive energies [28]. Ultrathin Pd films do not suffer from perturbations of hydrogen absorption [29], which often encumbers voltammetric characterization of Pd bulk samples. Of particular interest is the possible emergence of properties that are otherwise absent in the pure state of each constituent. These novel properties often vary concomitantly with ultrathin-film-to-bulk transition [30]. The search for electrochemical surface probes to monitor this transition is worthwhile pursuing to provide a robust alternative to UHV-based electron spectroscopies.

In one of the earliest studies of Pd-film formation on single-crystal Pt substrates, Attard and Bannister [31] reported the presence of a voltammetric

peak associated with hydrogen adsorption on monolayer and submonolayer coverages of Pd. A second hydrogen adsorption peak was later on observed by Clavier and coworkers [32]. Studies using surface X-ray scattering [33] and electrochemical scanning tunneling microscopy [34] indicated a Stranski-Krastanov growth mode for Pd; i.e. the first Pd monolayer is pseudomorphic with the Pt(111) substrate and subsequent Pd adatoms form islands.

Halides exhibit interesting interfacial behavior on ultrathin Pd film surfaces. LEED studies on the coverage-dependent interaction of iodide ions with ultrathin Pd films on Pt(111) [35] revealed that, for 1-2 ML Pd/Pt(111), mixed iodine domains of (3x3) and (√3x√3) were observed; at higher Pd coverages, chemisorbed iodine exhibited only a (√3x√3) LEED pattern. On pristine surfaces, iodine distinctly forms a (3x3) adlattice on Pt(111) and a (√3x√3) adlattice on Pd(111). The aforementioned results underscored the possibility of using chemisorbed halides in monitoring ultrathin-film-to-bulk transition.

One of the challenges in electrodepositing ultrathin metallic films is to achieve surface order in an electrochemical environment replete with solvent molecules and other solution species. The present report describes the preparation, surface characterization, and interfacial electrochemistry of ultrathin Pd films on Pt(111) surfaces. The interaction of bromine with the prepared ultrathin films provided a premise for a proposed electrochemical analogue to thermal annealing. Programmed electrode-potential excursions to regions bordering dramatic surface perturbations (hydrogen adsorption and

surface anodic oxidation) are demonstrated to produce surface smoothening effects; this potential cycling is dubbed as electrochemical annealing (EC annealing).

For the purpose of this investigation, Pd multilayers (6 to 8 ML) that clearly manifest H-atom desorption-adsorption peaks for terrace and step sites were chosen. The underpotential deposition of hydrogen on Pd is notably a *thin-film* phenomena because, in the presence of bulk Pd, the extremely high hydrogen uptake makes adsorption virtually indistinguishable from absorption. The appearance of these anomalous *thin-film* peaks on thick (bulk-like) films is attributed to surface defects such as steps and pits; hence, these peaks can be used as voltammetric markers for the progress of the so-called EC-annealing process.

Ultrathin Co Films on Pd

Prospects of using superlattices of Co and Pd or Pt in the next-generation magneto-optical (MO) storage devices provided the motivation to investigate the preparation, growth, and interfacial properties of ultrathin Co films. Both novel systems offer greater chemical stability and better polar Kerr activity at prolonged exposures to blue to blue-green lasers [36-38]. Of the two next-generation MO materials, the Co-Pd superlattice is the better choice when it comes to coercivity. Coercivity is the magnitude of the applied field needed to flip the magnetic domain from one state to another; hence, it is related to the stability of stored information in an MO device [39].

Multiple stacking of magnetic and non-magnetic interfaces gives rise to perpendicular magnetic anisotropy, as predicted by the Néel mechanism [37]. This mechanism maintains that interfacial symmetry discontinuities and changes in the nearest-neighbor coordination lead to orientation-dependent magnetization behavior. Strain anisotropy resulting from a large lattice mismatch further enhances PMA [38]; such case is typified by the superlattices of Co (fcc a_o = 3.552Å) and Pd (fcc a_o = 3.89Å). Another essential determinant of PMA is spin-orbit interaction that emanates from both spin and orbital angular momenta of electrons. Experimental evidence shows that Co thin films deposited onto Pd have greatly enhanced orbital moment compared to bulk Co [40].

Tailoring the magnetic properties of Co-Pd superlattices requires a clear understanding of the growth mechanism of this bimetallic system. Early studies utilizing low-energy ion scattering spectroscopy (LEIS) and X-ray photelectron spectroscopy (XPS) describe the formation of islands with uniform thickness [41]. However, contradictory reports indicate a Volmer-Weber growth mode where pseudomorphic multilayer Co islands are observed up to 20 monolayers; within the first two monolayers, a slight tetragonal distortion of the Co fcc structure is implied by X-ray photoelectron diffraction (XPD) data [42]. Such distortion is also the subject of contention from research groups using reflection high-energy electron diffraction (RHEED) and low-energy electron diffraction (LEED) [43, 44]. Recent studies using ultrahigh vacuum scanning tunneling microscopy (UHV-STM) reveal layer-by-layer epitaxy up to a thickness of 2

monolayers (ML); at high coverages of *ca*. 10 ML, the surface becomes uniformly strewn with three-dimensional clusters [45].

These mechanistic discrepancies possibly originate from the nature of the various preparative methods [42]. Popular methods include, *inter alia*, sputtering [36] and vapor deposition [37]. Although the MO properties of sputtered films are comparable to those of evaporated films, the magnitude of these properties is often determined by parameters inherent to the method such as substrate temperature and sputtering agents [46]. Subtle differences in physico-chemical properties may also arise from the extent of atomic mingling at the interface. Impacts coming from bombarding species during sputtering are shown to favor interfacial alloying; evidences are provided by XPS shape-pattern recognition [47] and polarized extended X-ray absorption fine structure (EXAFS) [48]. Enhancement of MO properties, such as remanent magnetization and PMA, has been observed for sputtered surfaces [49]. Claims of better MO properties are also noted from the evaporated films with intentionally alloyed layers [50].

The absence of deposition techniques that allow precise layer-by-layer control and monitoring of interfacial structures provided strong impetus towards the proposal of experimental protocols that can delineate monolayer and multilayer depositions.

Electrodeposition is an attractive, yet underutilized, option for the synthesis of metallic multilayered structures. Since the process is generally carried out at temperatures much lower than those employed in vapor deposition and sputtering techniques, sharper interfaces are produced due to

minimal, if not negligible, interdiffusion. Electrodeposition employs low-cost instrumentation and offers a flexible choice of precursor materials for the constituent layers of the superlattice. Deposition parameters, such as applied potential, current density, solution pH, supporting electrolyte and agitation, can be strategically programmed to yield compositionally controlled layers with desired target properties.

The ability of electrochemical methods to prepare contaminant-free heteroepitaxial ultrathin layers with sharp interfaces –- a proposition once deemed to be exclusively accomplished under ultrahigh vacuum conditions –- has been clearly demonstrated in the electrodeposition of ultrathin magnetic films of Co and Cu [51**]**. Aside from the Co-Cu [52] system, investigations of electrodeposited magnetic multilayered structures are generally limited to Co-Pt [53-55] and Co-Au [56-57].

To accumulate fundamental knowledge of the interfacial chemistry of Co and Pd, systematic studies were pursued on the electrodeposition of Co onto both polycrystalline and single-crystal substrates.

Ultrathin Bi Films on Pd

A gaping void exists on the systematic investigation of Bi thin films on Pd single crystals. It is interesting to note that studies of Bi underpotential deposition (upd) on Pt(*hkl*) have already been elegantly performed [58-61]. While insights and useful forecasts on the Bi-Pd system can often be gleaned from parallel studies employing Pt, such juxtaposition is not always valid considering the so-called "palladium anomaly" [5].

Early studies by Adziç [62] demonstrated Bi upd onto polycrystalline Pd and its electrocatalytic effect on the oxidation of HCOOH. Bi was believed to exert a "third-body effect," i.e., Bi precludes the adsorption of reaction-intermediate poisons. Details on the stability, electrochemical reactivity, electrovalency and adsorption isotherm of the electrodeposited Bi remain unexplored.

The role of Bi as a catalytic promoter of Pd for the electrooxidation of *D*-glucose had received some attention [63, 64]. Several patents have been formulated based on the Bi-Pd catalyst whose superior activity and selectivity toward the aerobic conversion of *D*-glucose to gluconate is comparable with enzymatic processes [65]. Reasons for the sustained interest on this electrochemical reaction are practically two-fold: (*i*) the need to develop simple yet efficient glucose sensors and (*ii*) the drive to develop biologically compatible fuel cells suitable for human implantation [66, 67]. The Bi-Pd catalyst has also been used in the oxidation of other carbohydrates such as lactose and in the production of fine chemicals typified by the partial oxidation of 2-hydroxybenzyl alcohol [68].

The lack of atomic-level details on the chemical events that lead to the unusually high activity and selectivity of Bi-Pd catalysts underscores the need for surface-sensitive spectroscopic measurements on this bimetallic system. This research, therefore, attempts to fill in this information gap by examining the surface electrochemistry of idealized (single-crystal) Pd surfaces modified by structurally well-characterized adlayers of Bi.

Objectives

The study primarily aimed to establish electrochemical protocols for the deposition of well-defined ultrathin films of Pd, Co, and Bi onto noble-metal surfaces. The chosen adlayer-substrate pairs represented a gamut of interfaces whose structure, composition, and electrochemical reactivity bear significant impact on the formulation and advancement of surface science concepts in selected emerging technological applications. Experiments were designed to address three-pronged objectives:

(i) The interfacial properties of well-defined Pd/Pt(111) adlayers exposed to aqueous bromide were investigated to propose an electrochemical analogue of thermal annealing.

(ii) Studies on ultrathin films of Co on polycrystalline Pd and Pd(111) were launched to explore the possibility of electrodepositing Co, notwithstanding the imminent interference of hydrogen evolution and the large (bulk) lattice mismatch between Co and Pd.

(iii) The interfacial chemistry of Bi ultrathin films on Pd(111) was documented using a combination of electron spectroscopic techniques (*viz.* LEED, AES, and XPS) and classical electrochemical methods (coulometry and voltammetry). The chemisorption of iodine and the electrooxidation of D-glucose were employed as probe reactions to interrogate the nature of the Bi-Pd(111) interface.

METHODOLOGY

Ultrahigh Vacuum (UHV) Surface Analysis

Atomic-level interfacial studies on electrodeposited ultrathin films require the use of single crystals as model substrates for surface-structure–electrochemical-reactivity correlations. Prior to any electrochemical experiment, a single-crystal electrode needs to be *well-defined*, i.e. the composition and geometric structure of the surface have to be precisely established. Interrogation of well-defined electrode surfaces, therefore, becomes more meaningful because reproducible qualitative and quantitative comparison of surface behavior is now possible before and after each electrochemical treatment.

The aforementioned task is fulfilled by spectroscopic techniques that typically rely on electrons and/or photons for signal generation and detection. The surface sensitivity of these tools emanate from the fact that the shallow penetration depth of impinging low-energy electrons can be fine-tuned to examine the topmost surface layer; similarly, electrons escaping from surface atoms have characteristically short inelastic mean free paths, making these ejected electrons excellent surface probes. To ensure that the detected electrons represent signals from the surface, not from processes resulting from collisional energy losses, an ultrahigh vacuum (UHV) environment is imperative for surface science investigations [9].

UHV conditions involve an operative pressure range of ≤ 10^{-9} torr. In such environment, the mean free path of residual gases is kept reasonably large to minimize contact with probe electrons. The Kinetic Theory of Gases also stipulates that UHV conditions minimize the rate of bombardment of background gases onto the electrode surface. For instance, at a high vacuum (HV) environment of 10^{-6} torr containing traces of a common contaminant gas, CO, assuming a sticking probability of 1, it takes 2.6 s to form a monolayer on the surface at 300 K. Under similar conditions, it takes 7.3 hours to replicate such monolayer formation at UHV [67].

All the surface-sensitive methods used in this investigation are briefly described in the succeeding sections.

Low Energy Electron Diffraction

Low energy electron diffraction (LEED) is commonly employed to ascertain the surface order of single-crystal electrodes. In contrast to X-ray diffraction that generally probes three-dimensional bulk lattices of solids, LEED provides structural information regarding the surface unit mesh, i.e. two-dimensional surface lattice.

Just like any diffraction method, LEED relies on the elastic backscattering of the probe entity, in this case monoenergetic electrons. For diffraction to occur, the wavelength λ of the incident electrons must be less than, but of the same order of magnitude, as the interatomic spacing. Wave-particle duality treatment of an electron yields the following modified de Broglie equation:

$$\lambda\,(\text{Å}) \;=\; \frac{h}{\sqrt{2m_e E}} \;=\; \sqrt{\frac{150.6}{E(eV)}} \qquad (1)$$

where h is Planck's constant, m_e is the mass of an electron, and E is energy measured in electron volts (eV).

The surface specificity of LEED diffraction patterns lies in the judicious control of the electron beam energy. The so-called Universal Curve (Figure 1) proposed by Seah and Dench reveals that electrons with energies of 20 – 500 eV have short inelastic mean free paths. Thus, ordered atomic layers within a 5-Å region from the surface typically contribute to the resulting LEED diffraction pattern.

All surface crystallographic information presented in this work was obtained using PE 15-120 LEED Optics and PE 11-020 LEED Electronics system (Perkin-Elmer, Eden Prairie, MN). A schematic diagram of the LEED apparatus is presented in Figure 2. An electron gun releases a stream of monoenergetic electrons that are focused onto a well-grounded single-crystal surface. Diffracted electrons are backscattered into a series of concentric grids, G1 to G4. The four-grid retarding field analyzer (RFA) is designed to allow only elastically backscattered electrons to reach the phosphor-coated collector screen. Such energy-selective process is accomplished by the negatively biased G2 and G3 that act as cut-off filters for the entering electrons. Grid 1 has to be grounded to shield the electron trajectory from electromagnetic fields generated by G2 and

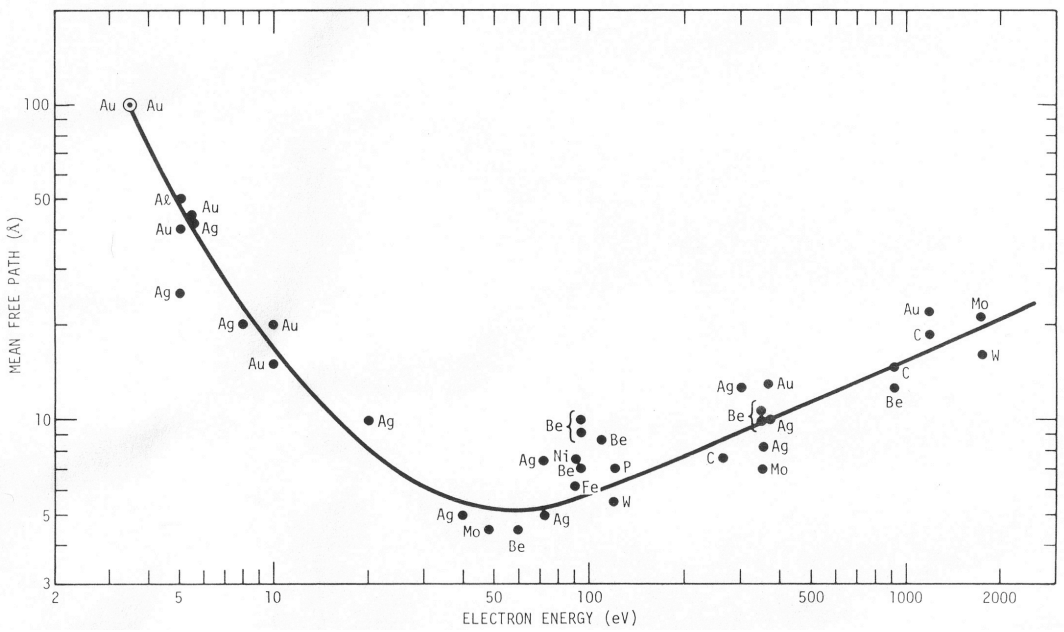

Figure 1. The "Universal Curve" of inelastic mean free path as a function of electron energy [9].

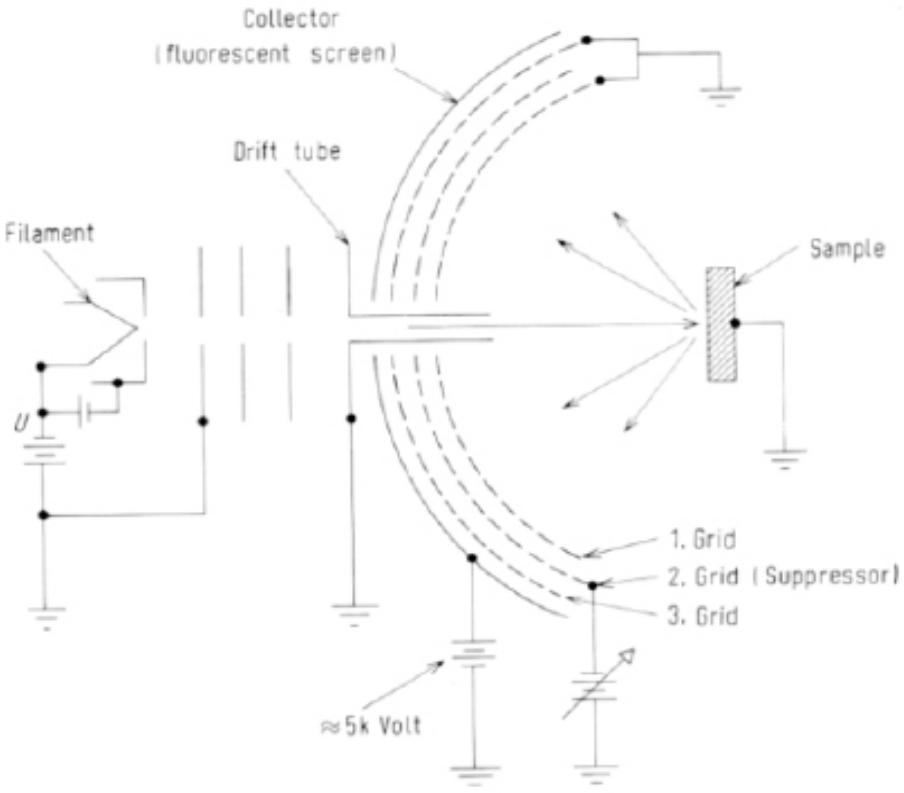

Figure 2. Schematic diagram of the LEED apparatus.

G3. A large positive potential (2 – 5 kV) is imposed on the collector screen to accelerate the admitted electrons so that they have sufficient kinetic energy to induce light emission from the collector screen. The grid nearest to the screen (G4), therefore, also needs to be grounded. A Nikon Coolpix E5200 digital camera (Nikon Corporation, China) was used to take photographs of LEED patterns.

LEED diffraction patterns represent the reciprocal-space lattice of the surface. From the position of the spots, the periodicity of the actual surface unit mesh can be deduced using the following rules [9, 66, 67]:

$$\mathbf{G} = n\mathbf{a}^* + m\mathbf{b}^* \quad (2)$$

$$|\mathbf{a}^*| = \frac{2\pi}{|\mathbf{a}|}; \qquad |\mathbf{b}^*| = \frac{2\pi}{|\mathbf{b}|} \quad (3)$$

$$\mathbf{a} \bullet \mathbf{b}^* = \mathbf{a}^* \bullet \mathbf{b} = 0 \quad (4)$$

The reciprocal lattice vector $\mathbf{G}$ can be expressed as contribution of the elementary vectors $\mathbf{a}^*$ and $\mathbf{b}^*$ of the reciprocal two-dimensional unit cell; m and n are integers. Equation (3) shows that a large real-space interatomic distance, represented by vectors $\mathbf{a}$ and $\mathbf{b}$, implies closely packed spots in reciprocal space.

Nuances in the spot brightness, sharpness, and shape are qualitative indicators for structural changes of the surface. Table 1 summarizes LEED pattern features and their corresponding surface topographical meaning. Further refinement of surface geometrical assignment is also possible by quantitatively analyzing spot intensity vs. beam energy; such data treatment is,

Table 1. Qualitative correlations between LEED pattern features and surface morphology (Adapted from [68]).

LEED pattern	**Surface morphology**
Diffuse background	Disordered adlayer; random adatoms; random vacancies
All spots broadened at all beam energies	Small (<100 Å) domain size
Spot broadening greater for diffraction beams of higher order	Random strain
Increased broadening of all spots with increasing beam energies	Mosaic structure (microcrystals)
Emergence of additional spots or change in intensity-energy profile of the (1x1) adlayer	Ordered adlayer; large surface domains
Mixed sharp and broad spots at all beam energies	Antiphase domains
Multiple (00) beams	Faceting
Alternately split and sharp spots with changing beam energy	Ordered steps
Alternately split and broad spots with changing beam energy	Random steps

however, not available in the present UHV system employed in this investigation.

The number of emerging diffraction spots detected by the collector screen can be theoretically predicted using the Ewald sphere construction [1]. Since surfaces are two-dimensional, the sphere reduces into a circle whose radius is equal to the magnitude of wavevector, $|\mathbf{k_o}|$, of the incident electron, defined as $|\mathbf{k_o}| = \frac{2\pi}{|\mathbf{a}|}$, where λ is the de Broglie wavelength given in Equation 1.

Figure 3 shows the Ewald construction for a Pd(111) surface probed by an electron beam of 52 eV. Given that the lattice parameter *a* for Pd is 3.89 Å and its nearest-neighbor distance in the (111) Miller-index plane is $|\mathbf{a}| = a/\sqrt{2} = 2.75$ Å, the geometrical solution for the reciprocal-space lattice reveals that only six spots, equally spaced from each other according to Equation 2, can be viewed arranged in a hexagonal array under the present experimental conditions.

Given in Figure 4 is a series of experimentally acquired LEED patterns at various beam energies: (a) 62 eV, (b) 52 eV, and (c) 42 eV. While the sharpest LEED spots were obtained at 62 eV, the pattern at 52 eV represented the one with optimum brightness. Spots at 42 eV occupy the border of the visible area of the screen, thus creating an apparent elongation.

Two single-crystal electrodes were employed in this study: Pd(111) and Pt(111). Both surfaces exhibit a hexagonal array of LEED diffraction spots. The acquired LEED patterns were compared with those obtained from calculations

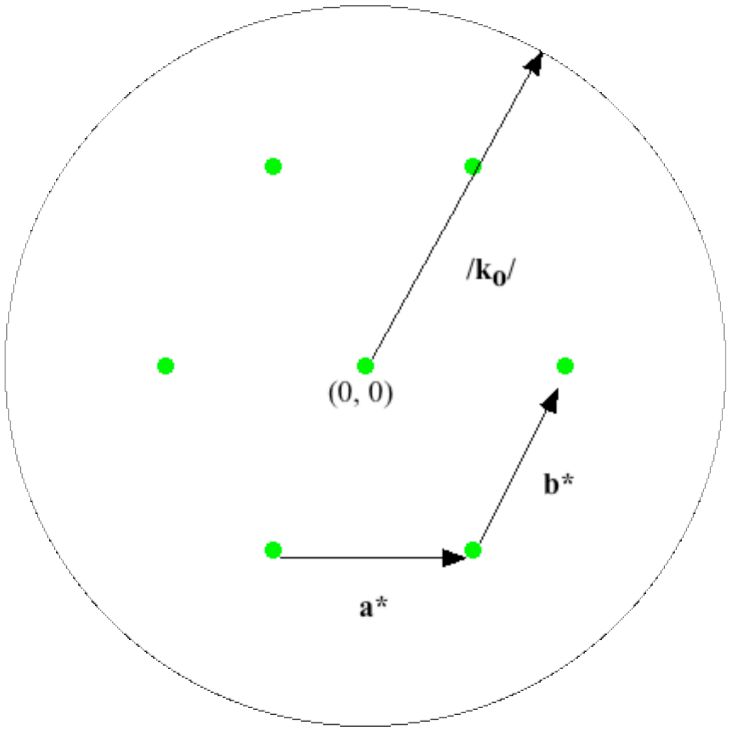

Figure 3. A (1×1) LEED pattern for a clean and well-ordered Pd(111) electrode surface as predicted by a Ewald sphere construction for a beam energy of 52 eV.

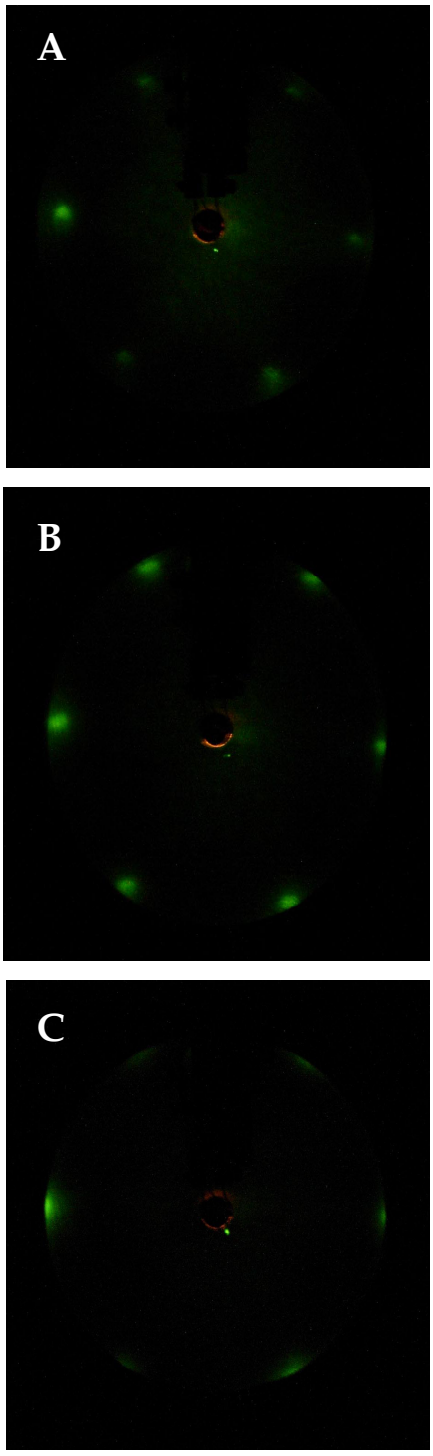

Figure 4. LEED pattern of a clean, well-ordered Pd(111) electrode as a function of beam energy: (a) 62 eV, (b) 52 eV, and (c) 42 eV.

[69]. Wood's notation [70] was used to describe the structural information derived from the LEED patterns.

X-ray Photoelectron Spectroscopy

X-ray Photoelectron Spectroscopy (XPS) is a surface science tool that provides information about elemental surface composition. In this respect, XPS is supplementary to Auger Electron Spectroscopy (AES) and, therefore, is also referred to as Electron Spectroscopy for Chemical Analysis (ESCA). Conventionally, the binding energy, E_b is measured with respect to the Fermi level (highest occupied level) of the spectrometer to which the sample is connected. From Einstein's relation, E_b can be converted to kinetic energy: $E_{Kin} = h\nu - E_B - \phi$, where ϕ is the work function, i.e. the minimum energy needed to remove an electron from the highest occupied level in the solid to the vacuum. Since changes in the electronic environment often alter the binding energy of core-level electrons, subtle shifts in the XPS peak position can be used to determine the oxidation state of surface elements [71]. The entire XPS process is depicted in Figure 5.

XPS measurements made in this investigation were performed using a Kratos Axis Ultra Imaging X-ray photoelectron spectrometer, under the auspices of the Texas A&M University Materials Characterization Facility. The X-ray source used was a Mg anode that emitted the K_α line (1253.6 eV) with a full-width at half-maximum of 0.7 eV. The bandpass energy of the concentric hemispherical energy analyzer was set at 25 eV.

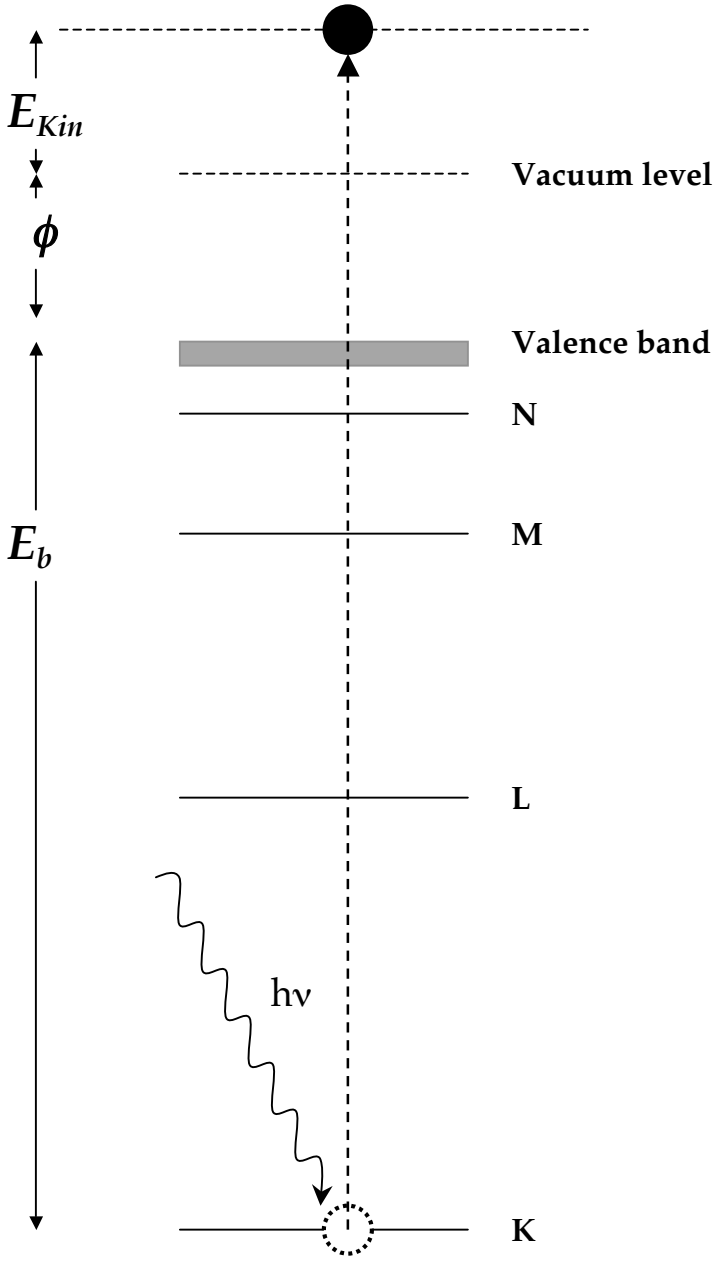

Figure 5. Core-level excitation involved in X-ray photoelectron spectroscopy.

Auger Electron Spectroscopy

When a low-lying inner core electron is ejected from an atom, the positively-charged "hole" that is created can be neutralized via two competing processes: (*i*) photoemission of X-ray fluorescence and (*ii*) the Auger process. The Auger process is a radiationless process involving an upper-level electron that relaxes to fill in the vacancy. The released energy ejects a third electron, called the Auger electron, whose kinetic energy is diagnostic of a particular element [67]. Figure 6 shows a schematic representation of the (a) photoemission and (b) Auger processes.

Using the electronic transitions depicted in Figure 6 as an example, the kinetic energy of the Auger electron is given by:

$$E_{Kin} = [E_K - E_L] - E_M - \phi$$

where the term $[E_K - E_L]$ refers to the energy available to the Auger electron as an L-shell electron fills the K-shell electron vacancy; the last two terms account for the energy required for the Auger electron to escape into the vacuum: E_M is the binding energy of the electron at the M-shell; ϕ is the work function of the spectrometer. In this example, the Auger transition is called a KLM transition.

The elemental specificity of this technique originates from that fact that the kinetic energy of the Auger electron is characteristic of the three energy levels involved. Elements with three or more electrons can be qualitatively

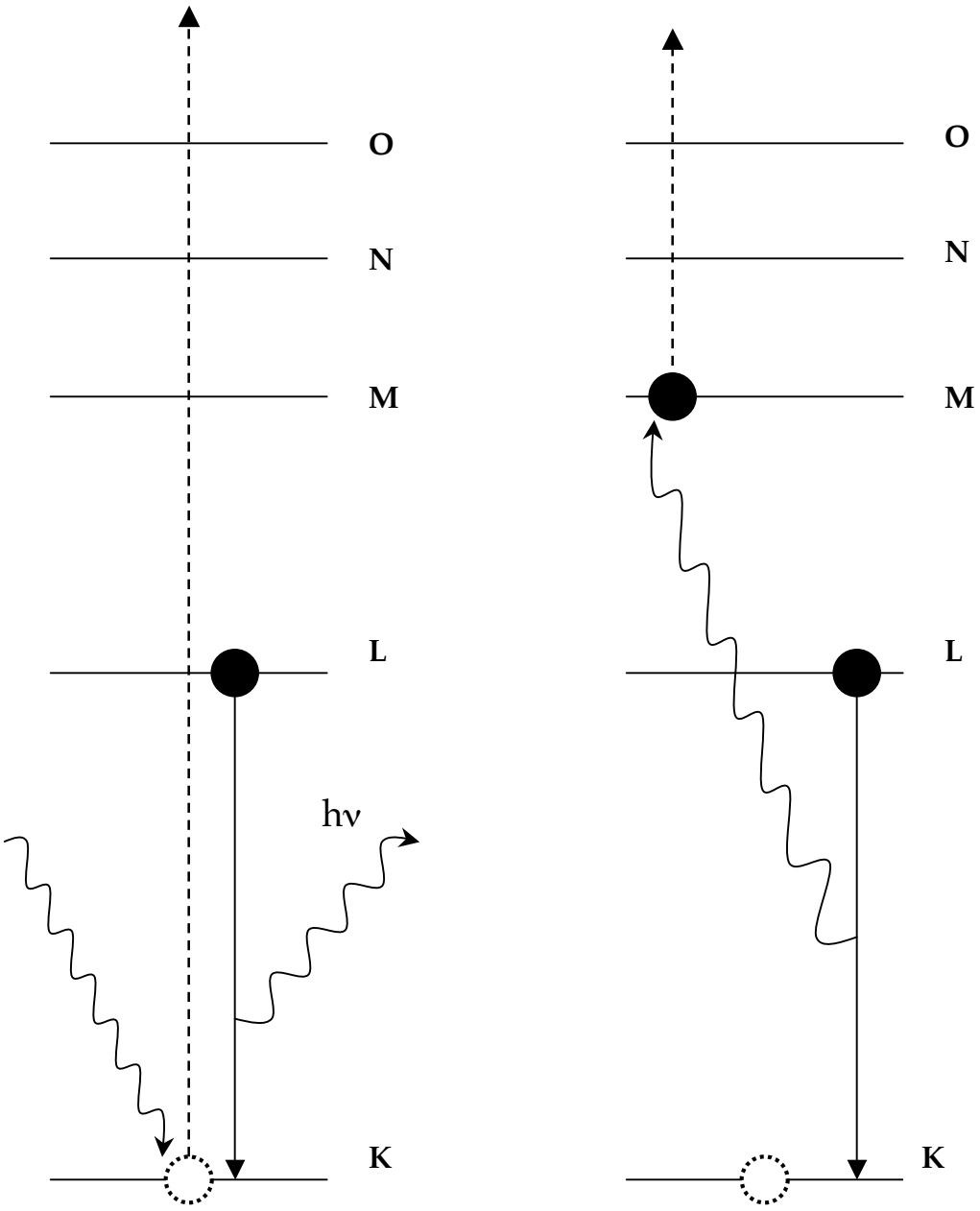

Figure 6. Electronic relaxation of a K-shell vacancy via (a) X-ray photoemission and (b) Auger process.

assayed using AES, although the Auger relaxation process predominates among elements with low atomic numbers ($Z \leq 20$) [66].

This investigation uses a PE AES system (Perkin Elmer, Eden Prairie, MN) that consists of the following modules: PE 10-155 Cylindrical Auger-Electron Optics, PE 32-150 Digital AED Control, PE 32-100 Electron Multiplier Supply, PE 11-010 Electron Gun Control, and PE 96B V/f Preamplifier. A schematic diagram of the AES system is given in Figure 7.

Initial core-level excitation is induced by an electron beam (typically with a primary energy E_p = 2 keV) emanating from a normal-incidence electron gun. The scattered electrons enter a cylindrical mirror analyzer (CMA), which discriminates the Auger electrons from a plume of secondary electrons. During data collection, the negative DC voltage on the outer cylinder is ramped so that only those electrons with appropriate kinetic energy can pass through the exit slit and reach the electron multiplier. The kinetic energy resolution of the CMA is 0.6%; the resulting band pass window is scanned at 2 eV/s. A low incident current is maintained (1 μA above the background) to minimize electron-beam-induced surface damage.

Auger peak identification is often difficult because of the superimposition of the signal over a large sloping background originating from the inelastic scattering of the incident electron beam. To circumvent this problem, the Auger signal voltage is electronically differentiated to give a derivative spectrum of the electron energy distribution, reported as dN(E)/dE; N(E) represents the number

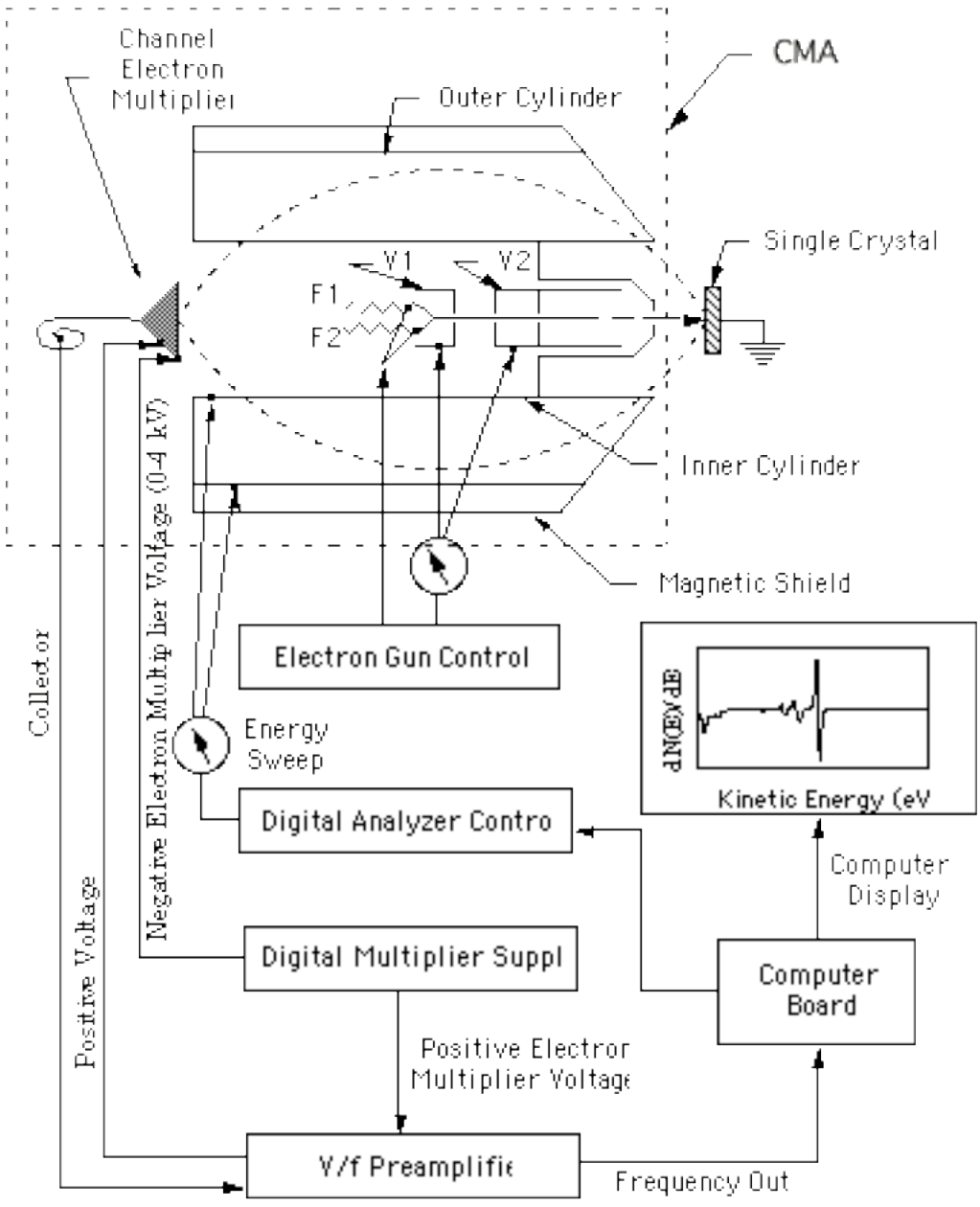

Figure 7. Schematic diagram of the AES module.

of counts for a particular kinetic energy, E. Consequently, the signal-to-noise ratio is greatly enhanced, giving rise to a detection limit 0.1% of a monolayer [72].

Shown in Figure 8 is the Auger spectrum of Pd in its (a) integrated and (b) differentiated modes. Peak-area integration of the major AES transition peaks, obtained from reference materials of known purity, can be used as a direct measurement of the atomic concentration of surface species. Assuming that peak shape does not vary with coverage, the integrated peak area correlates well with peak-to-peak height. In this investigation, quantitative information was derived by normalizing the peak-to-peak heights of the adatoms with respect to the heights of the pristine substrate prior to electrodeposition; such quantitation is typically used in conjunction with coulometric measurements. Other methods of determining absolute surface coverages, such as double integration of the second harmonic amplitude, are discussed elsewhere [73].

Electrochemistry

A CV-27 Voltammograph (Bioanalytical Systems, West Lafayette, IN) was used in all electrochemical experiments. Unless otherwise stated, Ag/AgCl (1 mM NaCl) was employed as reference electrode paired with a piece of Pt wire as the auxiliary electrode. Completing the three-electrode potentiostat assembly was a single-crystal working electrode made of Pt(111) or Pd(111). Current and charge measurements were recorded using a VP-6414S X-Y recorder (Soltec, Sun Valley, CA).

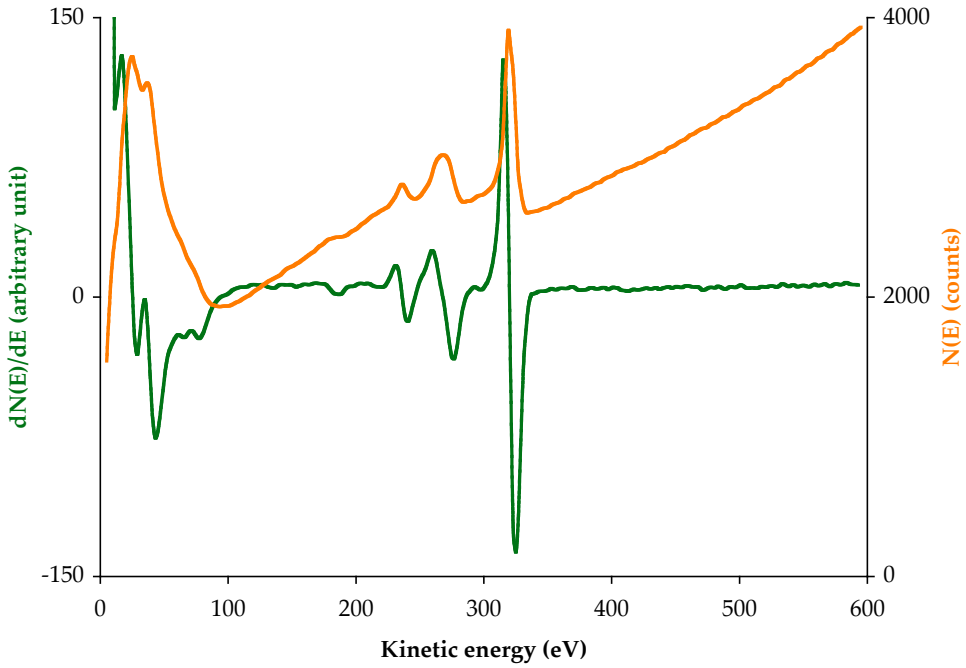

Figure 8. Auger spectrum of Pd in its differentiated and integrated modes.

Preliminary survey of the electrochemical behavior of the ultrathin films was performed using thin-layer electrochemistry (TLE). A thin-layer electrode is typically a flame-annealed metal billet inserted into a glass cell specially designed to allow a minute volume (*ca.* 4 μL) of the analyte solution to come in contact with the electrode. This design ensures that the thickness of the adsorbed layer is less than the Nernst diffusion layer; thus, voltammetric waves are not complicated by mass transport effects.

Voltammetry

Voltammetry is an electrochemical method that involves measuring current as a function of applied potential. The electrode potential is initially poised at a desired value, and is subsequently swept at a particular scan rate. Linear sweep voltammetry is a technique that involves terminating the potential scan at a final potential different from that of the original. When the potential scan is returned to the initial potential, the technique is referred to as cyclic voltammetry.

Cyclic voltammetry is routinely used in inorganic electroanalytical chemistry to characterize the chemical reversibility of certain redox processes. Typical scan rates lie between 20 mV/s and 100 mV/s. In this investigation, slow scan rates (5 mV/s to 0.1 mV/s) are strategically employed to enhance peak separation and probe kinetically hindered surface processes [74].

Coulometry

Switching the applied potential from the double-layer region (where no Faradaic charge is accumulated) to a pre-determined final potential is equivalent

to a voltammetric sweep at an infinitely fast scan rate. Coulometry involves measuring the charge (integrated current) obtained during this potential-step experiment. If the charge is monitored as a function of time, the technique is called chronocoulometry.

From Faraday's Law, the amount of electrodeposited material (expressed as Γ in $\mathrm{nmol/cm^2}$) can be quantitatively calculated using charge measurements (Q). If the area (A) of the electrode is known, Γ can be evaluated from the equation:

$$Q - Q_{blank} = nFA\Gamma$$

where n is the number moles of electrons required or given up per mole of redox process, and F is Faraday's constant. Faraday's Law underpins the construction of an electrodeposition isotherm, which is practically a calibration curve of adsorbate surface coverage vs. the final applied potential for a defined period of time.

UHV-EC Instrumentation

Surfaces of polycrystalline electrodes, such as those used in TLE experiments, provide complicated and preparation-dependent morphology and reactivity. The use of well-oriented single crystals as substrates for electrodeposition is desirable for studies that aim to explore atomic-level phenomena. To preserve the monocrystallinity and cleanliness of a single-crystal electrode, experiments have to be performed under ultrahigh vacuum conditions where the mean free path of residual gases are kept reasonably large to minimize contact with or contamination of the surface electrode.

Tandem UHV-EC experiments were performed using a stainless steel assembly (Perkin-Elmer, Eden Prairie, MN) consisting of an antechamber, where electrochemistry experiments were conducted; a gate-valve (MDC Vacuum Products, Hayward, CA) that isolated the antechamber from the surface-analysis chamber; and a valve-isolable ion pump well. An X-Y-Z manipulator (Varian, Lexington, MA) mounted on a linear positioning table (Lintech, Los Angeles, CA) allowed rotational and translational displacement of the single-crystal electrode inside the UHV-EC assembly. A custom-built electrochemical cell can be introduced into the EC antechamber via another gate-valve (MDC Vacuum Products). Figure 9 is a photograph of the UHV-EC assembly.

The surface analysis chamber housed the modules for LEED, AES, and temperature-programmed desorption-mass spectrometry (TPD-MS). Oxygen (for oxidation thermal annealing) and argon (for surface bombardment) were introduced into the chamber using two separate variable leak-valves (Varian, Lexington, MA). A custom-built ion gun was employed for argon-ion sputtering.

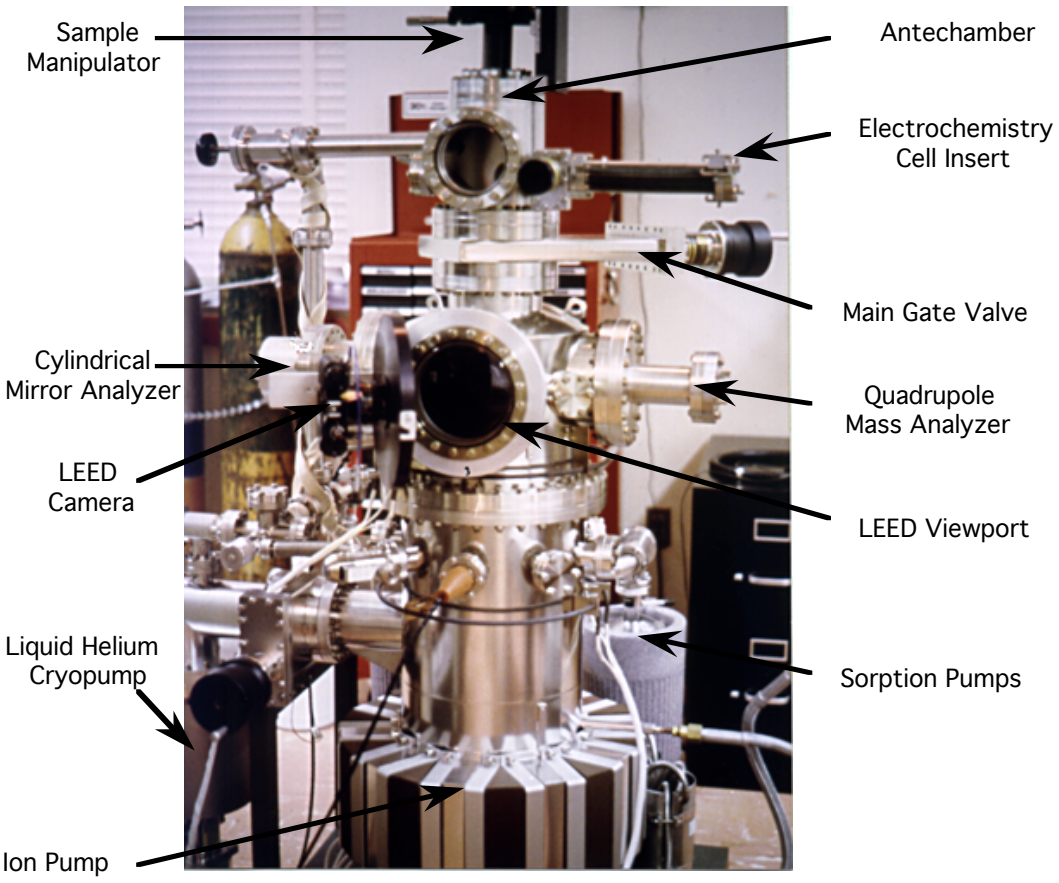

Figure 9. The UHV-EC assembly composed of an antechamber for electrochemical experiments, and a gate-valve-isolable surface analysis chamber, which houses both LEED and AES.

A three-stage pump-down procedure was used in reducing the pressure inside the chamber to UHV conditions. Two liquid-nitrogen-cooled sorption pumps were operated to remove most of the moisture and N_2 that typically prevailed after an electrochemical experiment in the antechamber. Once the pressure reached 10^{-3} torr, a cryopump (AP-8 Displex Cryopump, APD Cryogenics, Inc., Allentown, PA) was used to further reduce the pressure to 10^{-7} torr. Ultimate pressure reduction to 10^{-10} torr was accomplished using an ion pump (Perkin-Elmer TNBX Series 1000) coupled with a cryogenically cooled titanium sublimation pump. A four-day 200-^{o}C bake-out of the UHV-EC assembly was regularly conducted, especially if the base pressure exceeded 10^{-9} torr.

Well-defined Working Electrodes

Commercially oriented and metallurgically polished 99.999% pure Pt(111) and Pd(111) (Aremco Products, Ossining, NY) disc electrodes were used. For Pt(111), the electrode area exposed to the electrochemical cell was measured to be 1.12 cm^2 based on the hydrogen underpotential deposition-desorption charge; the value is very close to the calculated geometric area of 1.1192 cm^2. The geometrical surface area of the Pd(111) electrode is 1.9796 cm^2; unlike Pt(111), no generally accepted experimental protocols exist to determine the real surface area of Pd single-crystals. The single crystal was suspended from the manipulator via a pair of 0.5 mm Pt or Pd wires (99.99% purity, Johnson-Matthey Inc., Seabrook, NH) that were spot-welded to the disc edge. Two Pt(10%)-Rh(90%) thermocouple wires were also spot-welded to the disc edge to

allow resistive heating using a crystal temperature controller (Omega Engineering).

Prior to any electrochemical experiment, the single-crystal electrode was cleaned by multiple cycles of Ar^+ bombardment (Ar^+ current = 4 -10 μA) and thermal oxidation at 550°C (P_{O2} = 5 x 10^{-6} torr); ultimately, the electrode was annealed to 750°C-800°C under UHV conditions to restore long-range surface order. The cleaning cycle was repeated until surface purity and order were verified by AES and LEED, respectively.

Reagents and Gases

All pieces of glassware were cleaned using hot chromic acid (3% $K_2Cr_2O_7$ in 10 M H_2SO_4). All solutions were made up using 18.2 Ω Millipore water (Millipore Systems, Houston, TX). The following high-purity reagents were used without further purification: $PdSO_4$ (Aldrich, Milwaukee, WI), fuming H_2SO_4 (Aldrich), NaI (Curtin Matheson Scientific, Houston, TX), NaBr (Johnson Mathey, England), NaCl (Johnson Mathey), NaF (Aldrich), $Cu(ClO_4)_2$ (Aldrich), CF_3COOH (Aldrich), D-glucose (Aldrich), Bi_2O_3 (Sigma-Aldrich) and $K_2Cr_2O_7$ (EM Science, Gibbstown, NJ). High-purity N_2 (BOTCO, Bryan, TX), Ar (BOTCO), and O_2 (Proxair, Dunbury, CT) gases were used.

RESULTS AND DISCUSSION

An underlying theme of this investigation is the electrodeposition of well-defined ultrathin metallic films onto Pt(111) and Pd(111) surfaces. The first section is a discourse on the electrochemical preparation of Pd adlayers on Pt(111). Also described herein is the interaction of aqueous and adsorbed bromine on these electrodeposits, as probed by voltammetric and surface spectroscopic methods. The second section describes a systematic attempt at electrodepositing Co ultrathin films on Pd surfaces. An extended part of this investigation is conducted on smooth polycrystalline Pd; results from these studies are juxtaposed with the experimental challenges encountered in establishing electrochemical protocols for the deposition of Co on the Pd(111) surfaces. The final section deals with the electrosynthesis and interfacial characterization of ultrathin Bi films on Pd(111).

Electrodeposition of Ultrathin Pd Films on Pt(111)

Various electrochemical methods for the preparation of thin Pd films have been described in the literature [31-34]. In this study, electrodeposition of Pd was performed under potentiostatic control. The deposition potential (E_{dep}) window was set between the open-circuit potential (ocp, typically 0.40 V) and –0.20 V; further excursions to more negative potentials were not made to avoid complications from the hydrogen evolution reaction (HER). Various coverages of Pd can be electrodeposited, at the same potential, using different deposition times; it was initially decided to employ a 2-minute deposition time to limit the

exposure of the electrochemical antechamber of the UHV system to air and other contaminants.

The amount of Pd electrodeposited at a particular potential was determined from chronocoulometric measurements during the potentiostatic deposition. All charge (Q) measurements were duly corrected for background charge using Pd-free 0.1 M H_2SO_4 as blank electrolyte. Calculations from Faraday's law revealed that the deposition charge of a full monolayer (1 ML) of Pd, assuming pseudomorphic morphology on a Pt(111) electrode with a surface area of 1.12 cm^2, is 539 μC. Under the present experimental conditions, the potential that afforded this deposition charge was 0.221 V. Verification of this result was made using two strategies: (*i*) titration of bare Pt(111) with underpotential deposition (UPD) of Cu; and (*ii*) $I_{(ads)}$-catalyzed dissolution of Pd. The surface-structure sensitivity of the peak position of Cu UPD [75] was exploited to verify the exact potential at which 1 ML Pd was deposited. At submonolayer coverages of Pd deposited at 0.222V, signature Cu UPD peaks on both Pt and Pd surfaces were evident (broken-line trace in Figure 10). Deposition and stripping peaks between –0.14 and –0.05 V corresponded to Cu on Pd [76, 77] while the redox pair between 0.06 and 0.12 V belonged to Cu on Pt [78]. A Pd deposition potential of 0.221 V marked the *threshold* at which the Cu-on-Pt peaks were fully attenuated (solid trace in Figure 10); this result closely

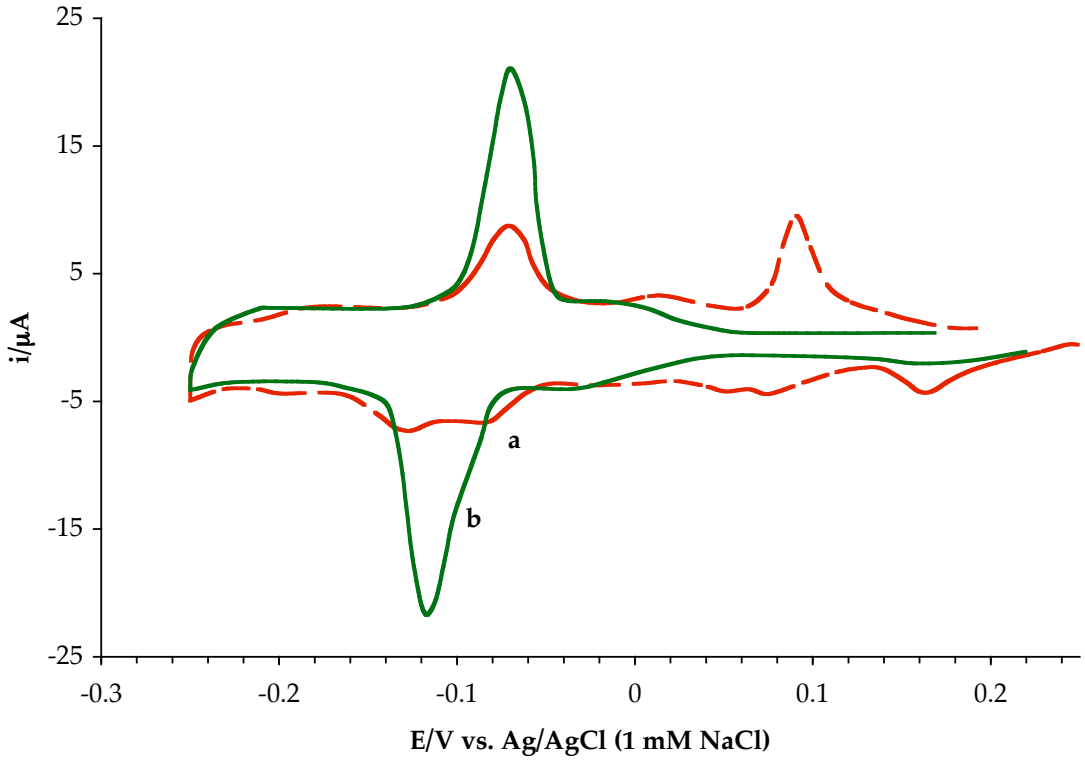

Figure 10. Cu UPD peaks on Pt(111) with (a) submonolayer and (b) 1 ML coverages of Pd.

concurred with the chronocoulometric experiments that showed the formation of 1 ML Pd at 0.221 V.

Quantitation of the amount of electrodeposited Pd was also done using $I_{(ads)}$-catalyzed dissolution of Pd [35]. Peak-area integration of the anodic signal due to Pd stripping in the presence of $I_{(ads)}$ yielded Q = 455.4 ± 9.0 μC at E_{dep} = 0.222 V and Q = 547.2 ± 8.0 μC at E_{dep} = 0.221 V. Within the acceptable error margin for this quantitative technique, the potentiostatic deposition at 0.221 V yielded 1 ML Pd. Linear sweep voltammograms for various E_{dep} were displayed in Figure 11.

Based on the agreement between charge measurements obtained during electrodeposition and stripping, the following equivalence was defined: 1 ML Pd ≡ 539 μC; in this case, Θ_{Pd} = 1 ML represents a full surface coverage of 1 Pd adatom for every 1 Pt atom. All coulometric data, therefore, can be transformed into coverages using this definition. Figure 12 is a plot of Pd coverage as a function of E_{dep}.

Interfacial Electrochemistry of Ultrathin Pd Films

Two supporting electrolytes were employed in the electrochemical characterization of the prepared ultrathin Pd films: H_2SO_4 and acidified NaF. Extensive studies had already been published on the merits of each electrolyte. The rationale for the use of both systems in the current investigation is driven by the intention to compare, contrast, and consolidate the present results with those earlier published.

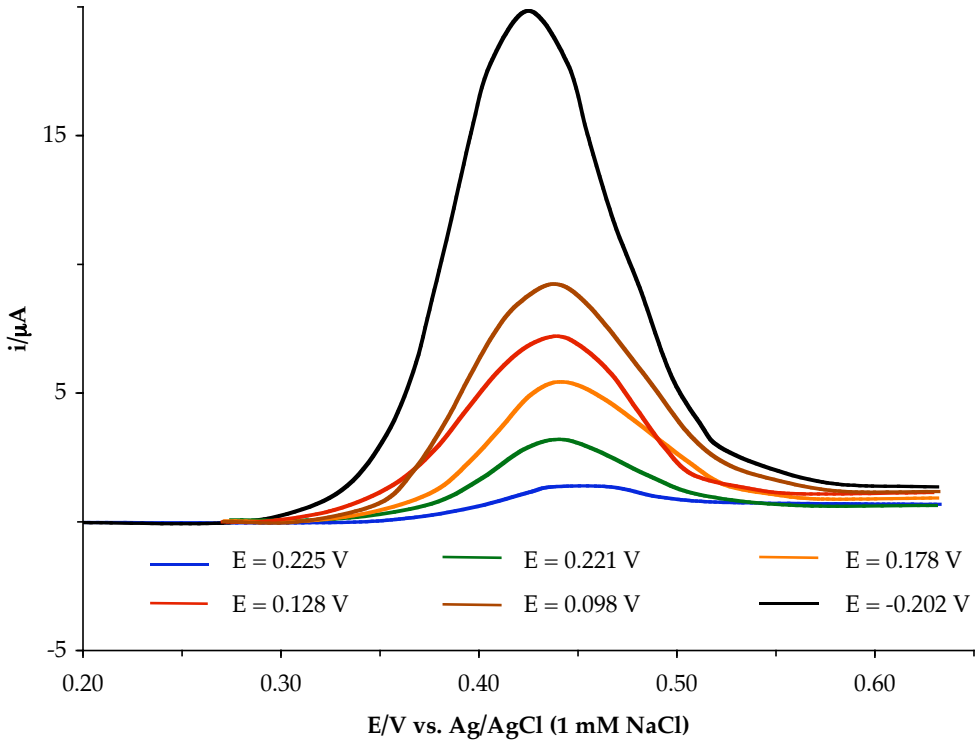

Figure 11. Linear sweep voltammograms of I_{ads}-catalyzed anodic dissolution of ultrathin Pd films deposited at various potentials. Ultrathin films were prepared using 0.5 mM $PdSO_4$ in 0.1 M H_2SO_4. Geometric area of disk electrode = 1.12 cm^2. Scan rate = 0.5 mV/s.

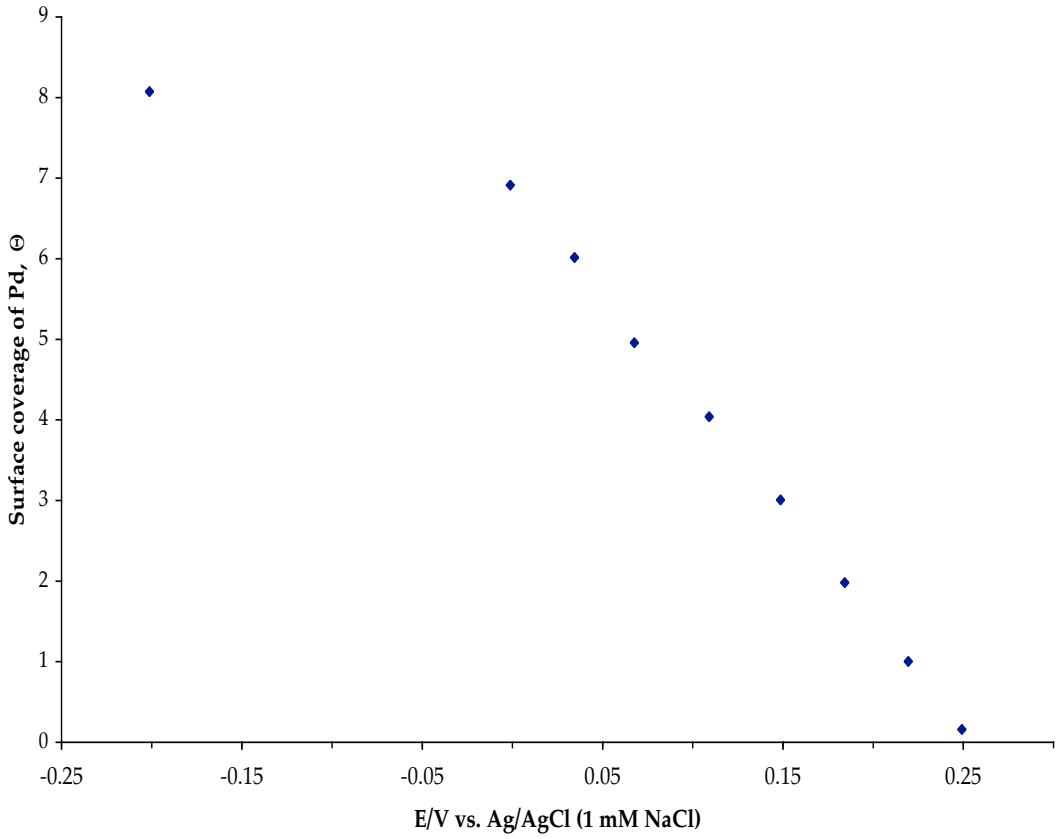

Figure 12. Electrodeposition isotherm of Pd on Pt(111). Ultrathin films were prepared using 0.5 mM $PdSO_4$ in 0.1 M H_2SO_4.

Electrochemical Behavior in Sulfuric Acid Electrolyte

The electrochemical behavior of the prepared ultrathin Pd films in 0.1 M H_2SO_4 was investigated using cyclic voltammetry. The voltammetric profile of a clean, well-ordered Pt(111) electrode is given in Figure 13. Prior to any deposition experiment, the emergence of "butterfly" peaks between –0.17 V and 0.00 V, ascribed to (bi)sulfate desorption/adsorption [79, 80], was inspected as a diagnostic electrochemical marker for a well-defined Pt(111) surface in 0.1 M H_2SO_4. The broad peaks between –0.17 V and –0.45 V marked the hydrogen adsorption-desorption region. The anodic oxidation of Pt began at 0.17 V and peaked at 0.78 V; the corresponding reduction peak appeared at 0.24 V.

Before the describing further the voltammetric and spectroscopic data of the present investigation, a brief summary of the replicated work [81], is necessary:

(i) At coverages ranging from 0.5, 1, 2, 3, 4, and 8 ML Pd, a (1x1) hexagonal LEED pattern was obtained. The LEED spots were brightest for 1 ML Pd on Pt(111) and progressively decreased in intensity with increasing Pd surface coverage.

(ii) The Auger electron spectra showed concomitant increase in the MNN transition peak for Pd at 330 eV with increasing Pd surface coverage. The Pt signal at 168 eV became negligible above 1 ML Pd.

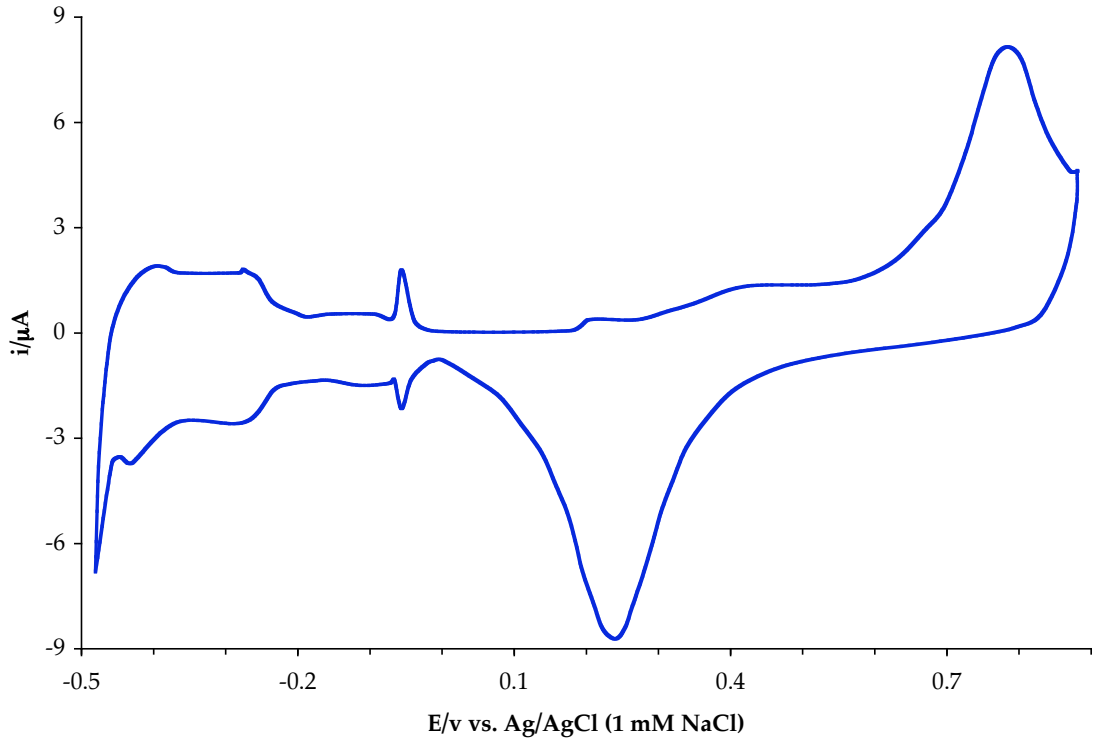

Figure 13. Cyclic voltammogram of a clean, well-ordered Pt(111) in 0.1 M H_2SO_4. Geometric area of the disc electrode is 1.12 cm^2. Scan rate = 2 mV/s.

(iii) Pd *thin-film* behavior was voltammetrically manifested by the emergence of H UPD adsorption-desorption peaks that are otherwise absent in the presence of bulk Pd [32, 82]. The reversible peaks at *ca*. –0.34 V and –0.29 V (Figure 14 a-f) were ascribed to the adsorption-desorption of H UPD and/or HSO_4^-–SO_4^{2-} on terrace and step sites, respectively [34, 79-80].

(iv) A Stranski-Krastanov growth mode was indicated for the potential-step electrodeposition of Pd on Pt(111).

(v) A thin-film-to-bulk transition was observed at a coverage of 3 ML Pd, based on the voltammetric peaks associated with H UPD on terrace sites. Thick *non-annealed* Pd multilayers exhibited *non-bulk* voltammetric properties; i.e. at 8 ML Pd, *thin-film-like* voltammetric H UPD peaks were still observed.

Built on the premise of this previous report (*cf*. Appendix), the current study focused on the interfacial electrochemistry of aqueous and adsorbed bromide.

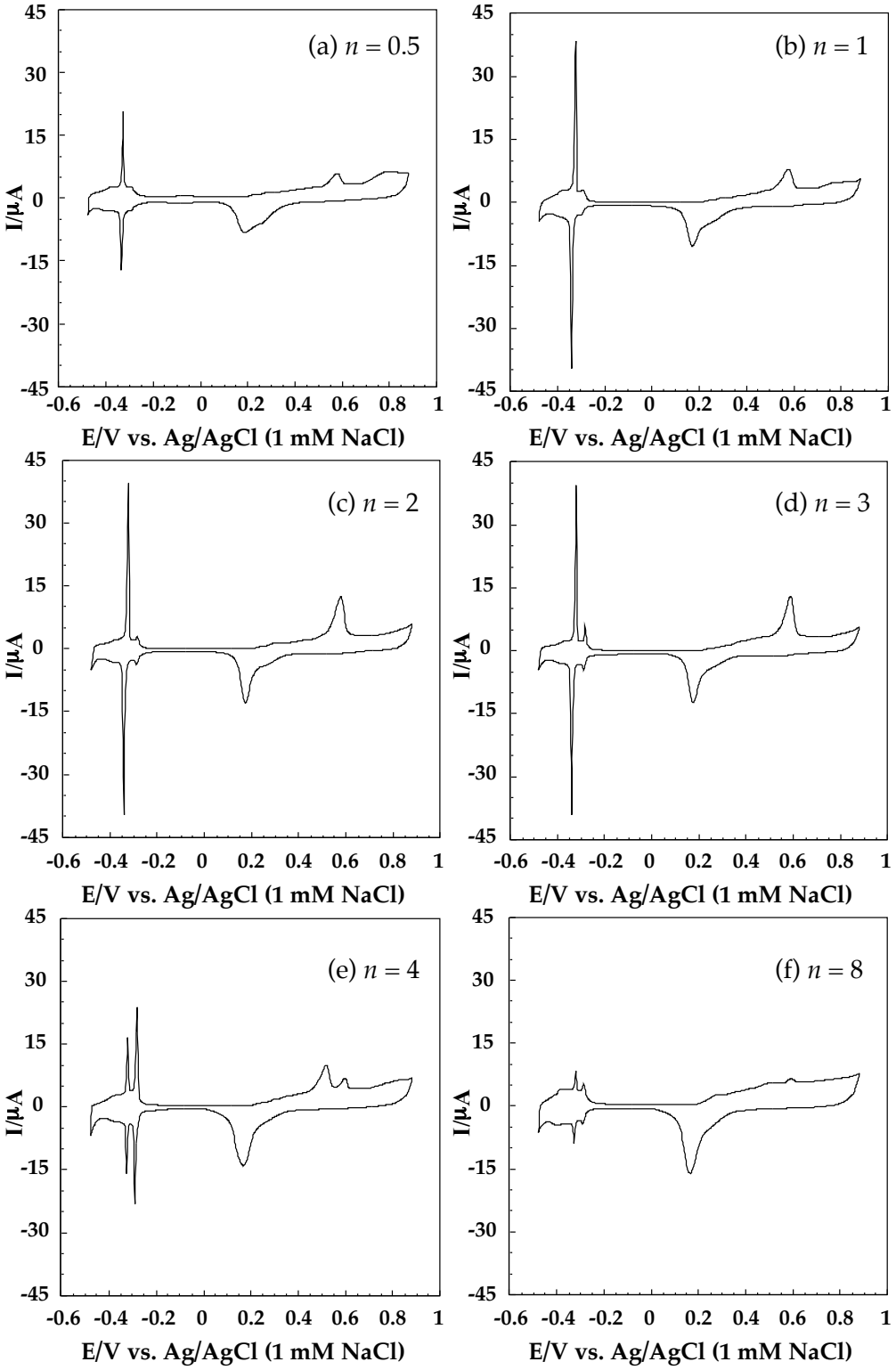

Figure 14. Cyclic voltammograms of *n*-ML Pd on Pt(111) in 0.1 M H_2SO_4 [81].

Previous studies on the interaction of bromine with well-defined surfaces [83] were carried out using 0. 1 M NaF, adjusted to pH = 4 with trifluoroacetic acid (TFA), as supporting electrolyte; thus, the same experimental conditions were employed here. The choice of the electrolyte system was dictated by the fact that, in contrast with the sulfate-bisulfate ions, both F^- and trifluoracetate ions are non-specifically adsorbed on the Pt(111) surface, and therefore do not compete with the chemisorption of Br [83].

Electrochemical Behavior in NaF Solution (pH 4)

The nondescript features of the voltammogram of Pt(111) in 0.1 M NaF (pH = 4) (Figure 15) attested to the surface inertness of the prevailing ions in the blank solution. Except for the absence of the so-called "butterfly" peaks, the voltammetric features resembled those obtained in 0.1 M H_2SO_4: (*i*) H UPD adsorption-desorption region between –0.55 V and –0.33 V; (*ii*) the Pt surface oxidation peaks at 0.35 V and 0.65 V; (*iii*) the reduction peak for the oxided surface centered at 0.07 V.

In the presence of 1 ML Pd on Pt(111), a pair of relatively sharp H UPD adsorption-desorption peak, not found on either bulk Pd(111) [84] or Pt(111), emerged at –0.43 V (Figure 16). Surface oxidation of the Pd adlayer was observed at a relatively broad potential window between –0.10 V and 0.70 V. The Pd reduction peak appeared at –0.01 V.

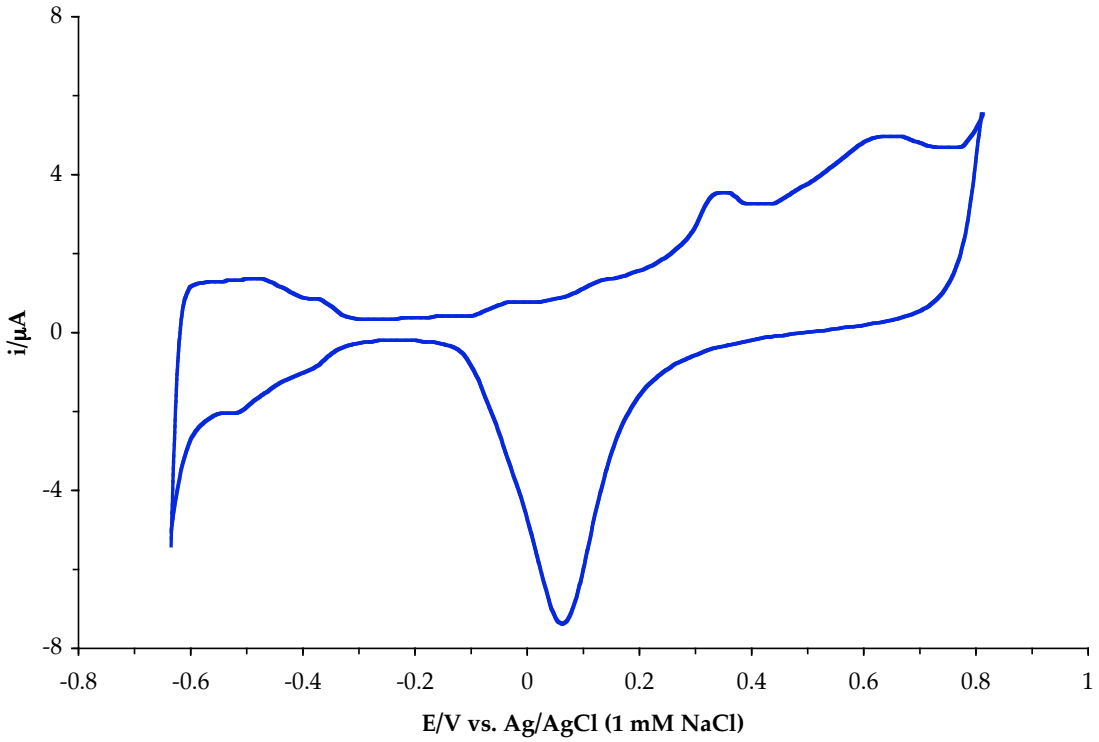

Figure 15. Cyclic voltammogram of clean, well-ordered Pt(111) in 0.1 M NaF. Solution pH was adjusted to 4 using concentrated trifluoroacetic acid (TFA). Geometric area of disk electrode = 1.12 cm^2. Scan rate = 2 mV/s.

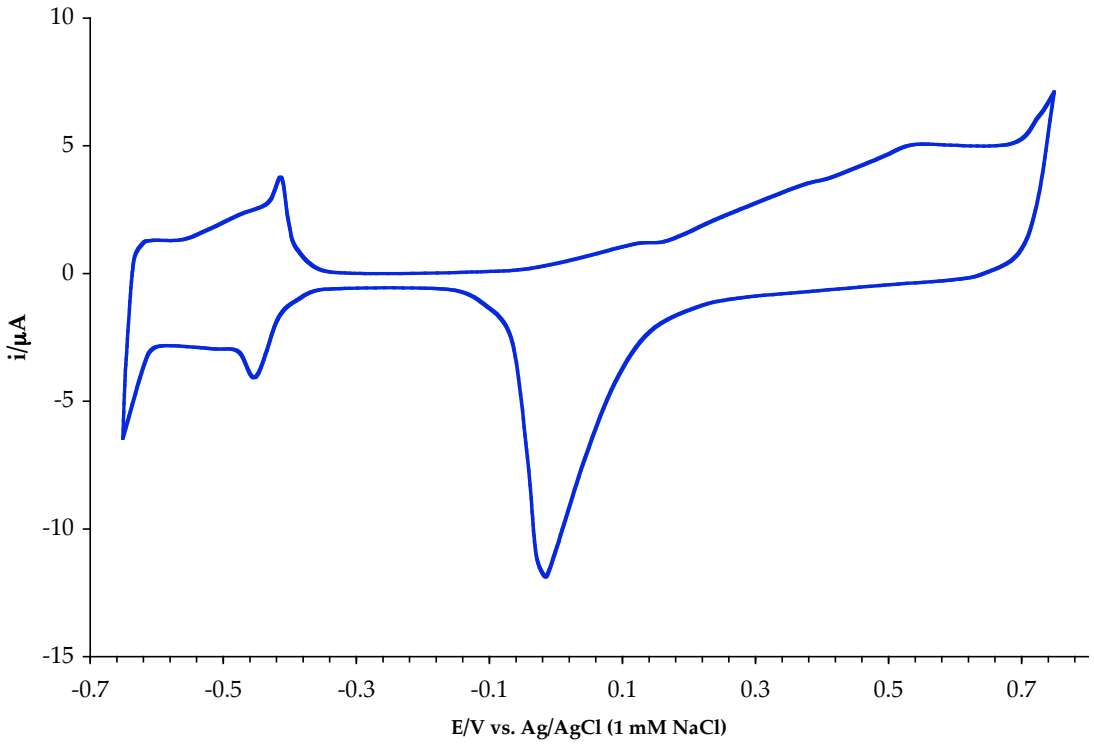

Figure 16. Cyclic voltammogram of 1 ML Pd on Pt(111) in 0.1 M NaF with pH adjusted to 4 using TFA. Geometric area of disk electrode = 1.12 cm^2. Scan rate = 2 mV/s.

Electrochemical Behavior in NaBr-NaF Solution (pH 4)

Cyclic voltammetry of 1 ML Pd on Pt(111) in 1 mM NaBr–0.1 M NaF (pH 4) solution produced a reversible set of H UPD adsorption-desorption peaks at –0.45 V. Notably, the anodic oxidation peak of the Pd film at 0.35 V became more prominent and a reduction peak for Pt appeared at 0.18 V. The emergence of the substrate signal during the cathodic scan implied that the ultrathin Pd film was stripped off in the presence of bromine. Potential excursion to 0.55 V led to the oxidation of aqueous Br^- to BrO_3^-. Reduction of the electrogenerated BrO_3^- ions registered a peak at 0.67 V during the cathodic scan.

Br-Assisted Electrochemical Annealing

Proposed nonthermal analogues for the annealing process of ultrathin Pd films had been previously carried out in H_2SO_4 [81], although the smoothening effects were not dramatic. Electrochemical (EC) annealing is anchored on the fact that, by cycling the electrode between potentials that border surface perturbation, surface atoms can be rearranged to desirable equilibrium positions. A continuation of the preliminary work on the effects of chemisorbed bromine (Br_{ads}) and aqueous Br^- ions was launched in the present investigation using multiple cycles of large-amplitude potential steps.

A surface coverage of 8 ML Pd was chosen to represent a bulk Pd surface that exhibited *non-bulk* voltammetric peaks typified by the terrace- and step-site H UPD adsorption-desorption peaks. Bromine was chemisorbed onto the prepared ultrathin Pd film by exposing it to 1 mM NaBr in 0.1 M NaF (pH 4) solution at 0.22 V for 3 min. For this EC-annealing process in the presence of

$NaBr_{(aq)}$, a complete potential cycle consisted of initially setting the potential at E_1 = 0.22 V (at which Br chemisorption occurred) and then switching it to E_2 = –0.40 V (near the onset of HER). A waiting time of 3 minutes was sufficient to allow the measured current to drop to zero after the imposition of each potential. A total of 10 cycles was performed; the final potential was poised at –0.40 V. Figure 17 shows a diagrammatic representation of a complete potential cycle.

The electrochemically annealed Pd film was rinsed thrice in blank electrolyte solution under potential control (E_2 = –0.40 V). Cyclic voltammetry was performed in Br-free 0.1 M H_2SO_4 (pH = 4) solution. Figure 18 displays the voltammograms of both pre- and post-EC-annealed surfaces. The dramatic extinction of the H UPD adsorption-desorption peaks after EC-annealing heralded the disappearance of surface step-sites that are most likely the origin of this anomalous thin-film-like behavior. The resultant post-EC-annealing voltammogram displayed the expected voltammetric features of *bulk* Pd electrodes.

The disappearance of surface defects, and thereby the restoration of long-range surface order, was further corroborated by the acquisition of sharper (1x1) LEED pattern (Figure 19) for post-EC-annealed surfaces. A comparison of the peak-to-peak heights for the Pd AES transition (Figure 20) revealed that, within the expected precision of such AES signal quantitation (± 0.05 cm), the Pd surface coverage on Pt(111) remained virtually the same after multiple potential

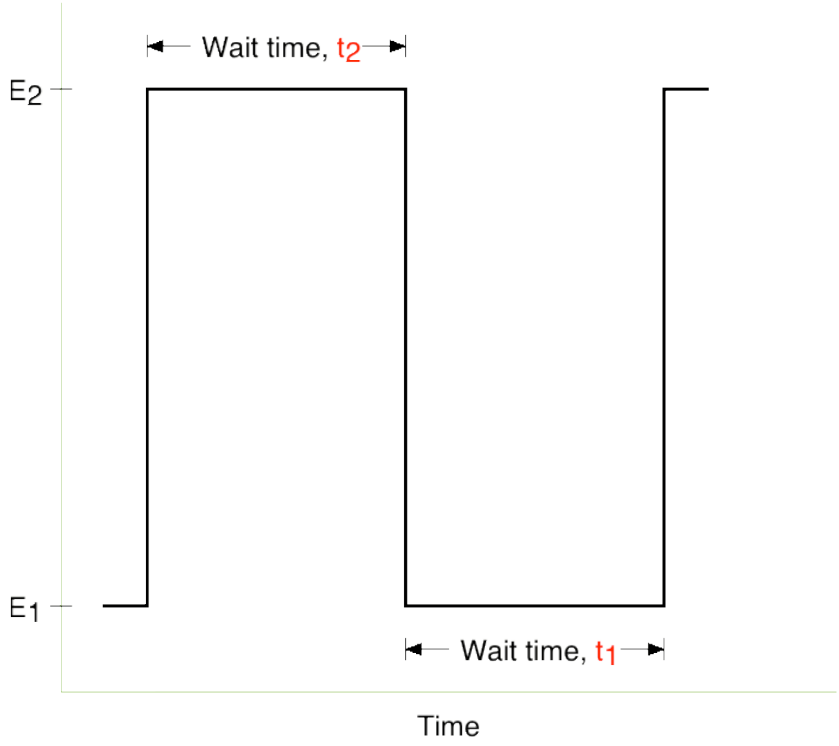

Figure 17. Schema of a complete potential cycle during electrochemical annealing in NaBr solution.

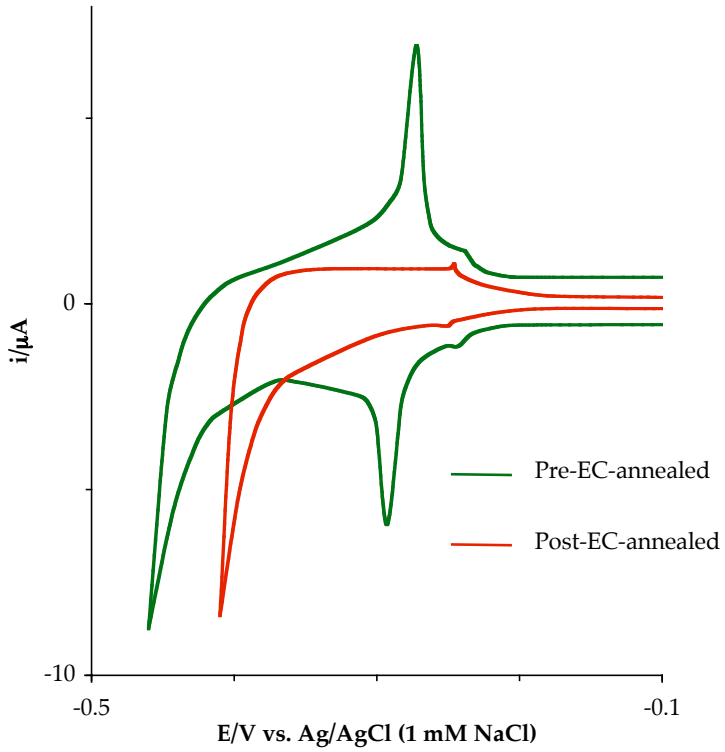

Figure 18. Current-potential profile of 8 ML Pd/Pt(111) before and after electrochemical annealing in 1 mM NaBr–0.1 M NaF (pH = 4) solution. The cyclic voltammograms were obtained in Br-free 0.1 M NaF (pH = 4) solution at a scan rate of 2 mV/s.

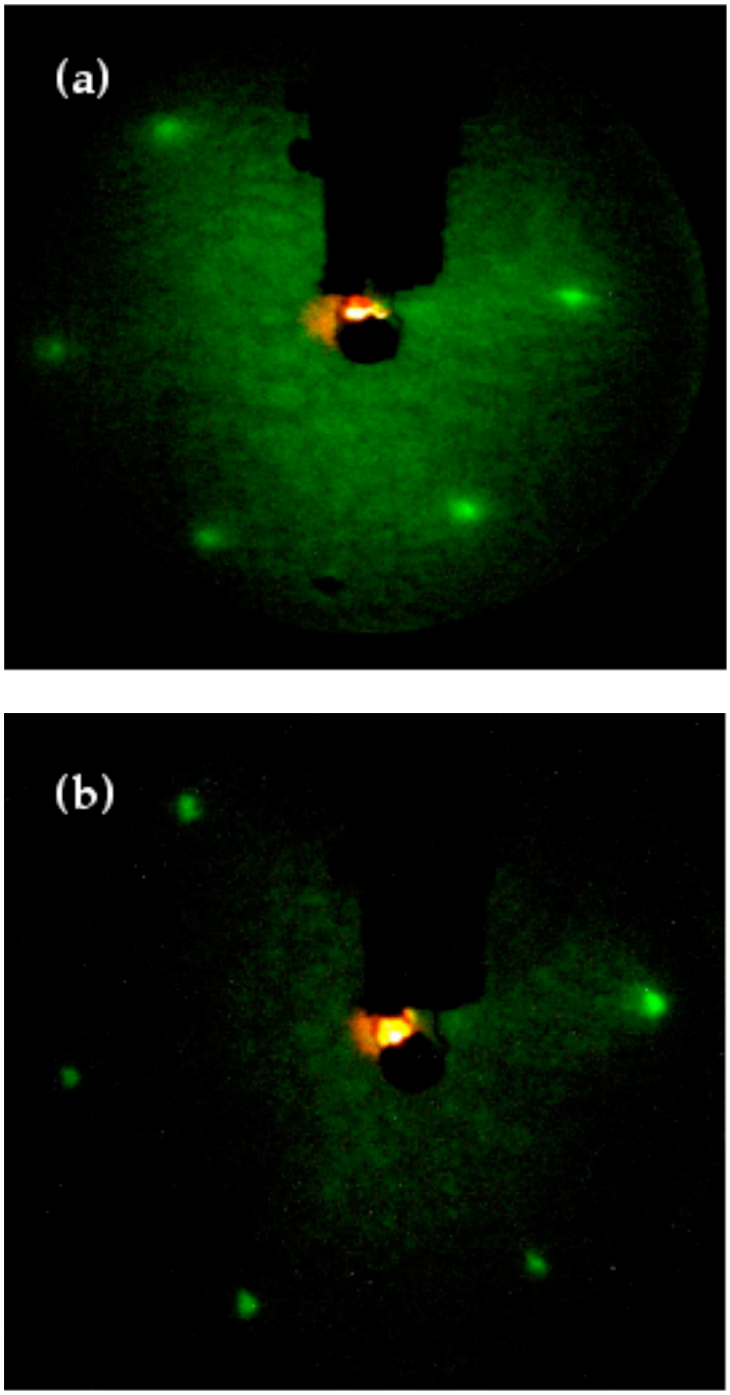

Figure 19. LEED pattern of 8 ML Pd/Pt(111) (a) before and (b) after electrochemical annealing in $NaBr_{(aq)}$. Beam energy = 62 eV; beam current = 2 μA.

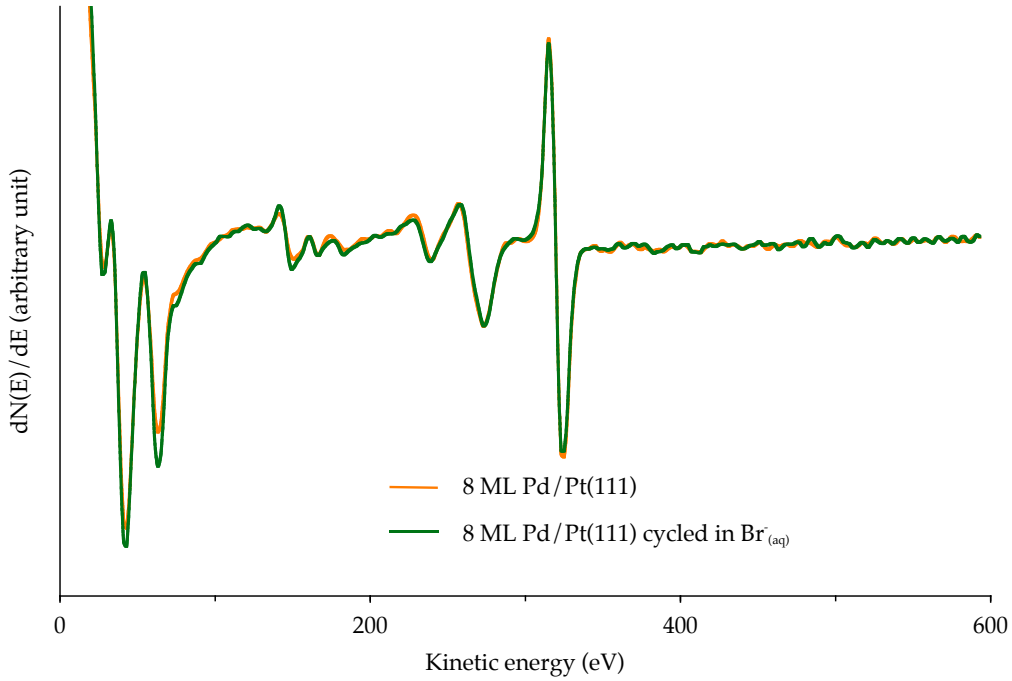

Figure 20. Auger electron spectrum of 8 ML Pd/Pt(111) after electrochemical annealing in 1 mM NaBr/0.1 M H_2SO_4 (pH = 4). Incident beam = 2 keV; beam current = 1 μA.

cycling; further verification was afforded by the similarity of the pre- and post-EC-annealed Pd stripping charges assayed by I_{ads}-catalyzed anodic dissolution of Pd. Thus, during EC-annealing in the presence of $NaBr_{(aq)}$, Pd adatoms occupying defect sites were rearranged to assume equilibrium positions on well-ordered terraces of the (111)-texture.

Interfacial Electrochemistry of Bromine Chemisorbed on Ultrathin Pd Films

The ability of bromine to facilitate Pd adatom rearrangement is reminiscent of the surfactant-like action of chemisorbed iodine (I_{ads}) in restoring the atomic-level smoothness of electrochemically roughened and ion-bombarded electrode surfaces [85]. Previous studies have uncovered interesting surface-confined phenomena by examining the electrochemistry of I_{ads} in iodide-free solution [35]. For instance, a place-exchange mechanism [86] has been demonstrated to transpire between the I_{ads} and Pd during the anodic dissolution of Pd electrodes in I-free sulfuric acid; i.e. iodine always stays on the surface during the ensuing stripping process. Along the same vein, the electrochemical behavior of Br_{ads} on ultrathin Pd films, *in Br-free electrolyte solution*, demands special attention. For this purpose, Br was chemisorbed onto a well-defined 6 ML Pd/Pt(111) surface by immersing it into a solution of 1 mM NaBr/0.1 M NaF (pH = 4) at 0.22 V for 3 minutes. The acquisition of a (√3x√3)-Br adlattice (Figure 21), under this experimental condition, was consistent with previous reports [87].

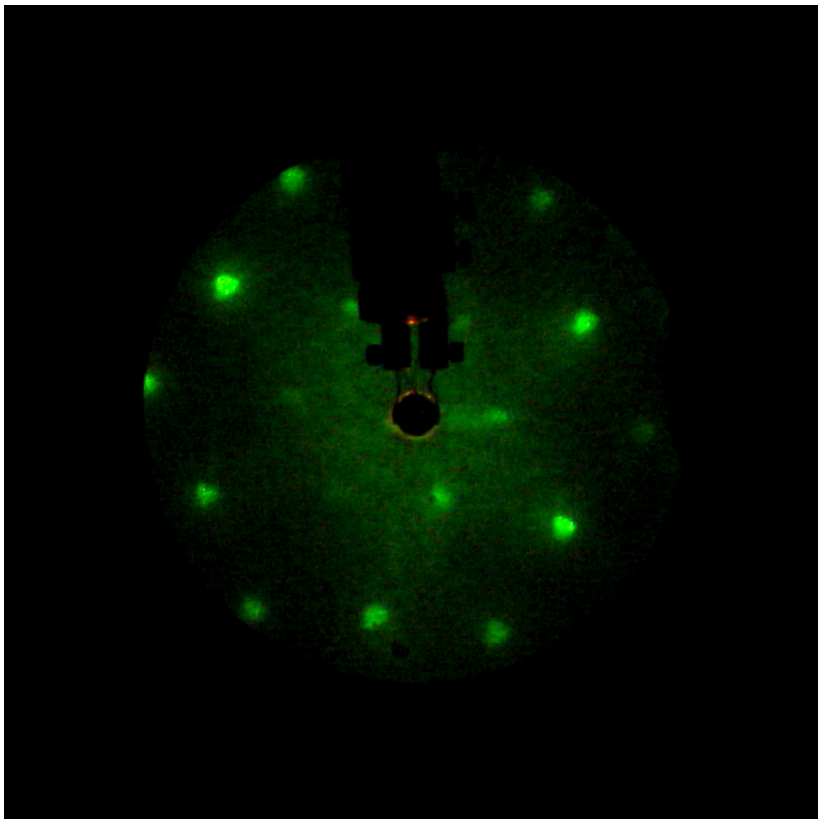

Figure 21. LEED pattern for 6 ML Pd/Pt(111) obtained after emersion from 1 mM NaBr in 0.1 M NaF (pH = 4). Beam energy = 62.0 eV; beam current = 2 μA.

The prepared Br adlayer was transferred to Br-free 0.1 M H_2SO_4. The potential was switched from 0.22 V to 0.41 V; the final potential corresponds to the shoulder of a huge peak ascribed to be a composite of the anodic dissolution of both ultrathin Pd film and the chemisorbed Br adlayer (Figure 22) [81]. In this polarization experiment, the potential was strategically poised at the chosen value to ascertain if – in a manner similar to the I_{ads}-catalyzed anodic dissolution of Pd – chemisorbed Br would stay on the ultrathin Pd film surface until the film would be exhaustively removed.

As revealed by the chronocoulogram in Figure 23, a monotonic increase in the electrolytic charge was noted. Compositional analysis by AES (Figure 24) showed a 10% decline in the Pd signal due to anodic dissolution, as indicated by the linear rise in electrolytic charge beyond 12 minutes of polarization at 0.41 V. The rapid increase in charge during the first 3 minutes of polarization was ascribed to the anodic oxidation of chemisorbed Br. This finding was supported by the absence of both the AES Br signal and the characteristic (√3 x √3) pattern (Figure 25).

Quantitative analysis, by I_{ads}-catalyzed dissolution, of the Pd film remaining after polarization at 0.41 V indicated a Pd surface coverage of 4.8 ML. The amount of anodically dissolved Pd (1.2 ML) represented adatoms that occupy terrace and step sites. It was evident from the linear increase in electrolytic charge after 10 minutes (Figure 23) that the anodic dissolution of ultrathin Pd film would have proceeded towards completion if the imposition of

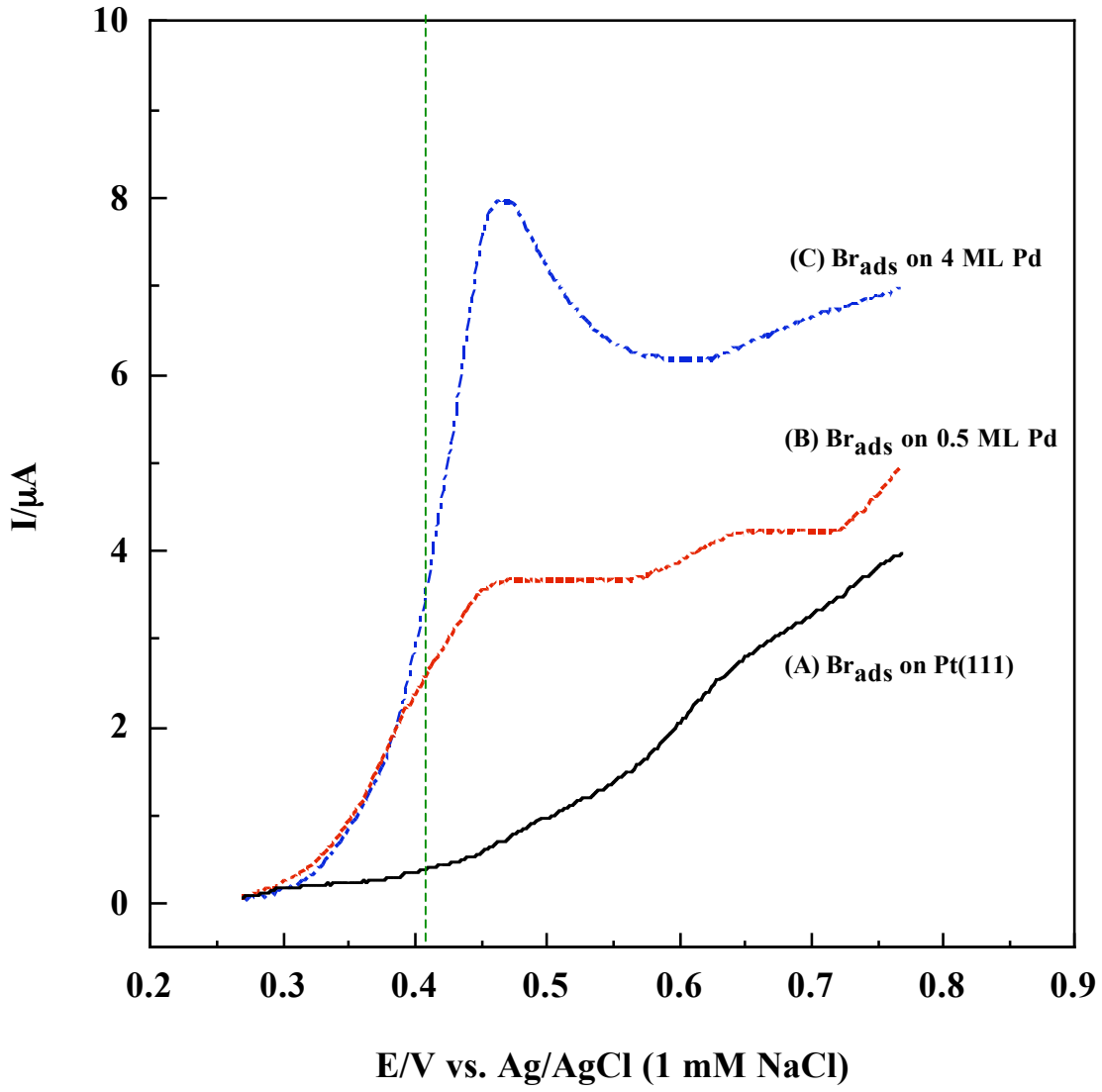

Figure 22. Voltammograms for Br_{ads} on (a) Pt(111), (b) 0.5 ML Pd film, and (c) 4 ML Pd film in 0.1 M H_2SO_4. Sweep rate = 2 mV/sec. Electrode area = 1.12 cm^2. [81].

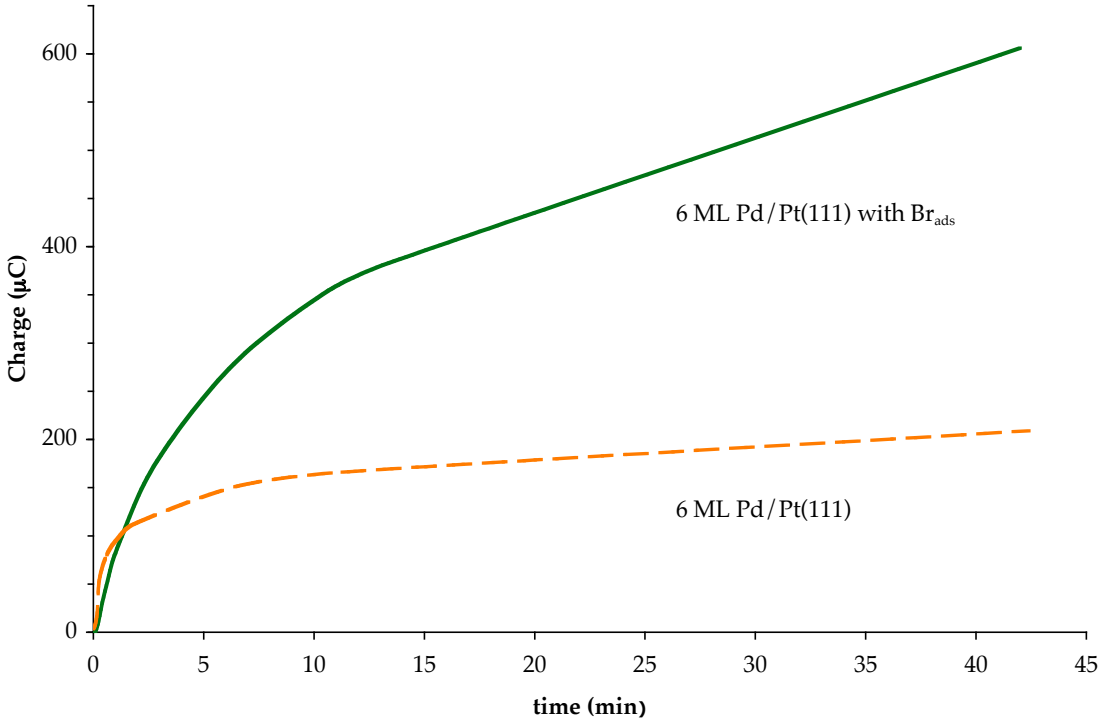

Figure 23. Chronocoulogram of Br-modified 6 ML Pd/Pt(111) in 0.1 M H_2SO_4 as the potential was switched from 0.22 V to 0.41 V.

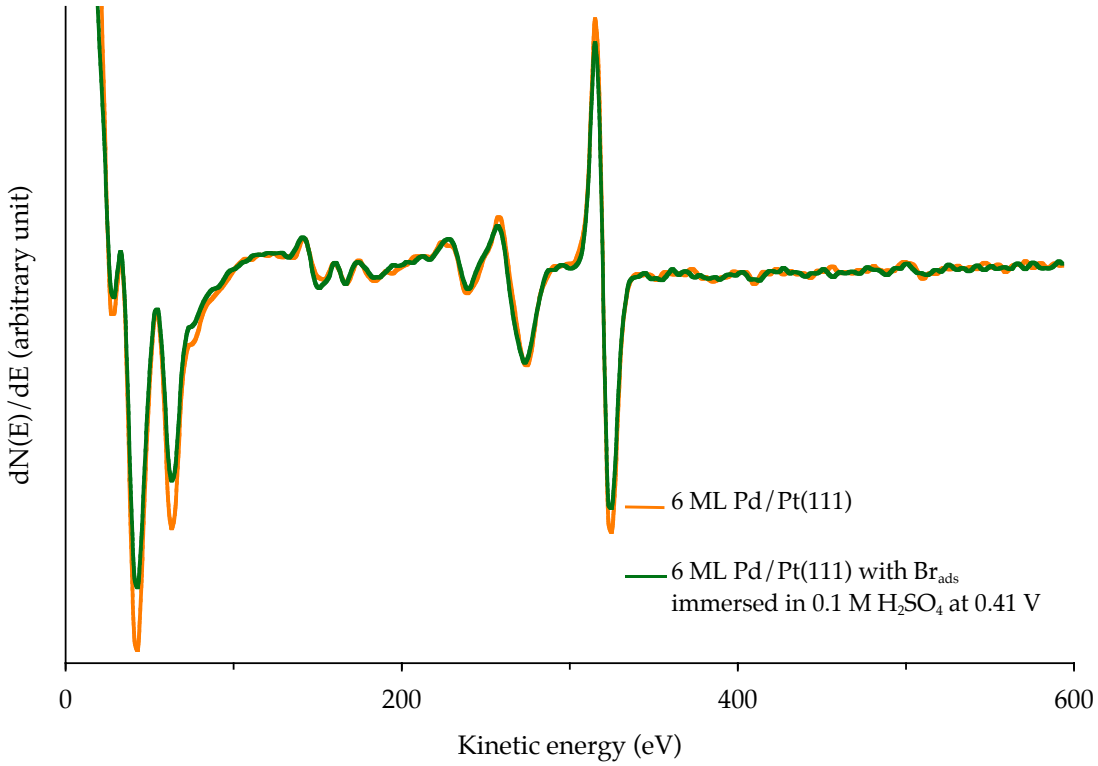

Figure 24. Auger electron spectrum of Br-coated 6 ML Pd/Pt(111) after immersion in 0.1 M H_2SO_4 at E = 0.41 V. Incident beam = 2 keV; beam current = 1 μA.

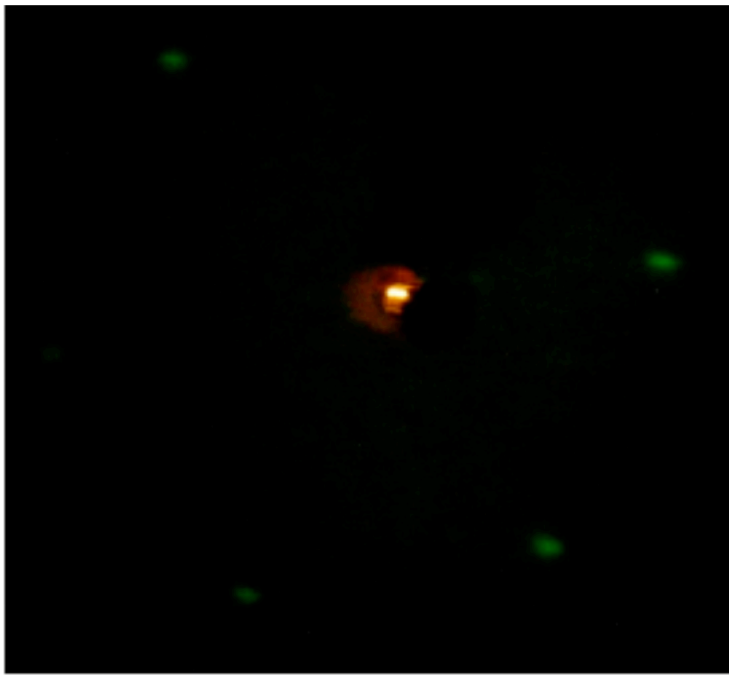

Figure 25. LEED pattern after exposing Br-coated 4 ML Pd/Pt(111) in 0.1 M H_2SO_4 at E = 0.41 V. Beam energy = 62 eV; beam current = 2 μA. Experimental details are described in the text.

potential were continued. This scenario is different from bulk Pd electrodes at which anodic dissolution (at *ca.* 0.41 V) is impeded by the formation of surface oxides [5].

Cyclic voltammetry of the resultant adlayer in 0.1 M H_2SO_4 showed the disappearance of the H UPD peak on step-sites and the dramatic decrease in the signal intensity for the H UPD peak on terraces (Figure 26). The presence of chemisorbed Br activates the preferential anodic dissolution of *step-site* Pd adatoms. This claim is borne out of the observation that, in the absence of chemisorbed Br, the step-site H UPD feature still persists (Figure 27) even after multiple sweeps involving switching potentials greater than 0.41 V [81]. The presence of the terrace-related peak is not surprising since the anodic dissolution process leaves behind a Pd adlayer of ultrathin film coverages.

The ability of chemisorbed Br to facilitate anodic dissolution of ultrathin Pd films is, hence, different from that of iodine. Since the Pd-Br bond is weaker relative to that of Pd-I bond, Br adatoms preferentially seek out the more reactive surface defects (e.g., steps) on Pd, thereby making the chemisorption more site-selective. In contrast, I adatoms are readily chemisorbed and tenaciously sticks to the surface even at potentials bordering the anodic surface oxidation of Pd. Within the same potential region, Br adatoms are easily desorbed, consequently giving rise to a Br-free Pd surface as evidenced by both AES and LEED. While it is certain that the above voltammetric results imply Br_{ads}-enhanced surface mobility of Pd atoms, the mechanism of such enhancement remains to be elucidated. The proximity of the potentials needed

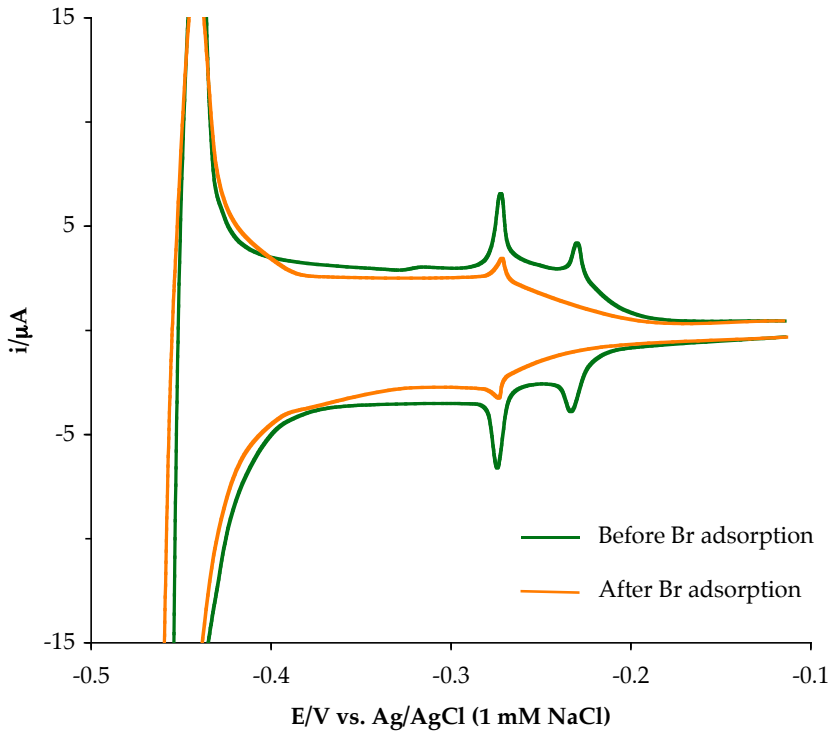

Figure 26. Cyclic voltammogram of 6 ML Pd/Pt(111) in 0.1 M H_2SO_4, before and after Br chemisorption and subsequent polarization at –0.41 V. Scan rate = 2 mV/s. Experimental details are described in the text.

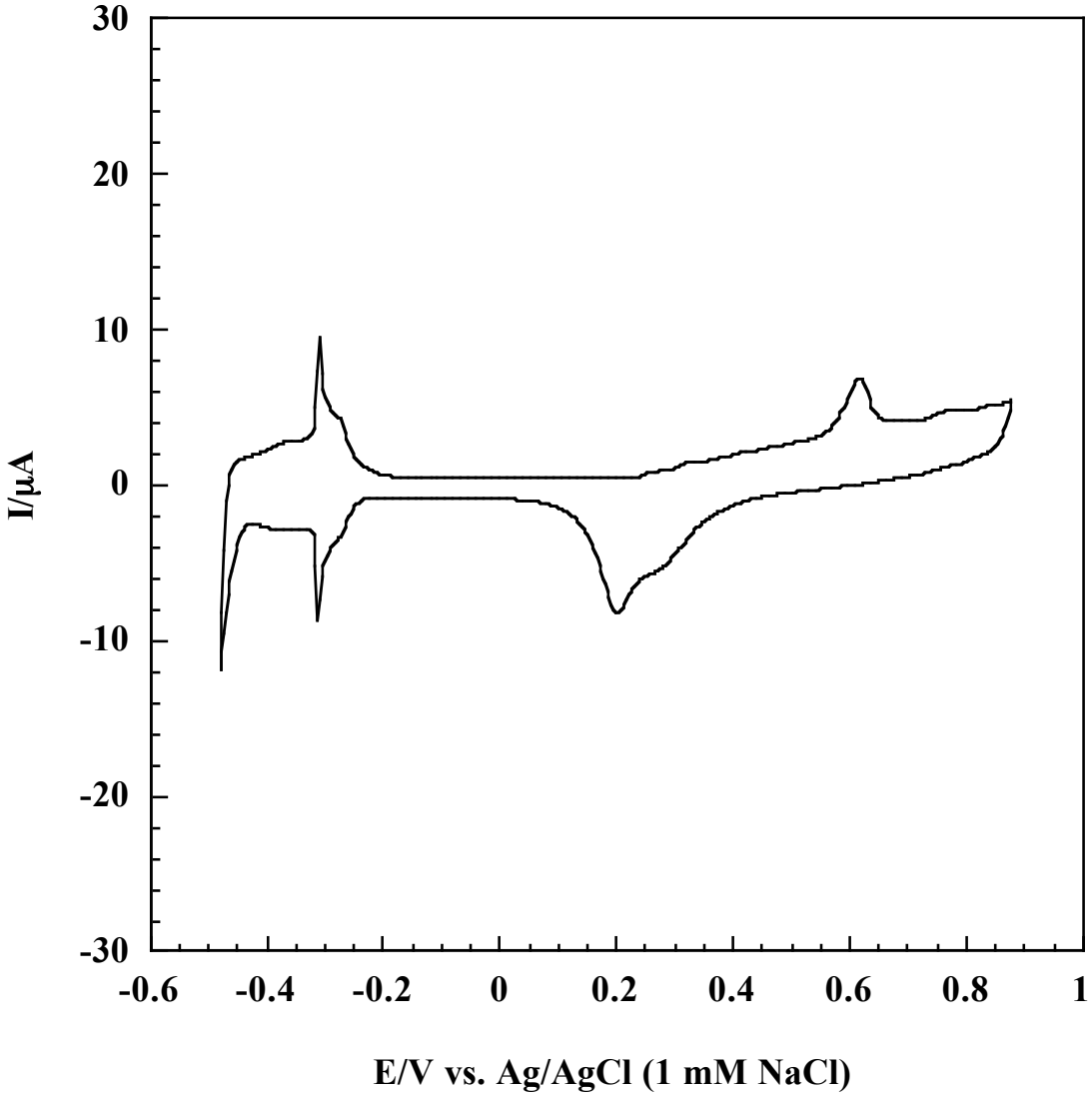

Figure 27. Cyclic voltammogram for 4 ML Pd film on Pt(111) after the 8th potential cycle in 0.1 mM H_2SO_4. Scan rate = 2 mV/sec. Electrode area = 1.12 cm^2.

to initiate both Pd anodic dissolution and Br desorption accrues to the complexity of electrochemically delineating the two processes.

Electrodeposition of Ultrathin Co Films on Pd Surfaces

Efforts to deposit electrochemically Co films on the Pd surfaces remain exceedingly sparse, if not non-existent, because of the proximity of the Nernstian deposition potential of Co and the onset potential of the hydrogen evolution region. Furthermore, Co^{2+} ions precipitate out as hydroxides or hydrated oxides in aqueous solutions close to neutral pH, and form sparingly soluble salts with carbonates, phosphates, and sulfides [88]. Such combination of chemical behavior limits the selection of supporting electrolytes and narrows down the pH window to regions where the onset of the HER is delayed to capture the Co deposition and stripping peaks.

Search for the Ideal Supporting Electrolyte

A good starting point for the electrolyte selection was the host of industrial recipes that aim to deposit *bulk* Co coatings without prescriptive concerns for well-defined surface coverages. Only feasible combinations were ventured, considering that Pd surfaces are readily "poisoned" by organic functionalities, e.g. –SH, -OH, $-NH_2$, and phenyl groups, [5] that may be found in elaborate buffer systems.

This broad survey was performed on thermally annealed *polycrystalline* Pd surfaces; favorable results obtained from this work were used as basis for the electrochemical protocols in the UHV-EC experiments. Documented on Table 2

Table 2. Various electrolyte systems tested for the feasibility of electrodepositing ultrathin Co films of well-defined coverages on polycrystalline Pd surfaces. Experimental conditions were as described in the text.

Electrolyte System	Feasibility of Co Electrodeposition
H_2SO_4	No discernible Co deposition and stripping peaks:
(i) 1 M	Onset of HER close to ocp, at E = –0.03 V
(ii) 0.1 M	Onset of HER close to ocp, at E = –0.05 V
Na_2SO_4	
(i) 0.1 M, pH = 7	Broad cathodic shoulder, centered at –0.65 V, riding on a highly steep cathodic baseline, suggests simultaneous occurrence of HER; broad anodic peak at –0.35 V
(ii) 0.1 M, pH = 4 (added with H_2SO_4)	No discernible Co deposition and stripping peaks: Early onset of HER at E = –0.07 V
(iii) 0.1 M, pH = 4 (buffered with 0.1M CH_3COOH –0.1 M CH_3COONa)	Broad cathodic shoulder, centered at –0.95 V, riding on highly steep cathodic baseline, suggests simultaneous occurrence of HER; two irresolvable anodic peaks
(iv) 0.1 M, pH = 7 (buffered with 0.1M CH_3COOH –0.1 M CH_3COONa, adjusted with drops of 0.01M NaOH)	Broad cathodic shoulder, between –0.10 V and –0.40 V, riding on highly steep cathodic baseline, suggests simultaneous occurrence of HER; two irresolvable anodic peaks
(v) 0.1 M, 0.1 M H_3BO_3	Very small cathodic shoulder between –0.10 V and –0.20 V; riding on a highly steep cathodic baseline, suggests simultaneous occurrence of HER; two irresolvable anodic peaks
$NaClO_4$	
(i) 0.1 M, pH = 7	Broad cathodic shoulder, centered at –0.65 V, riding on a highly steep cathodic baseline, suggests simultaneous occurrence of HER; broad anodic peak at –0.35 V
(ii) 0.1 M, 0.1 M H_3BO_3	

are the electrolytes used in various attempts to deposit quantitatively ultrathin Co films. The comments and observations were derived from cyclic voltammetric experiments using 10 mM $CoSO_4 \bullet 7H_2O$ at a slow scan rate of 2 mV/s. The potential scan was initiated in the cathodic direction and was reversed typically at *ca.* –0.75 V to –1.10 V at which bulk deposition of Co should have commenced; all potential readings were referenced against a Ag/AgCl (1M NaCl) electrode. The feasibility of observing a Co-stripping peak was also assessed for each complete potential cycle. None of these systems offered feasible protocols for a quantitative electrodeposition of Co on Pd.

Employing a slow scan rate of 0.1 mV/s partly resolved the apparent impasse presented by the tested electrolyte systems. This modification, however, introduced additional challenges. To finish scanning the dynamic potential window for a complete cyclic voltammetric survey (typically from ocp to a negative switching potential ranging from –0.70 to –1.1V, and then back to the double-layer potential region) required *at least* 3 hours. Such atypically long deposition periods necessitated a constant supply of inert gas hovering over the solution to prevent the entry of atmospheric contaminants such as O_2.

Both the Na_2SO_4 and $NaClO_4$ electrolyte systems showed promising deposition and stripping peaks for Co at slow scan rate. Figures 28 and 29 showed that Co deposition and HER peaks can be separated at a scan rate of 0.1 mV/s. Special attention was, however, directed to the use of $NaClO_4$ because of the fact that sulfate ions form specifically adsorbed ordered adlayers on Pd and

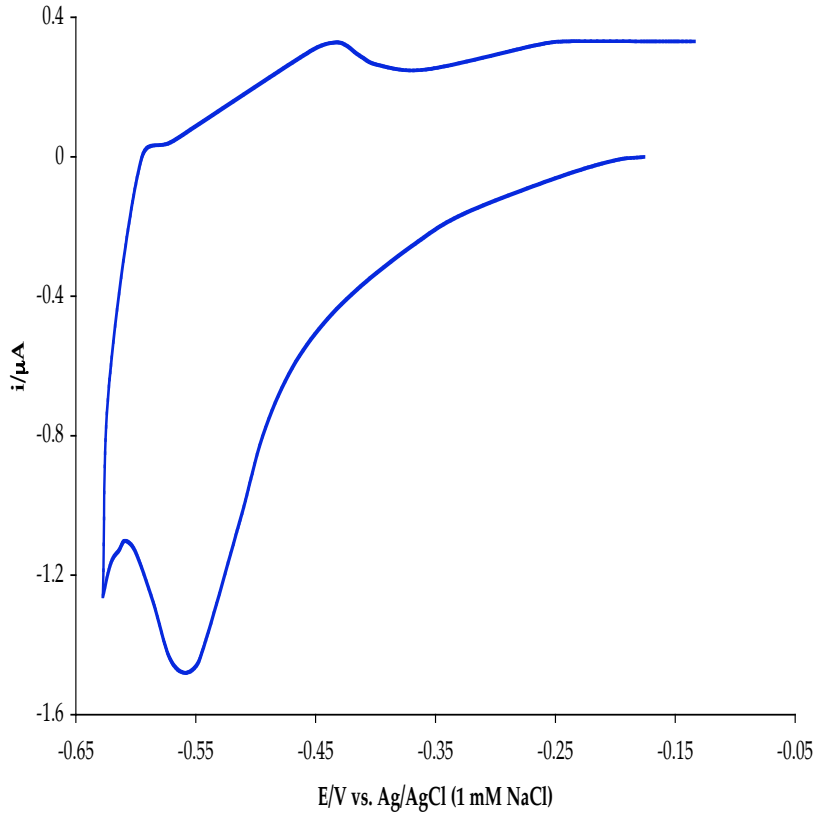

Figure 28. Voltammetric profile for the electrodeposition and stripping of Co on Pd using 2 mM $CoSO_4$ in 0.1 M Na_2SO_4 at a slow scan rate of 0.1 mV/s.

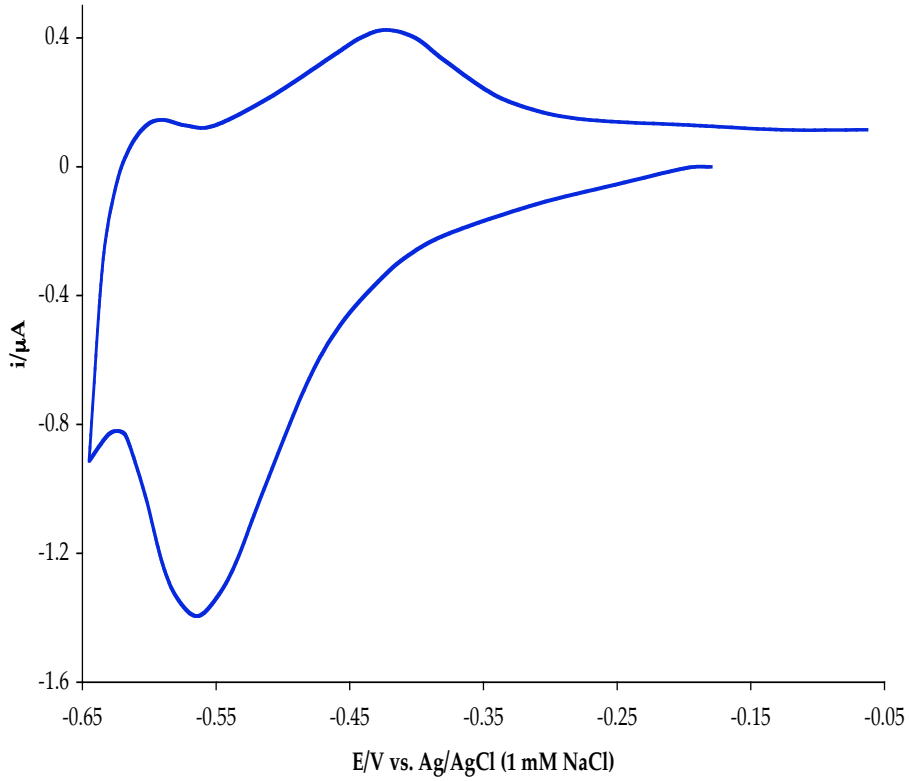

Figure 29. Voltammetric profile for the electrodeposition and stripping of Co on Pd using 2 mM $CoSO_4$ in 0.1 M $NaClO_4$ at a slow scan rate of 0.1 mV/s.

Pt surfaces [89] while perchlorate ions are considered surface inactive within the potential window of interest [90].

Potentiodynamic Electrodeposition of Co

The voltammetric profile of the chosen blank electrolyte, 0.1 M $NaClO_4$, is shown in Figure 30. All scans were initiated in the cathodic direction at a scan rate of 1.0 mV/s. The positive switching potential ($E_{+\lambda}$) was set at –0.65V while the following negative switching potentials ($E_{-\lambda}$) were employed: –0.50 V, –0.60 V, –0.65 V, –0.70 V, and –0.75V.

The inception of HER was observed at *ca*. –0.10 V. The position and intensity of the hydrogen desorption peak were dependent on the negative switching potential, with the peak centered at –0.48 V for $E_{-\lambda}$ = -0.75 V and –0.38 V for $E_{-\lambda}$ = –0.50 V. The double-layer region lay between *ca*. 0.10 V to 0.20 V. Surface oxidation of Pd commenced at *ca*. 0.40 V

A series of cyclic voltammetric experiments was conducted using 1, 2, 5, and 10 mM Co^{2+} in 1.0 M $NaClO_4$. Figure 31 revealed that the intensity of both the cathodic and anodic features concomitantly increased with Co^{2+} ion concentration. The peak separation, ΔE, between the cathodic and anodic peaks decreased with increasing bulk Co^{2+} ion concentration.

A clear delineation of the Co deposition and stripping peaks allowed a quantitative determination of the amount of Co electrodeposited on the Pd surface. Calculations were based on the numerical integration of the area of the cathodic and anodic peaks whose baselines were defined by the superimposition of the corresponding blank-electrolyte voltammograms. The

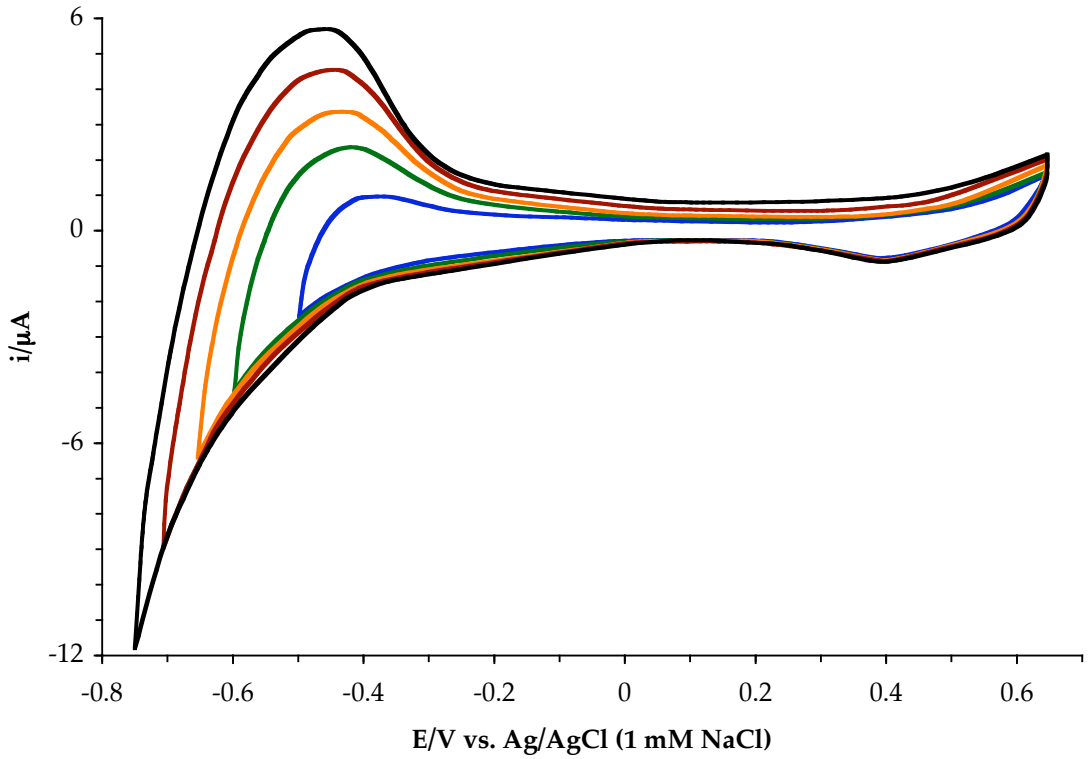

Figure 30. Cyclic voltammograms of Pt(111) in 0.1 M $NaClO_4$ obtained at different negative switching potentials. Experimental details are described in the text.

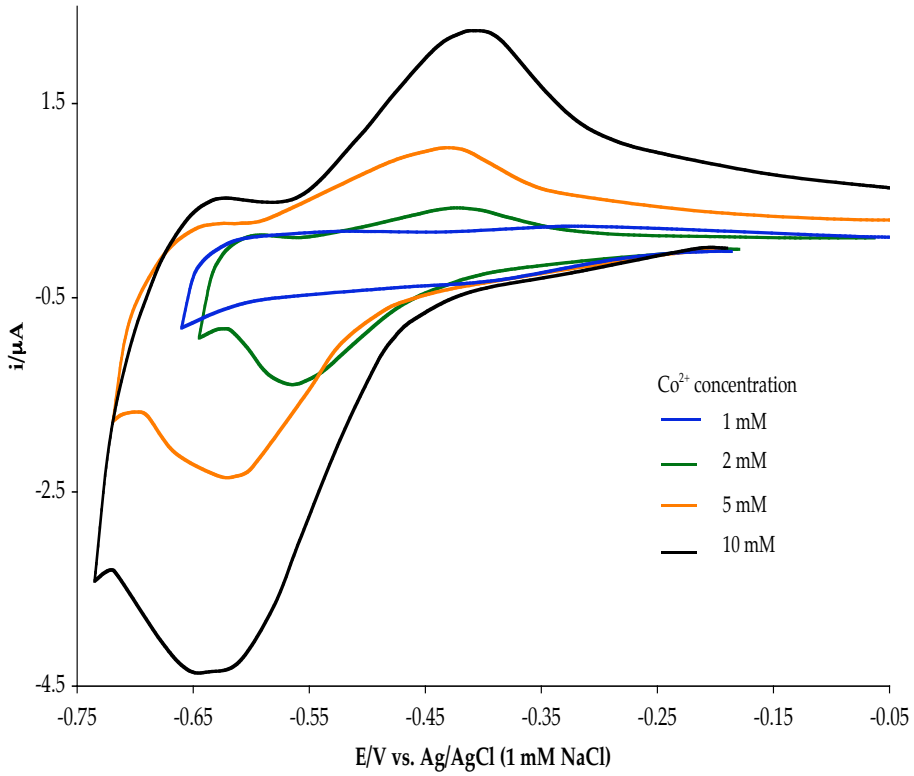

Figure 31. Potentiodynamic deposition and stripping of Co on Pd surfaces in the presence of different concentrations of Co^{2+}. Experimental conditions are described in the text.

following approximations were employed: (*i*) Previous studies demonstrated that a thermally annealed Pd polycrystalline surface is a composite of the (111) (with a surface atom density, $\Gamma = 1.5282 \times 10^{15}$ atoms/cm^2) and (100) ($\Gamma = 1.3235 \times 10^{15}$ atoms/cm^2) facets in an empirical surface-area ratio of 55:45 [91]. (*ii*) Akin to the Co/Pt system, ultrathin films of Co grew pseudomorphically on these facets, i.e. a fully covered Pd surface contained one Co adatom for every one Pd surface atom. The proximity of the lattice parameters of Pt and Pd made this assumption not unreasonable. Based on these two approximations, the integrated charges during the voltammetric scan can be nominally converted to Co surface coverages, using the factor $Q_{1\ ML} \equiv 598\ \mu C$ for a $2e^-$-electrodeposition process.

Table 3 shows the subsequent increase in deposition charges as a function of the bulk Co^{2+} ion concentration. It is important to note that the choice of the negative switching potentials was determined by the emergence of the HER peak, as evidenced by the formation of a cathodic plateau that terminated the developing deposition peak. It can be inferred from the tabulated values that only submonolayer coverages of Co can be formed using this slow potentiodynamic deposition.

To obviate the long deposition times associated with such slow voltammetric deposition, a combination of moderately fast deposition coupled with ultraslow post-deposition analysis was tested. It was previously demonstrated that a scan rate greater than 2 mV/s did not produce any observable Co deposition peak; thus, it was not surprising to obtain a broad

Table 3. Deposition and stripping charges as a function of the bulk Co^{2+} ion concentration during a slow voltammetric scan from the double-layer region to various negative switching potentials.

$\mathbf{[Co^{2+}]}$ (mmol/L)	$\mathbf{Q_{deposition}}$ (μC)	$\mathbf{Q_{stripping}}$ (μC)
1	43.89	24.84
2	98.92	56.95
5	191.89	163.18
10	469.08	402.61

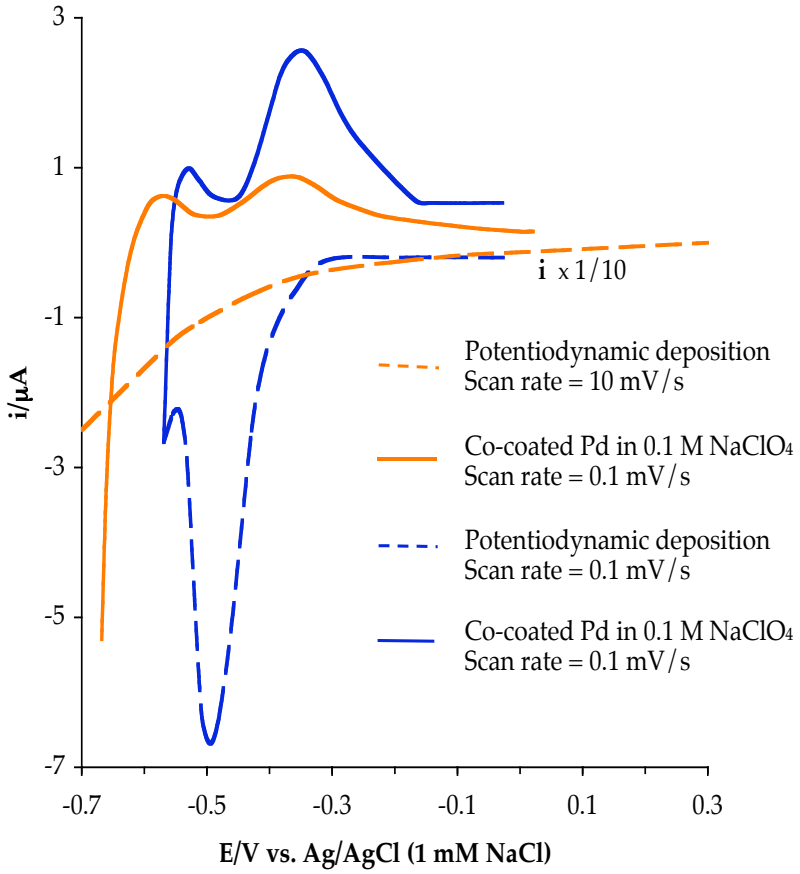

Figure 32. Potentiodynamic deposition of Co at various scan rates, followed by electrochemical stripping at ultraslow scan rate.

cathodic peak in Figure 32. Results, however, clearly demonstrated the possibility of quantitating the amount of electrodeposited Co after the fast deposition (scan rate = 10 mV/s) because of the separation of anodic peaks during a slow *post-deposition* analysis.

Potentiostatic Electrodeposition of Co

Prospects of depositing Co using a potential step experiment were explored. Attempts of measuring the potentiostatic deposition charge were stymied by the fact that the background charge (in 0.1 M $NaClO_4$ as blank electrolyte) was larger than the charge measured during Co deposition. It can be inferred from these observations that Co and H compete for Pd surface sites, i.e. the presence of Co on the surface slows down, if not impedes, the entry of H into the Pd bulk. At potentials poised not far inside the HER ($E < 0.75$ V), Co can coexist with H on a partly perturbed surface.

Various deposition potentials, ranging from the open-circuit value to –0.75V (the deposition potential dictated by the Nernst equation), were tested. The assumption that Co deposition can transpire at potentials more positive than the Nernstian value was based upon the expected underpotential deposition (UPD) phenomenon predicted by Kolb and Gerischer's correlation using work function differences between Co and Pd [92]. A typical potentiostatic deposition experiment involved immersing a smooth Pd electrode into a solution of 3 mM Co^{2+} in 0.1 M $NaClO_4$ at the double-layer region (*ca.* 0.20 V) for 1 minute and switching the potential to the desired value for 5 minutes.

The electrode was then rinsed thrice, under the chosen deposition potential, with 0.1 M $NaClO_4$ before conducting linear sweep voltammetry in Co-free blank electrolyte at a slow scan rate of 0.1 mV/s.

At a deposition potential of –0.70 V (Figure 33), a large envelope anodic peak was observed. Evident from the superimposed voltammogram for the blank (broken-line trace) was the fact that the stripping charge from the Co-coated electrode was larger than that of the bare Pd. Taking the difference between the measured anodic charges of the pristine and Co-coated electrodes did not represent the amount of electrodeposited Co since, as the deposition charges suggested, the extent of H absorption-desorption for both surfaces was highly dissimilar. It was, however, clear from a comparison of the full-width-at-half-maximum values for both anodic peaks in Figure 33, that Co-stripping and H-desorption intricately overlapped. The possibility of improving the resolution of these two peaks was explored by performing a post-deposition stripping in basic media, in which H-desorption effects were expected to be minimized.

Electrochemical Behavior of Ultrathin Co Films in Alkaline Medium

Before the interfacial electrochemistry of the prepared ultrathin Co films in basic medium can be fully investigated, the electrochemical behavior of clean, smooth Pd electrodes needs to be established under the current experimental conditions.

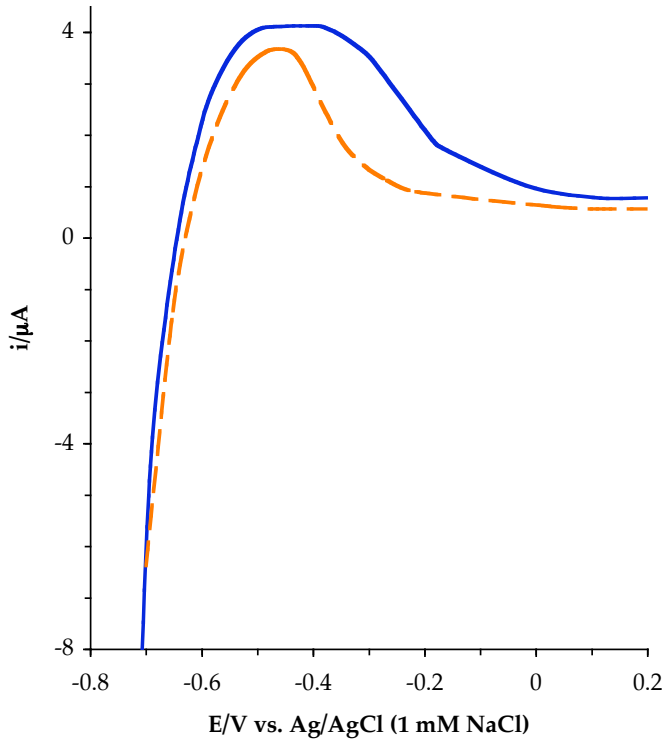

Figure 33. Linear sweep voltammogram of potentiostatically deposited ultrathin Co film on Pd. Electrodeposition potential was set at –0.70 V for 5 minutes.

The steady-state voltammetric profile of Pd in 0.1 M NaOH is presented in Figure 34. All scans were initiated from the open-circuit potential (*ca*. –0.20 V). Typically after the second cycle, a steady-state voltammogram can be obtained. Two scan rates were employed for comparison: 1 mV/s and 10 mV/s. The voltammetric features depicted in Figure 34 are congruent with the generally accepted current-potential profile of Pd in basic medium [5]. It is important to note that the reference electrode used for this purpose was a Ag/AgCl electrode containing a saturated solution of NaCl; the measured potential for this electrode was –0.60 V vs. a standard hydrogen electrode. The onset of HER was observed to shift negatively, depending on the scan rate: *ca.* –0.50 V at 1 mV/s, and –0.60 V at 10 mV/s. The early inception of Pd-surface oxidation at *ca*. –0.30 for both scan rates was not surprising since previous studies have demonstrated that the electrochemical behavior of Pd in neutral-to-basic aqueous solutions is predominantly governed by the surface-coordination chemistry of Pd hydroxo complexes.

The prospect of performing post-deposition analysis in basic medium to delineate different surface coverages of Co was investigated. Co electrodeposits were potentiostatically prepared at –0.90 V using 2 mM and 10 mM $Co(ClO_4)_4$ in 0.1 M $NaClO_4$ at a fixed deposition time of 5 min. A large overpotential was employed to ensure that sufficient Co was electrodeposited. The adlayers were rinsed thoroughly with 0.1 M $NaClO_4$ while holding the potential at –0.90 V before initiating the scan in the anodic direction.

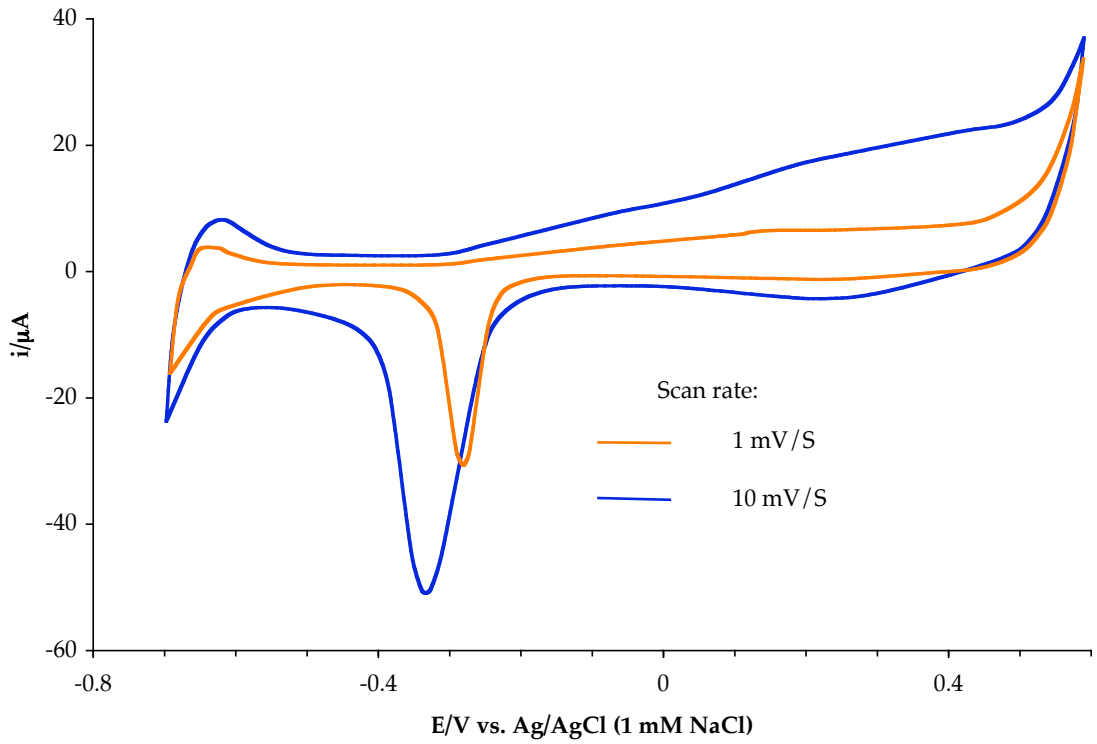

Figure 34. Cyclic voltammogram of Pd in 0.1 M NaOH. Experimental details are described in the text.

The Pourbaix diagram for Co stipulates [88] that Co is converted to CoO or its hydrated form when in contact with 0.1 M NaOH at –0.89V. Thus, upon immersing the prepared Co adlayer into 0.1 M NaOH, at a potential of –0.90V, a positive upsurge in current was detected, indicating a solid-state anodic conversion of zerovalent Co into divalent Co oxide. The current then declined towards a stable negative reading after 2 minutes; the steady-state negative current at –0.90 V implied that the oxided Co adlayer appeared to be permeable towards hydrogen absorption and/or evolution.

The broad anodic oxidation peak (Figure 35) centered at *ca*. –0.70 V marked the hydrogen desorption process. The asymmetric peak at 0.17 V signaled the formation of Co oxides of higher oxidation states. Beyond 0.55 V, extensive oxygen evolution occurred. In the reverse scan, the reduction of the oxided Co was marked by two cathodic peaks at 0.12 V and –0.10 V. At the positive switching potential (0.65 V) employed in the anodic scan, the Co oxide layer was peeled off. Subsequently, the exposed Pd substrate was oxidized, as can be inferred from the emergence of Pd-oxide reduction peak at *ca*. –0.30 V.

Results showed that, under potentiostatic conditions, the amount of Co that can be electrodeposited at a chosen overpotential depends upon the initial Co^{2+} concentration of the deposition bath. The fact that the Pd-oxide reduction peak at *ca*. –0.30 V was smaller for the Co adlayer potentiostatically deposited using 10 mM Co^{2+} implied that a higher initial surface coverage was prepared using more concentrated Co^{2+} solution. Also, the intensity of the Co-oxide

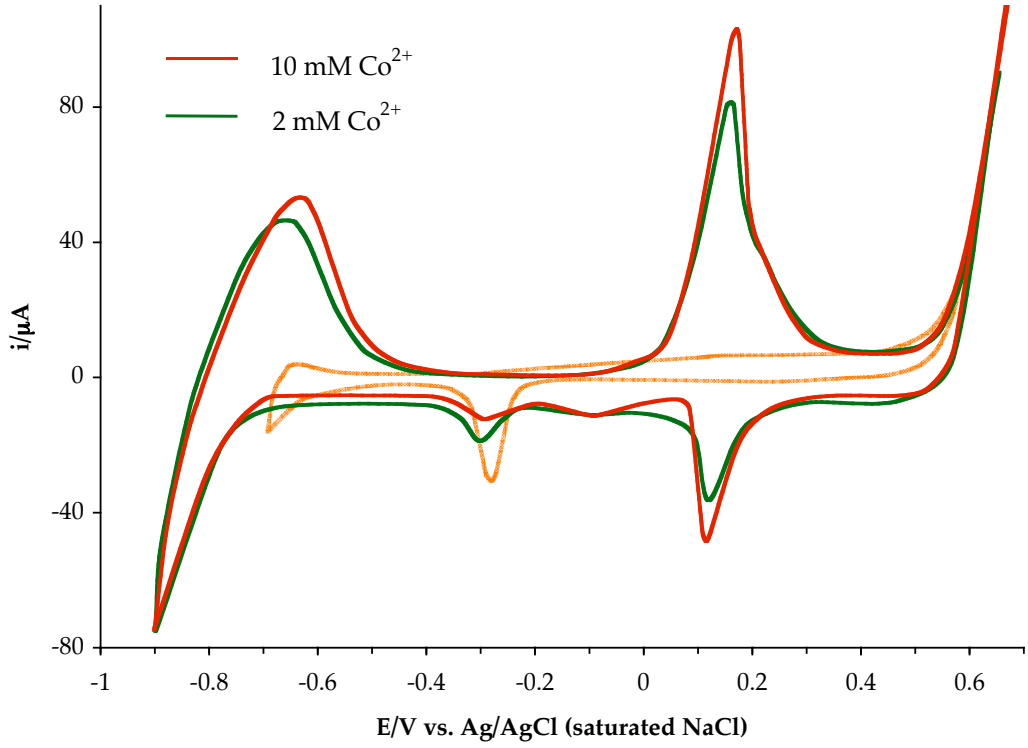

Figure 35. Cyclic voltammetric profile of Co-coated Pd electrodes in Co-free 0.1 M NaOH. Scan rate = 1.0 mV/s. Co electrodeposits were potentiostatically prepared as described in the text. Superimposed is the voltammogram of bare Pd in 0.1 M NaOH.

formation/reduction peaks was found to be dependent on the initial surface coverage of Co.

The nature of the asymmetric anodic peak at 0.17 V was elucidated by performing multiple voltammetric cycles (Figure 36). A Co adlayer, prepared by potentiostatic electrodeposition using 10 mM Co^{2+}, was cycled in Co-free 0.1 M NaOH at a scan rate of 1.0 mV/s. The second cycle revealed that the anodic peak at 0.17 V was actually composed of two peaks: the first peak at 0.02 V was proposed to represent the formation of Co(III) oxide and/or oxide while the peak at *ca*. 0.24 V marked its conversion to Co(IV) form. These assignments were corroborated by the color changes that accompanied the potential sweep: Vestiges of pink $CoO/Co(OH)_2$ were transformed into a black-brown film [$Co(OH)_2$ or $Co_2O_3 \bullet 3H_2O$] as the potential hit 0.0 V in the anodic scan.

Multiple cycling led to the diminution of the redox-couple peaks for the Co(II) → Co(III) and Co(III) → Co(IV) solid-state transformation. A possible anodic dissolution of these oxides at 0.65 V transpired, leading to the regeneration of a voltammetric profile that resembled that of a Co-free Pd surface in 0.1 M NaOH.

Electrochemical Behavior of Ultrathin Co Films in Aqueous Iodide

The ability of chemisorbed iodine to facilitate the surface ordering of electrochemically roughened Pd surfaces is well-documented [93]. The unique

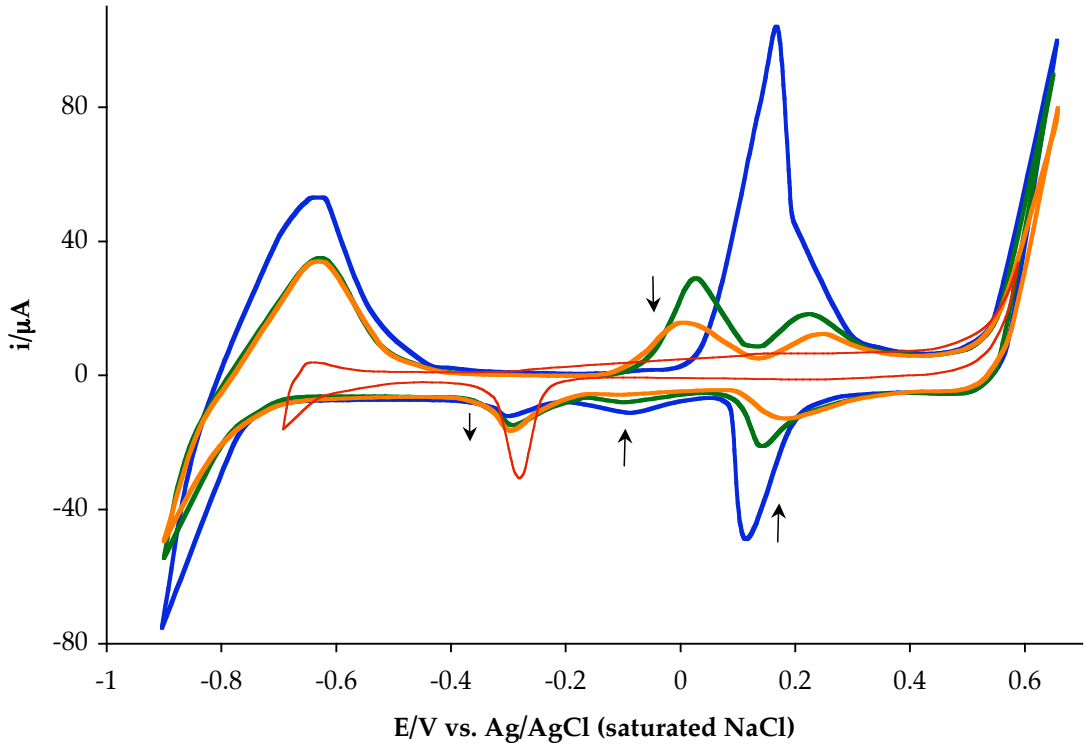

Figure 36. Multiple cycling of Co-coated Pd electrode in 0.1 M NaOH. Scan rate = 1.0 mV/s.

interfacial chemistry of between Pd and iodine provided the rationale for studying the influence of this halogen on Co adlayers Pd surfaces.

Superimposed in Figure 37 are cyclic voltammograms for Pd immersed in a Co deposition bath with and without 1 mM NaI. A slow scan rate of 0.1 mV/s was employed. The deposition bath was composed of 3 mM $Co(ClO_4)_2$ in 0.1 M $NaClO_4$. Similar voltammetric features were observed for both runs, except for the notable peak potential shifts. In the presence aqueous iodide, Co was electrodeposited at a more negative potential, registering a peak at *ca*. –0.60 V. This result implied that additional potential was required to deposit the same amount of Co obtained under iodine-free conditions.

The anodic sweep gave identical onset potential for the Co-stripping process. Although the anodic peak in the presence of aqueous iodide appeared more drawn out than that of the iodine-free system, a comparison of the background-corrected Co-stripping charges for both cases revealed that they are identical. Thus, the anodic Co dissolution process was evidently not altered by the presence of iodine in bulk solution. This finding was further confirmed when the experiment was repeated by potentiodynamically electrodepositing Co in iodine-free conditions, and then anodically scanning the potential while the Co adlayer was exposed to 1 mM NaI in 0.1 M $NaClO_4$. Results in Figure 38 clearly showed that the voltammograms obtained with and without iodine are indeed congruent.

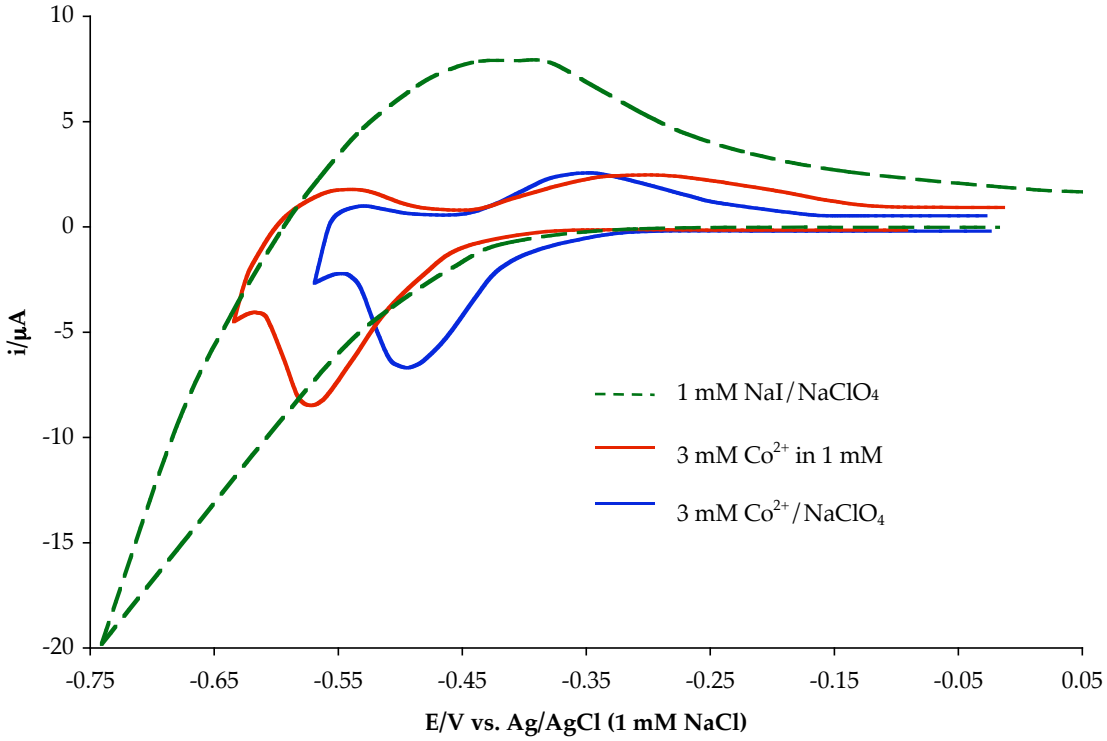

Figure 37. Cyclic voltammetry of Pd in 3 mM $Co(ClO_4)_2$ in the presence and absence of 1 mM NaI. Cyclic voltammogram for 1 mM NaI in 1.0 M $NaClO_4$ was included for comparison. Scan rate = 0.1 mV/s.

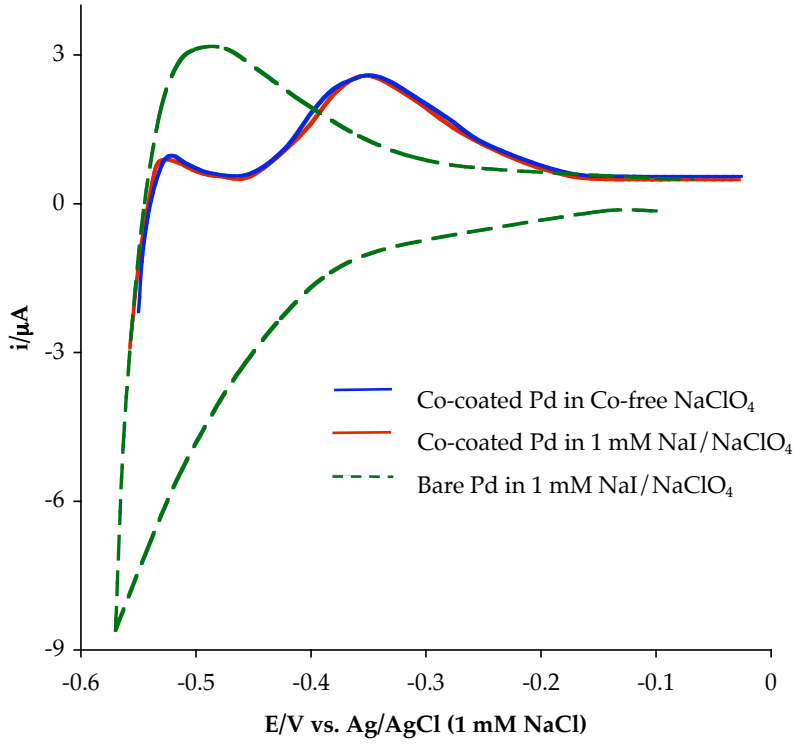

Figure 38. Linear sweep voltammogram of 8 ML Co/Pd(poly) in the presence and absence of 1 mM NaI in 0.1 M $NaClO_4$. The Co film was prepared by potentiodynamic deposition from the open-circuit potential to –0.55 V. Included for comparison is the cyclic voltammogram for a smooth Pd electrode in 1 mM NaI in 0.1 M $NaClO_4$. Scan rate = 0.1 mV/s.

Attempts at Electrodepositing Co on Pd(111)

The electrochemical preparation and characterization of ultrathin Co films described in the previous sections were a prolegomenon to the experimental protocols needed for the electrodeposition of Co on well-defined single-crystal Pd surfaces.

Just like in the thin-layer electrochemical work, the interfacial electrochemistry of a well-defined Pd(111) electrode in 0.1 M $NaClO_4$ needed to be characterized. Voltammetric features similar to those observed on polycrystalline Pd surfaces were observed. At a scan rate of 0.5 mV/s, the inception of the HER was at *ca*. –0.35 V while the H-desorption process was centered at *ca.* –0.15 V. Figure 39 shows an overlay of the voltammetric profiles of the blank electrolyte and that of 10 mM $Co(ClO_4)_2$ in 0.1 M $NaClO_4$. No Co electrodeposition and stripping peaks were discernible. Similar negative results were obtained when a much slower scan rate of 0.1 mV/s was employed.

The Auger electron spectrum (Figure 40), obtained after the replicating the potentiodynamic deposition protocols established earlier, revealed the absence of any Co deposit. It is important to note that even at an extremely high Co concentration of 1.0 M, no Co deposition was observed from voltammetric and AES analyses.

When cyclic voltammetry in 0.1 M $NaClO_4$ was performed using a Pd(111) electrode that had been previously subjected to very positive potentials ($E \geq 0.70$ V), dramatic changes in the voltammetric profile of the blank electrolyte were observed. Figure 41 is a collection of cyclic voltammograms of

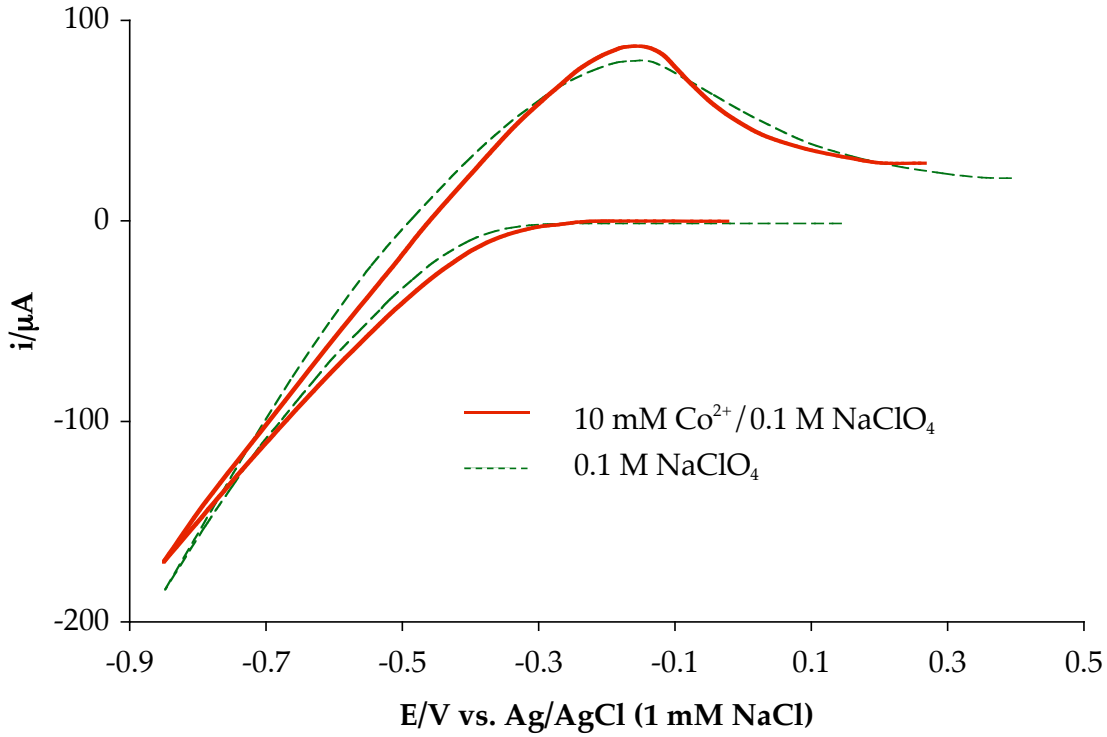

Figure 39. Cyclic voltammetry of clean, well-ordered Pd(111) electrode in 10 mM $Co(ClO_4)_2$/0.1 M $NaClO_4$. Scan rate = 0.5 mV/s.

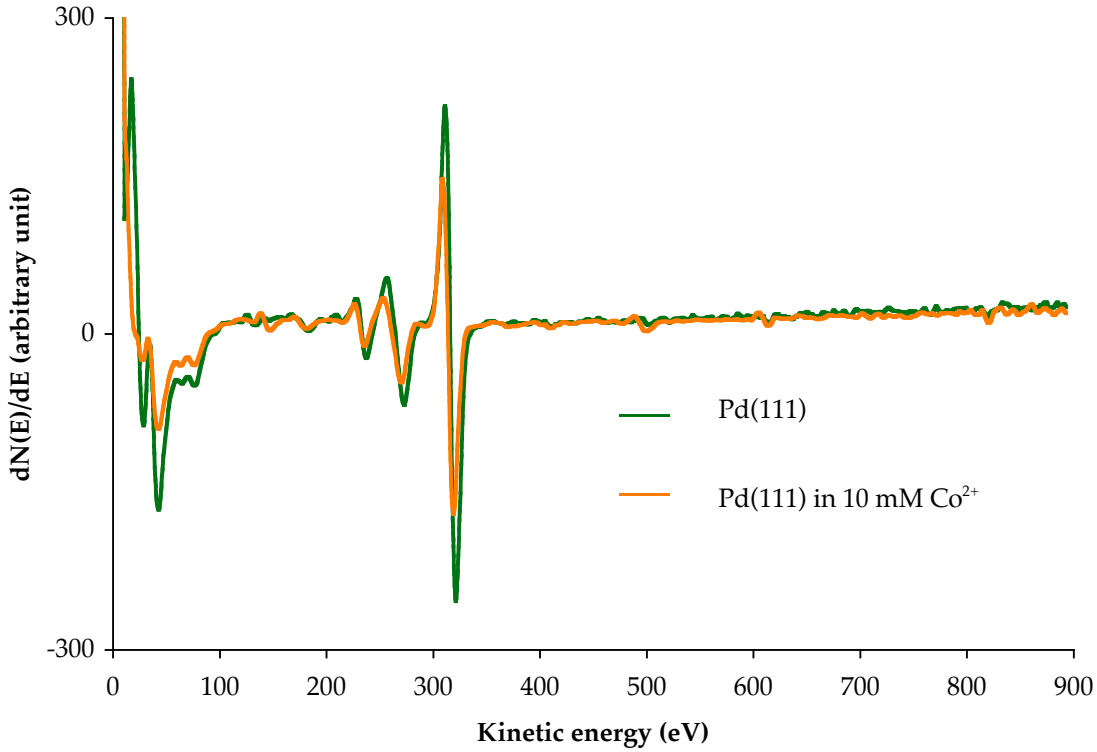

Figure 40. AES of Pd(111) after attempts of slow potentiodynamic deposition using 10 mM $Co(ClO_4)_2$ in 0.1 M $NaClO_4$ from ocp to –0.85 V. Incident beam energy = 2 keV; beam current = 1 μA.

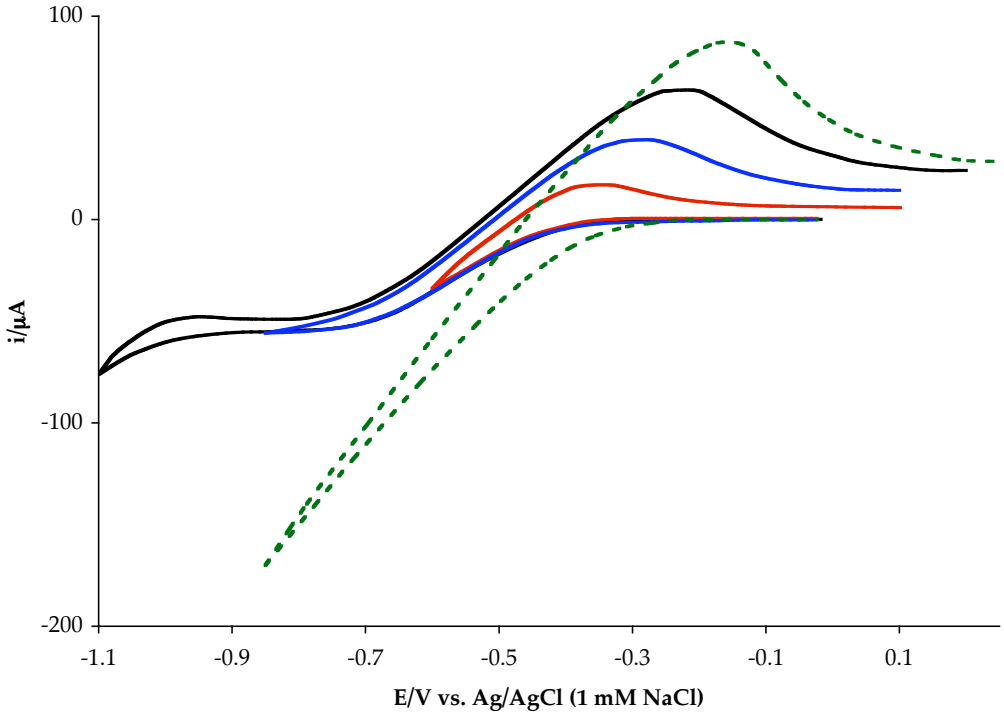

Figure 41. Cyclic voltammogram of ORC-roughened Pd(111) in 0.1 M $NaClO_4$ at various negative switching potentials. Scan rate = 0.5 mV/s. Superimposed for comparison is the voltammogram (broken-line trace) for clean, well-ordered Pd(111) in 0.1 M $NaClO_4$.

Pd(111) electrode in blank electrolyte (0.1 M $NaClO_4$) at various negative switching potentials; the electrode was roughened by oxidation-reduction cycles (ORC). Included for comparison was the voltammetric profile of a highly-ordered Pd(111) electrode. Specifically, a cathodic plateau developed between –0.70 V and –1.0 V; the potential range for such plateau depended on the duration and applied potential during anodic polarization. The H-desorption peak in the anodic scan appeared very delayed and overlapped the region where Co-stripping was expected to occur.

The extent of surface disorder brought about by anodic roughening upon immersing the electrode in 0.1 M $NaClO_4$ at 0.75 V for 2 minutes is clearly depicted by the LEED pattern shown in Figure 42.

Attempts to deposit Co potentiodynamically were repeated using electrochemically roughened Pd(111) substrates. Cyclic voltammograms in 10 mM Co^{2+} (Figure 43) showed the emergence of a new anodic peak centered at –0.68 V. The origin of this peak was ascribed to the Co-stripping process, as can be deduced from the overlaid voltammetric profile of the blank solution.

The Co electrodeposition peak appeared as an ill-defined shoulder near –0.75 V. Results suggest that, on the electrochemically roughened Pd(111), the Co adlayer has to be stripped off first before H-adsorption can begin. This result differed with observations from polycrystalline surfaces that indicated the H-permeability of the formed Co adlayer.

The electrodeposition of Co on ORC-roughened surfaces was also performed potentiostatically. A previously roughened Pd(111) electrode was

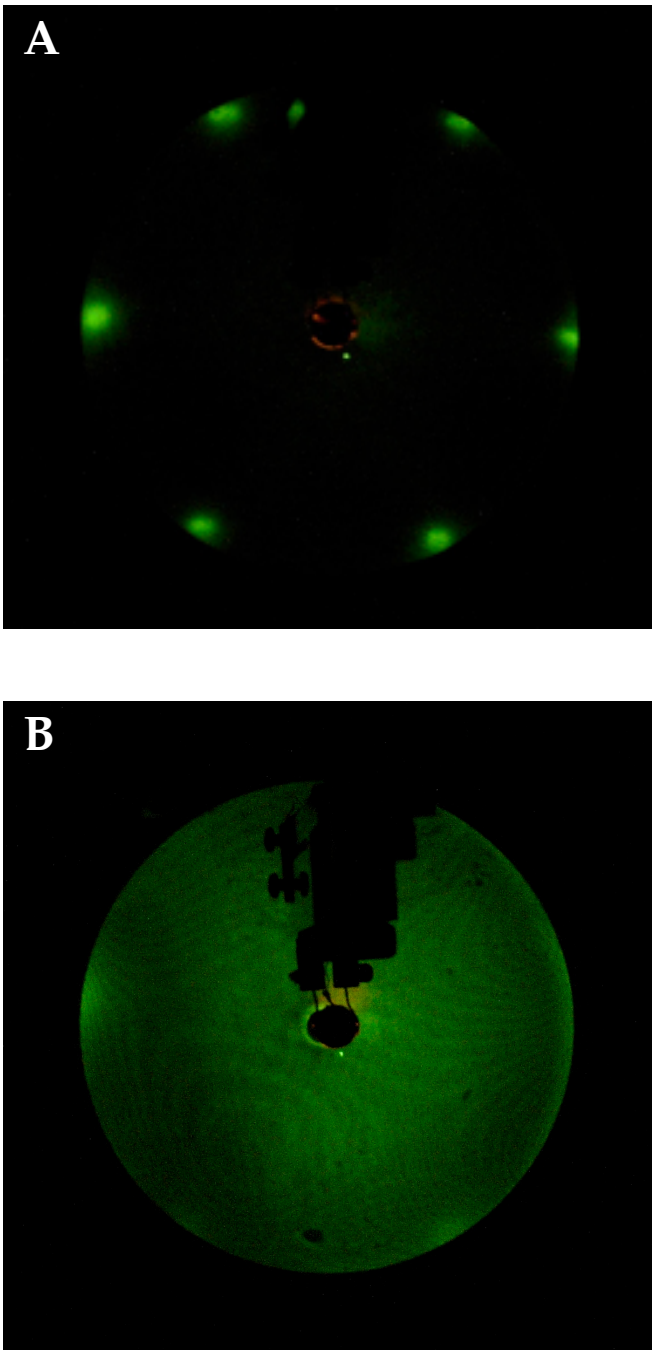

Figure 42. LEED pattern of Pd(111) (a) before and (b) after anodic roughening at 0.75 V for 2 minutes. Beam energy = 52 eV; beam current = 2 μA.

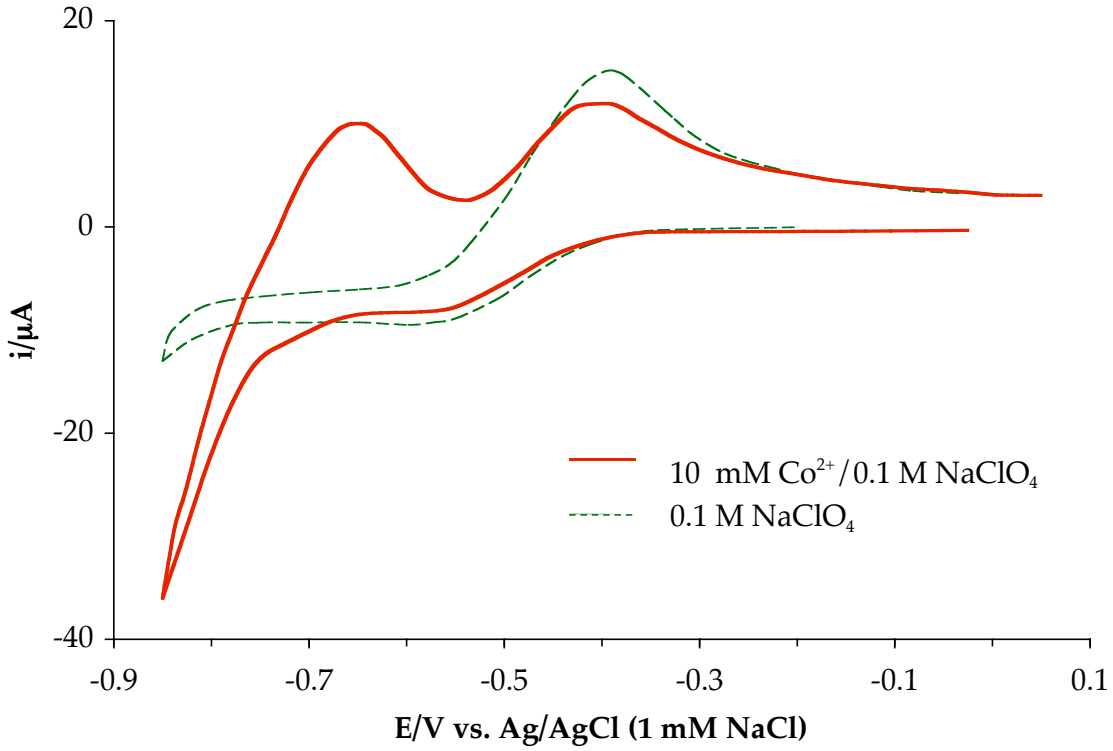

Figure 43. Cyclic voltammetry of anodically roughened Pd(111) electrode in 10 mM $Co(ClO_4)_2$/0.1 M $NaClO_4$. Scan rate = 0.5 mV/s.

exposed to 10 mM $Co(ClO_4)_2$ in 0.1 M $NaClO_4$. Co was electrodeposited by switching the potential from the double-layer region to –0.85 V; deposition time was set at 2 minutes. A linear sweep voltammogram was recorded (Figure 44) in Co-free 0.1 M $NaClO_4$ at a scan rate of 0.5 mV/s. The voltammetric signal at –0.68 V resembled that obtained from the potentiodynamically electrodeposited Co adlayer in Figure 43. A comparison of superimposed voltammograms for the blank and the prepared adlayer clearly showed that the Co stripping and H-desorption peaks were distinctly separated.

The presence of Co electrodeposits on the electrochemically roughened Pd(111) surface was confirmed by Auger electron spectroscopy (Figure 45). Co registered a trio of peaks at *ca.* 650 eV, 710 eV, and 780 eV. The appearance of Cl and O peaks was noticeable amid the fact that the emersed electrode was thoroughly rinsed *ten times* with water. It can be argued that the application of very positive potentials, close to the oxygen evolution region, introduced surface defects that physically entrapped any remnant supporting electrolyte. The proposed occurrence of electrochemical surface roughening was supported by the absence of any discernible LEED pattern.

It is interesting to note that if the ORC-roughened Pd(111) electrode was treated with 0.1 mM NaI in 0.1 M $NaClO_4$ at open-circuit potential – an *in-situ*, nonthermal procedure known to restore surface order [5] – no Co peaks were discernible from voltammetric and AES analyses. That an electrochemically roughened Pd(111) surface is prerequisite to a successful Co electrodeposition precluded further pursuits in establishing structure-reactivity correlations.

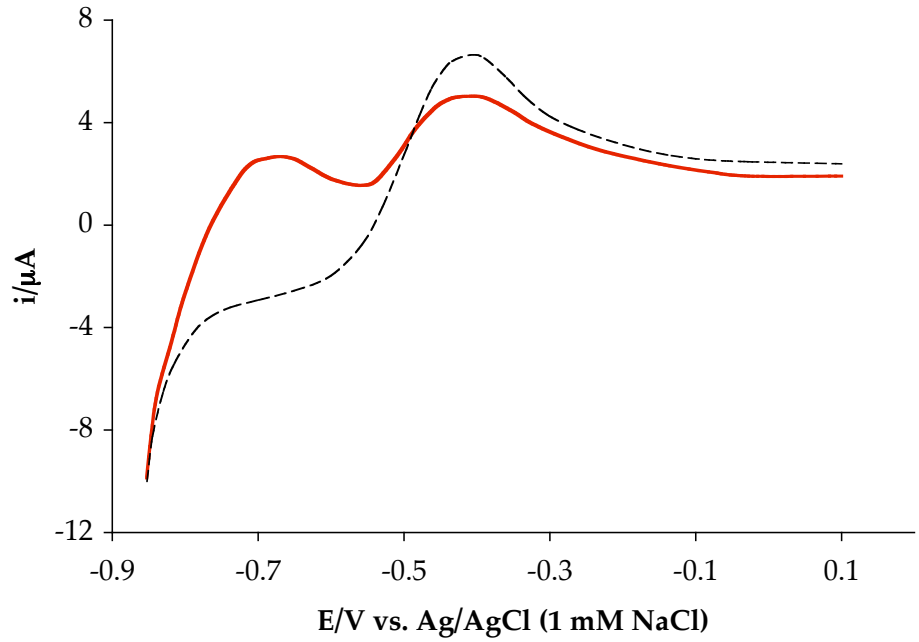

Figure 44. Linear sweep voltammogram of potentiostatically deposited Co on electrochemically roughened Pd(111) in 0.1 M $NaClO_4$. Co was electrodeposited as described in the text. Scan rate = 0.5 mV/s.

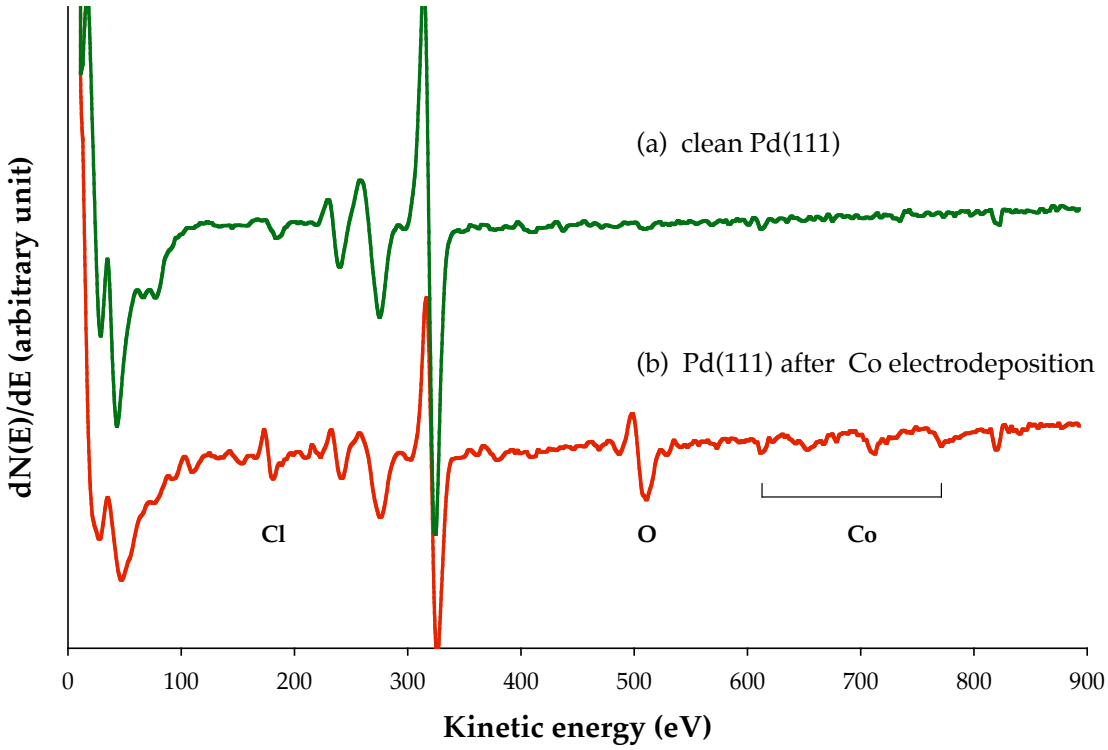

Figure 45. Auger electron spectrum of Pd(111) after potentiodynamic deposition of Co. Incident beam energy = 2 keV; beam current = 1 μA.

Electrodeposition of Ultrathin Bi Films on Pd(111)

The so-called "green chemistry" movement has provided impetus for designing environmentally friendly materials in various applied fields, such as industrial catalysis, where the use of toxic transition heavy metals is conceptually *de rigueur* [94]. For this purpose, bulk bismuth electrodes have been investigated as alternative materials in mercury-based electroanalytical detection of trace heavy metals [95]. Additional research interest emanates from the special propensity of biomolecules, such as D-ribose [96] and adenosine [97], to electrosorb at well-defined Bi(111) surfaces. Thus far, no investigations have been made on how the aforestated properties are affected if bulk Bi was strategically scaled down to ultrathin film dimensions.

The following section describes the electrochemical preparation and subsequent surface characterization of ultrathin Bi films on Pd(111) using combined ultrahigh vacuum-electrochemical methods. The interfacial chemistry of the prepared Bi electrodeposits was explored using the chemisorption of iodine and the electrooxidation of D-glucose as surface probe reactions.

Cyclic Voltammetry of Pd(111) in Sulfuric Acid

Figure 46 displays a typical current-potential profile for a clean, well-ordered Pd(111) disc. The following features closely match with those reported in previous works [89]:

(*i*) The onset of hydrogen evolution at –0.30 V is often preceded by a cathodic spike close to –0.20 V; the origin of this shoulder and its anodic counterpart at –0.25 V is ascribed to the hydrogen adsorption-desorption [98].

(*ii*) A prominent peak centered at 0.55 V marks the anodic surface-oxidation of Pd. Step-like shoulders at 0.27 V and 0.39 V originate from the oxidation of the polycrystalline edges of the Pd(111) disc and the Pd wires of the crystal holder. By changing the level of immersion of the electrode, such that the exposed portion of the polycrystalline wires is minimized, it can be verified that majority of the anodic signal observed within this potential region is ascribable to the (111) facet (Figure 46).

(*iii*) The oxygen evolution region begins at *ca.* 0.70 V.

(*iv*) The large cathodic peak at 0.15 V indicates the reduction of the oxided Pd surface. The peak position slightly shifts negatively with increasing positive switching potential as can be seen from Figure 47.

Electrochemical Behavior of Pd(111) in Aqueous Bi^{3+}

A systematic study of the electrodeposition of Bi on Pd(111) entails documenting the voltammetric profile of the electrode in the presence of Bi^{3+} ions in bulk solution. Figure 48 shows the cyclic voltammogram of a clean Pd(111) in 1 mM Bi^{3+} in 0.1 M H_2SO_4. All scans were initially headed to the cathodic direction.

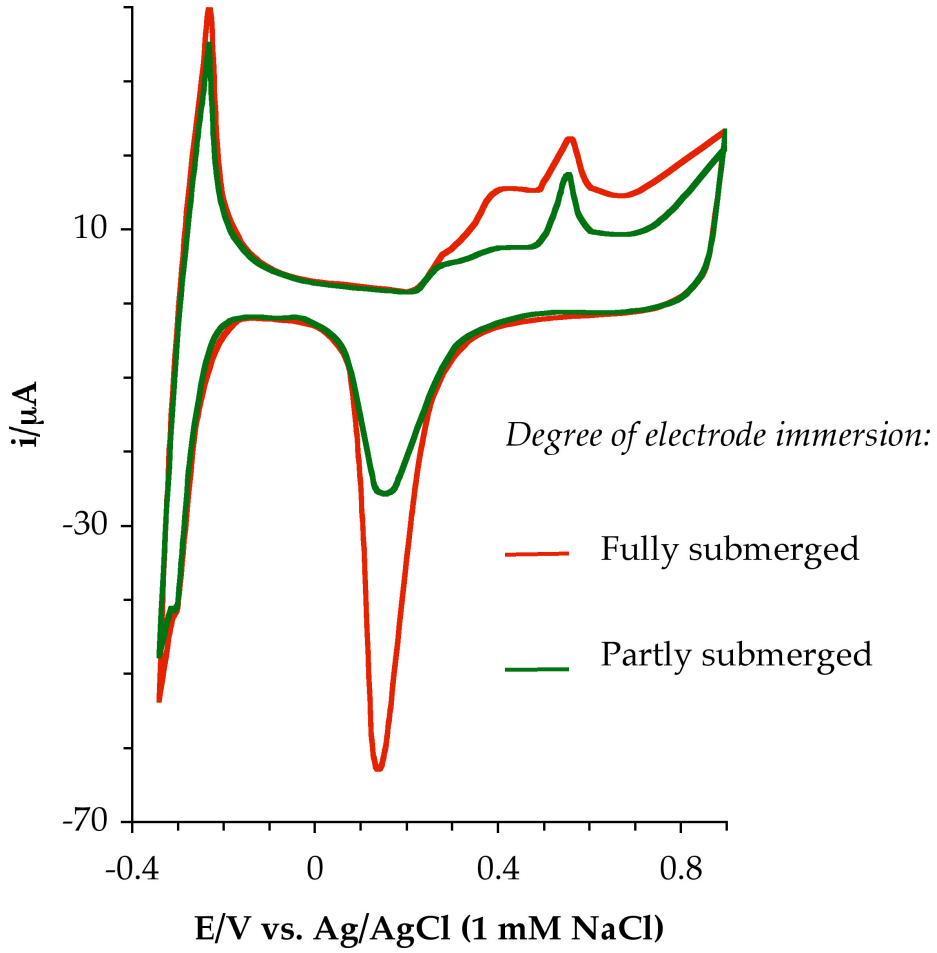

Figure 46. Current-potential profile of clean, well-ordered Pd(111) disk electrode at various levels of immersion in 0.1 M H_2SO_4. Scan rate = 5 mV/s. Geometrical area = 1.9796 cm^2.

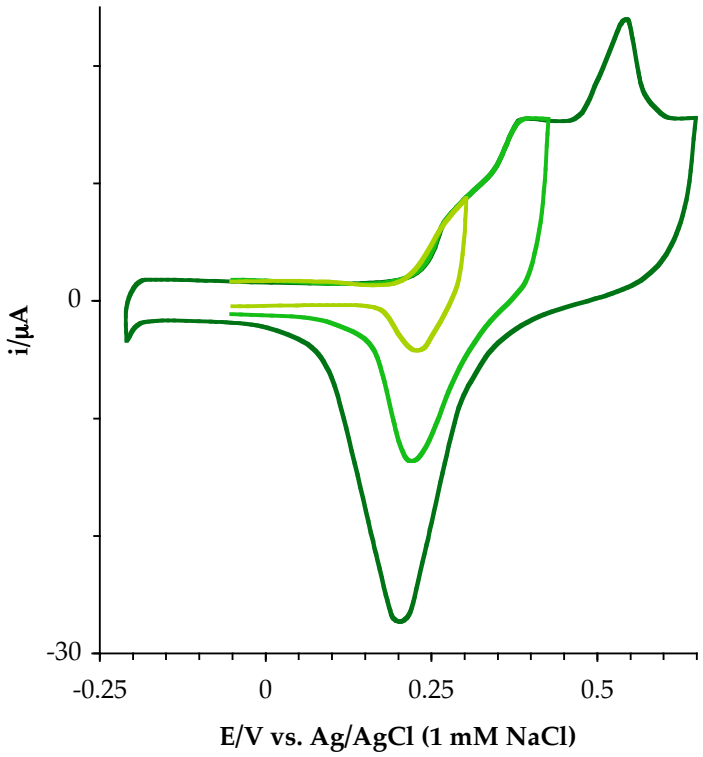

Figure 47. Effect of different positive switching potential on the reduction potential of oxided Pd-surface. Scan rate = 5 mV/s.

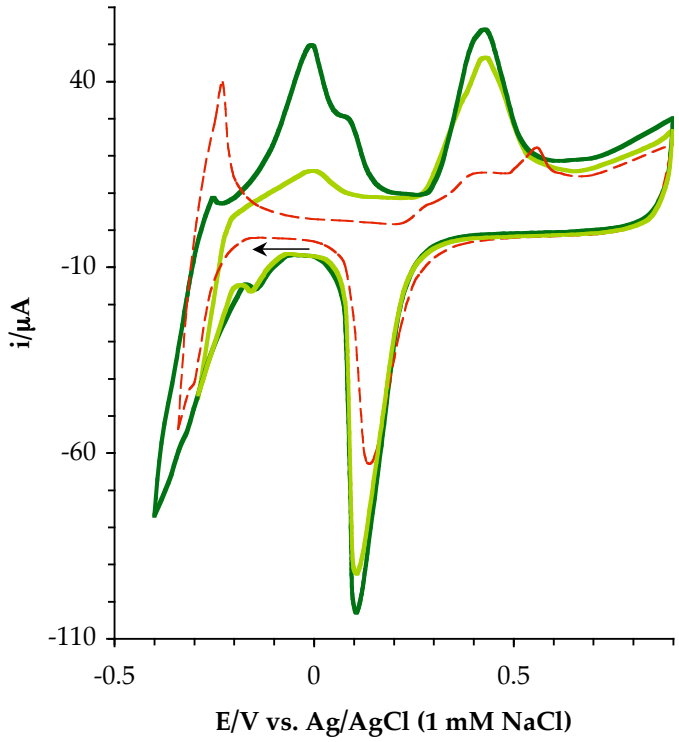

Figure 48. Cyclic voltammogram of Pd(111) in 1 mM Bi^{3+}/0.1 M H_2SO_4 at different negative switching potentials. Scan rate = 5 mV/s. Experimental details are described in the text. The broken-line trace corresponds to the voltammetric profile of 0.1 M H_2SO_4.

Under the present experimental conditions, the electroreduction of Bi^{3+} to zerovalent Bi is expected to occur at –0.27 V. The emergence of a sharp cathodic peak at –0.20 V signified the underpotential deposition (UPD) of Bi (*from hereon designated as* Bi_{UPD}). Excursions to negative potentials that border the HER led to the *bulk* deposition of Bi; its subsequent stripping appeared at *ca.* –0.04 V. Adjacent to this bulk-stripping peak was a small shoulder (*ca*. 0.02 V) whose position depended on the negative switching potential; by reversing the scan just before the onset of bulk Bi deposition (Figure 48), this anodic peak appeared at *ca.* 0.0 V. This switching-potential-dependent peak was assigned to the stripping of Bi_{UPD}.

The nature of the large anodic peak at 0.45 V deserved additional attention. The superimposed voltammogram of the blank electrolyte (broken-line trace in Figure 48) showed that, on a pristine Pd(111) electrode, surface oxidation began at *ca*. 0.22 V. It was, therefore, not unreasonable to invoke the possibility that the oxidative process represented by the peak at 0.45 V was a composite of anodic signals from Pd surface-oxidation and anodic oxidation of remnant Bi_{UPD}. Essential to the understanding of the origin of this peak was the observation that (*i*) its onset was more positive than that of the Pd-surface oxidation; (*ii*) a flat double-layer potential region exists prior to its emergence; the significantly large difference between the double-layer currents of bare Pd(111) and its Bi-coated state can be ascribed to the capacitive contribution of Bi^{3+} in bulk solution. To further elucidate the anodic processes occurring within

the 0.20 – 0.60 V region, a clean Pd(111) electrode was immersed in 1 mM Bi^{3+}/0.1 M H_2SO_4. A potential scan was initiated from the open-circuit potential (0.27 V) and headed to the anodic direction. Results are displayed in Figure 49. The anodic sweep yielded two sharp peaks: The peak at 0.55 V corresponded to the Pd surface-oxidation of the (111)-facet while the one at 0.45 V represented the anodic oxidation of Bi adspecies. These results, therefore, implied that by simply immersing the Pd(111) electrode in $Bi^{3+}_{(aq)}$, without any applied potential (i.e. at open-circuit condition), spontaneous electrodeposition of Bi on Pd(111) transpires.

Spontaneous Deposition of Bi on Pd(111)

The phenomenon of spontaneous deposition of metals on noble-metal surfaces has been noted in literature. For instance, mere exposure of Pt(*hkl*) electrodes to a solution $RuCl_3$ in acid electrolyte leads to the formation of Ru islands that enhances the electrocatalytic performance of Pt for methanol oxidation [99]. The electrodeposition of Bi on Pt(111) is an illustrative case where a less noble metal, like Bi, is reduced to form zerovalent Bi [58-61]. This apparently counterintuitive phenomenon is not surprising for catalytic surfaces [61], such as Pd, which show propensity to form surface hydroxo- and oxo-complexes, especially in neutral to basic media. It can be surmised that the signal between 0.20 V and 0.60 V is a result of the anodic oxidation of adsorbed

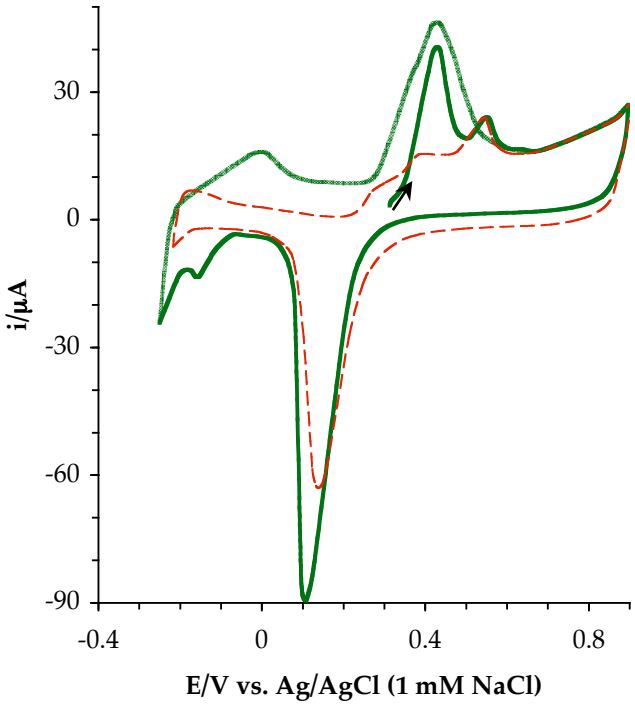

Figure 49. Anodically initiated potential scan in 1 mM Bi^{3+}/0.1 M H_2SO_4. Scan rate = 5 mV/s. Experimental details are described in the text. The broken-line trace corresponds to the voltammetric profile of 0.1 M H_2SO_4.

Bi^0 and/or contributions from Pd-surface oxidation that becomes more predominant at more positive potentials.

Coulometric charge measurements between 0.20 V and 0.65 V allowed a quantitative assessment of the contribution of each oxidative process. A pristine Pd(111), immersed in 0.1 M H_2SO_4, accumulated 955.2 ± 0.6 μC of anodic charge for 2 minutes, while a Pd surface modified by spontaneously deposited Bi produced a total anodic charge of 958.1 ± 0.6 μC. The difference between the two values (2.9 μC) represented the charge associated with the anodic process involving Bi electrodeposits. Such background-corrected anodic charge can be converted to the amount of Bi spontaneously deposited, by virtue of Faraday's Law, if the number of moles electrons released per mole reaction were known.

Similar challenges surrounding the determination of the exact anodic process between 0.20 V and 0.65 V were documented in electrodeposition studies of Bi on Pt(111). Clavilier originally proposed the possible formation of BiO_{ads} or $Bi(OH)_{2ads}$ [61]. Using temperature-dependent voltammetric measurements, Feliu and Jerkiewicz [58] claimed that the adsorbed Bi is anodically converted to $Bi(OH)_2$ via surface electronic effects; based on thermodynamic arguments, a Born-Haber cycle was constructed, allowing an empirically derived ΔH_f^o value of –44 kJ/mol ascribed to $Bi(OH)_2$. On the other hand, Kolb and coworkers inferred from *ex situ* XPS analysis the post-anodic presence of zerovalent Bi [60] even though a slight 0.5 eV-shift from the zerovalent Bi 5f core level was observed; such shift was ascribed to the strong

Bi-Pd interaction, the influence of coadsorbed anions, [60] and Bi-induced changes in the local potential of zero charge (pzc) for Pd(111) [100]. The absence of a consensus in the interpretation of the aforestated anodic process in the Bi-Pt(111) case prompted a similar *ex situ* XPS analysis of the Bi adlayer prepared in the present investigation.

Shown in Figure 50 is the XPS spectrum for a Bi adlayer electrodeposited onto a thermally annealed polycrystalline Pd foil at a deposition potential of –0.10 V for 2 minutes using 1 mM Bi^{3+}/0.1M H_2SO_4. The resulting Bi adlayer was thoroughly rinsed with blank electrolyte under potential control (–0.10 V), after which the potential was switched to 0.45 V for 2 min. Superimposed for comparison on the spectrum is a Bi_2O_3 standard.

XPS results revealed that the doublet (159.40 eV and 164.48 eV) exhibited by the anodically oxidized Bi adlayer corresponded to a set of slightly blue-shifted peaks (+0.31 eV) for a trivalent Bi. Binding energies for zerovalent Bi lie between 156.9 eV and 157.1 eV. While these results failed to render unambiguous evidence to the existence of divalent Bi, the peak positions demonstrated the absence of zerovalent Bi; i.e. it is possible that the metastable, anodically generated divalent Bi was converted to the thermodynamically stable trivalent state during sample transfer. A caveat to this interpretation is the inherently complicated nature of an *ex situ* analysis that is highly vulnerable to extraneous factors arising from the temporal gap between the electrochemical preparation and surface characterization. Moreover, the absence of a stable XPS

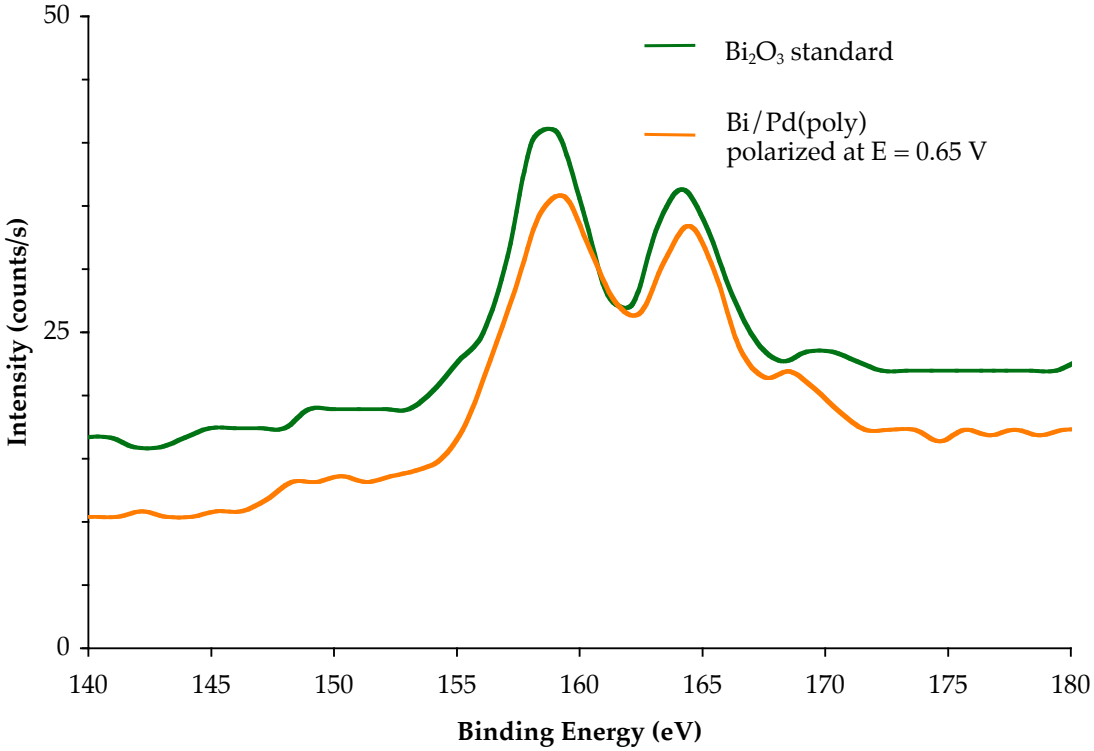

Figure 50. X-ray photoelectron spectrum of the Bi 4f core levels for a Bi/Pd foil adlayer prepared by potentiostatic deposition at –0.10 V followed by anodic polarization at 0.45 V. Included for comparison is the spectrum of Bi_2O_3 standard.

standard for the divalent species debilitated the elucidation of the real chemical state of Bi. Further support to the existence of this divalent Bi, however, can be gleaned from a background-corrected conservation-of-charge analysis [*vide infra*].

Efforts to document further the surface structure and geometry of spontaneously deposited Bi adatoms on Pd(111), using LEED and AES, were thwarted by the fact that there were no discernible differences between pre- and post-spontaneous-deposition LEED patterns (Figure 51), indicating the absence of long-range surface order. A similar case was observed UHV-prepared Bi adlayers on Pt(111), where it was concluded that, at very low coverages, Bi adatoms are randomly dispersed without forming two-dimensional surface islands [101, 102]. Complementary quantitation revealed that a Bi surface coverage of *ca*. 0.30 ML was spontaneously electrodeposited (Figure 52).

Underpotential Deposition of Bi on Pd(111)

Electrochemical preparation of ultrathin Bi films with well-defined coverages relies on the construction of an electrodeposition isotherm. Unlike most surface-coverage isotherms that assume reversible conditions, the isotherm presented in this study involves a thermodynamically irreversible deposition of Bi on Pd(111), i.e. the applied potential required for electrodeposition is distinctly different from the potential needed for dissolution.

Figure 48 had already demonstrated the existence of Bi UPD. A slow potential sweep, shown in Figure 53, however, revealed an additional UPD peak

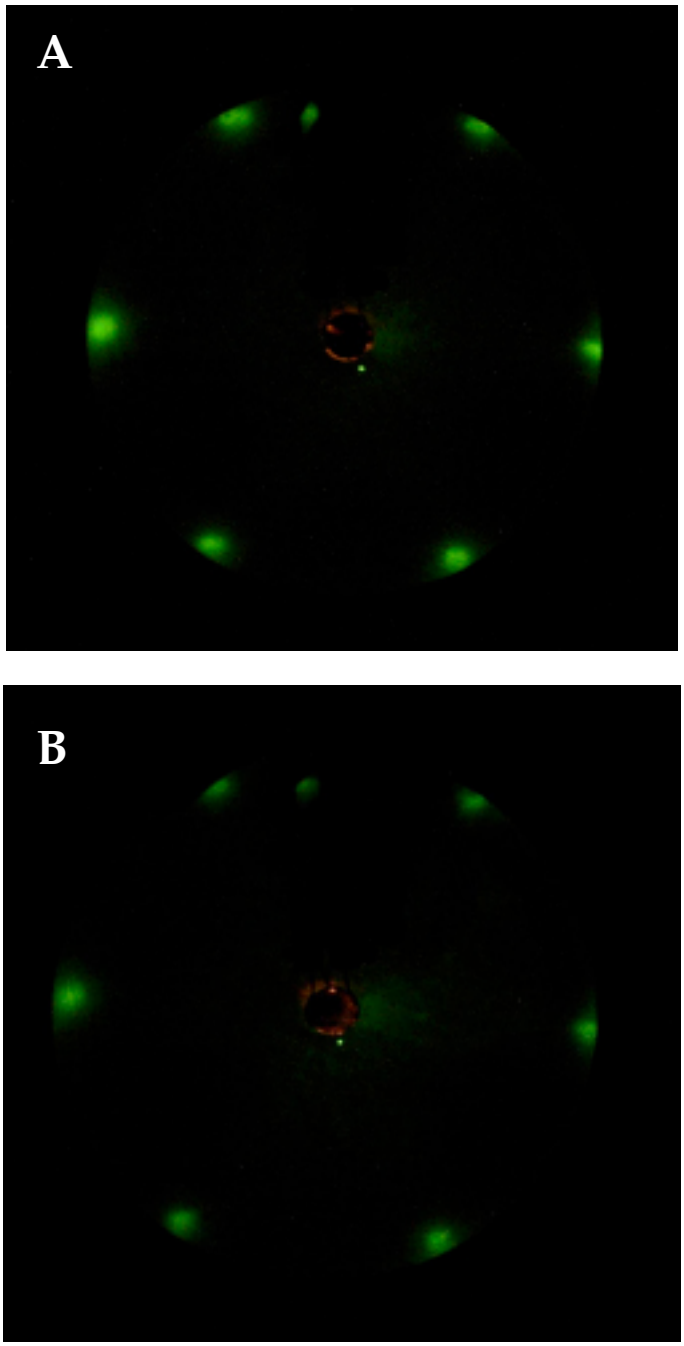

Figure 51. LEED pattern of Pd(111) surface (a) before and (b) after spontaneous electrodeposition of Bi. Beam energy = 52 eV; beam current = 2 μA.

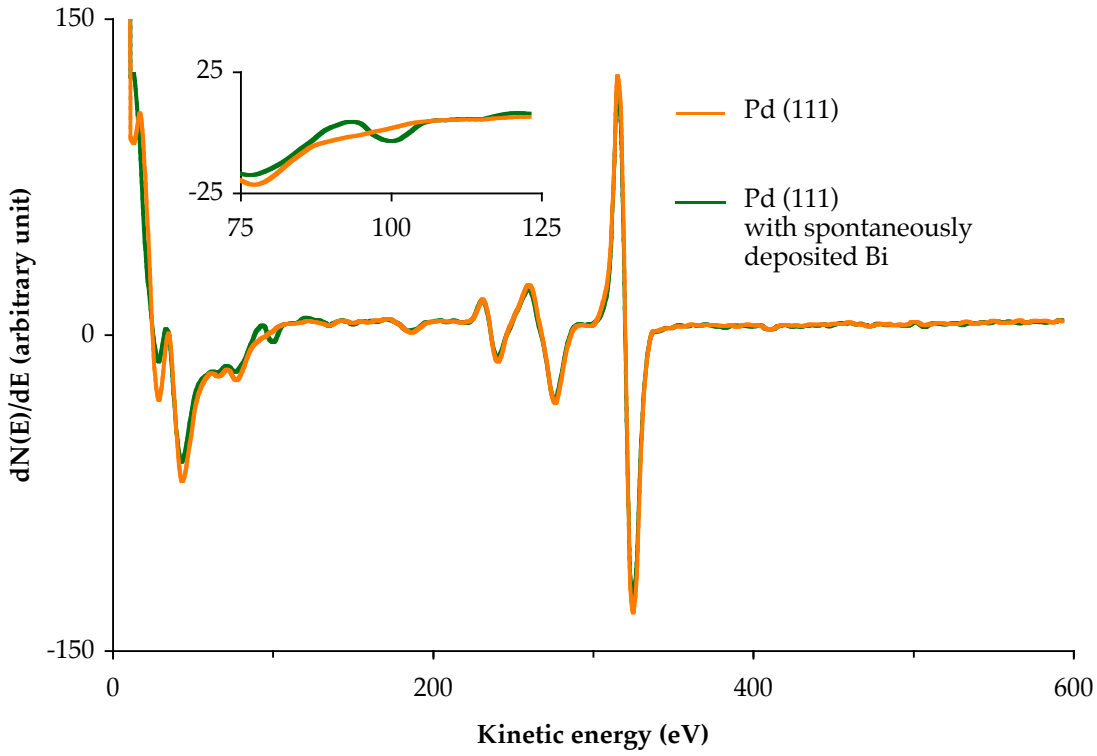

Figure 52. Auger electron spectrum of Pd(111) surface modified by spontaneously electrodeposited Bi. Incident beam energy = 2 keV; beam current = 1 μA.

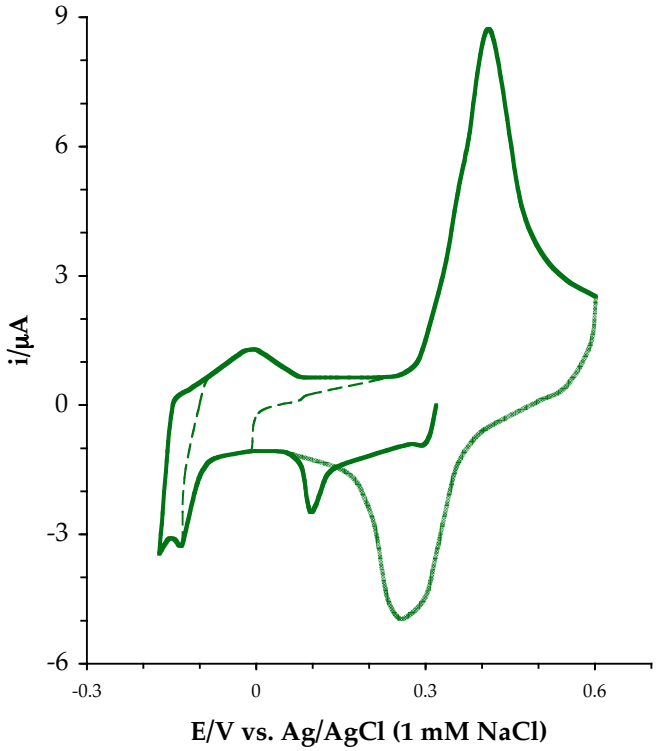

Figure 53. Underpotential deposition peaks of Bi on well-defined Pd(111) observed at a slow scan rate of 0.5 mV/s. Potential scans are carried at various negative switching potentials.

at 0.10 V. For multivalent ions, such as Cu^{2+}, the appearance of multiple UPD peaks is not uncommon [103].

That the first UPD peak was only discernible at a slow scan rate underscored the kinetic barrier for such deposition. Upon reversing the sweep after the completion of the first UPD peak (Figure 53), the anodic counterpart appeared to be a composite part of the huge peak centered at 0.45 V. When the scan was returned to the cathodic direction, the first UPD peak became ill-defined. This behavior is often associated with the fact that UPD is a highly surface-structure-sensitive process that is influenced by potential-induced surface perturbations. The first UPD, therefore, demands a smooth Pd surface; any topographical modification, possibly due to minuscule traces of Bi adatoms left after reducing the oxided Pd surface, precludes the already kinetically hindered UPD of Bi. On the other hand, the second UPD peak at –0.10 V appeared to be more kinetically facile and less structure sensitive, since its emergence was not seriously affected by the second round of potential scan and was observable at moderately slow sweep rates.

Electrodeposition Isotherm of Bi on Pd(111)

A series of potentiostatic deposition at various potentials, ranging from the open-circuit value to a slight Bi-deposition overpotential, was performed. For each selected potential, chronocoulometric measurements were obtained to determine the amount of electrodeposited Bi. Also, post-deposition quantitative analysis of Bi was performed using peak-to-peak measurements of the Auger Bi peak at 101 eV. Each peak-to-peak value of Bi was normalized by dividing it by

the corresponding value of the accompanying Pd MNN transition. It is important to note that, as the electrode is transferred from the electrolyte solution into the UHV chamber, the emersion layer surrounding the electrodeposited Bi adlayer contains a lot of sulfate ions. These remnant ions, however, can be removed by multiple rinsing with water, as can be gleaned from the Auger electron spectrum displayed in Figure 54.

Figure 55 shows the constructed electrodeposition isotherm for Bi. A well-defined Pd(111) electrode was immersed for two minutes in 1 mM Bi^{3+}/0.1 M H_2SO_4 at the following potentials: 0.0 V, –0.05 V, –0.10 V, –0.15 V, –0.20 V, and –0.30 V. The y-axis on the left represents Bi coverage, Θ_{Bi}, calculated from chronocoulometric analyses. In this case, Θ_{Bi} is the ratio of the surface packing density of Bi to that of the Pd substrate. It is, however, important to note that based on geometric considerations of the Bi metallic radius (1.85 Å), a full Bi monolayer is completed at $\Theta_{Bi} = 0.56$ [101].

The y-axis on the left represents the normalized peak-to-peak Bi Auger signals. While the nominal scale for both y-axes is different, the close morphological correspondence of the two isotherms points to the fact that one technique complements the other.

From the LEED pattern (Figure 56 a-f) that accompanies each deposition experiment, the following trends can be inferred:

(*i*) Submonolayer coverages of Bi ($\Theta_{Bi} \leq 0.2$) do not form long-range well-

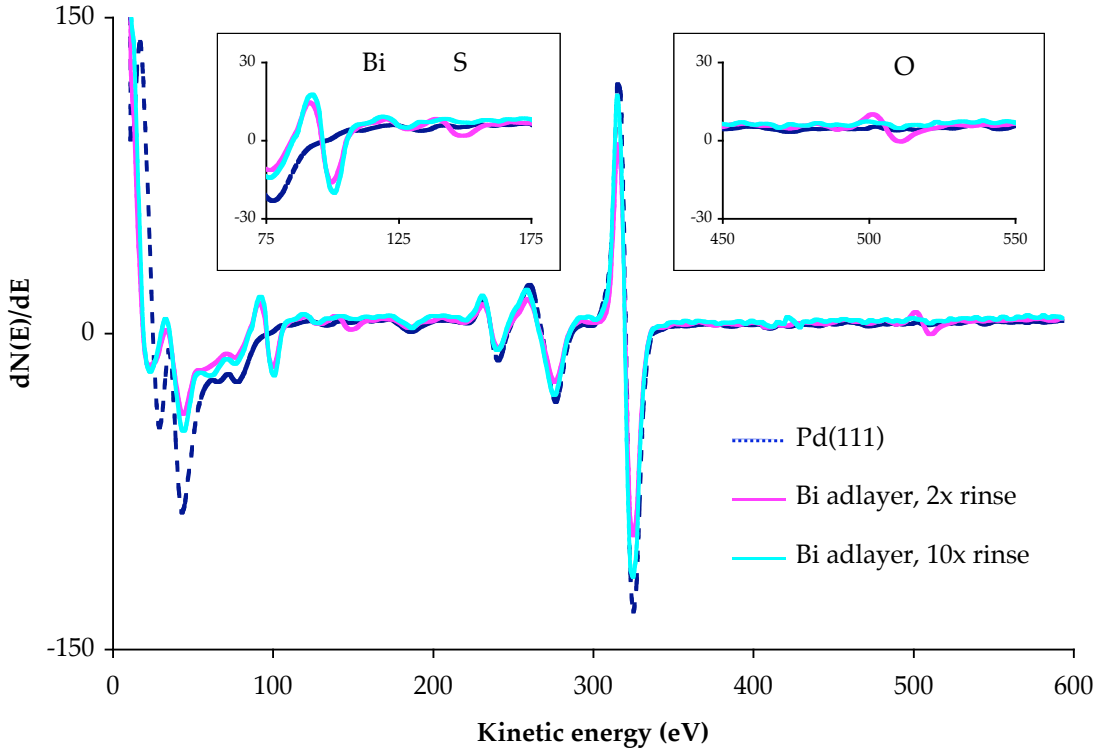

Figure 54. Effect of multiple water rinses on the surface composition of electrodeposited ultrathin Bi film as determined by AES. Incident beam energy = 2 keV; beam current = 1 μA.

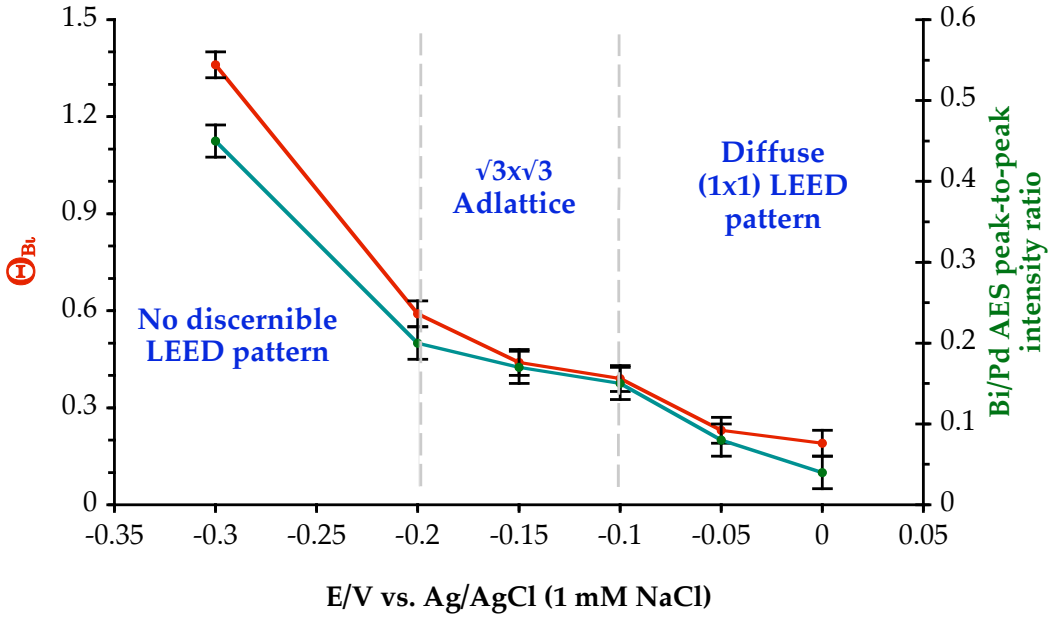

Figure 55. Electrodeposition isotherm of Bi on Pd(111) based on chronocoulometry (left axis) and Auger peak-to-peak analysis (right axis).

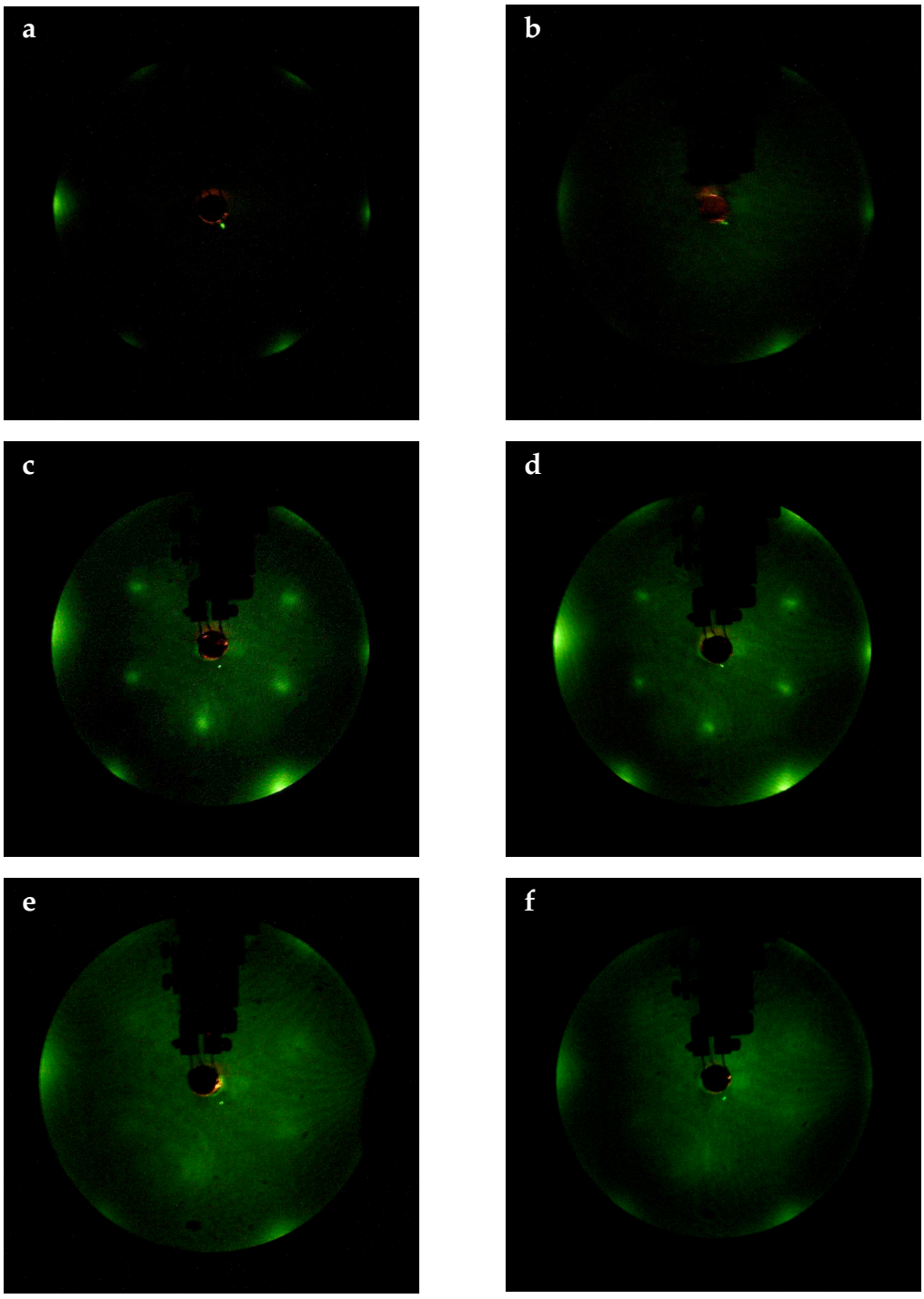

Figure 56. LEED patterns of (a) clean, well-ordered Pd(111); and ultrathin Bi films electrodeposited at (b) 0.00 V, (c) –0.10 V, (d) –0.15 V, (e) –0.20 V, and (f) –0.30 V. Beam energy = 42 eV; beam current = 2 μA. Corresponding Bi coverages are given in Figure 55.

ordered adlattices as indicated by the diffuse (1 x 1) hexagonal LEED pattern; this result is in contrast to the acquisition of *p*(2x2) LEED pattern from vapor deposited Bi films on Pt(111) at 110 K at $\Theta_{Bi} = 0.25$ [101].

(*ii*) The persistence of the (√3 x √3) adlattice geometry beyond $\Theta_{Bi} = 0.33$, terminating at $\Theta_{Bi} = 0.59$, implies that the electrodeposited Bi adlayer is compressible; i.e. additional Bi adatoms can be accommodated by the surface with minimal adlattice distortion that is undetectable the LEED system employed in the study.

(*iii*) Beyond the surface saturation coverage of $\Theta_{Bi} = 0.56$, a highly disordered surface is indicated, most probably due to island formation and growth. It can be deduced that the growth of Bi on Pd(111) follows the Stranski-Krastanov mode.

Electrochemical Behavior of Ultrathin Bi Films on Pd(111)

The interfacial electrochemistry of the prepared metal adlayer often varies significantly when exposed to an electrolytic solution that does not contain the corresponding metal ion. This behavioral change is predicted by the Nernst equation, which stipulates the logarithmic influence of solution ion concentration on the effective reduction/oxidation potential, E, of the metal film.

$$M^{n+}_{(aq)} + n\,e^- \rightleftharpoons M^0_{(s)}$$

$$E = E^o - \frac{0.0591}{n} \log \frac{1}{[M^{n+}]}$$

To establish that the redox peaks observed in Figure 53 were ascribable to surface-confined, not bulk solution, reactions, ultrathin Bi films of various coverages were subjected to a series of voltammetric experiments in blank electrolyte solution.

Emersion and Electrochemical Stability

Ultrathin Bi films, with coverages ranging from Θ_{Bi} = 0.2 to 1.4, were potentiostatically prepared at deposition potentials (E_{dep}) indicated by the constructed isotherm. The films were rinsed thrice with 0.1 M H_2SO_4 under potential control (specifically at E_{dep}) before they were exposed to a fresh batch of blank electrolyte solution without any applied potential. After 10 minutes, the open-circuit potential for all three Bi adlayers converged at *ca*. 0.20 V. Subsequent cyclic voltammetry, initiated in the anodic direction, gave rise to identical current-potential profile for the three adlayers as shown in Figure 57. The emergence of the anodic peak at 0.45 V suggested that submonolayer coverages of Bi remained on the Pd surface after the soaking experiment.

To preserve the integrity of the electrodeposited Bi adlayer, emersion techniques were employed after each electrodeposition; i.e. the electrode was removed from the deposition bath under potential control that corresponded to the deposition potential; subsequent rinses were also performed under the same potential control regimes. Figure 58 displays the voltammograms of the ultrathin Bi films emersed from various potentials. The similarity of the voltammetric features in Figure 58 with those obtained in the presence of bulk

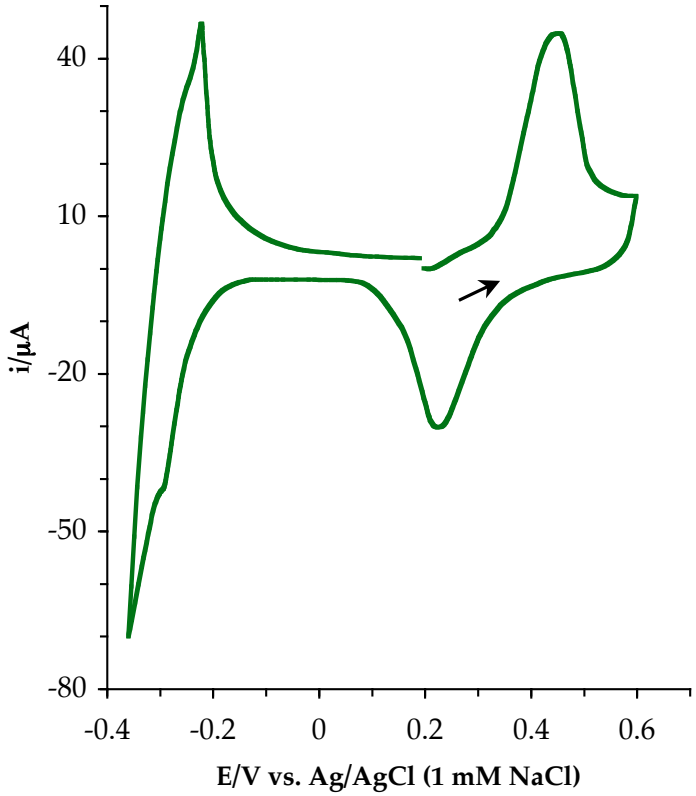

Figure 57. Cyclic voltammogram of ultrathin Bi films (Θ_{Bi} = 0.2 to 1.4) in 0.1 M H_2SO_4 obtained after immersing the film *without* potential control in 0.1 M H_2SO_4. Scan rate = 5 mv/s.

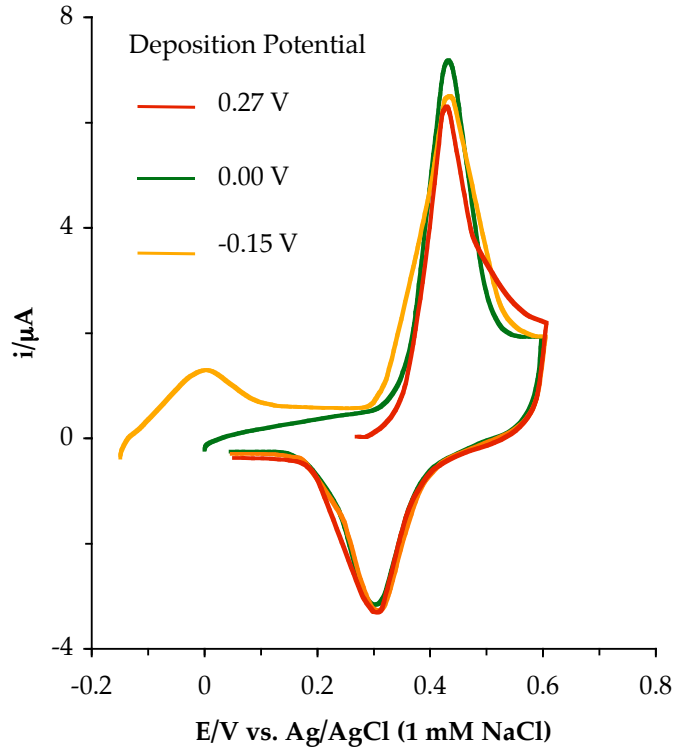

Figure 58. Ultrathin Bi films, emersed at their corresponding deposition potentials, and subjected to cyclic voltammetry in Bi-free 0.1 M H_2SO_4. Scan rate = 0.5 mV/s.

Bi^{3+} ions (Figure 49) supported the claim that the redox signals emanated from surface reactions.

A charge-balance analysis for the anodic oxidation for 0.39 and 1.4 ML Bi was performed. A potential-step experiment was conducted from the deposition potential, E_{dep}, to 0.65 V. The accumulated charge was measured after 2 minutes. All charge measurements were corrected using the background charge for a pristine Pd(111) immersed in 0.1 M H_2SO_4. At first glance, the total oxidation charge appeared smaller than the deposition charge as can be gleaned from the $Q_{oxidation}/ Q_{deposition}$ ratio, which is less than 1.0 (Table 4).

This apparent discrepancy was further scrutinized by performing a two-step sequential anodic oxidation at the following potential ranges: E_{dep} to 0.0 V; 0.0 V to 0.65 V. The choice for these potential regimes was dictated by the fact that 0.0 V marked the anodic oxidation of bulk Bi electrodeposited at the Nernstian potential, $E_{Bi^{3+}/Bi}$. Results are shown in Table 5.

Table 4. Deposition and anodic oxidation charge-analysis for a potential-step experiment from the deposition potential to 0.65 V.

Θ_{Bi}	$Q_{deposition}$ (mC)	$Q_{oxidation}$ (mC)	$\frac{Q_{oxidation}}{Q_{deposition}}$
0.39	0.49 ± 0.06	0.33 ± 0.08	0.67 ± 0.18
1.4	1.2 ± 0.01	0.89 ± 0.06	0.74 ± 0.05

Table 5. Deposition and anodic oxidation charge-analysis for a potential-step experiment carried out in two sequential stages: from the deposition potential to 0.0 V, followed by a potential switch from 0.0 V to 0.65 V.

Θ_{Bi}	$Q_{deposition}$ (mC)	$Q^{a}_{oxidation}$ (mC)	$Q^{b}_{oxidation}$ (mC)	$\frac{Q^{b}_{oxidation}}{Q_{deposition} - Q^{a}_{oxidation}}$
0.39	0.49 ± 0.06	0.00 ± 0.01	0.33 ± 0.06	0.67
1.4	1.2 ± 0.01	0.29 ± 0.01	0.61 ± 0.01	0.67

[a] *Potential was switched from E_1 = -0.10 V to E_2 = 0.0 V*
[b] *Potential was switched from E_1 = 0.0 V to E_2 = 0.65 V*

Conservation of deposition-oxidation charges was attained by proposing the following sequence of redox processes. Between –0.15 V and 0.0 V, Bi_{UPD} was anodically stripped off, releasing Bi^{3+} ions to the bulk solution. The stripping process was, however, not exhaustive. Remnant Bi_{UPD} was completely peeled off from the Pd(111) surface, as the potential was switched from 0.0 V to 0.65 V. Such anodic dissolution involved the conversion of Bi_{UPD} into Bi^{2+}, an electrogenerated metastable adspecies that has been previously reported on Pt(111) surfaces [58-59, 61]. The formation of Bi^{2+} was inferred from the observation that only 2/3 of the deposition charge remaining after the potential-step experiment terminated at 0.0 V was used up at 0.65 V. Cyclic voltammetry, after this 2-minute polarization at 0.65 V, yielded a current-potential profile of a Bi-free Pd(111) electrode, suggesting complete anodic dissolution of Bi adatoms.

From the above results, it can be deduced that for multilayer Bi-on-Bi surface ensembles (typified by $\Theta_{Bi} = 1.4$), anodic dissolution proceeds at potentials between –0.15 V and 0.0 V, until only a full monolayer of Bi remains on the Pd(111) surface. To strip off Bi adatoms that are directly in contact with the Pd surface requires the application of more positive potential ($E \geq 0.65$ V).

The following equations summarize the coverage-dependent anodic processes of ultrathin Bi films:

(*i*) $\quad Pd(111)–Bi–Bi \rightleftharpoons Bi^{3+}_{(aq)} + 3e^- \quad E = 0.0$ V

(*ii*) $\quad Pd(111)–Bi \rightleftharpoons Bi^{2+}_{(aq)} + 2e^- \quad E \geq 0.65$ V

The accompanying reduction reaction is surmised to be the conversion of aqueous H^+ to hydrogen gas:

(*iii*) $2\,H^+_{(aq)} + 2e^- \rightleftharpoons H_{2\,(g)}$

Influence of Halides on the Electrochemical Behavior of Ultrathin Bi Films

Interest on examining the effects of iodide and bromide ions on the interfacial electrochemistry of ultrathin Bi films on Pd(111) emanates from the fact that: (*i*) Iodide ions are oxidatively chemisorbed onto Pd surfaces to form a well-characterized zerovalent iodine adlayer that retains the metallic nature of the substrate [5, 104]. (*ii*) While I_{ads} is strongly bound to Pd, the Br_{ads}-on-Pd system represents a prototypical case of intermediate surface-ligand-to-metal-substrate interactions among members of the halogen family. (*iii*) Bismuth ions form insoluble precipitates with iodide and bromide ions; in the presence of excess halide, the precipitate dissolves to form the halo complex, BiX^{2-} [105].

A well-defined Pd(111) electrode was immersed for 2 minutes in a solution of 0.1 mM NaI/0.1 M H_2SO_4 at a potential slightly more positive than the open-circuit value (*ca*. 0.28 V). The resulting adlayer had a (√3 x√3) geometry (Figure 59) as previously reported [35].

The current-potential profile of the iodine-modified Pd electrode immersed in 1 mM Bi^{3+}/0.1 M H_2SO_4 (Figure 60) shared similar features with a pristine Pd(111) electrode exposed to the same deposition bath (inner trace of Figure 48). Background-corrected anodic and cathodic currents were, however, almost twice as large as those obtained from unmodified Pd electrodes. Such

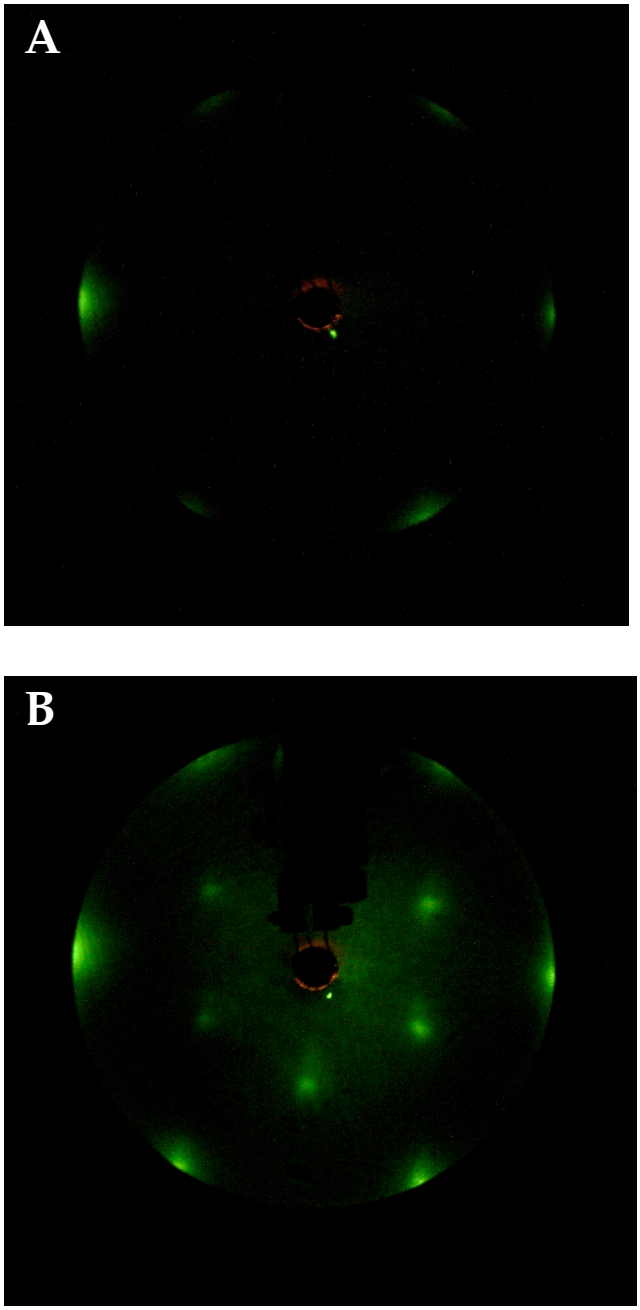

Figure 59. LEED pattern obtained (a) before and (b) after immersing Pd(111) into a solution of 0.1 mM NaI/0.1 M H_2SO_4 at 0.28 V. Beam energy = 42 eV; beam current = 2 μA.

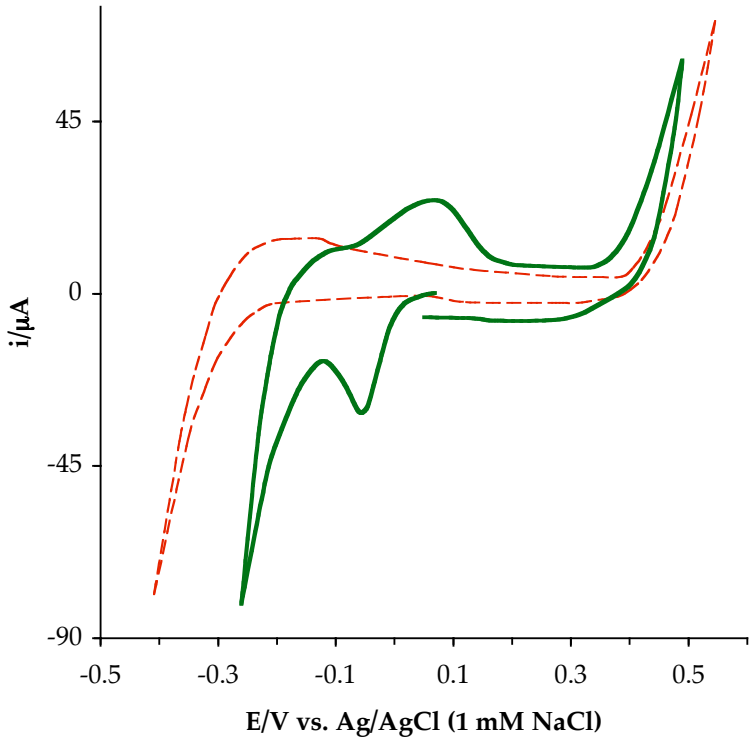

Figure 60. Cyclic voltammogram of Pd(111)(√3x√3)R30°-I in 0.1 mM Bi^{3+}/0.1 M H_2SO_4 at a scan rate of 5 mV/s. Broken-line trace is the voltammetric profile of Pd(111)(√3x√3)R30°-I in 0.1 M H_2SO_4.

current-signal enhancement suggested that the electrodeposition-desorption of Bi_{UPD} was more kinetically facile on the Pd(111)(√3x√3)R30°-I electrode. Furthermore, the presence of I_{ads} altered the energetics of Bi_{UPD} electrodeposition: A full Bi coverage was achieved at a potential (–0.06 V) more positive than that on an unmodified Pd(111) surface (–0.15 V). The origin of this deposition-potential shift is not yet fully understood although it is reasonable to ascribe this shift to I_{ads}-induced changes in the electronic properties of Pd.

The effect of aqueous iodide on the electrodeposited Bi adlayers was investigated by emersing ultrathin Bi films of various coverages in 0.1 mM NaI/0.1 M H_2SO_4 at potentials corresponding to the those needed to deposit Bi potentiostatically. The resulting surface structure and composition were monitored by LEED and AES, respectively.

Post-iodine-emersion Auger electron spectra were monitored for Bi adlayers with different surface coverages. On a Pd(111) surface modified by spontaneously electrodeposited Bi adatoms, iodine was chemisorbed along with Bi at coverages of $\Theta_{Bi} = 0.07$ and $\Theta_I = 0.29$, as can be gleaned from the peak-to-peak analysis of the Auger Bi (Figure 61a) and I (Figure 62a) transitions. Such mixed Bi-I adlayer gave rise to a √3x√3 LEED pattern as shown in Figure 63. These results suggested that the presence of trace amounts of Bi on the Pd(111)-(√3x√3)-I adlattice did not drastically perturb the long-range order of the Pd-I interface; i.e. it can be argued that Bi (metallic radius, 1.85 Å) behaved like a substitutional impurity for I (van der Waal's radius, 1.96 Å) on the

Pd(111)(√3x√3)R30°-I adlattice. A proposed real-space model of this mixed adlayer is given in Figure 63c.

From the electrodeposition isotherm and its accompanying LEED pattern analysis (Figures 55 and 56), it had established that, within a potential window of –0.10 V to –0.20 V, Bi adatoms assumed a (√3x√3) geometry on the Pd(111) surface. When ultrathin Bi films with coverages of Θ_{Bi} = 0.33 and 0.59 were emersed from 0.1 mM NaI/0.1 M H_2SO_4, both adlayers yielded (√3 x √7) LEED patterns (Figure 64). Considering that at Θ_{Bi} = 0.56 the Pd(111) surface is already saturated by a full monolayer of Bi, it can be deduced that the iodine adatoms detected by AES (Figure 62) rest on the Bi adlayer. The slight decline in the Bi peak intensity after the iodine emersion process supports the notion that iodine forms a superlattice on top of Bi, thereby attenuating the Bi AES signal.

The (√3 x √7) Bi-I superlattice observed on both emersed ultrathin Bi films (Θ_{Bi} = 0.33 and 0.59) is most probably a composite of a (√3x√3)-Bi adlayer decorated with a fixed coverage of iodine as evidenced by the similarity of the AES I peak-to-peak heights for both systems (Figures 62 a and b). When an I-coated Pd(111) electrode was submerged to a Bi^{3+}-deposition bath at –0.10 V and –0.20 V (respectively corresponding to Θ_{Bi} = 0.33 and 0.59), the same (√3 x √7) Bi-I superlattice (Figure 64 c and d) was obtained. Hence, regardless of the order of deposition, iodine would always like to stay on surface of the superlattice in a manner reminiscent to what was observed between Ag and I on Pt(111) [106].

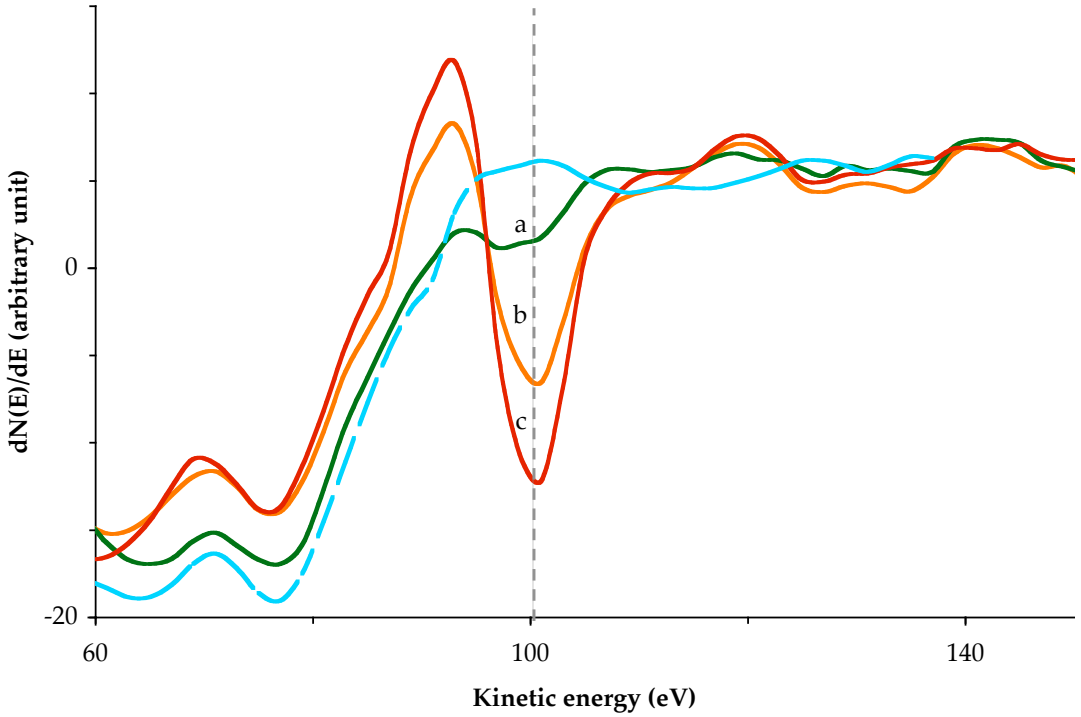

Figure 61. Effect of $NaI_{(aq)}$-emersion on the Auger Bi transition peak intensity for ultrathin films potentiodynamically prepared by scanning the potential from ocp to various final potentials : (a) ocp, 0.27 V (b) –0.10 V, and (c) –0.20 V. The broken-line trace is the spectrum for (*Bi-free surface*) Pd(111)(√3x√3)R30°-I adlayer.

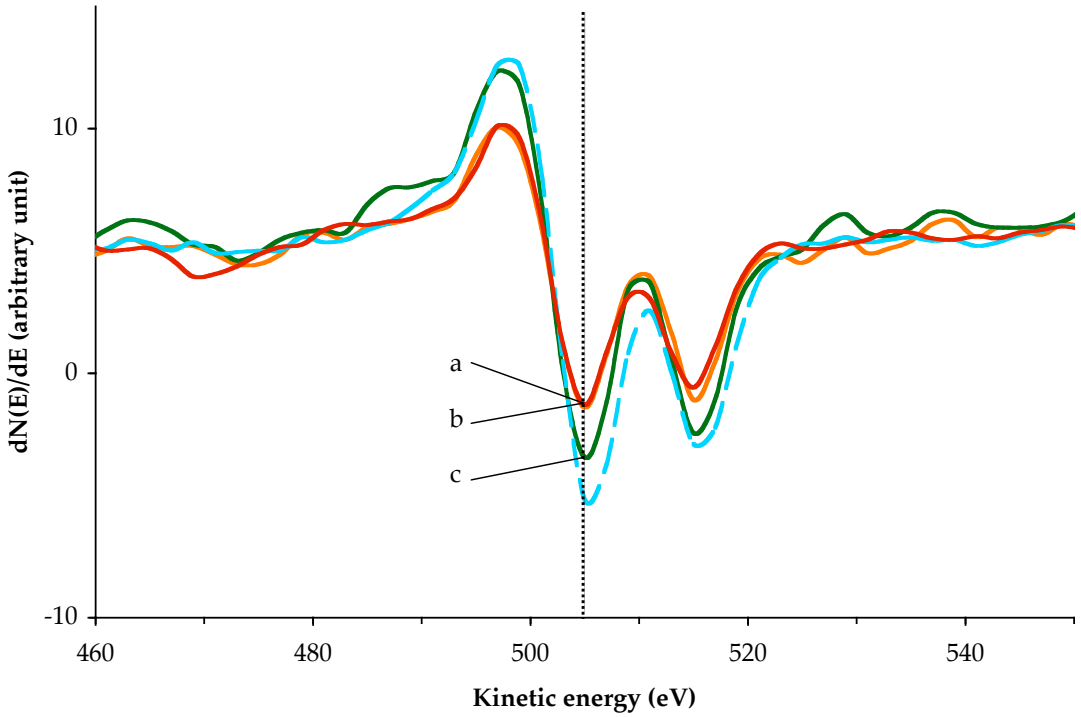

Figure 62. Effect of $NaI_{(aq)}$-emersion on the Auger I transition peak intensity for ultrathin films potentiodynamically prepared by scanning the potential from ocp to various final potentials : (a) ocp, 0.27 V, (b) –0.10 V, and (c) –0.20 V. The broken-line trace is the spectrum for (*Bi-free surface*) Pd(111)(√3x√3)R30°-I adlayer.

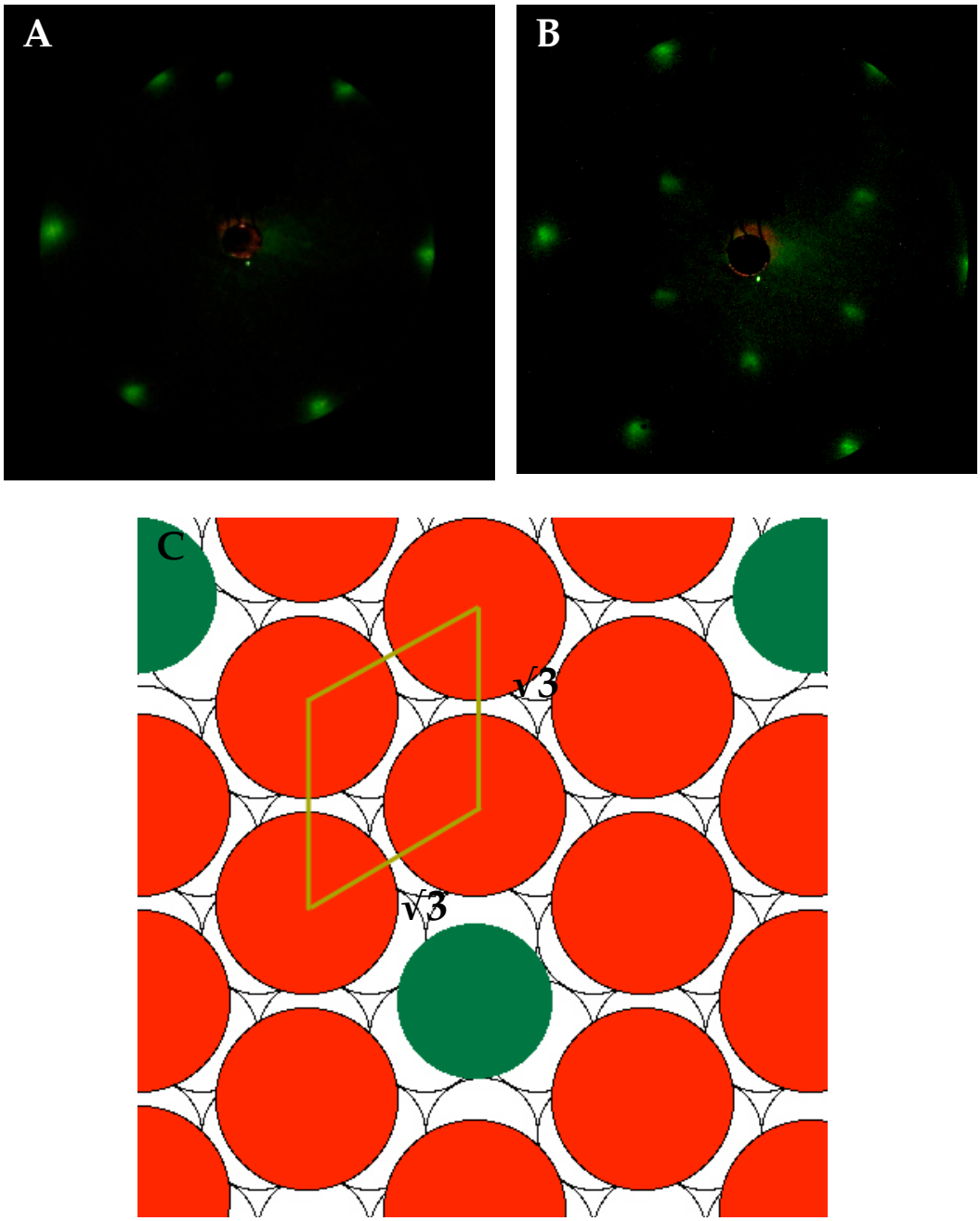

Figure 63. LEED pattern of Bi adlattice on Pd(111) deposited at open-circuit potential, 0.27V (a) before and (b) after emersion from 0.1 mM NaI in 0.1 M H_2SO_4 at 0.27 V; deposition time is 5 minutes; beam energy = 52 eV; beam current = 2.5 μA; (c) proposed real-space model for the observed LEED pattern: Red spheres = iodine; green spheres = bismuth; white spheres = palladium.

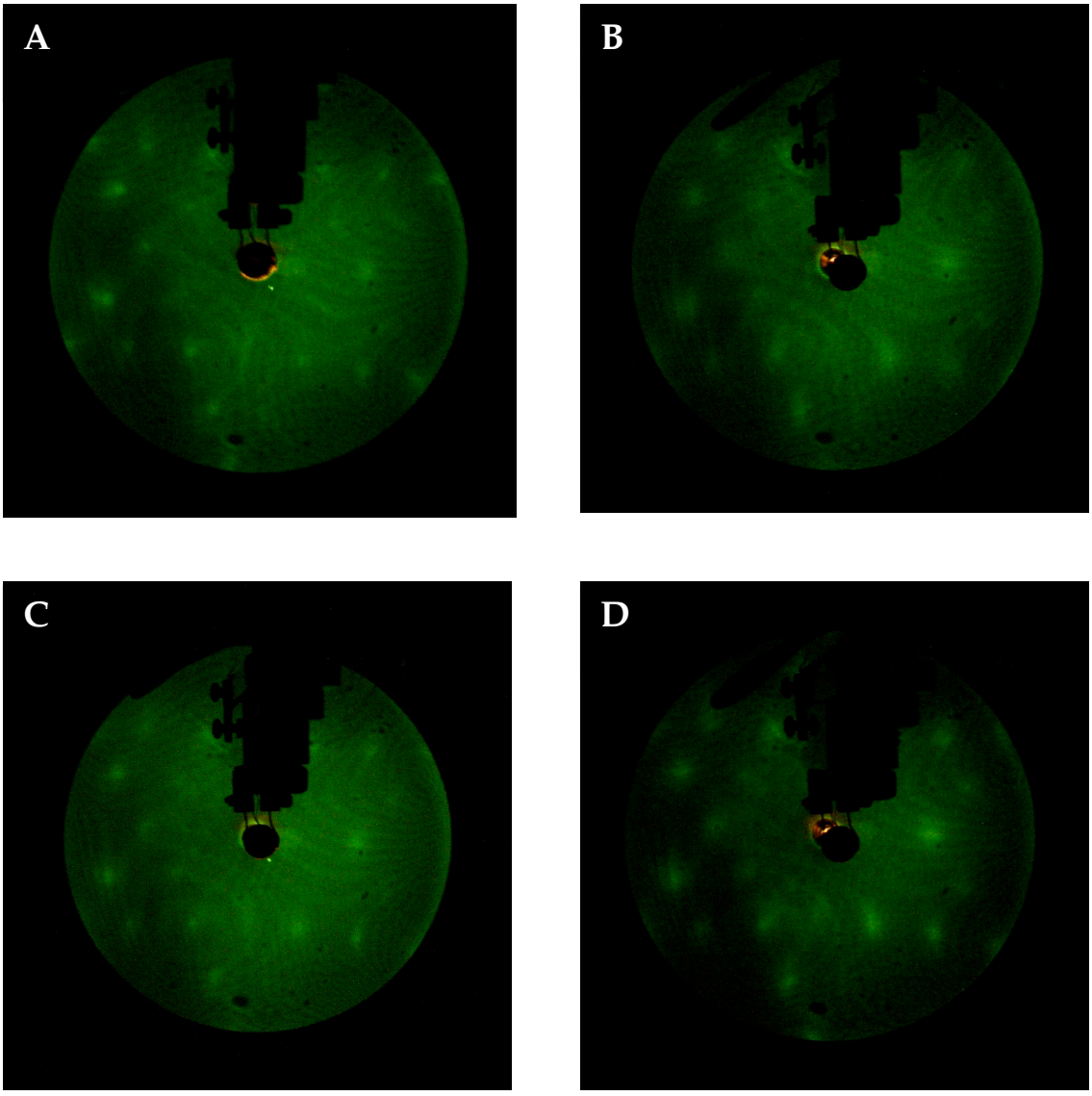

Figure 64. A (√3 x √7) LEED pattern obtained from (a) Bi adlayer electrodeposited at –0.10 V and then emersed from $NaI_{(aq)}$; (b) Bi adlayer electrodeposited at –0.20 V and then emersed from $NaI_{(a}$); (c) Bi adlayer electrodeposited at –0.10 V onto Pd(111)(√3x√3)R30°-I; (d) Bi adlayer electrodeposited at –0.20 V onto Pd(111)(√3x√3)R30°-I. Beam energey = 34 eV; beam current = 2 μA.

A proposed real-space model for the (√3 x √7) Bi-I superlattice is displayed in Figure 65. The (√3 x √7) notation pertains to the dimensions of unit mesh of the I adlayer on Bi. The proposed model posits the I atoms on the 3-fold site of the (√3 x √3) Bi adlattice; this site is also coincident with an exposed 3-fold hollow site of the underlying Pd substrate.

Electrooxidation of D-glucose on Bi/Pd(111) in Alkaline Media

Bismuth-modified Pd electrodes have been reported to exhibit enhanced electrocatalytic performance in the electrooxidation of HCOOH [62] and in the electrosynthesis of fine chemicals [68]. In this investigation, D-glucose was chosen as a surface probe to interrogate the aptitude of the prepared ultrathin Bi films towards electrooxidation. Current interest on the Bi-Pd system also lies on its potential as biocompatible fuel cell electrodes using glucose-based feedstock. The chosen experimental conditions were suited to match those that produce δ-gluconolactone, an industrially important ligand in the food and cosmetics industry.

Shown in Figure 66 is the base cyclic voltammetry of a clean, well-ordered Pd(111) electrode in 0.1 M Na_2SO_4 solution adjusted to pH 10 with drops of 1 M $NaOH_{(aq)}$. Anodic surface oxidation commenced quite early at 0.10 V, a phenomenon that was quite typical in basic media where the electrochemistry of Pd(111) was dominated by the formation of hydroxo surface complexes [5]. Unlike the case of 0.1 M H_2SO_4, no sharp signature peak corresponding to the anodic oxidation of the (111) facet was discernible.

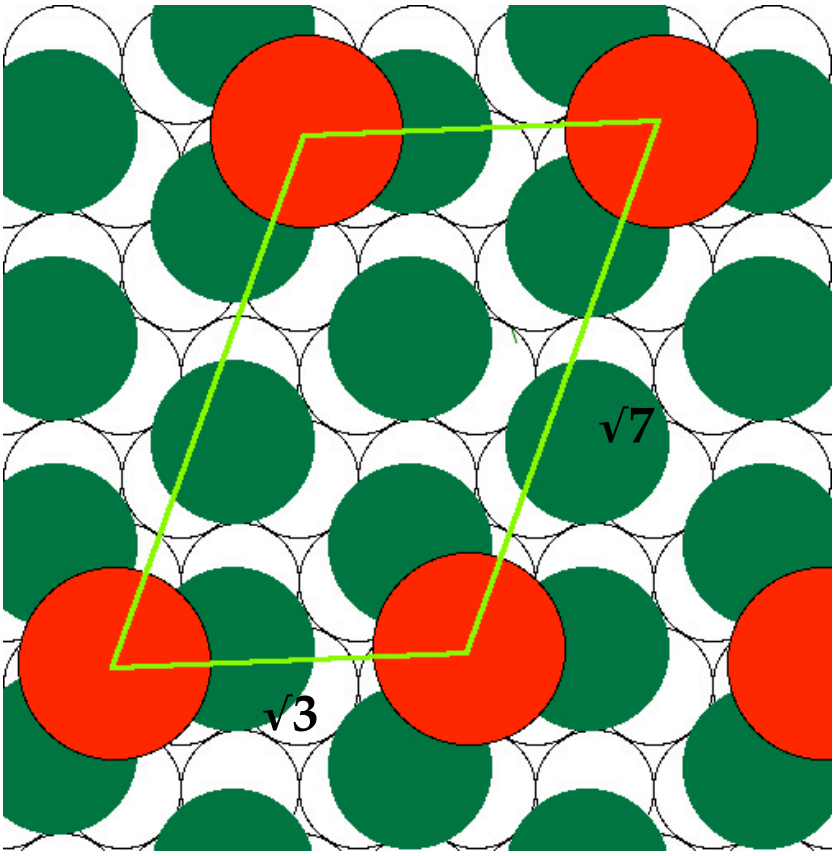

Figure 65. Proposed real-space model of (√3 x √7) LEED pattern. Red spheres = iodine; green spheres = bismuth; white spheres = palladium.

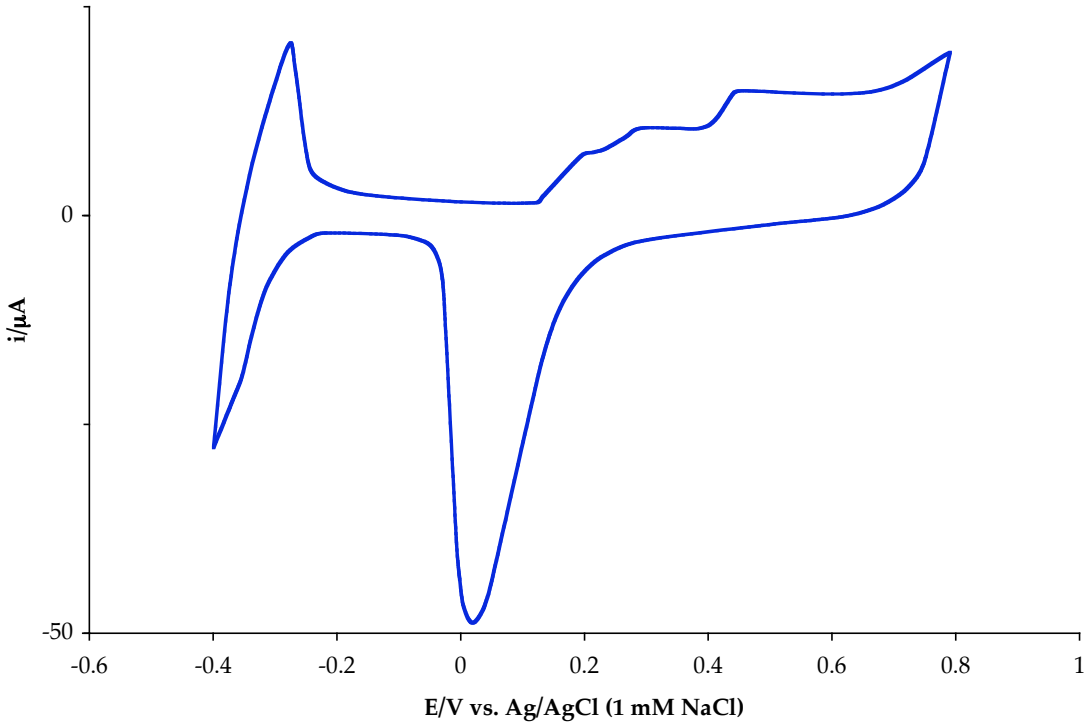

Figure 66. Cyclic voltammogram of clean and well-ordered Pd(111) in 0.1 M Na_2SO_4 (pH 10). Scan rate = 5 mV/s.

The electrochemical reactivity of bare Pd(111) surface towards the electrooxidation of D-glucose was surveyed in Figure 67. A potential scan initiated in the cathodic direction yielded a sharp anodic peak at –0.28 V, which marked the formation of δ-gluconolactone. As the scan was reversed at –0.70 V, a broad anodic envelope developed, with its center close to 0.0 V. This huge peak was attributed to the further oxidation of δ-gluconolactone. While the present experiment did not aim to identify these oxidation products, it was evident from the reverse scan at 0.35 V that the absence of any anodic peak between 0.0 V and –0.80 V (broken-trace in Figure 67) indicated the suppression of D-glucose electrooxidation by remnant oxidation products that blocked the Pd(111) surface from further reaction.

If the positive switching potential was poised at 0.80 V, where Pd-surface oxidation transpired, the anodic peak for the electrooxidation of D-glucose re-emerged. The onset of such process took place at a potential (–0.40 V) *more negative* than the initial scan, indicating a more energetically favored electrooxidation but the kinetics became sluggish as evidenced by the smaller anodic peak intensity.

The influence of ultrathin Bi films on the electrocatalytic effects of Pd was investigated by cycling a Bi adlayer ($\Theta_{Bi} = 1.4$) in 5 mM D-glucose/0.1 M Na_2SO_4 (pH 10). A quick comparison between Figures 67 and 68 suggested no dramatic kinetic enhancement brought about by the presence of ultrathin Bi films. However, no excursion to very positive potentials are necessary to remove the

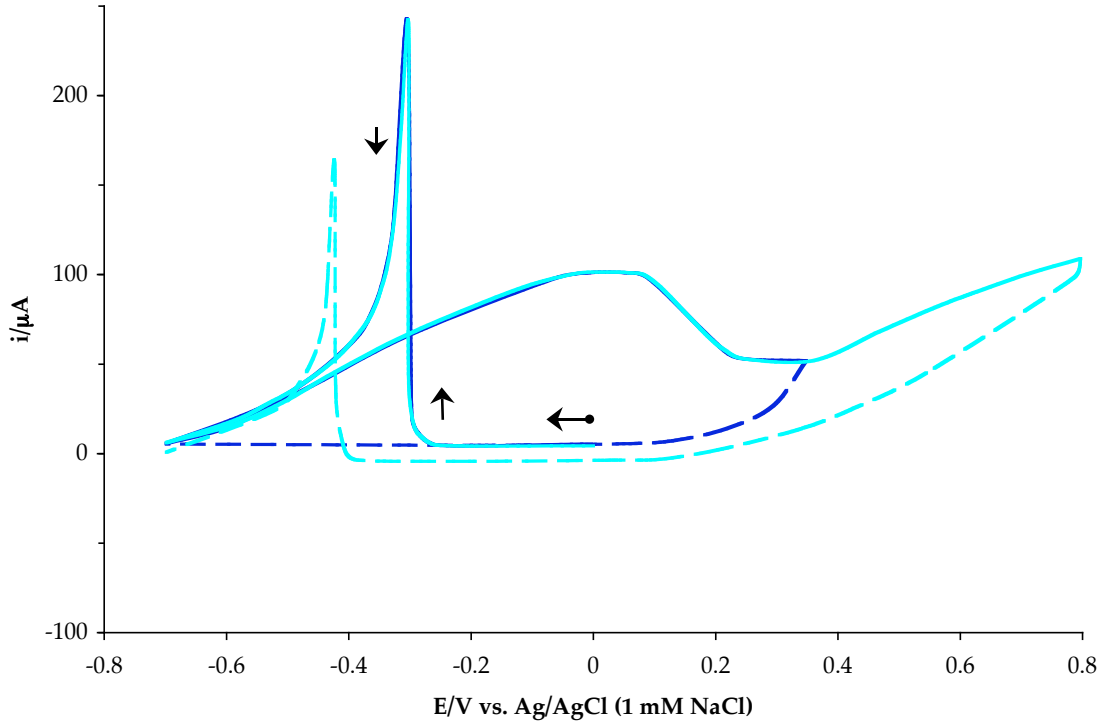

Figure 67. Cyclic voltammogram of Pd(111) in 5 mM D-glucose/0.1 M Na_2SO_4 (pH 10). Scan rate = 5 mV/s.

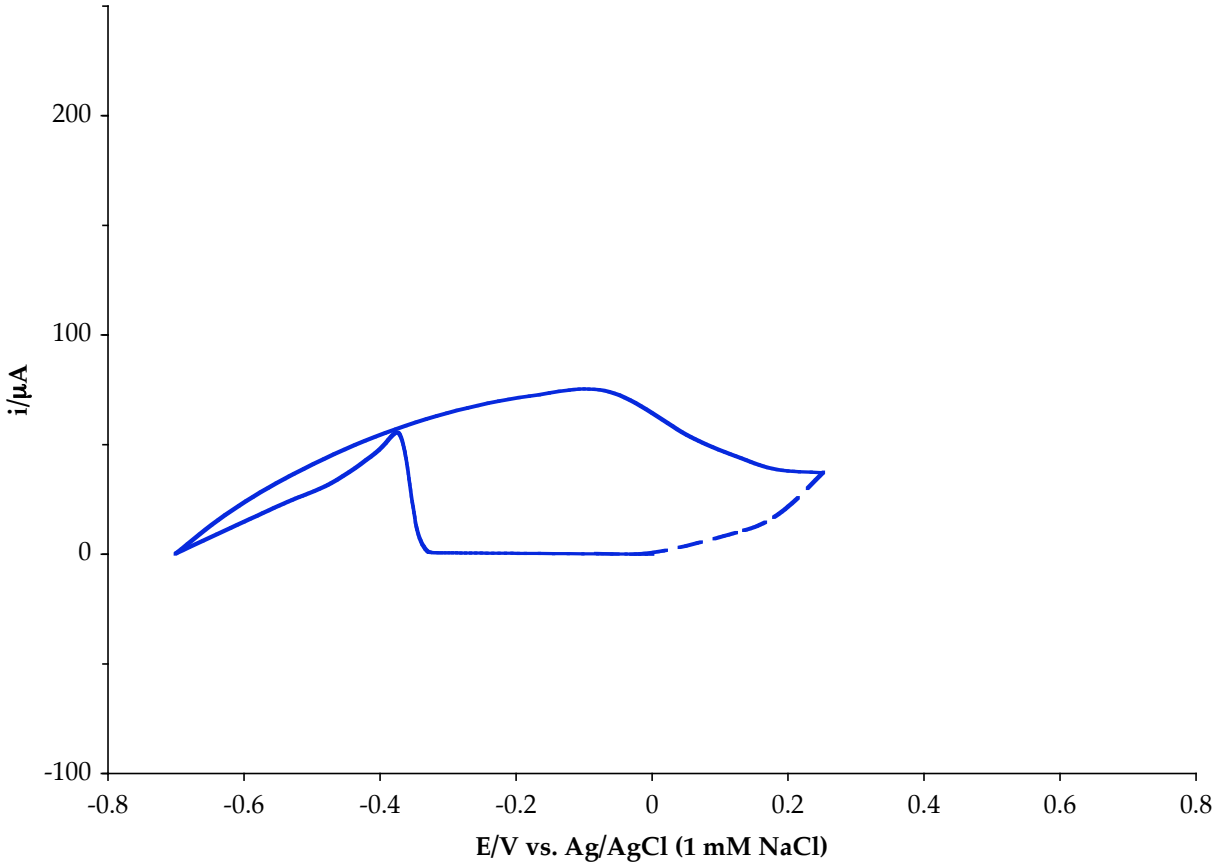

Figure 68. Steady-state cyclic voltammogram of ultrathin Bi film (Θ_{Bi} = 1.4) in 5 mM D-glucose/0.1 M Na_2SO_4 (pH 10). Scan rate = 5 mV/s.

oxidation products of δ-gluconolactone; i.e. the Bi-modified Pd(111) surface was not deactivated towards further electrooxidation of D-glucose. Under the same potential window, a bare Pd(111) electrode would have been poisoned by any remnant surface species. It is possible that these surface poisons are not strongly attracted to the ultrathin Bi film, and are therefore readily desorbed anodically at *ca*. 0.20 V.

The same electrooxidation experiment was repeated using an ultrathin Bi film with θ_{Bi} = 0.19. The absence of the signature anodic peak for D-glucose oxidation (Figure 69) implies that, at very low coverages, randomly dispersed Bi adatoms act as surface blocks for the electrosorption and subsequent electrooxidation of D-glucose. The same site-blocking effect was observed when a Pd(111)-(√3x√3)-Bi adlayer (θ_{Bi} = 0.33) was subjected to a voltammetric scan initially headed to the anodic direction. As previously demonstrated, excursions to potentials greater than 0.70 V led to the anodic dissolution of the electrodeposited Bi. The present results, however, showed that after the potential scan small traces of Bi remained on the surface, consequently preventing the electrooxidation of D-glucose (Figure 70).

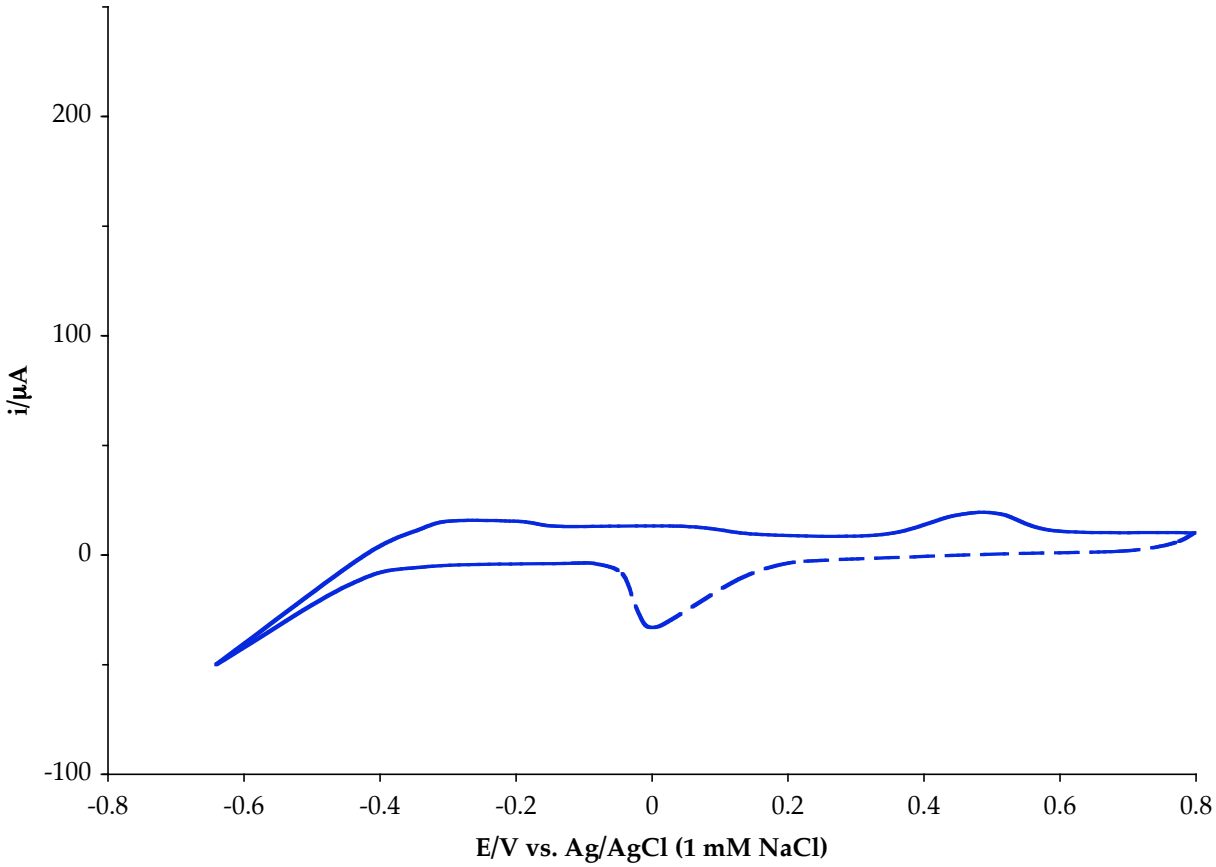

Figure 69. Cyclic voltammogram of ultrathin Bi film (Θ_{Bi} = 0.19) in 5 mM D-glucose/0.1 M Na_2SO_4 (pH 10). Scan rate = 5 mV/s.

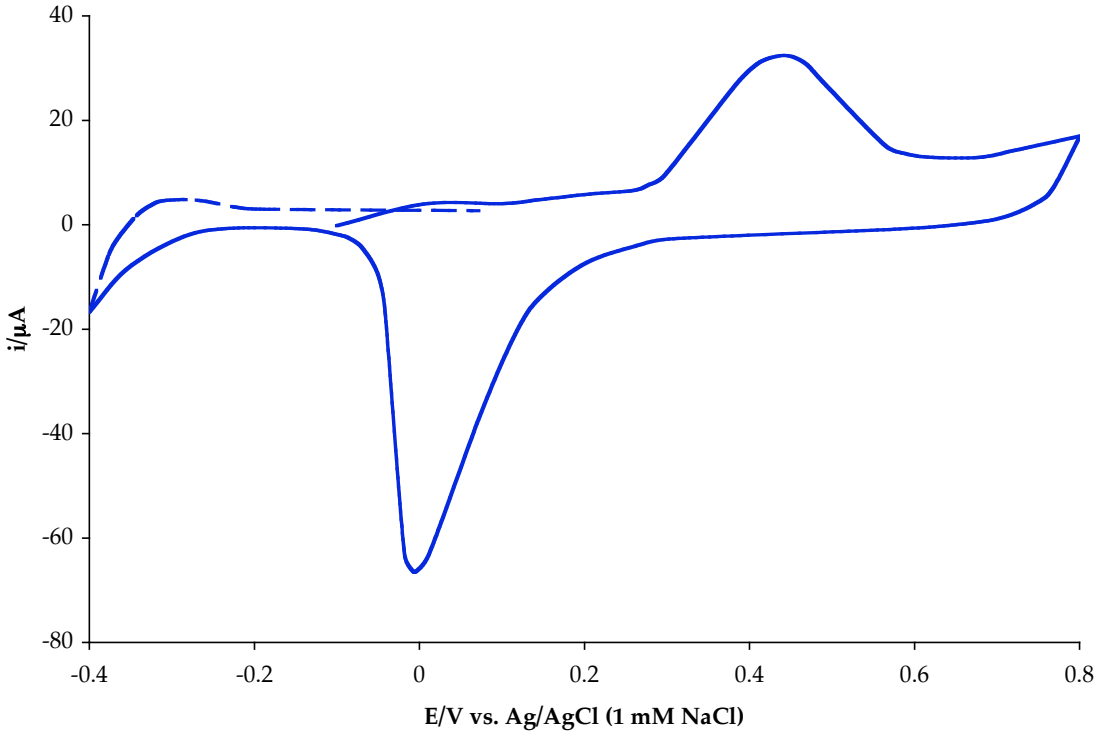

Figure 70. Cyclic voltammogram of ultrathin Bi film ($\Theta_{Bi} = 0.33$) on Pd(111) in 5 mM D-glucose/0.1 M Na_2SO_4 with a scan initiated in the anodic direction. Scan rate = 5 mV/s.

CONCLUSIONS

Electrochemical protocols were established for the potentiostatic deposition of ultrathin films of (*i*) Pd on Pt(111); (*ii*) Co on polycrystalline Pd and Pd(111); and (*iii*) Bi on Pd(111). The investigation consolidated the capabilities of conventional electrochemistry (voltammetry and coulometry) and ultrahigh vacuum electron spectroscopies (Auger electron spectroscopy, AES; low energy electron diffraction, LEED; X-ray photoelectron spectroscopy, XPS) to characterize the interfacial electrochemistry of the prepared adlayers.

Step-site-selective interaction of aqueous bromide with ultrathin Pd films on Pt(111) allowed the possibility of electrochemical annealing, a nonthermal analogue of inducing long-range surface order. Surface smoothening effects were anchored on the fact that, in the presence of chemisorbed bromine, Pd adatoms occupying defect sites (steps) were preferentially dissolved or rearranged by potential excursions to regions that *bordered* the hydrogen evolution reaction and the anodic surface oxidation of the ultrathin Pd film. Unlike chemisorbed iodine that tenaciously lingered on the Pd surface, the bromine case presented a relatively facile adsorption-desorption process that left behind an ordered, bromine-free and oxide-free Pd surface.

On a clean Pd(111) electrode, Co electrodeposition was virtually nil except when the surface was roughened by oxidation-reduction cycles (ORC); under this condition no Co surface coverages were measured. Electrodeposition was, however, possible on a thermally annealed polycrystalline Pd surface,

which is a composite surface of the (111) and (100) facets. The deposition process was electrochemically irreversible. In the absence of large overpotentials ($E > E^{o}_{Co^{2+}/Co}$), only submonolayer coverages of Co were formed.

Iodine chemisorption at Pd surfaces retarded not only the onset of hydrogen absorption but also the electrodeposition of Co. Exposure of the prepared Co adlayer to aqueous iodide did not alter the anodic behavior of the Co electrodeposit. The current-potential profile of the ultrathin Co films in basic medium was characterized by a complex set of anodic peaks representing the subsequent conversion of Co oxide/hydroxide into higher oxidation states.

Well-defined ultrathin Bi films were electrodeposited at controlled potential onto Pd(111). At submonolayer coverages ($\Theta_{Bi} \leq 0.2$), Bi adatoms did not form long-range well-ordered surface structures. The persistence of the $(\sqrt{3}x\sqrt{3})R30^{o}$ adlattice geometry between $\Theta_{Bi} = 0.33$ and $\Theta_{Bi} = 0.59$ demonstrated the compressibility of the Bi adlayer with minimal adlattice distortion. At higher coverages, the surface became strewn with island formation, indicating a Stranski-Krastanov film-growth mode.

Ultrathin Bi films emersed from aqueous iodide yielded a $(\sqrt{3}x\sqrt{7})$ I-*on*-Bi superlattice. The same superlattice was obtained when the order of deposition was reversed (iodine first, followed by Bi), indicating that iodine stayed on top of the superlattice.

The presence of an ultrathin Bi film on Pd(111) precluded the adsorption of by-products from the electrooxidation of D-glucose in basic medium;

consequently, Bi-modified Pd(111) surfaces need not be subjected to positive potentials ($E \geq 0.80$ V) in order to resume multiple electrooxidation cycles. Unfortunately, no significant enhancement in the electrooxidation current density was observed in the presence of Bi adlayers. The complete suppression of electrooxidation activity at Pd surfaces modified by very low submonolayer coverages ($\Theta_{Bi} \leq 0.19$) underscored the existence of a yet-undetermined threshold Bi- and Pd-domain size necessary for effective and sustained electrooxidation of D-glucose.

REFERENCES

[1] J. Evans, Platinum Metals Rev. 46 (2002) 165.

[2] P. Patnaik, Handbook of Inorganic Chemicals, McGraw-Hill, New York, 2001.

[3] F.A. Lewis, The Palladium Hydrogen System, Academic Press, London, 1967.

[4] P.J. Durrant, B. Durrant, Introduction to Advanced Inorganic Chemistry, John Wiley & Sons, Inc., New York, 1970.

[5] M.P. Soriaga, Y.-G. Kim, J.E. Soto, in: A. Wieckowski (Ed.), Interfacial Electrochemistry, Marcel Dekker, New York, 1999.

[6] E. Rach, J. Heitbaum, Electrochim. Acta 32 (1987) 1173.

[7] R. Winand, Electrochim. Acta 39 (1994) 1091.

[8] P.N. Ross, in: J. Lipkowski, P.N. Ross (Eds.), Electrocatalysis, Wiley-VCH, New York, 1998.

[9] G.A. Somorjai, Introduction to Surface Chemistry and Catalysis, John Wiley & Sons, Inc., New York, 1994.

[10] S. Mahajan, K.S. Sree Harsha, Principles of Growth and Processing of Semiconductors, McGraw-Hill, Boston, 1999.

[11] J.H. Sinfelt, Bimetallic Catalysts: Discoveries, Concepts, and Applications, John Wiley & Sons, New York, 1983.

[12] J. Stickney, in: R. Alkire, D.M. Kolb (Eds.), Advances in Electrochemical Science and Engineering, Vol. 7, John Wiley & Sons Ltd, England, 2002.

[13] M. Paunovic, M. Schlesinger, Fundamentals of Electrochemical Deposition, John Wiley & Sons, Inc., New York, 1998.

[14] M.J. Hampden-Smith, T.T. Kodas, A. Ludviksson, in: L. V. Interrante and M.J. Hampden-Smith (Eds.), Chemistry of Advanced Materials: An Overview, Wiley-VCH, New York, 1998.

[15] E. Leiva, T. Iwasita, E. Herrero, J.M. Feliu, Langmuir 13 (1997) 6287.

[16] B.E. Conway, H. Angerstein-Kozlowska, G. Czartoryska, Zeitschrift für Physikalische Chemie 112 (1978) 195-214.

[17] M.M. Jaksic, J. New Mater. Electrochem. Sys. 3 (2000) 153.

[18] J.M. Jaksic, N.M. Nikola, N.V. Krstajic, M.M. Jaksic, Int. J. Hydrogen Energy 23 (1998) 1121.

[19] D.W. Goodman, E.M. Stuve, ACS Symposium Series, Electrochem. Surf. Sci.: Mol. Phenom. Electrode Surf. 378 (1988) 154.

[20] J. Kua, W. Goddard III, J. American Chem. Soc. 121 (1999) 10928.

[21] N.M. Markovic, P.N. Ross, CATTECH 4 (2001, Volume Date 2000) 110.

[22] C. Rice, S. Ha, R.I. Masel, A. Wieckowski, J. Power Sources 115 (2003) 229.

[23] G. Palumbo, J.L. McCrea, U. Erb, in: H.S. Nalwa (Ed.), Encyclopedia of Nanoscience and Nanotechnology 1, American Scientific Publishers, Stevenson Ranch, California, 2004.

[24] J.M.D. Coey, Europhysics News 34 (2003) 246.

[25] T. Imokawa, G. Denuault, Chem. Sensors 20 (Suppl. A) (2004) 106.

[26] K.A. Friedrich, K.P. Geyzers, A.J. Dickinson, U. Stimming, J. Electroanal.

Chem. 524-525 (2002) 261.

[27] A.J. Arvia, R.C. Salvarezza, W.E. Triaca, J. New Mater. for Electrochem. Sys. 72 (2004) 133.

[28] F.R. Hartley, The Chemistry of Platinum and Palladium, John Wiley and Sons, New York, 1973.

[29] M.J. Llorca, J.M. Feliu, A. Aldaz, J. Clavilier, J. Electroanal. Chem. 351 (1993) 299.

[30] W.F. Egelhoff, Surf. Sci. Rep. 6 (1987) 253.

[31] G.A Attard, A. Bannister, J. Electroanal. Chem. 300 (1991) 467.

[32] J. Clavilier, M.J. Llorca, J.M. Feliu, A. Aldaz, J. Electroanal. Chem. 310 (1991) 429.

[33] M.J. Ball, C.A. Lucas, N.M. Markovic, V. Stamenkovic, P.N. Ross, Surf. Sci. 518 (2002) 201.

[34] R. Hoyer, L.A. Kibler, D.M. Kolb, Electrochim. Acta 49 (2003) 63.

[35] E.A. Lafferty, Y.-G. Kim, M.P. Soriaga, Electrochim. Acta 44 (1998) 1031.

[36] P. F. Carcia, A. d. Meinhaldt, A. Suna, Appl. Phys. Lett. 47 (1985) 178.

[37] F.J. A den Broeder, H.C. Donkersloot, H.J.G. Draaisma, W.J.M. de Jonge, J. Appl. Phys. 61 (1987) 4317.

[38] D. Weller, Y. Wu, J. Stöhr, M. G. Samant. Phys. Rev. B 49, 18 (1994), 12888.

[39] B.W. Bell Jr., D.K. Campbell in: T.W. McDaniel, R.H. Victora (Eds.), Handbook of Magneto-optical Data Recording: Materials, Subsystems, Techniques, Noyes Publications, Westwood, New Jersey, 1997

[40] Y. Wu, J. Stohr, B. d. Hermsmeier, M.G. Samant, D. Weller, Phys. Rev.

Lett. 69, (1992) 2307.

[41] U. Bardi., Appl. Surf. Sci. 51 (1991) 89.

[42] A. Atrei, G. Rovida, M. Torrine, U. Bardi, M. Gleeson, C. Barnes, Surf. Sci. 372 (1997) 91.

[43] T. Yamazaki, Y. Suzuki, T. Katayama, M. Taninaka, K. Nakagawa, A. Itoh, J. Appl. Phys. 70 (1991) 3180.

[44] S.T. Purcell, M.T. Johnson, N.W.E. McGee, W.B. Zeper, W. Hoving, J. Appl. Phys. 73 (1993) 1360.

[45] J. Kim, J.-W. Lee, J.-R. Jeong, S.-K. Kim, S.-C. Shin, J. Appl. Phys. 89 (2001), 7147.

[46] P. de Haan, Q. Meng, T. Katayama, J.C. Lodder, J. Magn. Magn. Mat. 113 (1992) 29.

[47] B. Lesiak, J, Zemek, P. de Haan, A. Jozwik, Surf. Sci. 346 (1996) 79.

[48] S.-K. Kim, V. A. Chernov, T.-M. Koo, J. Magn. Magn. Mat. 170 (1997) L7.

[49] S.-J. Oh, Wookje Kim, Wondong Kim, B.-H. Choi, J.-Y. Kim, H. Koh, H.-J. Kim, J.-H. Park, App. Surf. Sci. 169-170 (2001) 127.

[50] P. Poulopoulos, M. Angelakeris, Th. Kehagias, D. Niarchos, N.K. Flevaris, Thin Solid Films 371 (2000) 225.

[51] W. Schindler, J. Kirschner, Phys. Rev. B 55 (1997) R1989.

[52] W. Schindler, O. Schneider, J. Kirschner, J. Appl. Phys. 81 (1997) 3915.

[53] V. Georgescu, V. Mazur, O. Cheloglu, J. Magn. Magn. Mater. 156 (1996) 27.

[54] Y. Jyoko. S. Kashiwahara. Y. Hayahi, W. Schwarzacher, IEEE Trans.

Magn. 34 (1998) 3910.

[55] E. Herrero, J. Li, H.D. Abruña, Electrochim. Acta 44 (1999) 2385.

[56] J.L. Bubendorff, E. Beaurepaire, C. Meny, J.P. Bucher, J. Appl. Phys. 83 (1998) 7043.

[57] J. L. Bubendorff, E. Beaurepaire, C. Meny, P. Panissod, J.P. Bucher, Phys. Rev. B. 56 (1997) R7120.

[58] S. Blais, G. Jerkiewicz, E. Herrero, J. Feliu, J. Electroanal. Chem. 519 (2002) 111.

[59] S.P.E. Smith, H. D. Abruña, J. Phys. Chem. B. 102 (1998), 3506.

[60] U.W. Hamm, D. Kramer, R.S. Zhai, D.M. Kolb, Electrochim. Acta 43 (1998) 2969.

[61] J. Clavilier, J.M. Feliu, A. Aldaz, J. Electroanal. Chem. 243 (1988) 419.

[62] R.R. Adziç, M.D. Spasojevic, A.R. Despiç, J. Electroanal. Chem. 92 (1978) 31.

[63] I. Becerik, F. Kadirgan, Annali di Chimica 86 (1996) 463.

[64] M. Besson, F. Lahmer, P. Gallezot, P. Fuertes, G. Flèche, J. Catal. 142 (1995) 116.

[65] P. Gallezot., Catal. Today 37 (1997) 405.

[66] G. Attard, C. Barnes, Surfaces, Oxford University Press, Oxford, UK, 1998.

[67] G. Ertl, J. Kuppers, Low Energy Electrons and Surface Chemistry, VCH, Deerfield Beach, Florida, 1985.

[68] P.N. Ross, F.T Wagner, in: H. Gerischer, C.W. Tobias, Adv. Electrochem.

Electrochem. Eng. Volume 13, John Wiley & Sons, New York, 1984.

[69] B. Shardt, Computed LEED Patterns, Unpublished. Electrochemical Surface Science Laboratory (M.P. Soriaga), Texas A&M University, College Station, TX.

[70] E.A. Wood, J. Appl. Phys. 35 (1964) 1306.

[71] B.K. Agarwal, X-ray Spectroscopy: An Introduction, Springer-Verlag, New York, 1991.

[72] L.B. Leder, J.A. Simpson, Rev. Sci. Inst. 29 (1958) 571.

[73] M.P. Seah, Surf. Interface Anal. 1 (1979) 86.

[74] A.J. Bard, L.R. Faulkner, Electrochemical Methods: Fundamentals and Applications, John Wiley & Sons, Inc., New York, 2001.

[75] A. Al-Akl, G.A. Attard, J. Phys. Chem. B 101 (1997) 4597.

[76] A. Cuesta, L.A. Kibler, D.M. Kolb, J. Electroanal. Chem. 466 (1999) 165.

[77] J. Okada, J.Inukai, K. Itaya, Phys. Chem. Chem. Phys. 3 (2001) 3297.

[78] A.I. Danilov, E.B. Molodkina, A.V. Rudnev, Yu.M. Polukarov, J.M Feliu, Electrochim. Acta 50 (2005) 5032.

[79] M.J. Ball, C.A. Lucas, N.M. Markovic, V. Stamenkovic, P.N. Ross, Surf. Sci. 518 (2002) 201.

[80] V. Clement, N.M. Markovic, V. Stamenkovic, P.N. Ross, J. Phys. Chem B 104 (2000) 3116.

[81] Y.S. Park, Ph.D. Dissertation, Texas A&M University, 2005.

[82] G.A. Attard, R. Price, A. Al-Akl, Electrochim. Acta 39 (1994) 1525.

[83] A. Carrasquillo Jr., Ph.D. Dissertation, Texas A&M University, 1995.

[84] R.J. Barriga, Ph.D. Dissertation, Texas A&M University,1998.

[85] M.P. Soriaga, J.A Schimpf, A Carrasquillo Jr., J.B. Abreu, W. Temesghen, R.J. Barriga, J.-J Jeng, K. Sashikata, K. Itaya, Surf. Sci. 335 (1995) 273.

[86] Y.-G. Kim, M.P Soriaga, J. Phys. Chem. B 102 (1998) 6188.

[87] A. Carrasquillo Jr., J.-J Jeng, R.J. Barriga, W.F. Temesghen, M.P. Soriaga, Inorg. Chim. Acta 255 (1997) 249.

[88] M. Pourbaix, Atlas of Electrochemical Equilibria in Aqueous Solutions, National Association of Corrosion Engineers, Houston, 1974.

[89] Y.-G. Kim, J.B. Soriaga, Gy. Vigh, M.P. Soriaga, J. Coll. Interf. Sci. 227 (2000), 505.

[90] O.M. Magnussen, Chem. Rev. 102 (2002) 679.

[91] A. Hubbard, Chem. Rev. 88 (1988) 633.

[92] D.M. Kolb, H. Gerischer, J. Electroanal. Chem. Interfac. Electrochem. 54 (1974) 25.

[93] Y.-G. Kim, J.H. Baricuatro, M.P. Soriaga, D. Wayne Suggs, Journal of Electroanalytical Chemistry 509 (2001) 170.

[94] T.J. Collins, C. Walter, Sci. Am. 294 (2006) 83.

[95] R. Pauliukaite, S.B. Hocevar, B. Ogorevc, J. Wang, Electroanalysis 16 (2004) 719.

[96] A. Jänes, E. Lust, Electrochim. Acta 47 (2001) 967.

[97] E. Lust, A. Jänes, K. Lust, J. Electroanal. Chem. 449 (1998) 153.

[98] Y.-G. Kim, M.P. Soriaga, Phys. Chem. Chem. Phys. 3 (2001) 3303.

[99] W. Chrzanowki, A. Wieckowski, Langmuir 13 (1997) 5974.

[100] T.J. Schmidt, B.N. Grgur, R.J. Behm, N.M. Markovic, P.N. Ross Jr., Phys. Chem. Chem. Phys. 2 (2000) 4379.

[101] M.T. Paffett, C.T. Campbell, T.N. Taylor, J. Chem. Phys. 85 (1986) 6176.

[102] M.T. Paffett, C.T. Campbell, T.N. Taylor, J. Vac. Sci. Technol., A3 (1985) 812.

[103] K. Itaya, Prog. Surf. Sci 58 (1998) 121.

[104] Y.-G. Kim, M.P Soriaga, J. Colloid Interf. Sci. 236 (2001) 197.

[105] E. Högfeldt, Stability Constants of Metal-Ion Complexes, Part A: Inorganic Ligands, IUPAC Chemical Data Series, No. 21, Pergamon Press, New York, 1979.

[106] A.T. Hubbard, J.L. Stickney, S.D. Rosasco, M.P. Soriaga, D. Song, J. Electroanal. Chem. 150 (1983) 165.

APPENDIX

HIGHLY-ORDERED ULTRATHIN Pd FILMS ON Pt(111): ELECTRODEPOSITION AND SURFACE CHARACTERIZATION

Yeon Su Park, Jack H. Baricuatro, Mohammad A. Hossain and Manuel P. Soriaga*

Department of Chemistry

Texas A&M University

College Station, TX 77843

*To whom correspondence should be addressed

ABSTRACT

Well-defined ultrathin films of palladium, with coverages ranging from submonolayer, Θ_{Pd} ($\equiv \Gamma_{Pd}/\Gamma_{Pt}$) = 0.5 monolayer, to multilayer, Θ_{Pd} = 8, were potentiostatically deposited on Pt(111). Between the coverage regimes studied, the growth of the Pd films followed the Stranski-Krastanov mechanism.

The interfacial electrochemical properties associated with the film-to-bulk transition were characterized by conventional voltammetric techniques in combination with low-energy electron diffraction (LEED) and Auger electron spectroscopy (AES). Voltammetric peaks associated with H-atom adsorption and desorption on terrace sites indicated that the Pd electrodeposit started to exhibit bulk-like properties at $\Theta_{Pd} = 3$.

Voltammetric cycling in sulfuric acid solution, between the hydrogen evolution and the double-layer regions, was found to exert minimal influence on the annealing (smoothening) of the electrodeposited Pd films. However, cycling within the same potential region in the presence of bromide anions (at which Br^- adsorption/Br desorption takes place) smoothened the initially rough Pd films essentially as well as high-temperature annealing.

The influence of chemisorbed bromine on the anodic dissolution of Pd was also studied; this was for comparison with previous work on the anodic dissolution of Pd, in inert electrolyte, catalyzed by chemisorbed iodine. The present studies indicated that bromine was desorbed along with the dissolution of the Pd step atoms in a manner that may be described as electrochemical digital etching.

INTRODUCTION

Ultrathin metallic films on foreign metal surfaces exhibit surface phenomena that are of significant interest in catalysis [1, 2, 3] and magneto-optics [4, 5, 6]. The choice of the film-substrate combination is essentially determined by the intended resultant properties. For instance, the quest for high-performing fuel cell catalysts has stimulated investigations on the use of multimetallic films to improve the catalytic action and CO-poisoning tolerance of Pt [7]. Another illustrative example is the surface modification of Au, Pt, Pd, and Cu substrates by the deposition of ultrathin layers of ferromagnetic metals [*for examples see* Ref. 8, 9, 10, 11, 12] to create well-defined superstructures that can be incorporated in memory storage devices. In all these cases, the desired properties of the prepared material are highly dependent on surface coverage of the ultrathin metallic film. Establishing preparation methods that not only allow precise film-thickness control but also satisfy both technological demands and fundamental scientific interest remains to be an active research endeavor.

Deposition methods for the Pt-group metals classically involve ultrahigh vacuum (UHV) conditions that effectively minimize contamination and allow surface characterization [13,14]. However, for ultrathin films, whose function or application involves solid-liquid interfaces, such as electrocatalysts and protective coatings, the films are best prepared *and* characterized in situ. In this regard, electrochemical methods offers the advantage of creating surface structures that can be reproducibly controlled by judicious choice of supporting electrolytes, buffers, surfactants, applied electrode potential, and scan rate [15].

Furthermore, electrochemical quantitative analysis is afforded by Faraday's Law, which relates the accumulated electrodeposition charge to the amount of ultrathin film formed. Depending on the intended use of the ultrathin metallic films, the quality of electrodeposits can adequately rival that of vacuum-deposited materials [16, 17].

Considerable interest on the growth of ultrathin Pd films on well-defined Pt surfaces stems from the fact that the Pd-Pt pair represents a prototypical bimetallic system whose constituents share similar lattice parameters and atomic radii. Ultrathin Pd films do not suffer from perturbations of hydrogen absorption, which often encumbers voltammetric characterization of Pd bulk samples. Of particular interest is the possible emergence of properties that are otherwise absent in the pure state of each constituent. These novel properties often vary concomitantly with ultrathin-film-to-bulk transition. The search for electrochemical surface probes to monitor this transition is worthwhile pursuing to provide a robust alternative to UHV-based electron spectroscopies.

One of the challenges in electrodepositing ultrathin metallic films is to achieve surface order in an electrochemical environment replete with solvent molecules and other solution species. The present report describes the preparation, surface characterization, and interfacial electrochemistry of ultrathin Pd films on Pt(111) surfaces. The interaction of bromine with the prepared ultrathin films provided a premise for a proposed electrochemical analog to thermal annealing. Programmed electrode-potential excursions to regions bordering dramatic surface perturbations are demonstrated to produce

surface smoothening effects; this potential cycling is dubbed as electrochemical annealing (EC annealing).

For the purpose of this investigation, Pd multilayers (6 to 8 ML) that clearly manifest H_{upd} desorption-adsorption peaks for terrace and step sites are chosen. H_{upd} desorption-adsorption is notably a *thin-film* phenomenon because, in the presence of bulk Pd, the extremely high hydrogen uptake makes adsorption virtually indistinguishable from absorption. The appearance of these anomalous *thin-film* peaks on thick (bulk-like) films is attributed to surface defects such as steps and pits; hence, these peaks can be used as voltammetric markers for the progress of the so-called EC-annealing process.

EXPERIMENTAL METHODS

Experiments were conducted in an ultrahigh-vacuum electrochemistry (UHV-EC) apparatus that integrated gate-valve-isolable chambers for electrochemical and surface characterization. The surface analysis chamber is equipped with low-energy electron diffraction (LEED) optics (Perkin Elmer, Eden Prairie, MN); a cylindrical mass analyzer (Perkin Elmer, Eden Prairie, MN) for Auger electron spectroscopy (AES); and a quadrupole mass analyzer (Quadrex 100, Leybold Inficon, East Syracuse, NY).

A commercially oriented and metallurgically polished 99.999% pure Pt(111) (Aremco Products, Ossining, NY) disc electrode was used. The electrode area exposed to the electrochemical cell was measured, based on the hydrogen underpotential deposition-desorption charge, to be 1.12 cm^2, which is very close to the calculated geometric area of 1.1192 cm^2. Prior to any electrochemical experiment, the single-crystal electrode was cleaned by multiple cycles of Ar^+ bombardment (Ar^+ current = 4 -10 μA) and thermal oxidation at 550°C (P_{O2} = 5 x 10^{-6} torr); ultimately, the electrode was annealed to 750°C under UHV conditions to restore long-range surface order. The cleaning cycle was repeated until surface purity and order were verified by AES and LEED, respectively.

Electrochemical experiments were performed using a CV-27 Voltammograph (Bioanalytical Systems, West Lafayette, IN). The electrochemical cell consisted two compartments separated by a glass frit: one compartment for the Pt(111) working electrode and the other one for the Ag/AgCl (1 mM NaCl) reference electrode and Pt-wire counter-electrode.

Current-potential curves and chronocoulograms were monitored using a VP-6414S X-Y recorder (Soltec, Sun Valley, CA).

All pieces of glassware were cleaned using hot chromic acid (3% $K_2Cr_2O_7$ in 10 M H_2SO_4). All solutions were made up using 18.2 Ω Millipore water (Millipore Systems, Houston, TX). The following high-purity reagents were used without further purification: $PdSO_4$ (Aldrich, Milwaukee, WI), fuming H_2SO_4 (Aldrich), NaI (Curtin Matheson Scientific, Houston, TX), NaBr (Johnson Mathey, England), NaCl (Johnson Mathey), NaF (Aldrich), $Cu(ClO_4)_2$ (Aldrich), CF_3COOH (Aldrich), and $K_2Cr_2O_7$ (EM Science, Gibbstown, NJ). High-purity N_2 (BOTCO, Bryan, TX), Ar (BOTCO), and O_2 (Proxair, Dunbury, CT) gases were used.

RESULTS AND DISCUSSION

Electrodeposition of Ultrathin Pd Films. Ultrathin Pd films of various surface coverages were prepared by initially immersing the Pt(111) electrode into a solution of 0.50 mM $PdSO_4$ in 0.1M H_2SO_4 at open-circuit potential (0.42V) for 60 s before holding the applied potential at a predetermined value ranging from 0.230V to –0.400V for 120 s. For a given electrolysis time, at low overpotentials η_{Pd}, the deposition charge linearly increased with the applied potential until near-exhaustive electrolysis of the remaining $Pd^{2+}_{(aq)}$ occurs. Based on Faraday's Law, the amount of charge measured during this potential-step experiment, corrected for background capacitive charge, provided a quantitative measure of the amount of electrodeposited Pd.

The formation of a pseudomorphic 1 ML Pd was established using the underpotential deposition (UPD) of Cu. At submonolayer Pd coverages, it was not unexpected to see Cu UPD peaks associated with both Pd and Pt [18]. The complete attenuation of the Cu UPD-onto-Pt peak after a potential-step Pd deposition at 0.221V marked the formation of 1 ML Pd; under the present experimental conditions, 1 ML Pd corresponded to a deposition charge of 539 μC. When the electrodeposited 1 ML Pd was quantitatively stripped off by chemisorbed-iodine-catalyzed anodic dissolution [19], the stripping charge matched with the deposition charge. All Pd coverages reported in this study were, henceforth, based on the value 539 μC/ML. An electrodeposition isotherm based on this definition of coverage is shown in Figure 2.

Surface Characterization of Ultrathin Pd Films: LEED and AES. The surface geometry of Pd adatoms was monitored as function of coverage using LEED (Figure 1). Interfacial structures of the following coverages were compared: 0.5, 1, 2, 3, 4, and 8 ML. At a submonolayer coverage of 0.5 ML, where high surface-step density was expected, relatively dim spots were observed. The deposition of 1 ML Pd led to the formation of large, highly ordered Pd domains that fully cover the Pt(111) substrate, as evidenced by the acquisition of the sharpest and brightest LEED spots at this coverage. The slight, yet reproducible, decrease in the brightness of the LEED pattern obtained after the deposition of 2 ML marked the onset of three-dimensional island formation on top of the first conformal layer. Based on the progressive decline in spot brightness, it can be surmised that more island growth continued at 3 ML and became most prominent at 4 ML, as can be gleaned from the changes in spot brightness of the LEED patterns. Similar topographical changes could be inferred from the voltammetric profiles [*vide infra*] of the prepared ultrathin films.

Based on LEED and AES data (Figure 2) alone, no definitive descriptions could be made on the surface structural changes as the Pd coverage increased from 3 ML to 8 ML. Further characterization of the island growth and nucleation, at 3 ML and higher, would have been possible by LEED spot-intensity-vs-beam-energy analysis, which is currently unavailable in our laboratory.

The observed evolution of LEED spot sharpness and intensity suggests that the growth of the electrodeposited ultrathin Pd films proceeds via the

Stranski-Krastanov mechanism; i.e., the completion of the first full monolayer is followed by three-dimensional island formation. The observed growth mode is dictated by the interplay of the relative surface energy of the Pd film and Pt(111) substrate (σ_{Pd} and σ_{Pt}, respectively) and the specific free interfacial energy, σ_i. The relation, in its simplest form, can be expressed as $\Delta = \sigma_{Pd} + \sigma_i - \sigma_{Pt}$, where edge-, shape- and size-effects on the reported surface energies are neglected [20]. Three-dimensional island growth is observed when $\Delta > 0$ while layer-by-layer growth is expected when $\Delta \leq 0$.

Taking the specific surface free energies [21] of Pd (111) and Pt (111), as 1382 and 1656 ergs/cm^2, respectively, and considering the similarity in lattice parameter of both metals (hence, $\sigma_i \approx 0$ ergs/cm^2 for 1 ML or lower Pd coverage), it is expected that complete 1 ML Pd film is formed initially. At 2 ML or higher, island formation occurs, suggesting that the contribution of σ_i exceeds 274 ergs/cm^2. The Stranski-Krastanov growth mode of Pd on Pt substrate has been supported by previous studies using X-ray diffraction (XRD) [22], surface X-ray scattering [21], electrochemical-scanning tunneling microscopy (EC-STM) [23], and electrochemistry [21, 23].

Electrochemistry of Ultrathin Pd Films on Pt(111) in Halide-Free Electrolyte. Shown in Figure 3 is a typical cyclic voltammogram of the Pt (111) substrate used in this investigation. The following voltammetric features are consistent with previously reported current-potential profile of a clean and well-ordered Pt(111) disc electrode in 0.1 M H_2SO_4: (*i*) broad hydrogen adsorption-desorption region between –0.45 V and –0.17 V; (*ii*) the so-called butterfly peaks, between

–0.17 and 0.00 V, associated with (bi)sulfate desorption-adsorption [22,24]; (*iii*) Pt-surface oxidation peaks that initially emerge as a broad anodic feature at 0.17 V, leading to a large peak centered at 0.78 V; (*iv*) and a Pt reduction peak at 0.24 V.

The electrochemical behavior of the prepared ultrathin Pd films was characterized by cycling the ultrathin films in 0.1 M H_2SO_4 at a scan rate of 2 mV/s. Figure 4 displays the cyclic voltammograms of ultrathin Pd films at various surface coverages, *n*, expressed in terms of monolayers, ML. Common to all these ultrathin films were twin redox peaks whose intensities strongly depend upon Pd coverage: One reversible pair centered at –0.33 V that was associated with hydrogen underpotential adsorption-desorption (hereafter referred to as H_{UPD} adsorption-desorption) processes at *terrace* sites; and an analogous set at –0.29 V that was a voltammetric signature of *step* sites [22, 24]. Some researchers [23] have ascribed the redox pair at *ca*. –0.29 V to adsorption-desorption processes on terrace sites of *bulk* Pd deposits.

At submonolayer coverages of Pd (n = 0.5 ML, Figure 4a) two distinct anodic peaks were evident beyond the double-layer potential region. Based on the voltammogram of bare Pt(111) and the established redox peak positions for ultrathin Pd films [18, 24-29] and bulk Pt [30, 31] reported in literature, the peaks at 0.58 V and 0.78 V in Figure 4(a) corresponded to the oxidation of ultrathin Pd film and uncovered Pt substrate, respectively. The peak at 0.18 V was assigned to Pd reduction.

At submonolayer coverages of Pd, it was not surprising to detect voltammetric signals from the exposed Pt substrate, such as the nondescript features between –0.17 V and 0.00 V and the broad reduction peak at 0.24 V. A comparison of the voltammogram of 0.5 ML Pd film with that of 1 ML Pd film in Figure 4(b) showed an increase in the signal intensities of the terrace and step H_{upd} adsorption-desorption peaks — with the growth of the terrace-related peak much more dramatic than the step counterpart.

For 1 ML Pd/Pt(111), the surface was predominantly made up of large terraces as indicated by the very intense terrace H_{upd} adsorption-desorption peaks. The close agreement between the experimentally determined charge (213 μC) and the theoretical charge (212 μC) for a pseudomorphic Pd film on Pt(111) supported the assertion that the 1 ML Pd completely covers the Pt substrate. The disappearance of the characteristic broad voltammetric features of Pt(111) between –0.17 and 0.0 V rendered further evidence to this claim. Additional voltammetric evidence was also provided by the fact that only Pd-related Cu UPD signals are observed at a Pd coverage of 1 ML.

Voltammetric features of 2 and 3 ML Pd films, as shown in Figures 4(c-d), respectively, resembled those of 1 ML Pd film, except for the small differences in peak size. Compared to films of lower Pd coverages, a 4 ML Pd film (Figure 4(e)) showed much larger step H_{upd} adsorption-desorption peaks and much smaller terrace-related peaks. The fact that the step H_{upd} adsorption-desorption peaks are much larger than the terrace-related peaks suggested the existence of a lot of Pd islands on the 4 ML Pd film. Along with these changes it was also important

to note that the Pd oxidation peak at 0.52 V became larger than the one at 0.58 V. The former peak (at 0.52 V) was, therefore, ascribed to Pd-surface oxidation at steps sites, while the latter one was associated with the same process on the terraces.

Underpotential Deposition of Hydrogen (H_{UPD}). The desorption-adsorption of hydrogen on Pd is notably a *thin-film* phenomenon. In the presence of bulk Pd, surface H_{upd} is readily transformed into a stable Pd-H phase; this interfacial transformation is a result of the lowering of the hydrogen absorption energy barrier due to bulk Pd lattice relaxation. As the Pd film thickness decreases, both the diffusion coefficient and solubility of hydrogen in Pd are notably decreased [32]; thus it is not unexpected to observe H_{upd} adsorption-desorption *without absorption* in ultrathin Pd films.

The dependence of the H_{upd} deposition-desorption peak intensity on the Pd surface coverage is depicted on Figure 5 as a plot of H_{upd}-desorption charge as a function of Pd coverage. The conversion of submonolayer coverages (0.5 ML Pd) into a full monolayer (1 ML Pd) was accompanied by a remarkable increase in the terrace H_{upd} desorption charge. As the Pd coverage increased from 1 ML to 3 ML, the terrace H_{upd} desorption charge decreased slightly while step H_{upd} desorption charge marginally increased. A critical crossover in the trend for the desorption charges was observed between 3 ML to 4 ML: Terrace H_{upd} desorption charge became much smaller than that of the step H_{upd} desorption charge. Further increase in the Pd coverage, from 4 to 8 ML Pd, led to a decline of both terrace and step H_{upd} desorption charges.

Based on the changes in the voltammetric terrace- and step-peak charges from 1 to 3 ML Pd, the following surface events were deemed to transpire: The growth of three-dimensional islands occurred at the expense of the diminution of the surface area associated with ordered terraces. When Pd coverage increased from 3 to 4 ML, the number of islands on the film surface increased, thereby a substantial fraction of the terraces disappeared. As the Pd surface coverage continued to increase, so did the bulk-like character of the ultrathin film; thus, the overall H_{upd} desorption charge should concomitantly decrease with Pd surface coverage, considering that H UPD is a thin-film phenomenon.
It is, however, interesting to note that at a considerably high Pd coverage of 8 ML, H_{upd} adsorption-desorption peaks are still observed. Similar results have been reported in the literature [23] suggesting the pervasiveness of highly-stepped thin-film structures (manifested by H_{upd}) even up to 10 ML under various deposition conditions and anion effects.

Potential Cycling in Sulfuric Acid. The notion that programmed potential cycles can induce surface order was investigated. Shown in Figure 6 is the steady-state voltammogram obtained after multiply cycling (5 cycles) 4 ML Pd film in 0.1 M H_2SO_4 between the hydrogen evolution region (–0.48 V) and the double-layer region (–0.02 V). That the voltammetric profiles after the first and fifth scans are virtually identical indicates negligible surface smoothening effects.

Extending the positive switching potential to 0.88 V (at which Pd surface oxidation transpires) only led to a gradual dissolution of the Pd ultrathin film as

evidenced by the decrease in the Pd AES signal (Figure 7). At the end of the 8th potential cycle, only submonolayer coverages (less than 0.3 ML) of Pd remained on the Pt(111) surface.

Electrochemistry in Bromide-free NaF Solution. The use of 0.1 M sodium fluoride (NaF) solution, adjusted to pH 4 with trifluoroacetic acid (TFA), as the supporting electrolyte solution (hereafter referred as *NaF (pH 4)*) ensures a wide potential window for the formation of ordered bromine adlayers [33]. Both NaF and TFA are known not to chemisorb on Pd surfaces under the present experimental conditions. Using NaF (pH 4) as supporting electrolyte also allows direct comparison of results from the present study with those obtained from previous works utilizing bulk Pd(111).

Figure 8 displays typical features of a cyclic voltammogram of Pt(111) in 100 mM NaF (pH 4): (i) a broad H_{upd} adsorption-desorption region between –0.33 and –0.66V; (ii) a broad Pt oxidation region stretching from –0.12 to 0.78 V, which includes relatively large oxidation peaks at 0.35 and 0.65 V; and (iii) a Pt reduction peak at 0.07 V.

The cyclic voltammogram of 1 ML Pd film in 0.1 mM NaF (pH 4) is given in Figure 9. The observed features are very similar to those of bulk Pd(111) [34], except for the existence of H_{upd} adsorption-desorption peak. Furthermore, the Pd redox peak sizes associated with thin films are about 3 times smaller than those of bulk Pd(111) [34] because of the evidently smaller amount of Pd present on ultrathin Pd films. Broad voltammetric features for Pd oxidation can be

discerned between –0.10 and 0.70 V. The Pt reduction peak at 0.07 V is indistinguishable from the Pd reduction peak at –0.01 V.

Electrochemical Behavior of Ultrathin Pd Films in Aqueous Bromide. The following voltammetric features are observed when 1 ML Pd/Pt(111) was exposed to aqueous bromide solution (Figure 9): (i) a pair of sharp H_{upd} adsorption/desorption peaks at –0.45 V; (ii) Pd oxidation peak at 0.35 V; (iii) a large voltammetric wave, starting at 0.55 V, corresponding to bromide-to-bromate oxidation; (iv) a small bromate-to-bromide reduction peak at 0.67 V; and (v) a broad Pt reduction peak at 0.18 V. The notable enhancement of the Pd oxidation peak, along with the emergence of broad Pt reduction peak, in the presence of aqueous bromide, strongly suggests a bromide-induced Pd stripping phenomenon during the anodic scan.

Subtle differences exist between the voltammetric features of thin films and bulk Pd(111) in the presence of bromide ions [28]. Bulk Pd typically exhibits a large Pd reduction peak at 0.10 V but does not show H_{upd} adsorption-desorption. The observance of Pd reduction peak current about 10 times larger than that of ultrathin Pd films is a natural consequence of the fact that bulk Pd offers a much larger supply of Pd atoms available for redox reactions than thin films.

Potential-dependent Chemisorption of Br on Ultrathin Pd Films. Bromine chemisorption was carried out by immersing 1 ML Pd films in bromide-containing 0.1 M NaF (pH 4) at various constant potentials. Under the present experimental conditions, bromine adsorption on 1 ML Pd film occurred at

$E_{deposition} \geq -0.10$ V. Resulting adlayers were characterized using LEED and AES. Bromine adsorption was confirmed by the appearance of Auger Br peak at 102 eV and the observation of the characteristic (√3×√3)R30°-Br LEED pattern.

Bromine coverage strongly depends on the chemisorption potential. Potential-controlled chemisorption between –0.10 and 0.50 V yields the same characteristic (√3×√3)R30°-Br LEED pattern. Since Br chemisorption on Pd surfaces is known to be an oxidative process, potential excursions to positive regions are expected to increase bromine coverage; it is, therefore, not surprising to see such trend within the chemisorption potential range of –0.10 to 0.22 V (Figure 10b).

It can be seen in Figure 10a that the open circuit potential (0.22 V) corresponds to the inception of Pd dissolution into Pd^{2+} (Pd stripping). The drop in bromine coverage, from 0.22 V to 0.60 V, indicates that the adsorbed Br departs along with the stripped Pd. That the subsequent voltammetric Pd stripping peak is really small suggests that the amount of stripped Pd is also minuscule; hence, AES only detects a decrease in the Pd peak intensity at ca. 0.50 V or higher (Figure 11). As the Auger electron spectra reveals, bromide-induced Pd stripping occurs without the formation of surface oxides.

To understand the Br coverage upturn at 0.60 V, it is essential to underscore two experimental observations: (i) This potential marks the onset of the oxidation of aqueous bromide to aqueous bromate. (ii) The Auger Pd signal intensity essentially remains the same from 0.60 to 0.80 V. It is believed that an increase in Br coverage leads to the accumulation of Br as part of a passivating

$PdBr_2$ film in a manner akin to what has been previously observed in bulk Pd(111) [33, 34]. The highly diffuse (1×1) LEED pattern probably emanates from the Pd film covered with the passivating $PdBr_2$ layer. It is also important to note that the measured Br coverage at 0.80 V would have given rise to the usual (√3×√3)R30° pattern, but its absence indicates that the bromine is incorporated, in a disordered fashion, into the passivating film. The nature of this passivating film requires further elucidation.

Electrochemical (EC) Annealing in Aqueous Bromide. Electrochemical (EC) annealing was anchored on the fact that, by cycling the electrode between potentials that border surface perturbation, surface atoms can be rearranged to desirable equilibrium positions. The possibility of EC annealing by multiple potential cycles, at a scan rate of 2 mV/s, in bromide-containing 0.1 M NaF (pH 4) was scrutinized. In this case, EC annealing consisted of 5 potential cycles between –0.65 V (onset of HER) and 0.22 V (double-layer region). Smoothening effects were adjudged based on: (i) the widening of terraces and the disappearance of step sites and (ii) the enhancement of surface order evaluated by LEED.

Results indicated that surface imperfections were readily removed from 1 ML (Figure 12) and 2 ML (Figure 13) Pd films. The relative ease of smoothening was a consequence of the fact that the pre-annealed surfaces bear only very few step sites. 3 ML (Figure 14) and 4 ML (Figure 15) Pd films were initially strewn with three-dimensional islands; thus, a single potential cycle was inadequate to induce complete smoothening. Two cycles of EC annealing produced the same

effect as the first one, suggesting that more EC annealing cycles provided minimal changes in the surface order of Pd films.

The EC annealing process described above was modified by switching, instead of scanning, the potentials. A complete potential cycle consisted of initially setting the potential at E_1 = 0.22 V (at which Br chemisorption occurred) and then switching it to E_2 = –0.40 V (near the onset of HER). A waiting time of 3 minutes was sufficient to allow the measured current to drop to zero after the imposition of each potential. A total of 10 cycles was performed; the final potential was poised at –0.40 V. Figure 16 shows a diagrammatic representation of a complete potential cycle.

A surface coverage of 8 ML Pd was chosen to represent a bulk Pd surface that exhibited *non-bulk* voltammetric peaks typified by the terrace- and step-site H UPD adsorption-desorption peaks. After EC annealing, the resulting surface was rinsed thrice in blank NaF electrolyte solution under potential control (E_2 = –0.40 V). Cyclic voltammetry was performed in Br-free 0.1 M NaF (pH = 4) solution to ascertain any changes in the surface order. Figure 17 displays the voltammograms of both pre- and post-EC-annealed surfaces. The dramatic extinction of the H UPD adsorption-desorption peaks after EC-annealing heralded the disappearance of surface step-sites that were most likely the origin of this anomalous thin-film-like behavior. The post-EC-annealing voltammogram displayed the expected voltammetric features of *bulk* Pd electrodes.

The disappearance of surface defects, and thereby the restoration of long-range surface order, was further corroborated by the acquisition of sharper (1x1) LEED pattern (Figure 18) for post-annealed surfaces. A comparison of the peak-to-peak heights for the Pd AES transition (Figure 19) revealed that, within the expected precision of such AES signal quantitation (± 0.05 cm), the Pd surface coverage on Pt(111) remained virtually the same after multiple potential cycling. This result was also verified by I_{ads}-catalyzed dissolution of Pd, which revealed no changes in the Pd coverages before and after the cycling experiment. Thus, during EC-annealing in the presence of $NaBr_{(aq)}$, Pd adatoms occupying defect sites were rearranged to assume equilibrium positions on well-ordered terraces of the (111)-texture.

Thin-film-to-bulk Transition of EC Annealed Ultrathin Pd Films. The emergence of bulk-like properties of *step-free* films was monitored by the extinction of the voltammetric H_{upd} desorption-desorption peaks on terraces. Pd films began to manifest bulk-like properties, after EC annealing, at a Pd coverage of 3 ML. If the *post-EC-annealed* 3 ML Pd film were to behave purely like thin films, the terrace H_{upd} adsorption-desorption peaks would have increased due to the lowering of Pd island density; however, a decrease in the terrace H_{upd} adsorption-desorption peak intensity was noted, signifying the start of bulk-like behavior.

Chemisorbed Bromine-induced Anodic Dissolution of Ultrathin Pd Films. Ultrathin Pd films, unlike bulk Pd, readily undergoes anodic dissolution in the presence of chemisorbed bromine [33,19]. Such corrosive effects were examined

using a 5 ML Pd film coated with bromine chemisorbed at 0.22 V for 3 minutes. The resulting film was then transferred to a Br^--free 0.1 M H_2SO_4. The potential was scanned from the open-circuit potential to the potential tail-end of the Br_{ads}-induced Pd dissolution wave (typically ranging from 0.58 to 0.62 V). Before another dissolution cycle was launched, bromine is re-adsorbed to the Pd film.

Br_{ads}-induced dissolution cycles promoted the removal of both Pd and Br_{ads} (Figure 19) within the present potential window. Pd coverage decreased drastically (1.9 ML) at the 1st cycle and then decreased gradually in almost linear fashion (0.8 ML/cycle) between 2nd and 4th cycles. The 5th cycle, however, led to a slight decrease in Pd coverage, as compared to the 4th cycle.

After each dissolution cycle, the remnant Br_{ads} adlayer was less than a full coverage of 0.33 ML; this case was unlike the I_{ads}-induced dissolution where the remnant I_{ads} adlayer retained its original structure and coverage. The remnant Br_{ads} coverage was practically the same between 1st and 3rd cycles, but it decreased gradually thereafter. After one cycle, the resulting surface remained oxide-free and exhibited significant long-range order. A significant degree of surface order was still preserved after the 5th cycle as evidenced by the acquisition of a diffuse (√3×√3)R30°-Br pattern.

Interestingly, after the 1st cycle, a discernible (√3×√3)R30°-Br adlayer structure emerged along with a significant decrease in Pd coverage. Subsequent cycles, however, led to a further decrease in Pd coverage, almost linearly with the number of cycle while maintaining LEED patterns similar to that of the 1st cycle. Remnant Br_{ads} coverage remained essentially the same between the 1st and

3rd cycles, but gradually decreased as more of the Pt(111) substrate surface was exposed between the 4th and 5th cycles. These observations suggest that (i) Br_{ads} desorption occurs from the step Pd atoms; no Br desorption takes place from the terrace Pd atoms, (ii) Br_{ads}-induced dissolution of smooth Pd proceeds in layer-by-layer fashion, and (iii) only after all of the Pd is dissolved will the Br_{ads}, which then resides on the Pt(111) substrate, be oxidatively desorbed.

Br_{ads} desorption starts at the early stage of Pd film dissolution. This finding is derived from the fact that both Auger Pd and Br peak intensities decrease upon fixing the potential of the bromine-coated 5 ML Pd_{CPD} film at 0.41 V for 2 to 7 minutes after potential scanning from 0.22 to 0.41 V. The rate of Pd stripping is higher than the rate of Br desorption as can be gleaned from the time-dependent changes of the Pd and Br coverages. When the potential is held at 0.41 V, a very rough surface is obtained; the experiment does not induce oxide formation, as evidenced by the absence of the Auger O peak.

EC Annealing of Br_{ads}-modified Ultrathin Pd Films in Br-free Solution. The ability of bromine to facilitate Pd adatom rearrangement is reminiscent of the surfactant-like action of chemisorbed iodine (I_{ads}) in restoring the atomic-level smoothness of electrochemically roughened and ion-bombarded electrode surfaces. Previous studies have uncovered interesting surface-confined phenomena by examining the electrochemistry of I_{ads} in iodide-free solution. For instance, a place-exchange mechanism has been demonstrated to transpire between the I_{ads} and Pd during the anodic dissolution of Pd electrodes in I-free sulfuric acid; i.e. iodine always stays on the surface during the ensuing stripping

process [35]. Along the same vein, the electrochemical behavior of Br_{ads} on ultrathin Pd films, *in Br-free electrolyte solution*, demands special attention. For this purpose, Br was chemisorbed onto a well-defined 6 ML Pd/Pt(111) surface by immersing it into a solution of 1 mM NaBr/0.1 M NaF (pH = 4) at 0.22 V for 3 minutes. The acquisition of a (√3x√3)-Br adlattice (Figure 20), under this experimental condition, was consistent with previous reports [33].

The prepared Br adlayer was transferred to Br-free 0.1 M H_2SO_4, and the potential was stepped from 0.22 V to 0.41 V; the final potential corresponded to the shoulder of a huge peak ascribed to be a composite of the anodic dissolution of both ultrathin Pd film and the chemisorbed Br adlayer (cf. Figure 21). In this polarization experiment, the potential was strategically poised at the chosen value to ascertain if, in a manner similar to the I_{ads}-catalyzed anodic dissolution of Pd, chemisorbed Br would stay on the ultrathin Pd film surface until the film would be exhaustively removed.

As revealed by the chronocoulogram in Figure 22, a monotonic increase in the electrolytic charge was noted. Compositional analysis by AES showed a 10% decline in the Pd signal due to anodic dissolution, as indicated by the linear rise in electrolytic charge beyond 12 minutes of polarization at 0.41 V. The initially rapid increase in charge during the first 3 minutes of polarization was ascribed to the anodic oxidation of chemisorbed Br. This finding was supported by the absence of both the AES Br signal and the characteristic (√3 x √3) LEED pattern.

Quantitative analysis, by I_{ads}-catalyzed dissolution, of the Pd film remaining after polarization at 0.41 V indicated a Pd surface coverage of 4.8 ML. The amount of anodically dissolved Pd (1.2 ML) represented adatoms that occupied terrace and step sites. It was evident from the linear increase in electrolytic charge after 10 minutes of polarization (Figure 22) that the anodic dissolution of ultrathin Pd film would have proceeded towards completion if the imposition of potential were continued. This scenario is different from bulk Pd electrodes at which anodic dissolution is impeded by the formation of surface oxides [19, 35].

Cyclic voltammetry of the resultant adlayer in 0.1 M H_2SO_4 indicates the disappearance of the H UPD peak on step-sites and the dramatic decrease in the signal intensity for the H UPD peak on terraces (Figure 23). AES analysis (Figure 24) of the remaining film shows a decrease in the Pd surface coverage. Such decrease in coverage suggests that the presence of chemisorbed Br activates the preferential anodic dissolution of *step-site* Pd adatoms. This claim is borne out of the observation that, in the absence of chemisorbed Br, the step-site H UPD feature still persists (cf. Figures 6 and 7) even after multiple sweeps involving switching potentials greater than 0.41 V. The disappearance of step sites gives rise to a well-ordered film surface as can be gleaned from the LEED results in Figure 25.

The ability of chemisorbed Br to facilitate anodic dissolution of ultrathin Pd films is, hence, different from that of iodine. Since the Pd-Br bond is weaker relative to that of Pd-I bond, Br adatoms preferentially seek out the more

reactive surface defects (e.g., steps) on Pd, thereby making the chemisorption more site-selective. In contrast, I adatoms are readily chemisorbed and tenaciously sticks to the surface even at potentials bordering the anodic surface oxidation of Pd. Within the same potential region, Br adatoms are easily desorbed, consequently giving rise to a Br-free Pd surface as evidenced by both AES and LEED. The accompanying smoothening process is, therefore, similar to electrochemical digital etching, in which the etching agent (Br) can be strategically introduced (adsorbed) onto and removed (desorbed) from the surface upon the imposition of appropriate potentials. While it is certain that the above voltammetric results imply Br_{ads}-enhanced surface mobility of Pd atoms, the mechanism of such enhancement remains to be elucidated. The proximity of the potentials needed to initiate both Pd anodic dissolution and Br desorption accrues to the complexity of electrochemically delineating the two processes.

CONCLUSIONS

Ultrathin Pd films of various surface coverages were electrochemically prepared via potentiostatic deposition. The tandem use of surface science tools and conventional electrochemical techniques allowed the formulation of atomic-level descriptions of the interfacial structure and reactivity of the prepared ultrathin films in aqueous bromide solution.

At $\Theta_{Pd} = 1$, the electrodeposited film completely and pseudomorphically covered the Pt(111) substrate. At $\Theta_{Pd} > 1$, three-dimensional island formation and growth were indicated. The electrodeposited Pd films assumed a Stranski-Krastanov growth mode.

Voltammetric peaks associated with H_{upd} adsorption-desorption on terrace- and step-sites were surface-sensitive indicators of the thin-film-to-bulk transition of (thermally or electrochemically) annealed surfaces. Pd films began to manifest bulk-like properties at $\Theta_{Pd} = 3$, provided the film was atomically smooth and essentially defect-free. For non-annealed surfaces, non-bulk-like behavior was shown even at higher coverages.

Atomically smooth, well-defined ultrathin Pd films can be prepared using potential-controlled adsorption-desorption cycles of aqueous bromide. Similar smoothening effects were previously demonstrated using the chemisorption of iodine onto ultrathin Pd films followed by reductive desorption of $I_{(ads)}$ at pH 10 (where $E_{des} > E_{HER}$). Exposure of step-laden ultrathin Pd films to aqueous bromide led to its preferential chemisorption at step sites. Bromine-decorated step sites were thereby activated towards anodic dissolution

even in the absence of bromide ions in solution. Both $Br_{(ads)}$ and the Pd substrate were anodically stripped off leaving behind wide well-ordered Pd film terraces.

ACKNOWLEDGMENTS

Acknowledgment is made to The Welch Foundation and the National Science Foundation for the support of this research.

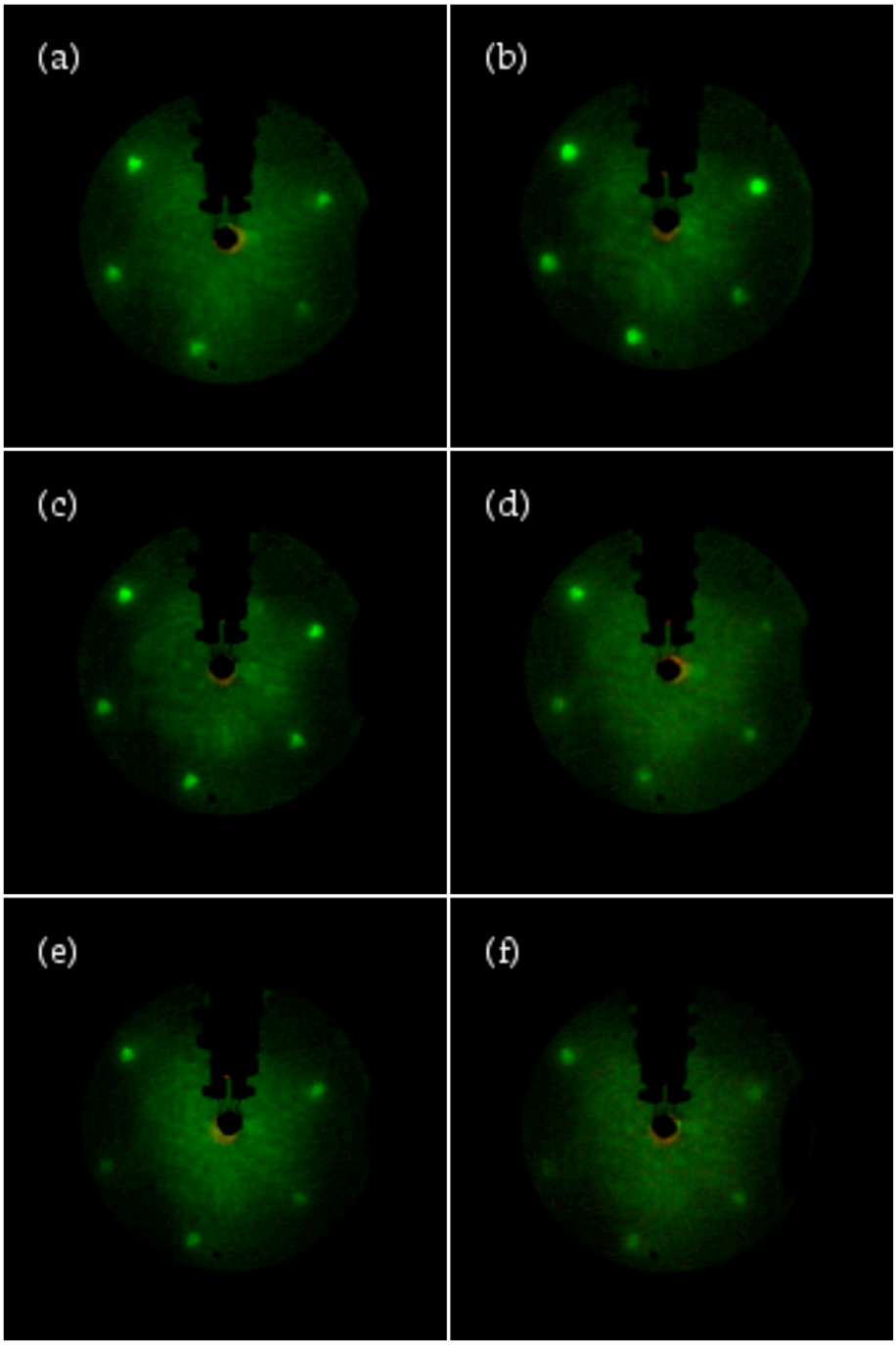

Figure A-1. LEED patterns for ultrathin Pd films on Pt(111) at various Pd coverages: (a) 0.5, (b) 1, (c) 2, (d) 3, (e) 4, and (f) 8 ML. Ultrathin films were electrochemically prepared by potentiostatic deposition. Beam energy = 62.0 eV; beam current = 2 μA.

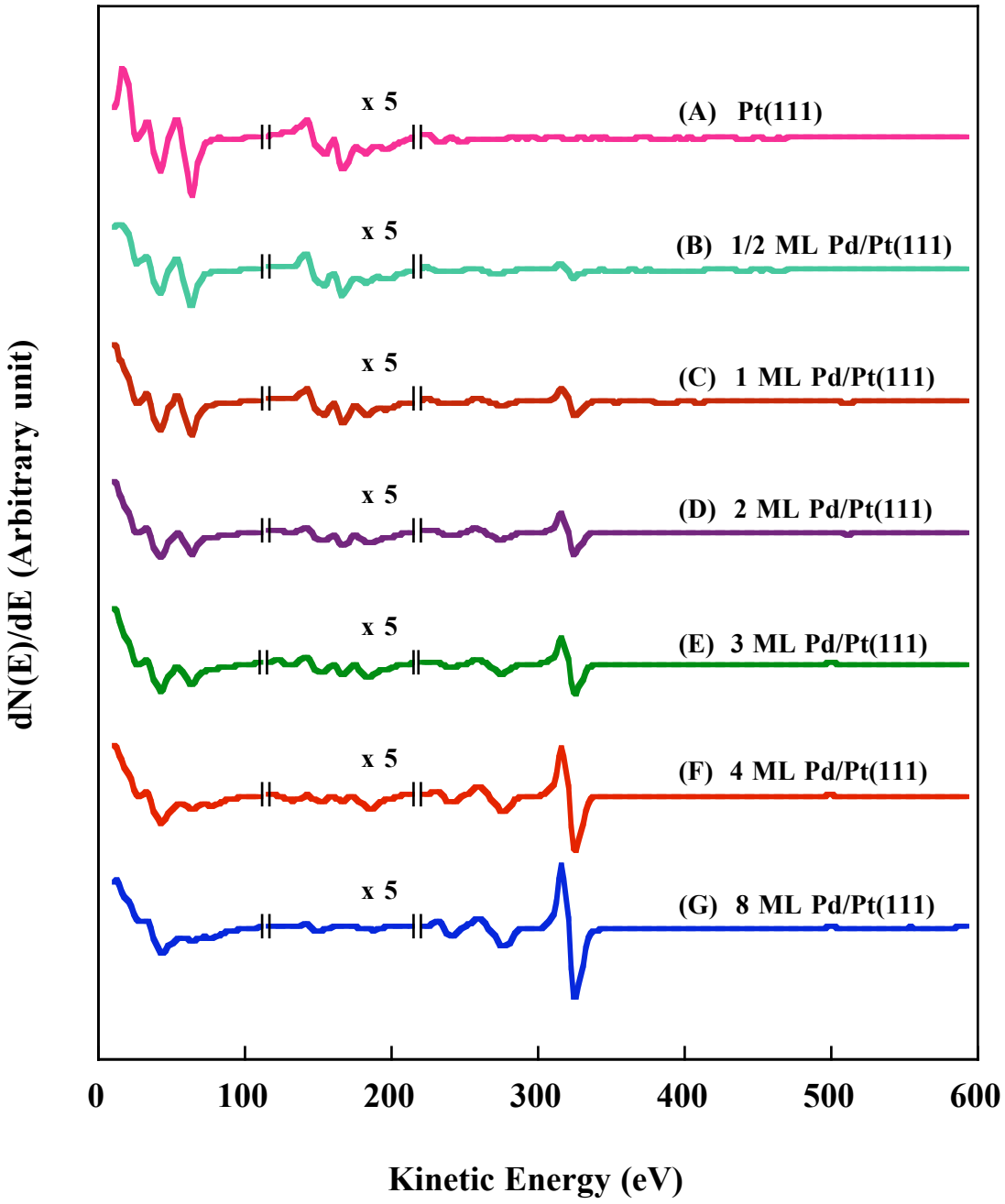

Figure A-2. AES spectra of ultrathin Pd films on Pt(111). Incident beam energy = 2 keV; beam current = 1 μA.

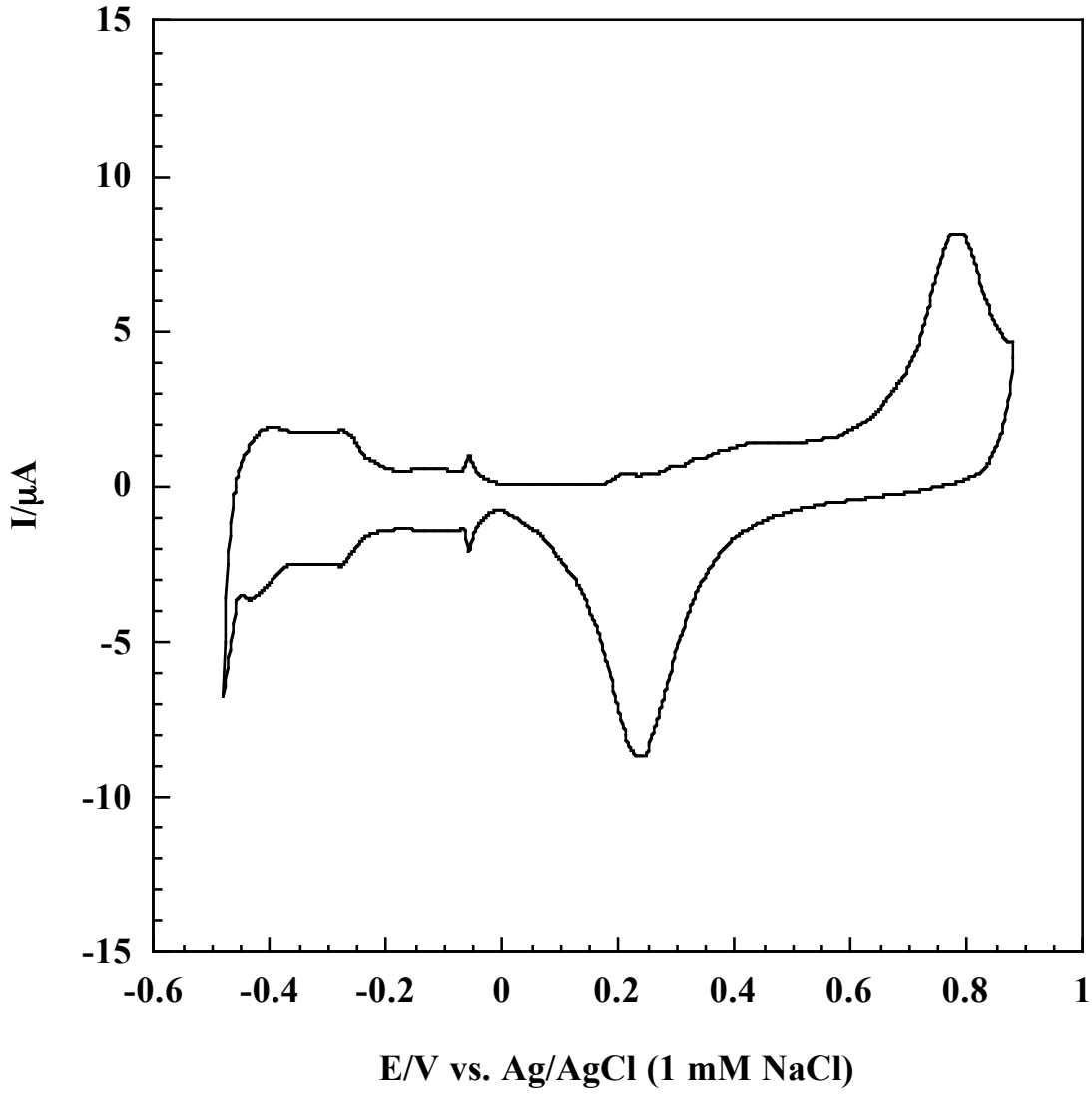

Figure A-3. Cyclic voltammogram of a Pt(111) disc electrode in 0.1 M H_2SO_4. Scan rate = 2 mV/sec. Electrode area = 1.12 cm^2.

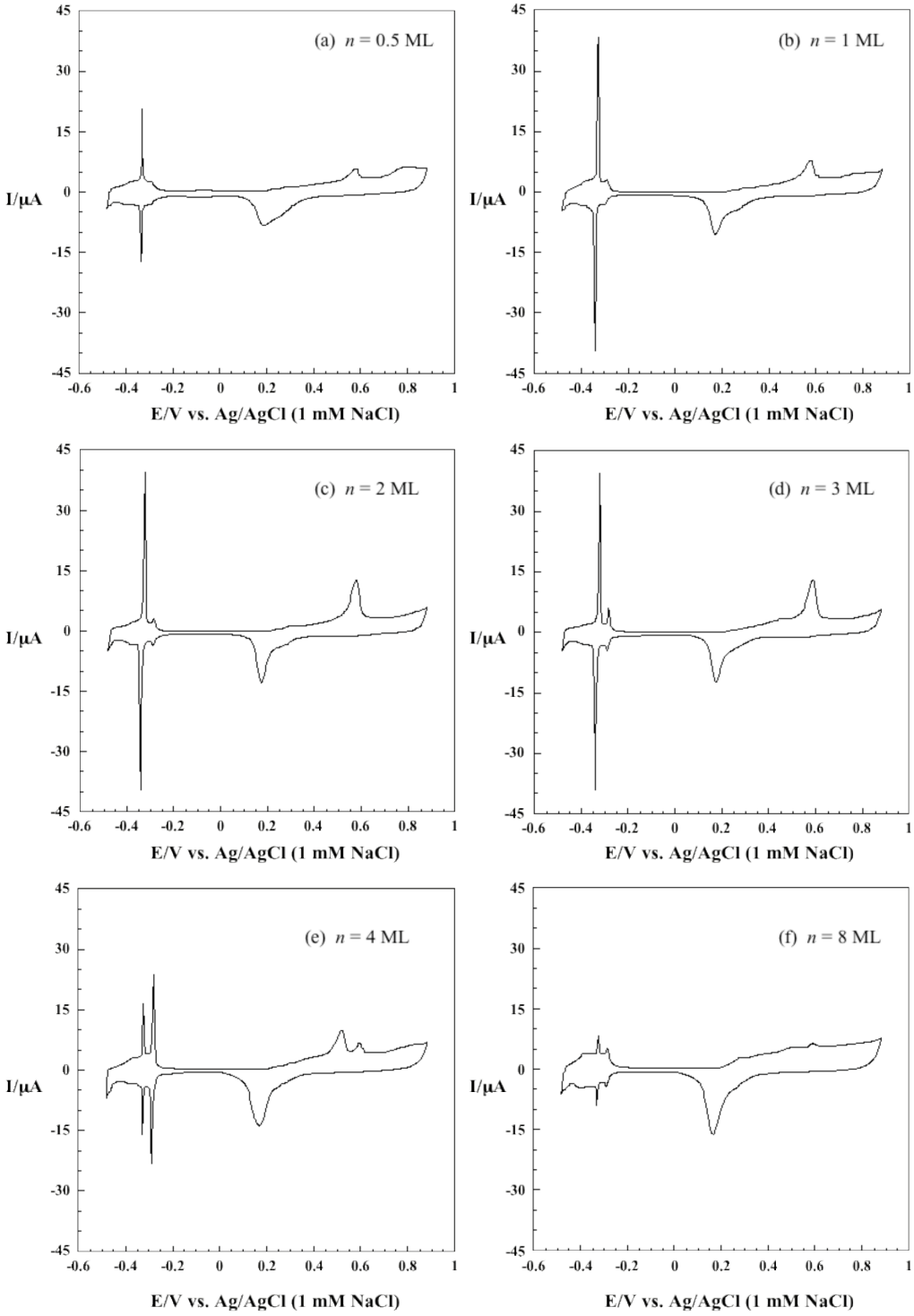

Figure A-4. Cyclic voltammograms of *n*-ML Pd on Pt(111) in 0.1 M H_2SO_4.

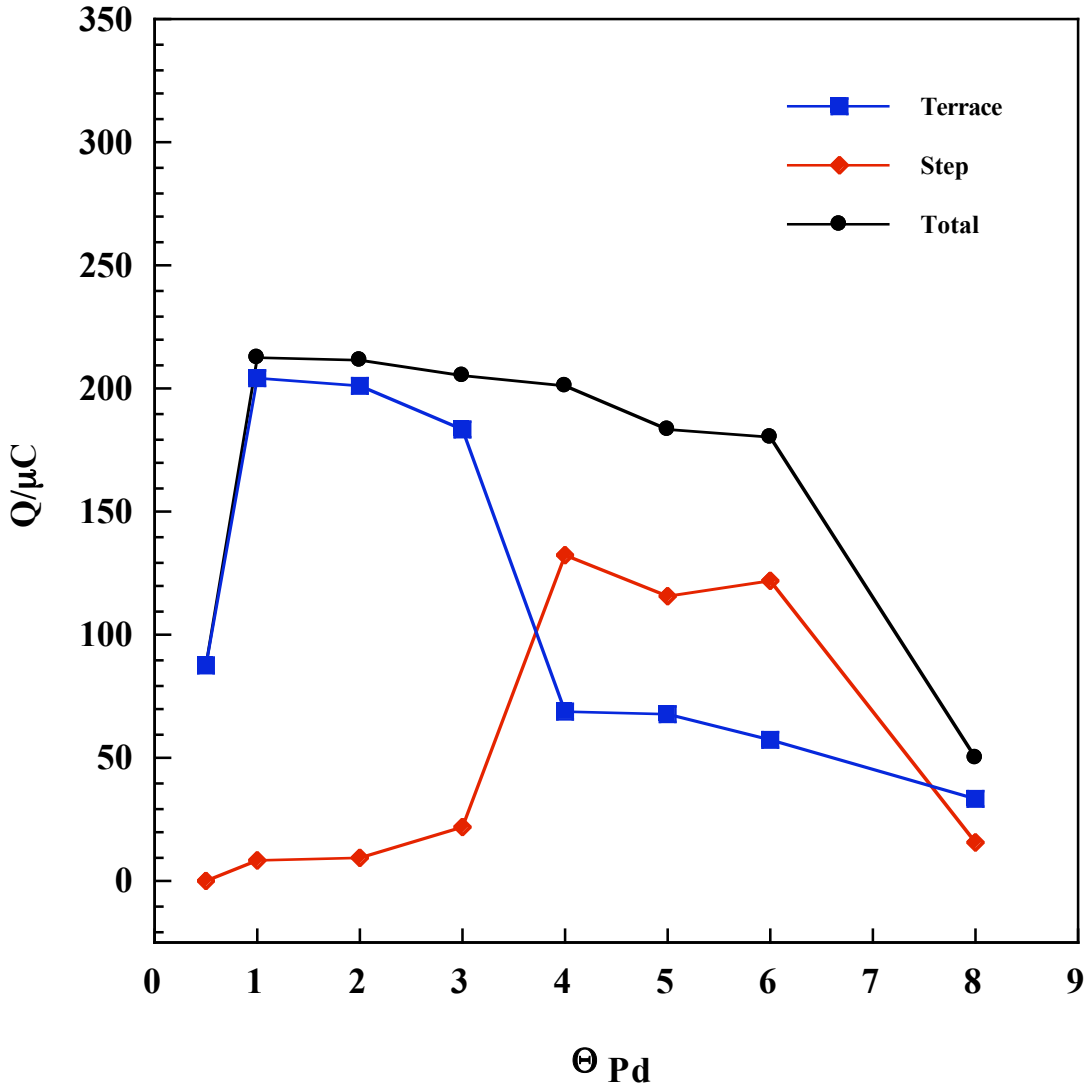

Figure A-5 . H_{upd} desorption charge of ultrathin Pd films as a function of Pd surface coverage. Experimental details are as in Figure 3.

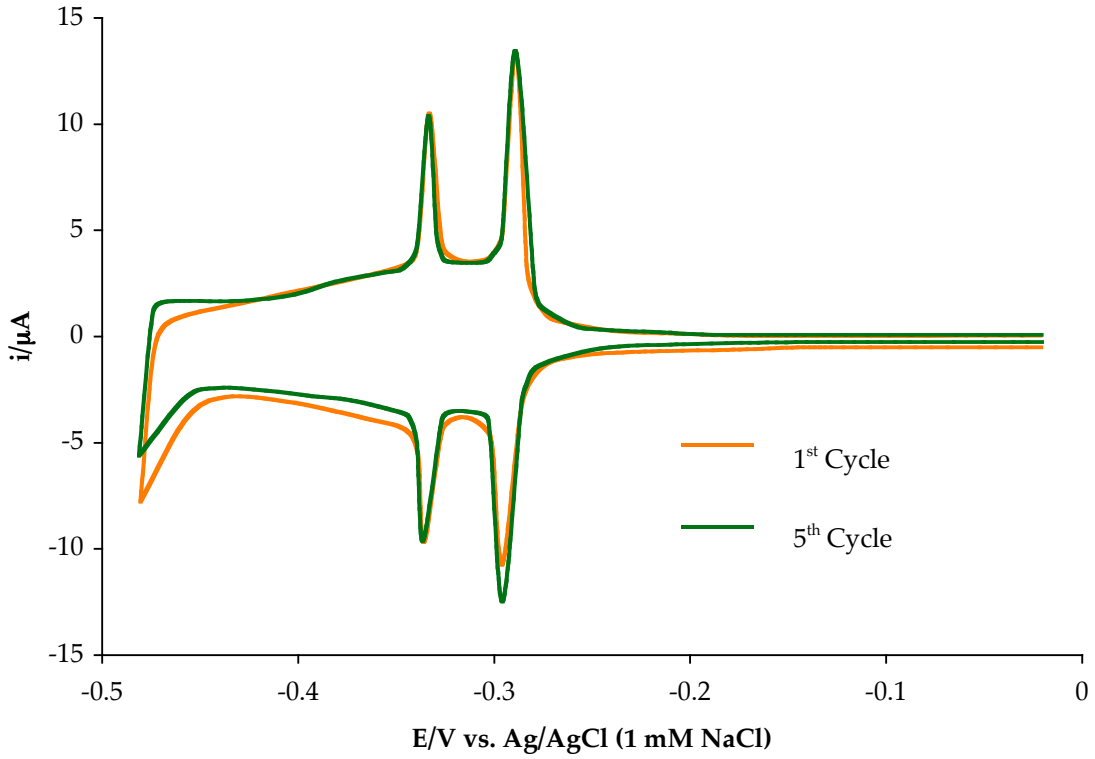

Figure A-6. Cyclic voltammograms for 4 ML Pd/Pt(111) during potential cycling in 0.1 M H_2SO_4 between the double layer and hydrogen evolution regions.

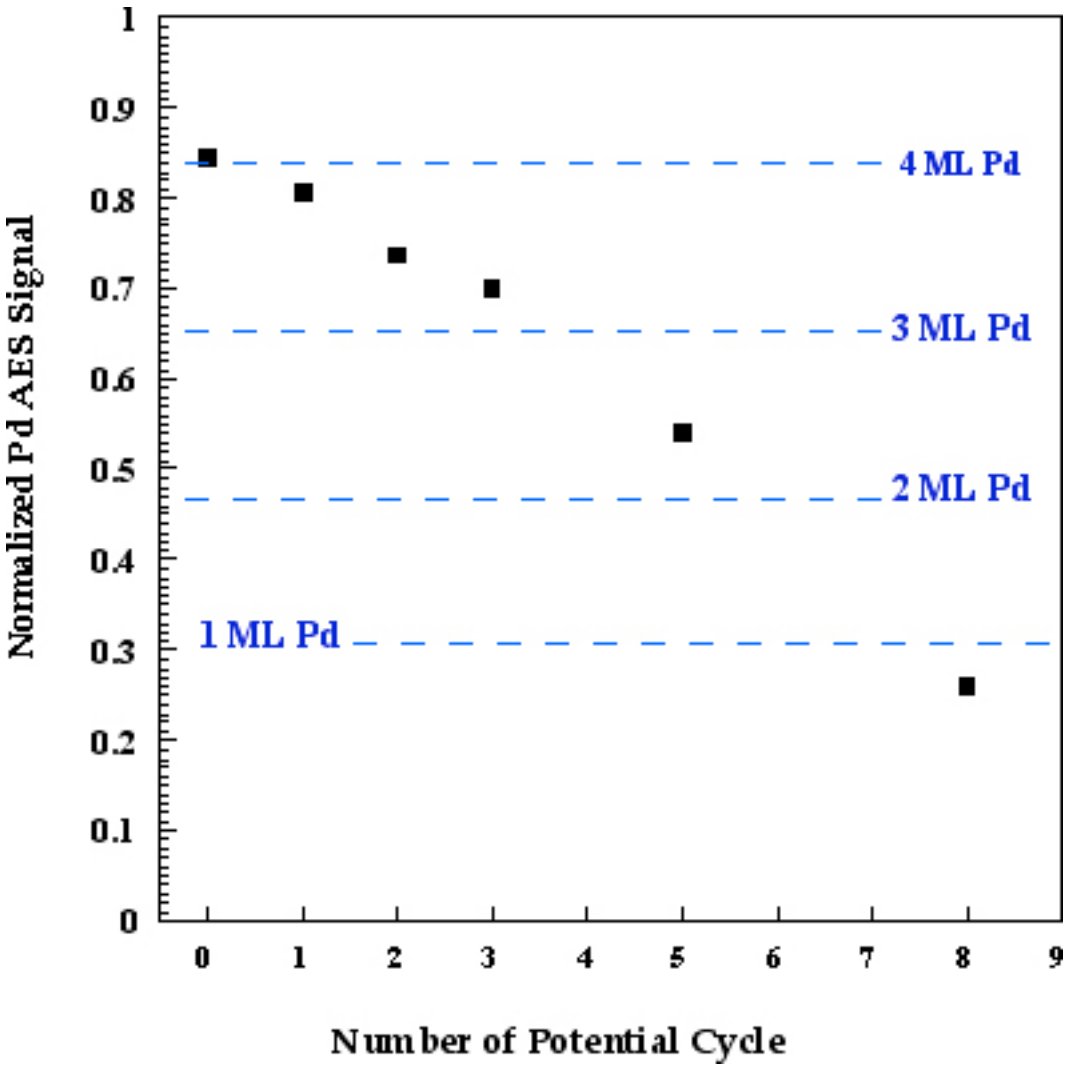

Figure A-7. Pd Auger signal intensity as a function of the number of potential cycles. The Pd intensity was obtained from Auger electron spectra of 4 ML Pd film after each potential cycle between –0.48 V and 0.88 V. Incident beam energy = 2 keV; beam current = 1 μA.

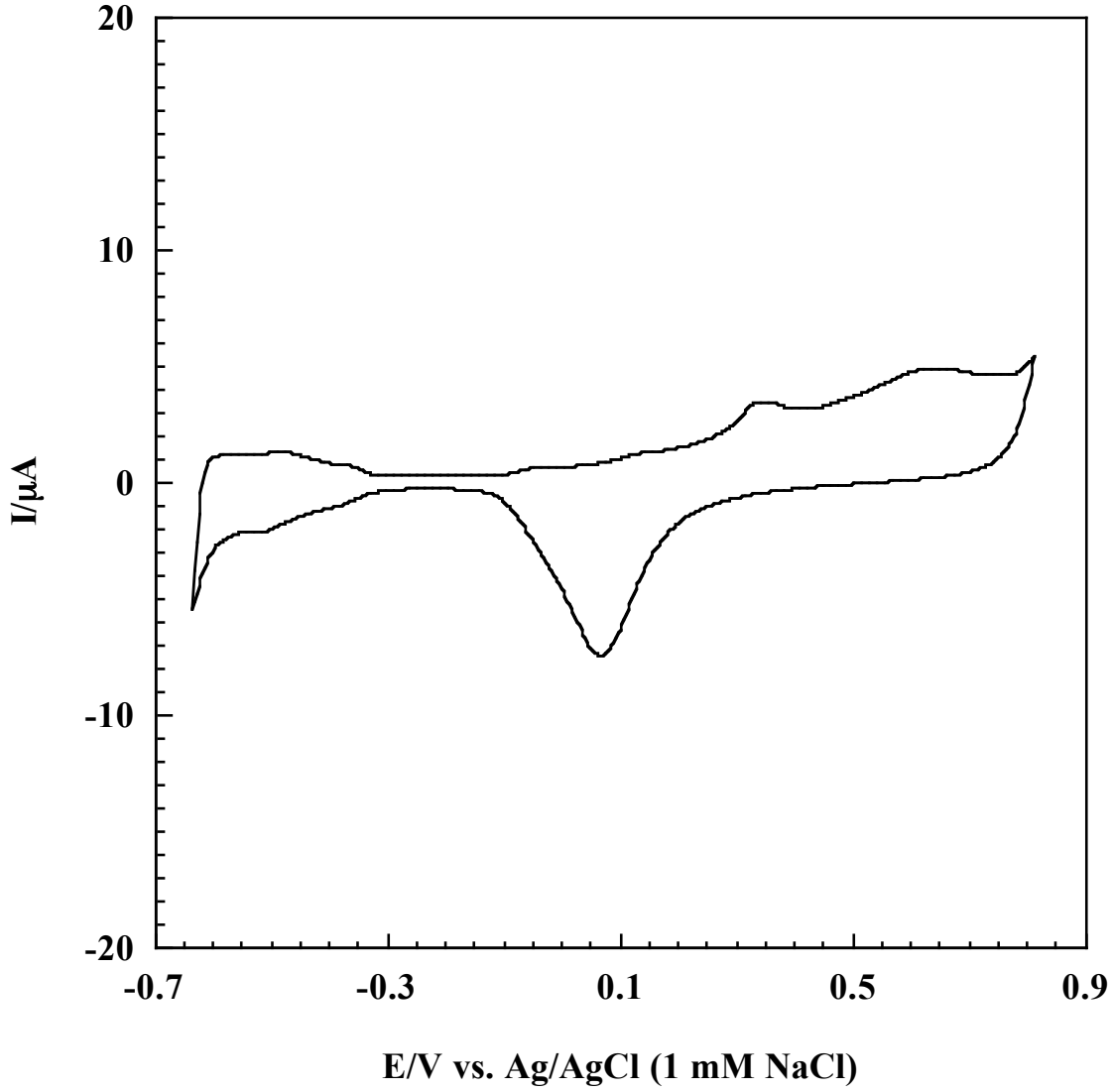

Figure A-8. Cyclic voltammogram of a Pt(111) disc electrode in 0.1 mM NaF solution adjusted to pH = 4 with trifluoroacetic acid (TFA). Scan rate = 2 mV/sec. Electrode area = 1.12 cm^2.

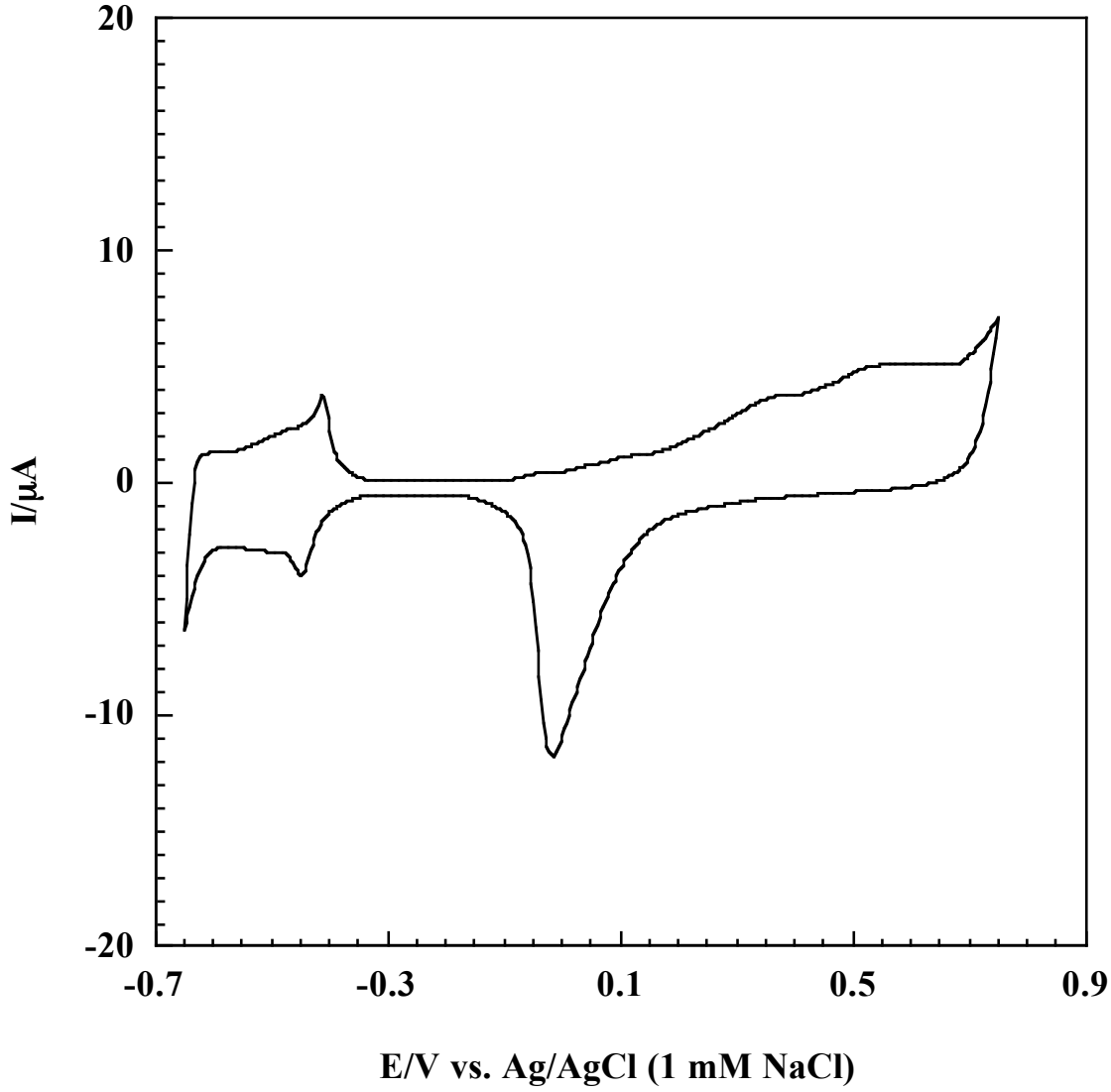

Figure A-9. Cyclic voltammogram of 1 ML Pd film on Pt(111) in 0.1 M NaF solution adjusted to pH 4 with trifluoroacetic acid (TFA). Scan rate = 2 mV/sec. Electrode area = 1.12 cm^2.

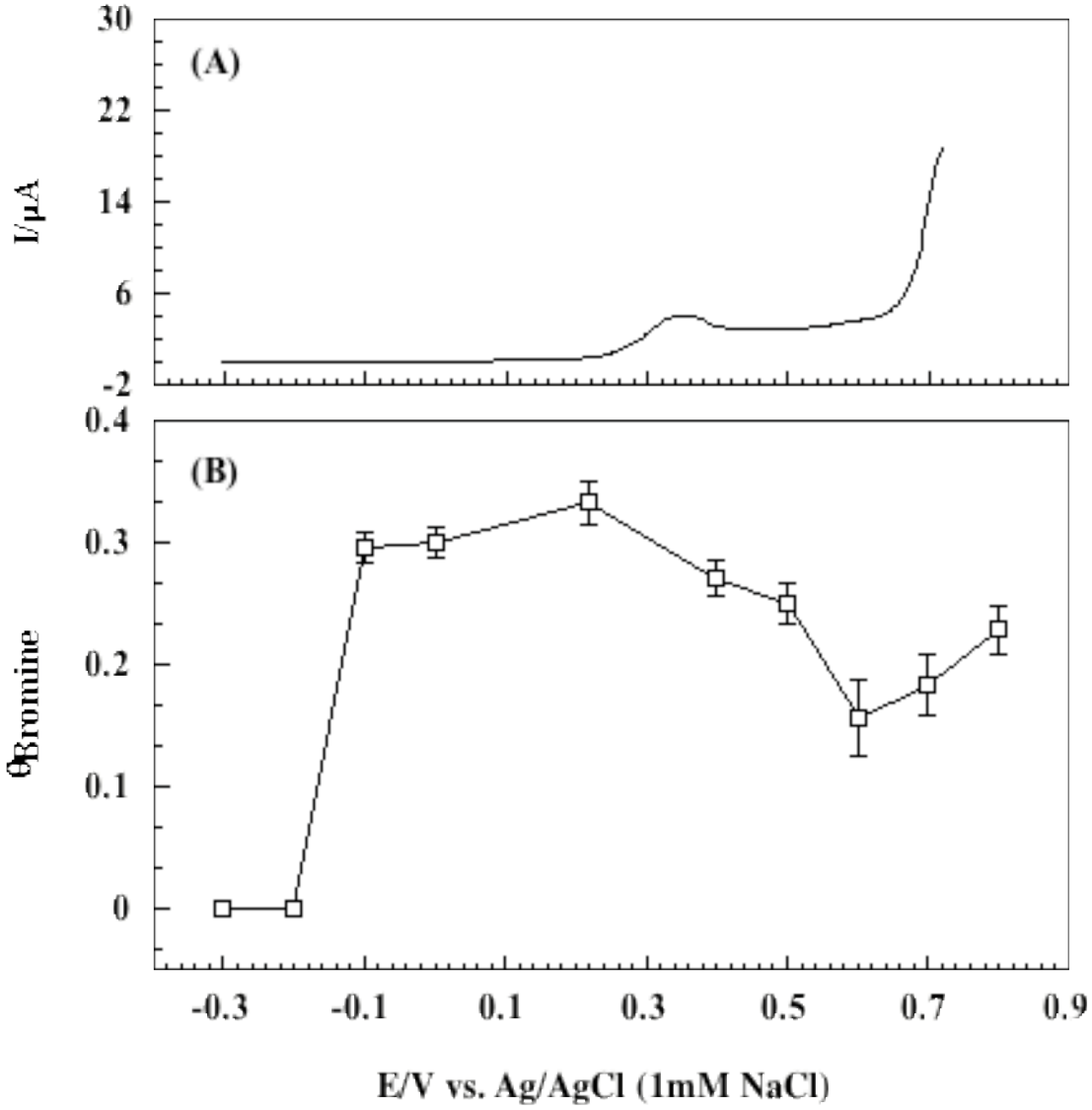

Figure A-10. Correlation between Br coverage and voltammetric features of 1 ML Pd film in bromide-containing electrolyte. (a) Linear sweep voltammogram of 1 ML Pd/Pt(111) in 1 mM NaBr in 0.1 M NaF (pH = 4) (b) Bromine coverage on 1 ML Pd film as a function of bromine adsorption potential. Bromine was adsorbed from 1 mM NaBr in 0.1 M NaF (pH = 4). Bromine adsorption time = 3 minutes.

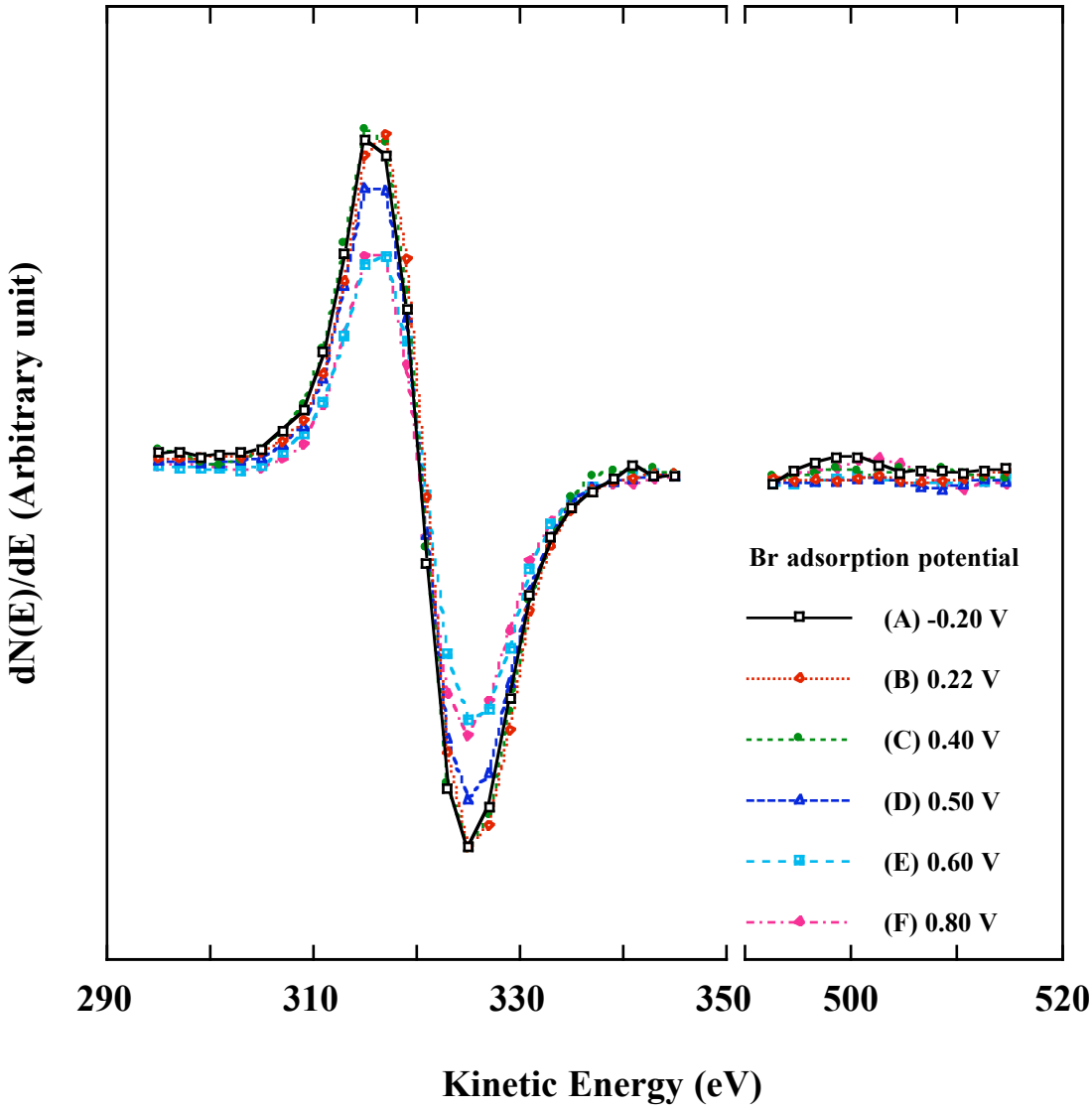

Figure A-11. Auger electron spectra showing changes in Pd and O signals after bromine adsorption onto 1 ML Pd/Pt(111) at various potentials. Incident beam energy = 2 keV; beam current = 1 μA.

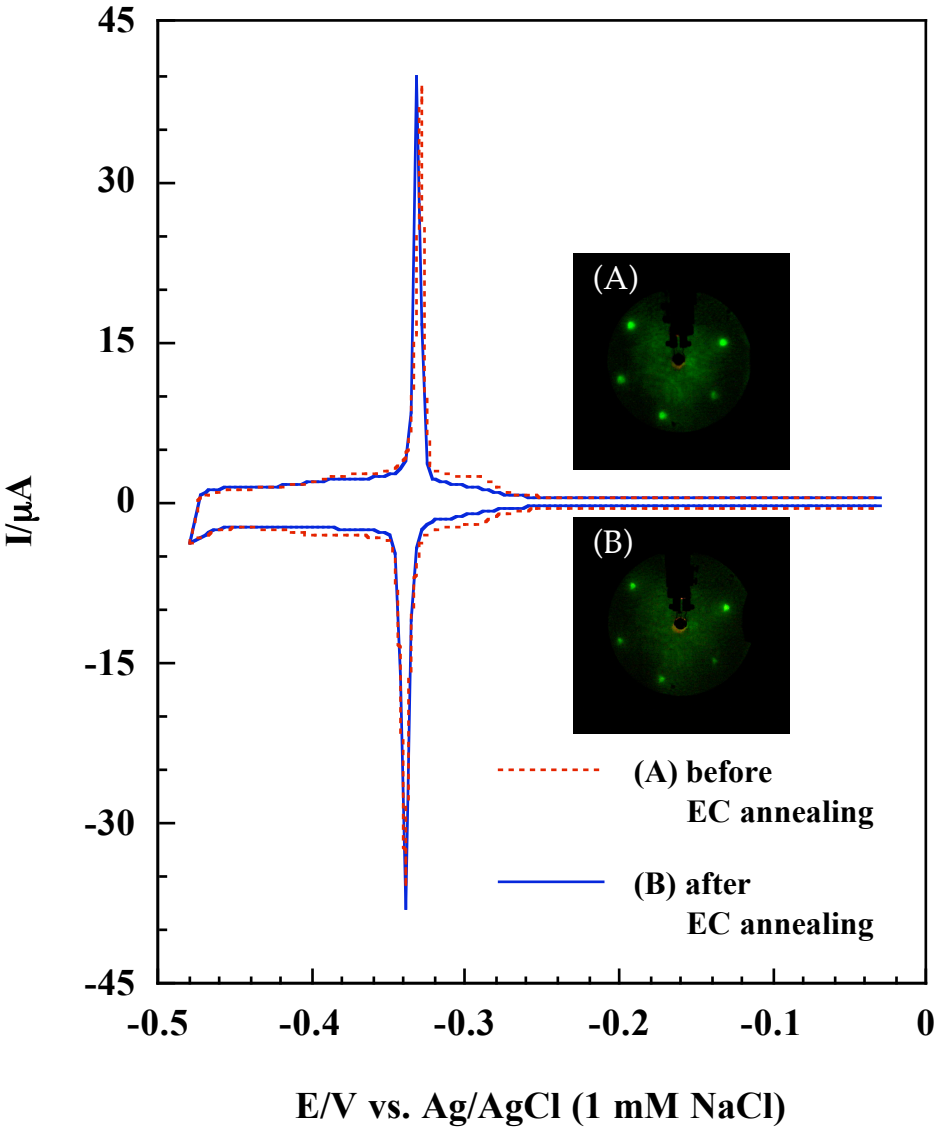

Figure A-12. Voltammograms for 1 ML Pd_{CPD} film on Pt(111) in 100 mM H_2SO_4 obtained (A) before and (B) after EC annealing. Scan rate = 2 mV/sec. Electrode area = 1.12 cm^2. Inset: LEED patterns obtained (A) before and (B) after EC annealing. Beam energy = 62.0 eV; beam current = 2 μA.

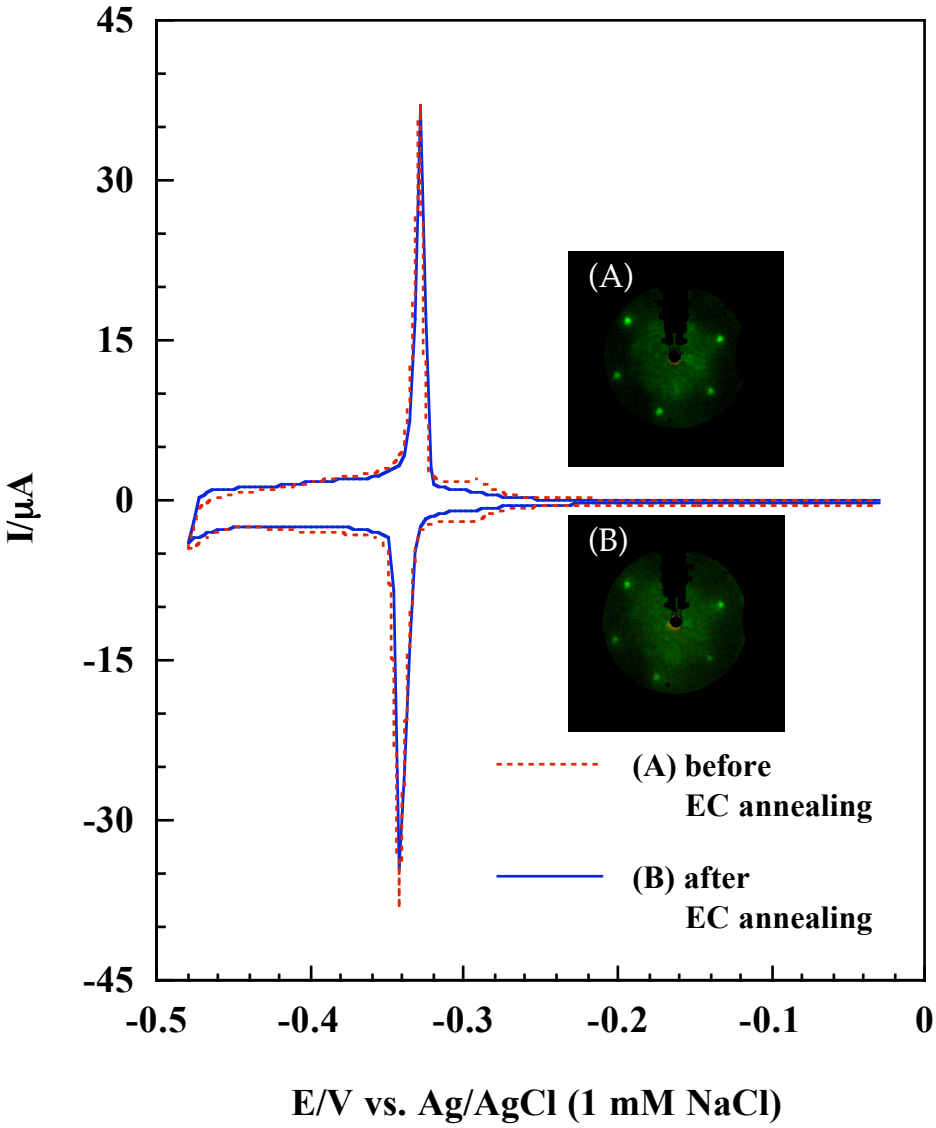

Figure A-13. Voltammograms for 2 ML Pd_{CPD} film on Pt(111) in 100 mM H_2SO_4 obtained (A) before and (B) after EC annealing. Scan rate = 2 mV/sec. Electrode area = 1.12 cm^2. Inset: LEED patterns obtained (A) before and (B) after EC annealing. Beam energy = 62.0 eV; beam current = 2 μA.

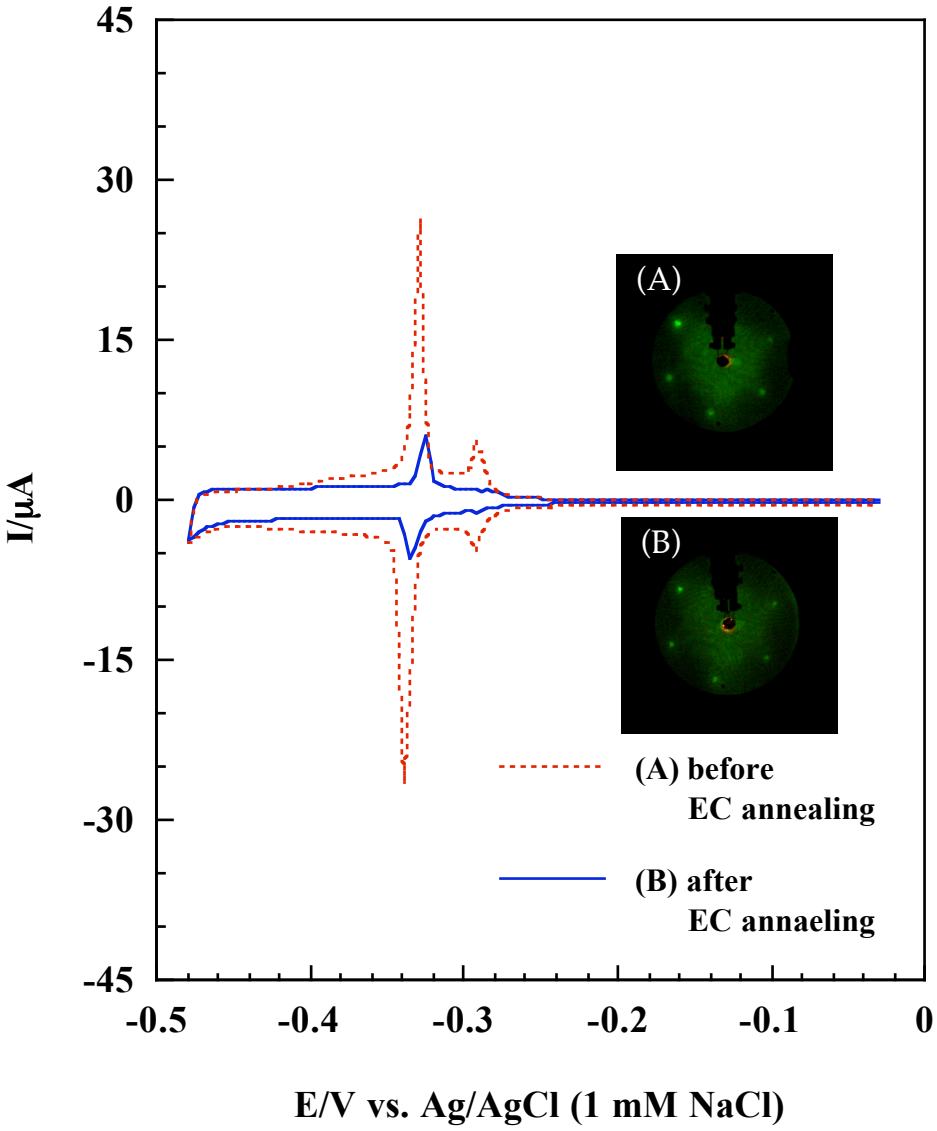

Figure A-14. Voltammograms for 3 ML Pd_{CPD} film on Pt(111) in 100 mM H_2SO_4 obtained (A) before and (B) after EC annealing. Scan rate = 2 mV/sec. Electrode area = 1.12 cm^2. Inset: LEED patterns obtained (A) before and (B) after EC annealing. Beam energy = 62.0 eV; beam current = 2 μA.

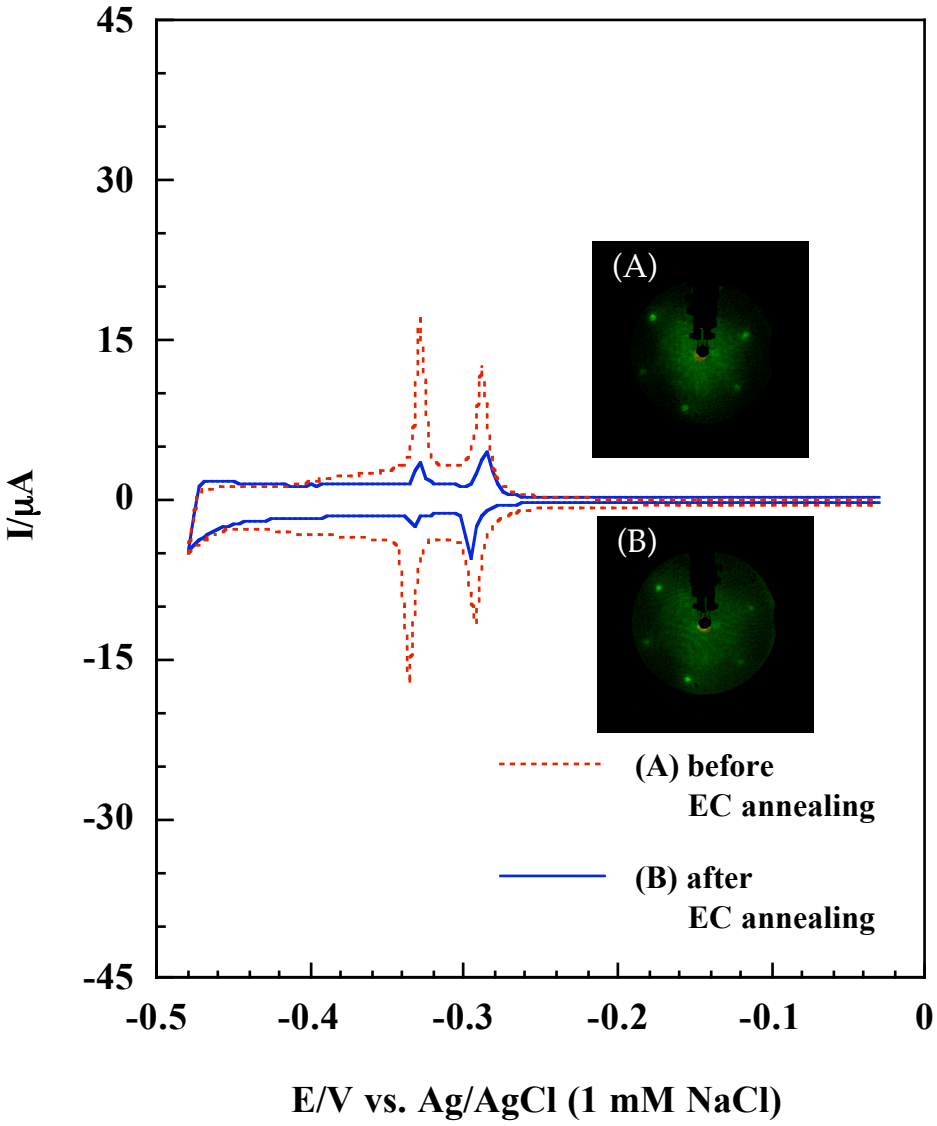

Figure A-15. Voltammograms for 4 ML Pd_{CPD} film on Pt(111) in 100 mM H_2SO_4 obtained (A) before and (B) after EC annealing. Scan rate = 2 mV/sec. Electrode area = 1.12 cm^2. Inset: LEED patterns obtained (A) before and (B) after EC annealing. Beam energy = 62.0 eV; beam current = 2 μA.

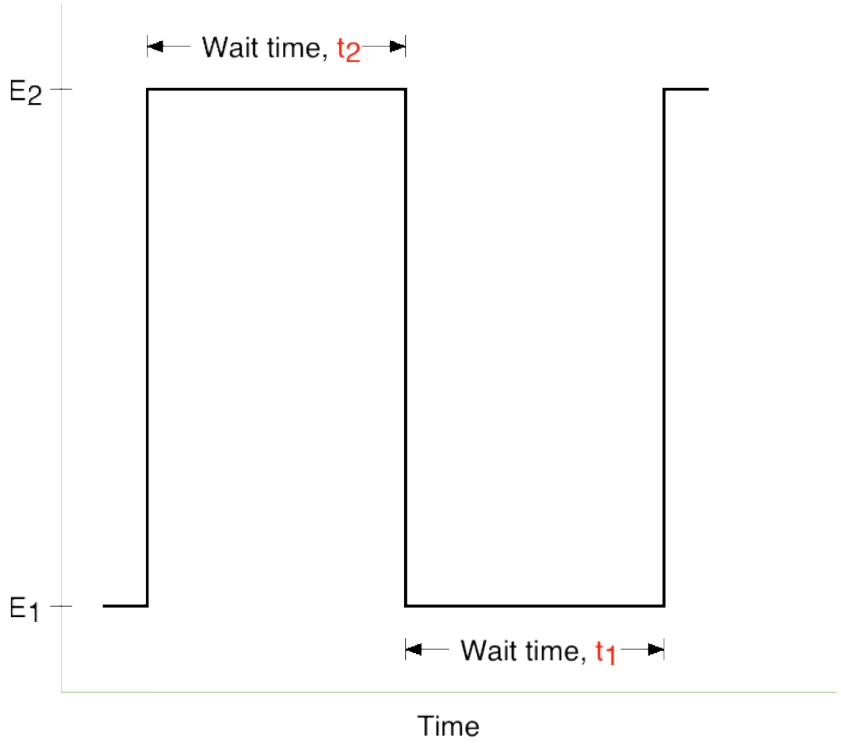

Figure A-16. Schema of a complete potential cycle during electrochemical annealing in NaBr solution. E_1 = 0.22 V, at which Br chemisorption occurred; E_2 = –0.40 V, near the onset of hydrogen evolution.

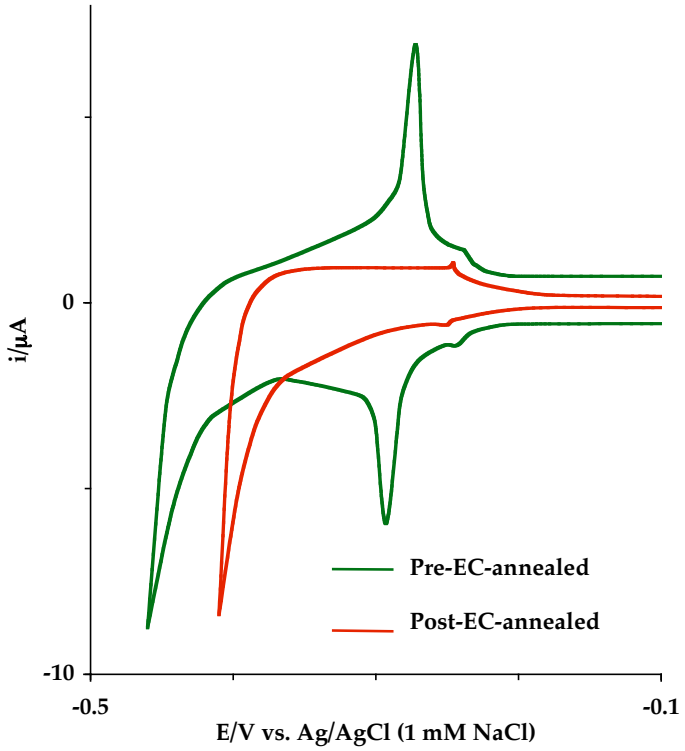

Figure A-17. Current-potential profile of 8 ML Pd/Pt(111) before and after electrochemical annealing in 1 mM NaBr–0.1 M NaF (pH = 4) solution. Cyclic voltammograms were obtained in Br-free 0.1 M NaF (pH = 4) solution at a scan rate of 2 mV/s.

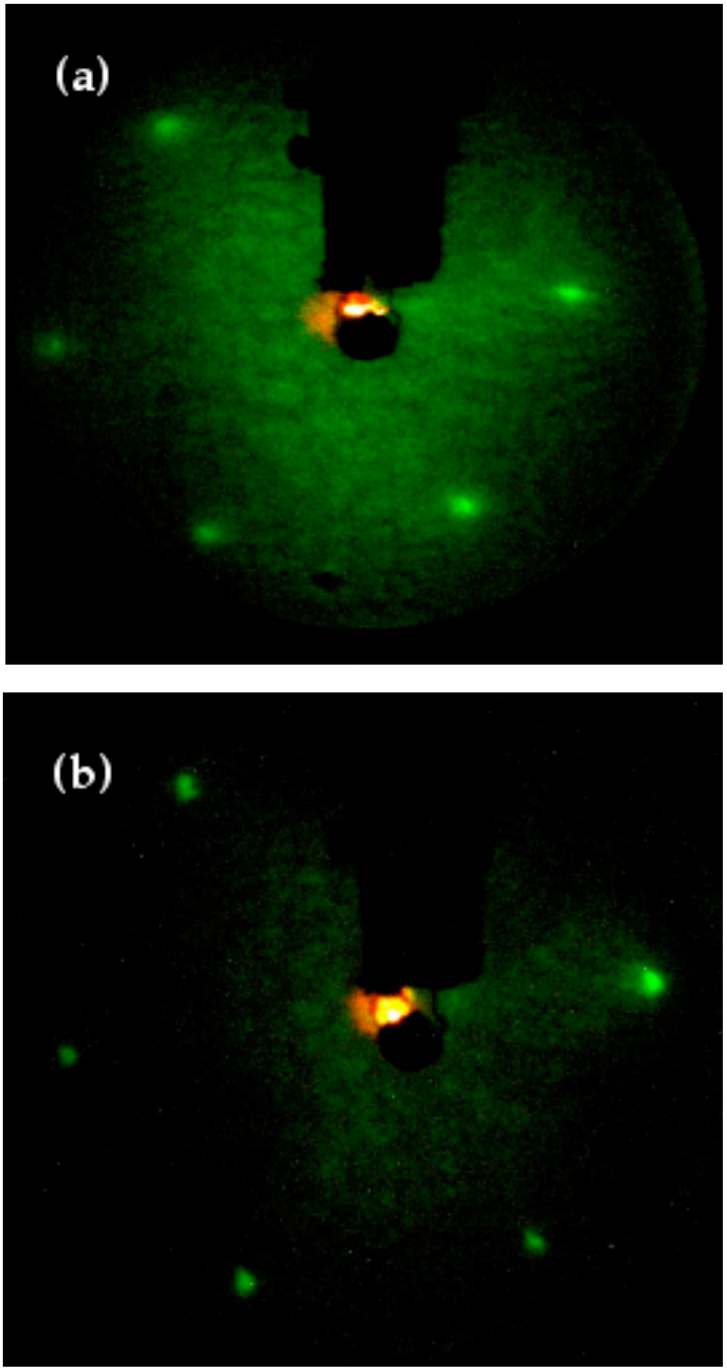

Figure A-18. LEED pattern of 8 ML Pd/Pt(111) (a) before and (b) after electrochemical annealing in $NaBr_{(aq)}$. Beam energy = 62 eV; beam current = 2 μA.

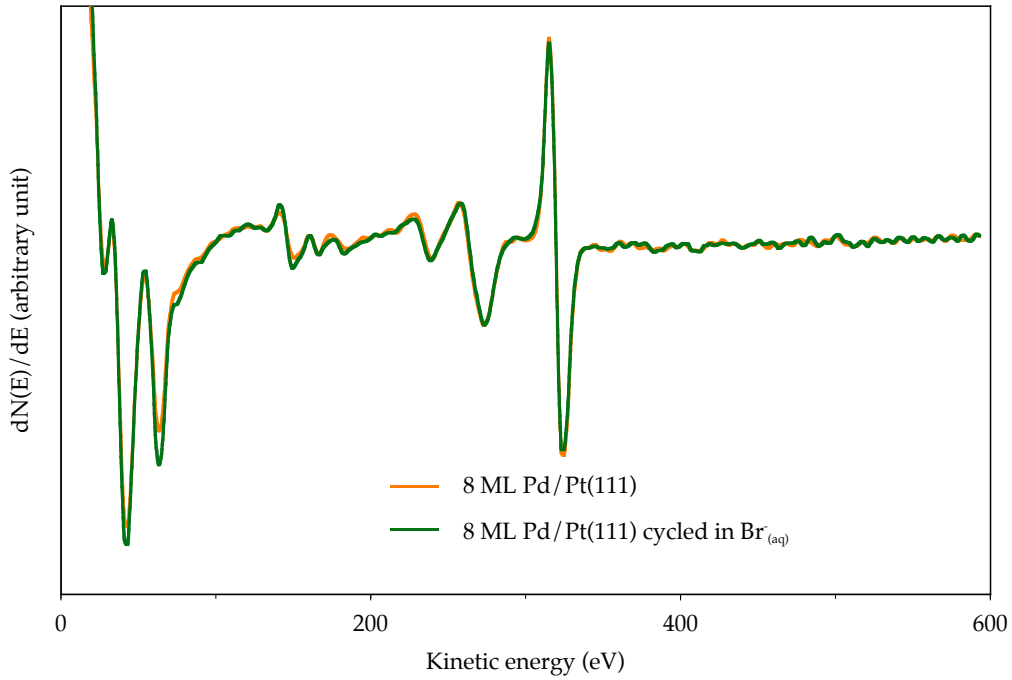

Figure A-19. Auger electron spectrum of 8 ML Pd/Pt(111) after electrochemical annealing in 1 mM NaBr/0.1 M NaF (pH = 4). Incident beam = 2 keV; beam current = 1 μA.

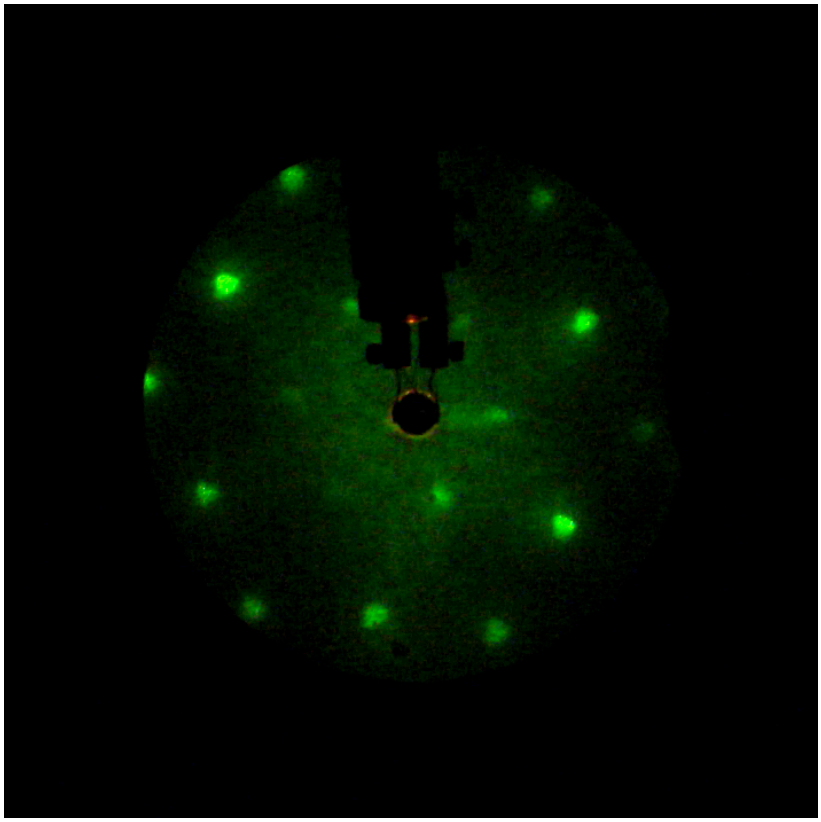

Figure A-20. LEED pattern for 6 ML Pd/Pt(111) obtained after emersion from 1 mM NaBr in 0.1 M NaF (pH = 4). Beam energy = 62.0 eV; beam current = 2 μA.

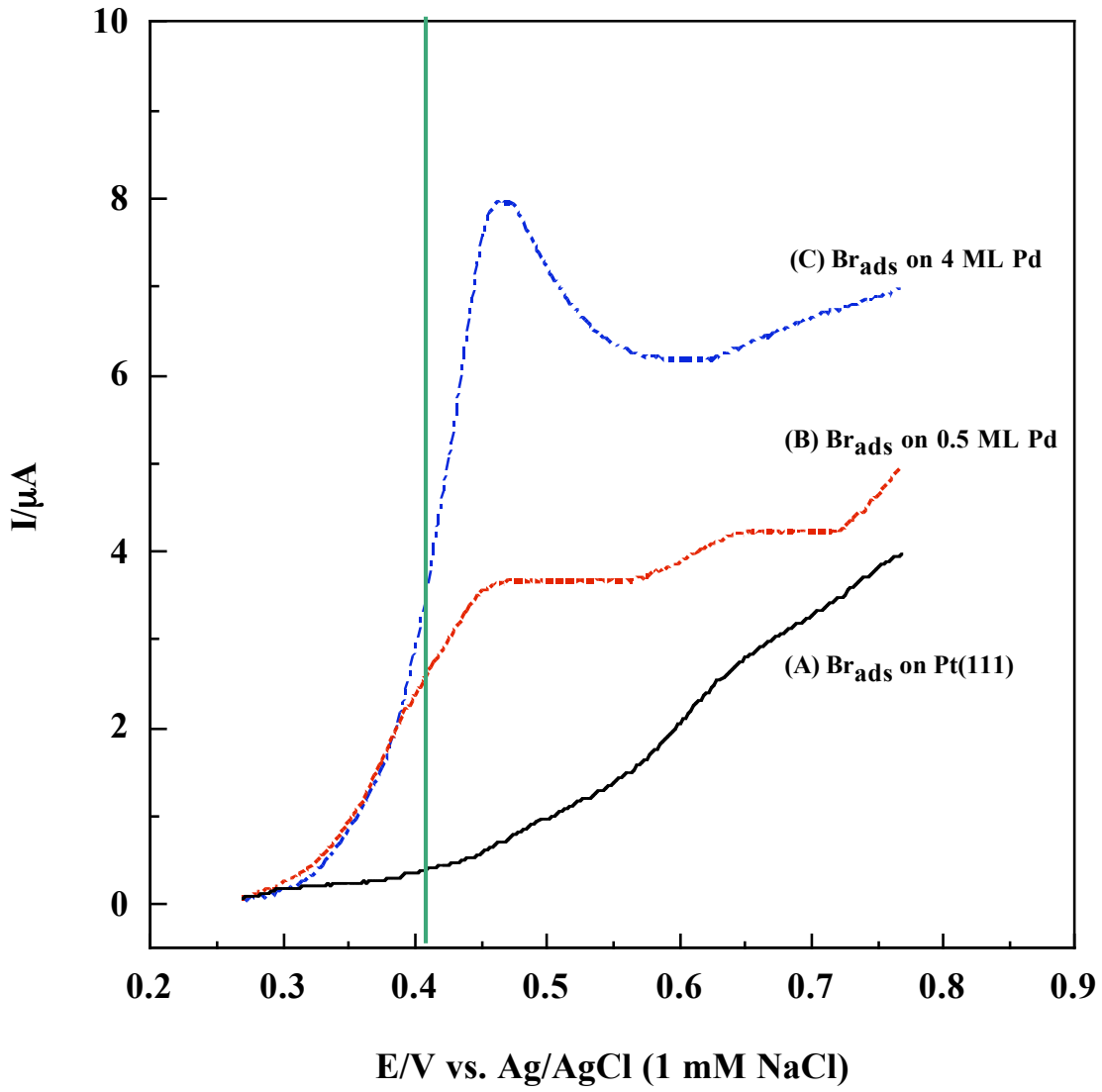

Figure A-21. Linear sweep voltammograms for Br_{ads} on (a) Pt(111), (b) 0.5 ML Pd film, and (c) 4 ML Pd film in 0.1 M H_2SO_4. Sweep rate = 2 mV/sec. Electrode area = 1.12 cm^2.

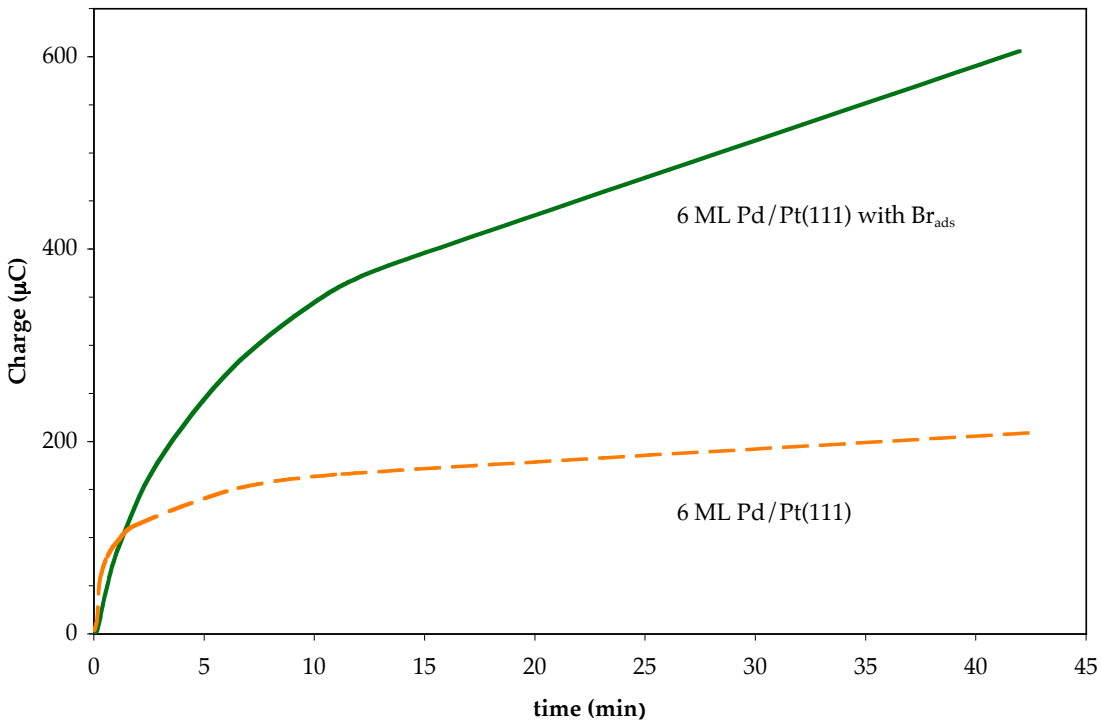

Figure A-22. Chronocoulogram of Br-modified 6 ML Pd/Pt(111) in 0.1 M H_2SO_4 as the potential was switched from 0.22 V to 0.41 V.

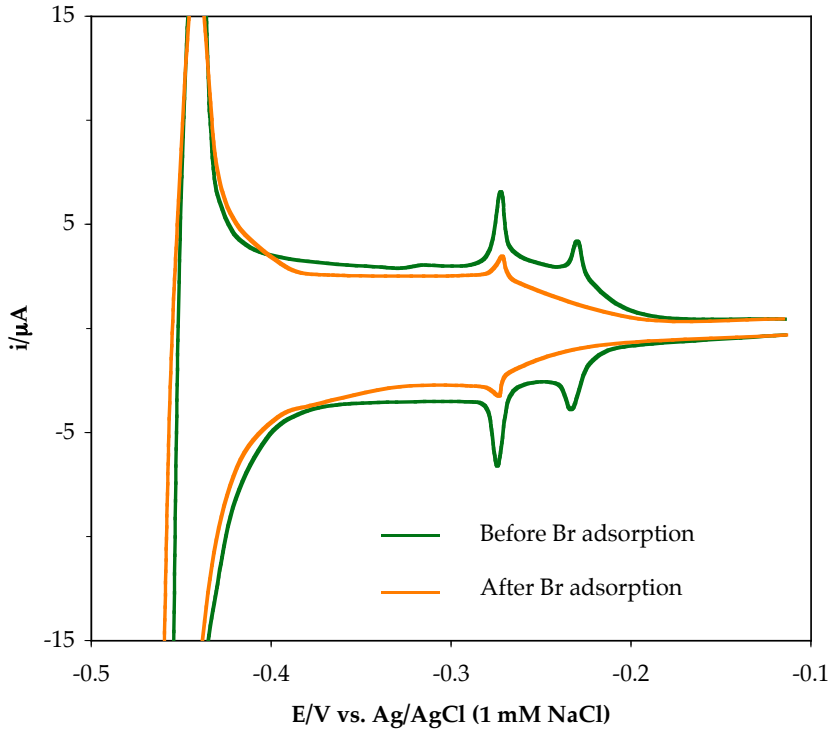

Figure A-23. Cyclic voltammogram of 6 ML Pd/Pt(111) in 0.1 M H_2SO_4, before and after Br chemisorption and subsequent polarization at 0.41 V. Scan rate = 2 mV/s. Experimental details are described in the text.

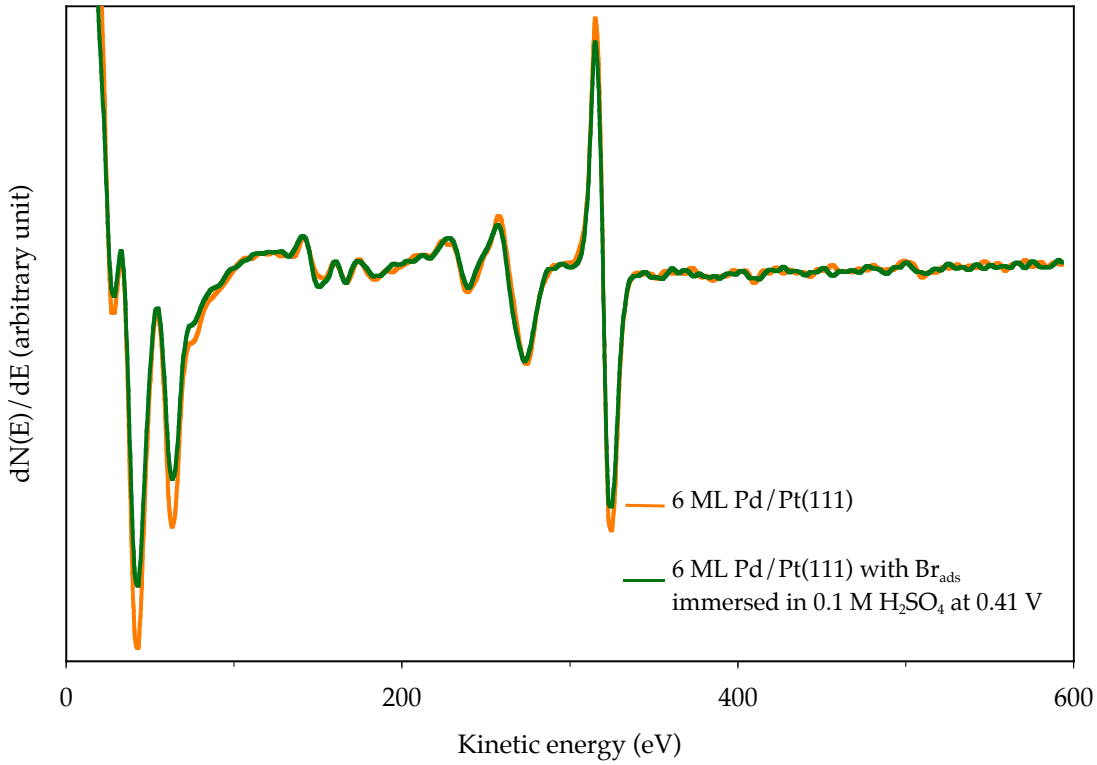

Figure A-24. Auger electron spectrum of Br-coated 6 ML Pd/Pt(111) after immersion in 0.1 M H_2SO_4 at E = 0.41 V. Incident beam = 2 keV; beam current = 1 μA.

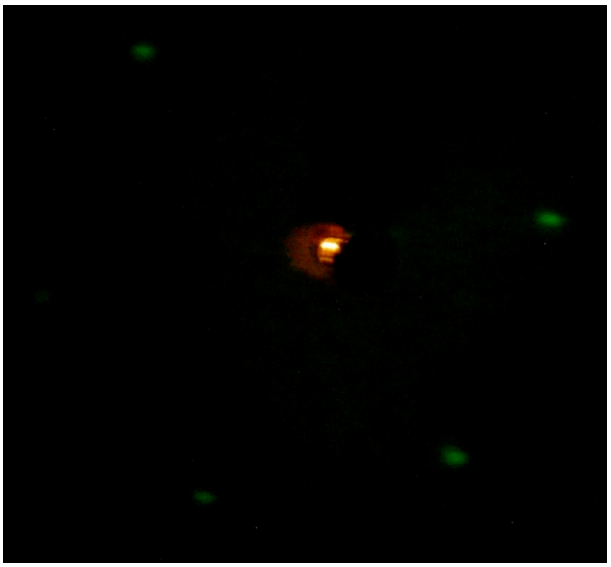

Figure A-25. LEED pattern after exposing Br-coated 4 ML Pd/Pt(111) in 0.1 M H_2SO_4 at E = 0.41 V. Beam energy = 62 eV; beam current = 2 μA. Experimental details are described in the text.

REFERENCES

A-[1] H.-J. Freund, G. Rupprechter, M. Baeumer, Th. Risse, N. Ernst, J. Libuda, NATO Science Series, II: Mathematics, Physics and Chemistry, Metal-Ligand Interactions 116 (2003) 65.

A-[2] F. Girgsdies, T. Ressler, U. Wild, T. Wuebben, T.J. Balk, G. Dehm, L. Zhou, S. Guenther, E. Arzt, R. Imbihl, R. Schloegl, Catal. Lett. 102 (2005) 91.

A-[3] T.E. Madey, NATO ASI Series, Series E: Applied Sciences, Chemisorption and Reactivity on Supported Clusters and Thin Films 331 (1997) 105.

A-[4] J. Camarero, J.J. de Miguel, R. Miranda, A. Hernando, J. Phys.: Condens. Matter 12 (2000) 7713.

A-[5] W. Schindler, Topics in App. Phys. 85 (2003) 243.

A-[6] J.N. Hilfiker, D.W. Glenn, S. Heckens, J.A. Woollam, K.W. Wierman, J. Appl. Phys. 79 (1996) 6193.

A-[7] M. Baldauf, D.M. Kolb, J. Phys. Chem. 100 (1996) 11375.

A-[8] W. R. Hendren, C. Cassidy, R. Atkinson, I.W. Salter, R.J. Pollard, J. Phys.: Condens. Matter 17 (2005) 5313.

A-[9] Y. Ren, C.L. Gao, Z.Z. Zhang, B. Ma, Q.Y. Jin, E. Ahmad, Y.B. Xu, J. Appl. Phys. 97 (2005), 10A305/1.

A-[10] C.W. Su, Y.D. Yao, C.S. Shern, J. Mag. Mag. Mater. 282 (2004) 84.

A-[11] S.-C. Shin, J.-W. Lee, S.-K. Kim, J. Kim, Appl. Phys. Lett. 81 (2002) 91.

A-[12] W. Kim, J.H. Choi, T.U. Nahm, S.H. Song, S.J. Oh, J. Korean Phys. Soc.

44 (2004) 722.

A-[13] K. Wasa, M. Kitabatake, H. Adachi, Thin Film Materials Technology: Sputtering of Compound Materials, Springer, Heidelberg, Germany, 2004.

A-[14] G. A. Somorjai, Introduction to Surface Chemistry and Catalysis, Wiley, New York, 1994.

A-[15] J.B. Bard, L.R. Faulkner, Electrochemical Methods: Fundamentals and Applications, Wiley, New York, 2001.

A-[16] W. Schindler, J. Kirschner, Phys. Rev. B: Condens. Matter 55 (1997) R1989.

A-[17] M. Hugelmann, P. Hugelmann, W.J. Lorenz, W. Schindler, Surf. Sci. 597 (2005) 156.

A-[18] A. Al-Akl, G. Attard, J. Phys. Chem. 101 (1997) 4597.

A-[19] E.A. Lafferty, Y.-G. Kim, M.P. Soriaga, Electrochim. Acta 44 (1998) 1031.

A-[20] E. Bauer, Appl. Surf. Sci. 11/12 (1982) 479.

A-[21] J.-M. Zhang, F. Ma, K. Xu, Appl. Surf. Sci, 229 (2004) 34.

A-[22] M.J. Ball, C.A. Lucas, N.M. Markovic, V. Stamenkovic, P.N. Ross, Surf. Sci. 518 (2002) 201.

A-[23] R. Hoyer. L.A. Kibler, D.M. Kolb, Electrochim. Acta 49 (2003) 63.

A-[24] V. Clement, N.M. Markovic, P.N. Ross, J. Phys. Chem. B 104 (2000) 3116.

A-[25] G.A. Attard, R. Price, A. Al-Akl, Electrochim. Acta 39 (1994) 1525.

A-[26] G.A. Attard, R. Price, Surf. Sci., 335 (1995) 63.

A-[27] N.M. Markovic, C.A. Lucas, V. Climent, V. Stamenkovic, N.P. Ross,

Surf. Sci. 465 (2000) 103.

A-[28] G.A. Attard, A. Bannister, J. Electroanal. Chem. 300 (1991) 467.

A-[29] J. Clavilier, M.J. Llorca, J.M. Feliu, A. Aldaz, J. Electroanal. Chem. 310 (1991) 429.

A-[30] R.M. Lambert, Surf. Sci. 27 (1971) 653.

A-[31] A. Capon, R. Parsons, J. Electroanal. Chem. 65 (1975) 285.

A-[32] C. Gabrielli, P.P Grand, A. Lasia, H. Perrot, J. Electrochem. Soc. 151 (2004) A1937.

A-[33] A. Carrasquillo, Jr., Ph.D. Dissertation, Texas A&M University, 1995.

A-[34] R.J. Barriga, Ph.D. Dissertation, Texas A&M University, 1998.

A-[35] Y.-G. Kim, M.P. Soriaga, J. Phys. Chem. B 102 (1998) 6188.

VITA

JACK HESS L. BARICUATRO
Dept. of Chemistry, c/o Dr. Manuel P. Soriaga, Texas A&M University
College Station, TX 77842-3012
Tel: (979) 845-6914; e-mail: baricuatro@mail.chem.tamu.edu

EDUCATION

Ph. D., Analytical Chemistry, Texas A&M University, College Station, TX, 2006
M. S. Chemistry, University of San Carlos, Philippines, 1997
B. S. Chemistry, *Summa cum laude,* University of San Carlos, Philippines, 1993

AWARDS

Distinguished Graduate Student Award, The Association of Former Students of Texas A&M University, Spring 2004

SELECTED PUBLICATIONS

1. Y.-G. Kim, J.H. Baricuatro, M.P. Soriaga and D.W. Suggs. "Adsorbate-induced Disorder-to-order Surface Reconstruction: Iodine on Pd(111) Revisited by EC-STM". Journal of Electroanalytical Chemistry (2001), 509(2), 170-174.
2. Y.-G. Kim, X. Chen, Y.-S. Park, J.H. Baricuatro, J. Sanabria-Chinchilla and M. P. Soriaga. "Surface Organometallic Chemistry of Well-defined Palladium Electrodes". Journal of the Argentine Chemical Society (Special Issue). (2003), 91(1-3), 1-22.
3. C. S. Wang, M. Marrero-Cruz, J.H. Baricuatro, M.P. Soriaga, D. Serafini and S. Srinivasan. "Corrosion Behaviour of AB_5-type Hydride Electrodes in Alkaline Electrolyte Solution". Journal of Applied Electrochemistry (2003), 33(3-4), 325-331.
4. C. S. Wang, M. Marrero-Cruz, J.H. Baricuatro, M.P. Soriaga, D. Serafini and S. Srinivasan. "Self-discharge Mechanisms of AB_5-type Hydride Electrode Used for Ni/MH Battery". International Journal of Hydrogen Energy (2006), 31(5), 603-611.
5. Y.-G. Kim, J.H. Baricuatro and M.P. Soriaga. "Molecular Adsorption at Well-defined Electrode Surfaces: Hydroquinone on Pd(111) Studied by EC-STM". Langmuir. Submitted (April 2006).
6. J.H. Baricuatro, Y.-S Park, M. Hossain and M.P. Soriaga. "Highly-ordered Ultrathin Pd Films on Pt(111): Electrodeposition and Structural Characterization". Journal of Electroanalytical Chemistry. To be submitted (June 2006).